

Search for Neutral Higgs Bosons Decaying to Pairs of τ Leptons at $\sqrt{s} = 7$ TeV

By

EVAN KLOSE FRIIS

B.S. (University of California at San Diego) 2005

DISSERTATION

Submitted in partial satisfaction of the requirements for the degree of

DOCTOR OF PHILOSOPHY

in

Physics

in the

OFFICE OF GRADUATE STUDIES

of the

UNIVERSITY OF CALIFORNIA

DAVIS

Approved:

Professor John Conway (Chair)

Professor Robin Erbacher

Professor Mani Tripathi

Committee in Charge

2011

3 Abstract

4 This thesis describes a search for the Higgs boson, a new particle predicted by a theory called
5 the Minimal Supersymmetric Model (MSSM). The Standard Model of particle physics, the
6 MSSM, and Higgs phenomenology are introduced briefly. The search presented in this thesis
7 uses a single final state configuration, in which the Higgs boson decays to two tau leptons,
8 where one tau decays to a muon and neutrinos, and the other decays to pions and a single
9 neutrino. Two new methods are introduced in this analysis, the Tau Neural Classifier tau
10 identification algorithm, and the Secondary Vertex fit tau pair mass reconstruction method.
11 Both methods are discussed in detail. The analysis uses the 2010 dataset from the Compact
12 Muon Solenoid (CMS) experiment, which contains 36 pb^{-1} of integrated luminosity at a
13 center of mass energy of 7 TeV. In total, 573 events are selected in the analysis; this value
14 is compatible with the Standard Model expectation. No excess of signal events is observed,
15 and we set an upper limit on cross section times branching ratio of a Higgs boson. This
16 limit is interpreted in the parameter space of the MSSM.

¹⁷ **Acknowledgments**

¹⁸

Hooray for everybody.

¹⁹ Table of Contents

²⁰ Introduction	¹
1 The Standard Model and Beyond	3
1.1 The Standard Model	3
1.1.1 Quantum Electrodynamics and Gauge Invariance	4
1.1.2 The Weak Interactions	6
1.1.3 Spontaneous Symmetry Breaking	8
1.1.4 The Higgs Mechanism	10
1.1.5 Electroweak Unification	12
1.1.6 Quantum Chromodynamics	16
1.2 Beyond the Standard Model	18
1.2.1 The Hierarchy Problem	19
1.2.2 Supersymmetry	20
1.2.3 The Minimal Supersymmetric Model	20
1.3 Searches for the Higgs boson	23
1.3.1 Standard Model Higgs boson phenomenology	23
1.3.2 MSSM Higgs Phenomenology	27
1.3.3 Results from LEP and Tevatron	30
1.4 The Physics of the Tau Lepton	33
2 The Compact Muon Solenoid Experiment	37
2.1 The Large Hadron Collider	38
2.2 Solenoid Magnet	40
2.3 Charged Particle Tracking Systems	41
2.4 Electromagnetic Calorimeter	43
2.5 Hadronic Calorimeter	45
2.6 Muon System	47
2.7 Trigger System	49
3 Tau Identification: The Tau Neural Classifier	52
3.1 Geometric Tau Identification Algorithms	53
3.2 Decay Mode Tau Identification: Motivation	53
3.3 The Tau Neural Classifier	54
3.3.1 Decay Mode Reconstruction	55
3.3.2 Neural Network Classification	58
3.4 Summary	72
3.5 HPS+TaNC: A Hybrid Algorithm	76
3.5.1 Decay mode reconstruction	76
3.5.2 Hadronic tau discrimination	78

56	3.6 Electron and Muon Rejection	79
57	4 Mass Reconstruction: The Secondary Vertex Fit	81
58	4.1 Existing mass reconstruction algorithms	81
59	4.2 The Secondary Vertex fit	83
60	4.3 Parametrization of tau decays	84
61	4.4 Likelihood for tau decay	85
62	4.4.1 Likelihood for reconstructed missing transverse momentum	85
63	4.4.2 Likelihood for tau lepton transverse momentum balance	87
64	4.4.3 Secondary vertex information	88
65	4.5 Performance	90
66	5 Analysis Selections	94
67	5.1 High Level Trigger	94
68	5.2 Particle Identification	95
69	5.2.1 Muons	95
70	5.2.2 Hadronic Taus	96
71	5.2.3 Missing Transverse Energy	96
72	5.3 Event Selections	97
73	6 Data–Driven Background Estimation	102
74	6.1 Background Enriched Control Regions	103
75	6.2 The Fake–rate Method	104
76	6.2.1 Parameterization of Fake–rates	107
77	6.2.2 Measurement of Fake–rates	108
78	6.2.3 Application of Fake–rates	108
79	6.2.4 “Simple” weight method	109
80	6.2.5 “CDF–type” weights	111
81	6.2.6 k–Nearest Neighbor Fake–rate Calculation	113
82	6.2.7 Results of Fake–Rate Background Estimation	114
83	6.3 Template method	116
84	7 Monte Carlo Corrections	129
85	7.1 Muon Identification Efficiency	129
86	7.2 Hadronic Tau Identification Efficiency	132
87	7.3 Muon and Tau Momentum Scale	134
88	7.4 Missing Transverse Energy Correction	135
89	7.5 Pile-up Event Weighting	136
90	8 Systematics and Limit Extraction	138
91	8.1 Signal normalization uncertainties	140
92	8.2 Background normalization uncertainties	140
93	8.3 Shape uncertainties	141
94	8.4 Theory uncertainties	142
95	8.5 Limit Extraction Method	142
96	9 Results	149
97	9.1 Selected Events	149
98	9.2 Limits on Higgs Production	150

99	9.3 Interpretation in the MSSM	151
100	Conclusions	160
101	Bibliography	160

102 List of Figures

103	1.1	Fermi contact interaction diagram	7
104	1.2	Muon decaying through intermediate gauge boson	7
105	1.3	QCD Feynman Diagrams	17
106	1.4	Loop corrections to Higgs mass	19
107	1.5	Higgstrahlung production diagram at e^+e^- colliders	24
108	1.6	Gluon fusion Higgs production diagram	24
109	1.7	Vector boson fusion Higgs production diagram	24
110	1.8	Parton luminosity comparison of the LHC and Tevatron	25
111	1.9	SM Higgs cross sections at the LHC	26
112	1.10	SM Higgs branching fractions	27
113	1.11	Cross sections of interest at hadron colliders	28
114	1.12	MSSM Higgs production with association b -quarks	29
115	1.13	MSSM Higgs cross sections at the LHC	29
116	1.14	LEP Standard Model Higgs limit plot	31
117	1.15	Tevatron low mass Standard Model Higgs limit plot	32
118	1.16	Tevatron high mass Standard Model Higgs limit plot	33
119	1.17	LEP MSSM exclusion limits	34
120	1.18	Tevatron MSSM exclusion limits	34
121	2.1	Schematic drawings of the CMS detector	39
122	2.2	Material budget of the CMS tracker	42
123	2.3	Momentum and impact parameter resolutions of CMS tracker	43
124	2.4	Energy resolution of the CMS ECAL	45
125	2.5	Muon system material budget and identification efficiency	47
126	3.1	Visible invariant mass of τ lepton decay products	54
127	3.2	Invariant mass photon pairs in reconstructed π^0 mesons	56
128	3.3	Neutral energy fraction in visible τ decays	57
129	3.4	Tau decay mode reconstruction performance	59
130	3.5	Kinematic dependence of decay mode reconstruction	60
131	3.6	Neural network over-training validation plots	63
132	3.7	Kinematic weighting of training sample	65
133	3.8	Neural network output in each decay mode	68
134	3.9	Performance curves for the neural networks used in the TaNC	69
135	3.10	Tau Neural Classifier performance curves for different p_T ranges	70
136	3.11	Tau Neural Classifier transformation performance	72
137	3.12	Transformed neural network output	73
138	3.13	Tau Neural Classifier performance comparison	74
139	3.14	Tau Neural Classifier kinematic performance	75

140	3.15 Invariant mass distribution of PF photon pairs	77
141	4.1 Coordinate system of the SVfit	86
142	4.2 Effect of p_T -balance term on SVfit performance	89
143	4.3 Effect of the visible p_T requirements on muon and hadronic τ decays	90
144	4.4 Effect of the visible p_T requirements for Z and Higgs events	91
145	4.5 Comparison of SVfit with the Collinear Approximation algorithm	92
146	4.6 Comparison of SVfit with the visible mass observable	93
147	5.1 Distributions of M_T and muon isolation discriminants	99
148	5.2 Reconstruction and distribution of P_ζ discriminant	100
149	6.1 Visible mass distribution of the backgrounds in the signal and control regions	105
150	6.2 SVfit mass distribution of the backgrounds in the signal and control regions	106
151	6.3 p_T and η dependency of tau ID performance	119
152	6.4 Comparison of fake-rate contribution from genuine taus in the simple and CDF methods	121
154	6.5 Muon transverse momentum in the Fake-rate method	122
155	6.6 Tau-jet transverse momentum in the Fake-rate method	123
156	6.7 Visible mass in the Fake-rate method	124
157	6.8 k -Nearest Neighbor classifier example	125
158	6.9 Comparison of visible mass and SVfit mass	126
159	6.10 Comparison of background shapes in the signal and control regions	127
160	6.11 Visible mass distribution in the final fit of the Template Method	128
161	7.1 Tag-probe muon isolation method	131
162	7.2 Muon isolation correction factors	133
163	7.3 Measurement of hadronic tau identification efficiency	134
164	7.4 Distribution of number of reconstructed primary vertices per event	137
165	9.1 Transverse momentum distributions of muon and tau in the final selected events	153
167	9.2 Distributions of the η and ϕ of the muon and tau candidates in the final selected events	154
169	9.3 Distributions of final selected events	155
170	9.4 Observed and expected limits on Higgs $\sigma \times \text{BR}$	158
171	9.5 Excluded regions of MSSM $\tan \beta - m_{A^0}$ parameter space	159
172	9.6 CMS combined exclusion of MSSM $\tan \beta - m_{A^0}$ parameter space	161

173 List of Tables

174	1.1	Chiral supermultiplets in the MSSM	21
175	1.2	Gauge supermultiplets in the MSSM	21
176	1.3	Higgs search channels at LEP	30
177	1.4	Decay modes of the τ lepton	35
178	3.1	Decay mode performance – naive reconstruction	58
179	3.2	Decay mode performance – TaNC reconstruction	58
180	3.3	Neural network training event statistics	62
181	3.4	Variables used in the different TaNC neural networks	80
182	5.1	High Level Trigger paths used to select $\mu + \tau_h$ events	95
183	5.2	Analysis backgrounds that include fake taus	97
184	5.3	Event selection summary	101
185	6.1	Criteria used to select background enriched control regions	117
186	6.2	Comparison of background control region yields in data and the prediction from simulation	118
187	6.3	Fake-rate “simple” method closure test results	120
188	6.4	Fake-rate “CDF” method closure test results	121
189	6.5	Fake-rate method results	125
190	6.6	Fake-rate Method predicted yields in like-sign control region	126
191	6.7	Background yields measured using the Template Method	126
192	7.1	Muon trigger, identification, and isolation correction factors	132
193	8.1	Effect of normalization uncertainties on signal efficiency times acceptance .	143
194	8.2	Correspondence of confidence levels and $2\Delta \ln \mathcal{L}$ intervals	145
195	8.3	Summary of systematic uncertainties	148
196	9.1	Final analysis yield and background expectations	150
197	9.2	Expected signal yields at $\tan \beta = 30$	156
198	9.3	Expected and observed 95% CL $\sigma \times \text{BR}$ upper limits	157
199	9.4	Contributions of different MSSM Higgs boson types at different m_{A^0}	157
200			

201 Introduction

202 This thesis describes a search for the Higgs boson, a new particle predicted by the Standard
 203 Model of particle physics. The search is optimized for a particular extension of the Standard
 204 Model, a theory called the Minimal Supersymmetric Model (MSSM). The analysis uses
 205 the 2010 dataset from the Compact Muon Solenoid (CMS) experiment, which contains
 206 36 pb^{-1} of integrated luminosity at a center of mass energy of 7 TeV. The Higgs boson
 207 is hypothesized to be the catalyst of Electroweak Symmetry Breaking, the phenomenon
 208 strongly believed to impart mass to particles that form our natural world.

209 Chapter 1 begins with an introduction to the Standard Model (SM) of particle physics.
 210 Emphasis is given to Electroweak Symmetry Breaking and the Higgs Mechanism, the the-
 211 oretical phenomena that motivate the presence of a Higgs boson. The theoretical issues
 212 which motivated the development of the MSSM are discussed, and a brief introduction is
 213 given. Finally, the phenomenology of Higgs bosons in the SM and MSSM is discussed, with
 214 an overview of Higgs searches performed at LEP and the Tevatron.

215 This thesis then documents the development of a complete search for MSSM Higgs
 216 bosons at CMS. The CMS experiment is introduced briefly in Chapter 2. Chapters 3 and 4
 217 document in detail two fundamental components of the search, an advanced tau identifi-
 218 cation algorithm, and a novel method for reconstructing the neutrinos associated to tau
 219 decays. The development of these algorithms was motivated by the challenges of this anal-
 220 ysis, and precipitated significant improvements in the final result. Finally, in Chapters 5-8,
 221 we describe the methods and results of the event selection, background estimation, and the
 222 systematic uncertainties, and finally compute an upper limit on the presence of an MSSM
 223 Higgs boson.

224 The studies presented herein were part of a larger effort at CMS to search for an MSSM
 225 Higgs boson decaying to tau lepton pairs. In addition to the $\mu - \tau_h$ channel described in

226 this thesis, final states with an electronic and hadronic tau decay ($e - \tau$) and electronic and
227 muonic ($e - \mu$) were considered. The combination of all three was used to set a limit on
228 the MSSM [1]. This result has recently been accepted for publication in Physical Review
229 Letters B. At the time of this writing, the CMS analysis sets the worlds strongest limit on
230 the MSSM Higgs boson using a direct search.

231

Chapter 1

232

The Standard Model and Beyond

233 §1.1 The Standard Model

234 The Standard Model (SM) is a “theory of almost everything” that describes the interactions
235 of elementary particles. The Standard Model is a *quantum field theory*, first appearing in its
236 modern form in the middle of the 20th century. The model is the synthesis of the independent
237 theories of electromagnetism, and the weak and strong nuclear forces. Each of these theories
238 was used to describe different phenomena, which each have extremely different strengths
239 and act at different scales. The interaction of light and matter is described by Quantum
240 Electrodynamics (QED), a relativistic field extension of the theory of electromagnetism.
241 The physics of radioactivity and nuclear decay was described by the Fermi theory of weak
242 interactions and the forces that strong nuclear force binds the nuclei of atoms was described
243 by Yukawa. An overview of these theories will be presented in this chapter.

244 The feature that united the disparate theories into the Standard Model was the appli-
245 cation of the principle of *local gauge invariance*. The principle of gauge invariance first found
246 success in QED, which predicted electromagnetic phenomenon with astounding accuracy.
247 Local gauge invariance is now believed to a fundamental feature of nature that underpins
248 all theories of elementary particles. Furthermore, the development of the complete Stan-
249 dard Model as it is known today was precipitated by Goldstones’s work on spontaneous
250 symmetry breaking [2, 3], which produces an effective Lagrangian with additional massless
251 “Goldstone” bosons. Higgs (and others) [4, 5, 6] developed these ideas into what isulti-
252 mately called the “Higgs Mechanism,” which uses a combination of new fields with broken
253 symmetry to give mass to the Goldstone bosons.

254 In the 1960s, Glashow [7], Weinberg [8], and Salam [9] developed the above ideas into
 255 the electroweak model, which unified QED with the weak force using intermediate weak
 256 bosons in a gauge theory with symmetry that is spontaneously broken using the Higgs
 257 mechanism. This unified theory has been incredibly experimentally successful and is the
 258 foundation of modern particle theory.

259 §1.1.1 Quantum Electrodynamics and Gauge Invariance

260 The theory of QED is a modern extension of Maxwell's theory of electromagnetism, describ-
 261 ing the interaction of matter with light. The development of QED is a result of efforts to
 262 develop a quantum mechanical formulation of electromagnetism compatible with the theory
 263 of Special Relativity. QED is a *gauge* theory, which means that the physical observables
 264 are invariant under local gauge transformations. Requiring local gauge invariance gives rise
 265 to a “gauge” field, which can be interpreted as particles that are exchanged during an
 266 interaction.

267 In the following, we first describe the Dirac equation for a free electron, which is the
 268 relativistic extension of the Schroedinger equation for spin 1/2 particles. We then show that
 269 requiring the corresponding Lagrangian of the free charged particle to be invariant under
 270 local gauge transformations creates an effective gauge boson field. This “gauge field” creates
 271 terms in the Lagrangian that represent interactions between the particles.

The Dirac equation is the equation of motion of a free spin 1/2 particle of mass m and
 is derived from the energy–momentum relationship of relativity

$$p^\mu p_\mu - m^2 c^2 = 0. \quad (1.1)$$

Dirac sought to express this relationship in the framework of quantum mechanics by applying
 the transformation

$$p_\mu \rightarrow i\hbar\partial_\mu \quad (1.2)$$

to equation Equation 1.1, but with the requirement that the resulting equation be first
 order in time.¹ To achieve this, Dirac factorized Equation 1.1 into

$$(\gamma^\kappa p_\kappa + mc)(\gamma^\mu p_\mu - mc) = 0, \quad (1.3)$$

¹A detailed discussion of this topic is available in [10].

where γ^μ is a set of four 4×4 matrices referred to as the Dirac matrices. The equation of motion is obtained by choosing either term (they are equivalent) from the left hand side of Equation 1.3 and making the substitution in Equation 1.2.

$$i\hbar\gamma^\mu\partial_\mu\psi - mc\psi = 0. \quad (1.4)$$

- 272 The solutions ψ of the Dirac equation are called “Dirac spinors,” and represent the quantum
273 mechanical state of spin 1/2 particles.

The Lagrangian corresponding to the Dirac equation (1.4) is

$$\mathcal{L} = \bar{\psi}(i\hbar c\gamma^\mu\partial_\mu - mc^2)\psi, \quad (1.5)$$

where ψ is the spinor field of the particle in question, \hbar is Planck’s constant, c the speed of light, and γ^μ are the Dirac matrices. As $\bar{\psi}$ is the Hermitian conjugate of ψ , the Lagrangian is invariant under the global gauge transformation

$$\psi' \rightarrow e^{i\theta}\psi. \quad (1.6)$$

The Lagrangian is invariant under *local* gauge translations if θ can be defined differently at each point in space, i.e. if $\theta = \theta(x)$ in Equation 1.6. However, as the derivative operator ∂_μ in Equation 1.5 does not commute with $\theta(x)$, the Lagrangian must be modified to satisfy local gauge invariance. This modification is accomplished with the use of a “gauge covariant derivative.” By making the replacement

$$\partial_\mu \rightarrow D_\mu = \partial_\mu - \frac{ie}{\hbar}A^\mu$$

in Equation 1.5, where $A^\mu = \partial^\mu\theta(x)$ and e is the electric charge, the Lagrangian becomes locally gauge invariant:

$$\mathcal{L} = \bar{\psi}(i\hbar c\gamma^\mu D_\mu - mc^2)\psi. \quad (1.7)$$

The difference between the locally (1.7) and the globally (1.5) gauge invariant Lagrangian is then

$$\mathcal{L}_{int} = \frac{e}{\hbar}\bar{\psi}\gamma^\mu\psi A_\mu.$$

This term can be interpreted as the coupling between the particle and the gauge boson (force carrier) fields. The coupling is proportional to the constant e , which is associated with the electric charge. This is consistent with the experimental observation that particles with zero electric charge do not interact electromagnetically with each other. In this interpretation, the electromagnetic force between two charged particles is caused by the exchange of gauge bosons (photons). The existence of this “minimal coupling” is *required* if the Lagrangian

is to satisfy local gauge invariance. The addition of a term with the gauge Field Strength Tensor to represent the kinetic term of the gauge (photon) field yields the QED Lagrangian:

$$\mathcal{L}_{QED} = \bar{\psi}(i\hbar c\gamma^\mu D_\mu - mc^2)\psi - \frac{1}{4\mu_0}F_{\mu\nu}F^{\mu\nu}.$$

The gauge symmetry group of QED is $U(1)$, the unitary group of degree 1. This symmetry can be visualized as a rotation of a two-dimensional unit vector. (The application of the gauge transformation $e^{i\theta}$ rotates a number in the complex plane.) In a gauge theory the symmetry group of the gauge transformation defines the behavior of the gauge bosons and thus the interactions of the theory.

§1.1.2 The Weak Interactions

The theory of Weak Interactions was created to describe the physics of radioactive decay. The first formulation of the theory was done by Fermi [11] to explain the phenomenon of the β decay of neutrons. The initial theory was a four-fermion “contact” theory. In a contact theory, all four fermions come involved in the β -decay are connected at a single vertex. The Fermi theory Hamiltonian for the β -decay of a proton is then [12]

$$H = \frac{G_\beta}{\sqrt{2}} [\bar{\psi}_p \gamma_\mu (1 - g_A \gamma_5) \psi_n] [[\bar{\psi}_e \gamma^\mu (1 - \gamma_5) \psi_\nu] + h.c., \quad (1.8)$$

where G_β is the Fermi constant and g_A is the relative fraction of the interaction with axially Lorentz structure. The value of g_A was determined experimentally to be 1.26. One of the most notable things discovered about the weak force is that weak interactions violate parity; that is, the physics of the interaction change (or become disallowed) under inversion of the spatial coordinates. This is evidenced by the $(1 - \gamma_5)$ term in Equation 1.8. This term is the “helicity operator”; the left and right “handed” helicity states are eigenstates states of this term.

$$h = (1 - \gamma_5)/2$$

$$h\psi_R = \frac{1}{2}\psi_R$$

$$h\psi_L = -\frac{1}{2}\psi_L$$

It is observed that only left-handed neutrinos (or right-handed anti-neutrinos) participate in the weak interaction.

The Fermi interaction can describe both nuclear β decay ($p \rightarrow n + e^+ + \bar{\nu}_e$) as well as the decay of a muon into an electron ($\mu \rightarrow \nu_\mu + e + \bar{\nu}_e$, Figure 1.1). Furthermore, the

Fixme: check handedness is correct

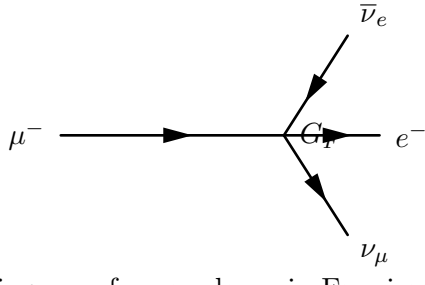


Figure 1.1: Feynmann diagram of muon decay in Fermi contact interaction theory.

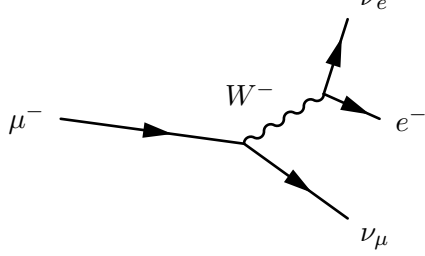


Figure 1.2: Feynmann diagram of muon decay proceeding through an intermediate gauge boson W^- .

coupling constant G is found to be a *universal* constant in weak interactions, in that it is the same for interactions regardless of the particle species participating in the interaction. That is, $G_\mu = G_e = G_F$. Using an Hamiltonian analogous to Equation 1.8 for muon decay, the decay amplitude M is found to be

$$M = \frac{G_F}{\sqrt{2}} \left[\bar{u}_{\nu_\mu} \gamma_\rho \frac{1 - \gamma_5}{2} u_\mu \right] \left[\bar{u}_{\nu_e} \gamma_\rho \frac{1 - \gamma_5}{2} u_e \right]. \quad (1.9)$$

However, the contact interaction form of Fermi's theory is not complete. When applied to scattering processes, the interaction violates unitarity: the calculated cross section grows with the center of mass energy, so that for some energy the probability for an interaction is greater than one. Furthermore, the techniques successfully used to "renormalize"² QED fail when applied to the Fermi interaction.

The first attempt to solve the problems with the Fermi theory was made by introducing an intermediate weak boson [7]. The contact interaction is replaced by a massive propagator, the W^\pm bosons. The decay of a muon to an electron and two neutrinos then proceeds as pictured in Figure 1.2 with an amplitude given [12] by

$$M = - \left[\frac{g}{\sqrt{2}} \bar{u}_{\nu_\mu} \gamma_\rho \frac{1 - \gamma_5}{2} u_\mu \right] \frac{-g^{\rho\sigma} + \frac{q^\rho q^\sigma}{M_W^2}}{q^2 - M_W^2} \left[\frac{g}{\sqrt{2}} \bar{u}_{\nu_e} \gamma_\rho \frac{1 - \gamma_5}{2} u_e \right]. \quad (1.10)$$

The presence of the large gauge boson mass term M_W^2 in the denominator of the central

²Renormalization of quantum field theories is a broad topic beyond the scope of this thesis. Briefly, the process involves "absorbing" infinite divergences that occur in higher-order interactions into physical observables [10].

term of Equation 1.10 is the reason why the contact interaction original formulated by Fermi effectively described low-energy weak phenomenon. When the momentum transfer q in the interaction is small compared to M_W , the effect of the propagator is an effective constant. In the low energy limit, the full propagator in Equation 1.10 is equivalent to the Fermi contact interaction in 1.9 as

$$\lim_{q/M_W \rightarrow 0} \frac{g^2}{8(q^2 - M_W^2)} = \frac{G_F}{\sqrt{2}}. \quad (1.11)$$

294 Unfortunately, the weak boson exchange model did not solve the problems of unitarity
 295 and renormalizability in the weak interaction. However, the form of the boson-exchange
 296 propagator in Equation 1.11 suggests the observed “weakness” of the weak interactions is
 297 an artifact of the presence of the massive propagator (M_W) and that the fundamental scale
 298 of the interaction g is the same order of magnitude as that of QED, $g \approx e$. This observation
 299 lead to the unification of the electromagnetic and weak forces, which we describe in the
 300 next sections.

301 §1.1.3 Spontaneous Symmetry Breaking

302 In the early 1960s Glashow, Weinberg, and Salam published a series of papers describing
 303 how the electromagnetic and weak forces could be unified into a common “electroweak”
 304 force. The fact that at low energy the electromagnetic and weak forces appear to be sep-
 305 arate phenomena is due to the fact that the symmetry of the electroweak gauge group is
 306 “spontaneously broken.” Modern field theories (both the Standard Model and beyond) are
 307 predicated on the idea that the all interactions are part of a single, unified symmetry group
 308 and the differences between various scales (electromagnetic, weak, etc.) at lower energies
 309 are due to the unified symmetry being spontaneously broken.

A symmetry of a Lagrangian is spontaneously broken when the ground state, or vacuum, is at a value about which the Lagrangian is not symmetric. In quantum field theories, a particle is interpreted as quantized fluctuations of its corresponding field about some constant (vacuum) ground state. The “effective” Lagrangian that we observe in the (low energy) laboratory would be the expansion of the Lagrangian about this stable point. The effective Lagrangian no longer obeys the original symmetry, which has been “broken.” We give a brief example of the phenomenological effects of a spontaneously broken symmetry

in a toy model, following the treatment in [12].

$$\mathcal{L} = \frac{1}{2} \partial_\mu \phi_1 \partial^\mu \phi_1 + \frac{1}{2} \partial_\mu \phi_2 \partial^\mu \phi_2 - V(\phi_1^2 + \phi_2^2) \quad (1.12)$$

The toy Lagrangian in Equation 1.12 has a global $U(1)^3$ symmetry and consists of two real-valued fields, ϕ_1 and ϕ_2 . The particle mass spectra of the theory is given by expanding the field potential $V(\phi_1, \phi_2)$ about its minimum, $(\phi_1^{min}, \phi_2^{min})$. The first three terms in the series are found by

$$\begin{aligned} V(\phi_1, \phi_2) &= V(\phi_1^{min}, \phi_2^{min}) + \sum_{a=1,2} \left(\frac{\partial V}{\partial \phi_a} \right)_0 (\phi_a - \phi_a^{min}) \\ &\quad + \frac{1}{2} \sum_{a,b=1,2} \left(\frac{\partial^2 V}{\partial \phi_a \partial \phi_b} \right)_0 (\phi_a - \phi_a^{min})(\phi_b - \phi_b^{min}) + \dots \end{aligned} \quad (1.13)$$

Since at the minimum the partial derivative of V is zero with respect to all fields, the second term in Equation 1.13 is zero. The third term determines the masses of the particles in the theory. Since a mass term for a particle corresponding to a field ϕ_n in the Lagrangian appears as $\frac{1}{2}m^2\phi_n\phi_n$, we can identify

$$\left(\frac{\partial^2 V}{\partial \phi_a \partial \phi_b} \right)_{\phi^{min}} \quad (1.14)$$

as the a th row and b th column in the “mass matrix”. Off diagonal terms in this matrix indicate mixing terms between the fields. By diagonalizing the matrix, the combinations of fields which correspond to the physical particles (the “mass eigenstates”) are found. The m^2 of each particle is then the corresponding entry in the diagonal of the mass matrix.

The particle spectra of the model depends heavily on the form of the potential. An illustrative form (that is renormalizable and bounded from below) of a possible configuration for the potential V in Equation 1.12 is

$$V(\phi_1^2 \phi_2^2) = \frac{m^2}{2}(\phi_1^2 + \phi_2^2) + \frac{\lambda}{4}(\phi_1^2 + \phi_2^2)^2. \quad (1.15)$$

If the parameters m^2 and λ are both positive, then the minimum of V is at the origin ($\phi_1 = \phi_2 = 0$). In this case, the mass matrix term in Equation 1.13 takes the form $\left(\frac{\partial^2 V}{\partial \phi_a \partial \phi_b} \right)_0 = \frac{m^2}{2} \delta_{ab}$, where δ_{ab} is the Kronecker delta function. Therefore the mass matrix is already diagonalized, and the ϕ_1 and ϕ_2 both correspond to particles with mass m . If the m^2

³Technically, the symmetric transformation is

$$\begin{pmatrix} \phi_1 \\ \phi_2 \end{pmatrix} \rightarrow \begin{pmatrix} \phi'_1 \\ \phi'_2 \end{pmatrix} = \begin{pmatrix} \cos \theta & -\sin \theta \\ \sin \theta & \cos \theta \end{pmatrix} \begin{pmatrix} \phi_1 \\ \phi_2 \end{pmatrix},$$

which is $\mathcal{O}(2)$. However, this transformation is equivalent to $U(1)$, as the two real fields ϕ_1 and ϕ_2 can be seen to correspond to the real and imaginary parts of a complex field ϕ that does transform according to $U(1)$.

322 parameter in Equation 1.15 is negative, the spectrum is dramatically different. After making
 323 the replacement $m^2 = -\mu^2 (\mu^2 > 0)$, the extrema of V are no longer unique. The requirement
 324 of $\frac{\partial V}{\partial \phi_i} = 0$ for all i is satisfied in two cases:

$$(\phi_1^{min}, \phi_2^{min}) = (0, 0) \quad (1.16)$$

$$(\phi_1^{min})^2 + (\phi_2^{min})^2 = \frac{\mu^2}{\lambda} = \nu^2. \quad (1.17)$$

If the vacuum state is defined at the point in Equation 1.16, the symmetry is unbroken and the mass spectra is unchanged. However, the system is unstable at this point, as it is a local maximum. The true global minimum is defined as the set of points which satisfy Equation 1.17, which form a continuous circle in $\phi_1 - \phi_2$ space (and is therefore infinitely degenerate). We can choose any point on the circle as the vacuum expectation value (VEV).

If the point $(\phi_1^{min} = \nu, \phi_2^{min} = 0)$ ⁴ is chosen, evaluating Equation 1.14 yields the mass matrix

$$\left(\frac{\partial^2 V}{\partial \phi_a \partial \phi_b} \right)_{\phi^{min}} = \begin{pmatrix} v^2 & 0 \\ 0 & 0 \end{pmatrix}.$$

325 Breaking the symmetry has changed the mass spectrum of the physical particles in the
 326 model. There is now a massive particle with $m = v^2$ and a massless particle. This massless
 327 particle is called the “Goldstone boson.” Goldstone found [2] that a massless particle appears
 328 for each generator in the symmetry group that is broken.

329 §1.1.4 The Higgs Mechanism

330 As in Section 1.1.1, extending the gauge symmetry requirement to be *locally* invariant
 331 creates interesting consequences for models that have spontaneously broken symmetry. This
 332 gives rise to the “Higgs Mechanism,” which we overview here. For simplicity we will again
 333 consider a model with $U(1)$ symmetry. The model is identical to the one presented in
 334 Section 1.1.3, with two exceptions. First, we express the two real fields ϕ_1 and ϕ_2 as a single
 335 complex-valued field ϕ . Second, the model is required to be locally $U(1)$ invariant, and so
 336 uses the gauge-covariant derivatives, minimal coupling to the gauge field, and contains the

⁴The point chosen for the VEV here is not arbitrary. One can chose any point that satisfies Equation 1.17 as the VEV. However, after the mass matrix is diagonalized, there will always be one physical field with a VEV= ν and one with a VEV= 0. Therefore the physical content of the theory does not depend on the choice of VEV.

³³⁷ kinetic term for the gauge field, as discussed in Section 1.1.1. The unbroken Lagrangian is

$$\mathcal{L} = -\frac{1}{4}F_{\mu\nu}F^{\mu\nu} + (D_\mu\phi^*)(D^\mu\phi) - V(\phi^*\phi) \quad (1.18)$$

$$V(\phi^*\phi) = -\mu^2\phi^*\phi + \lambda(\phi^*\phi)^2, \quad (1.19)$$

³³⁸ where $F_{\mu\nu}$ is related to the gauge field by $F_{\mu\nu} = \partial_\mu A_\nu - \partial_\nu A_\mu$. The Lagrangian is invariant

³³⁹ under the local $U(1)$ gauge transformation

$$\begin{aligned} \phi \rightarrow \phi' &= e^{-i\alpha(x)}\phi \\ A_\mu \rightarrow A'_\mu &= A_\mu - \frac{1}{2}\partial_\mu\alpha(x). \end{aligned}$$

The potential is minimized when $\phi^*\phi = \frac{\mu^2}{2\lambda}$. To simplify the algebra, we can re-parameterize the field into a real part $\eta(x)$ defined about ν , the minimum of V , and a complex phase parameterized by $\theta(x)/\nu$

$$\phi(x) = \frac{1}{\sqrt{2}}(\nu + \eta(x))e^{i\theta(x)/\nu}. \quad (1.20)$$

³⁴⁰ If the gauge transform is chosen to be $\alpha(x) = \theta(x)/\nu$, the fields of are defined in the so-called

³⁴¹ “unitary gauge”⁵ and have the special forms

$$\begin{aligned} \phi(x) \rightarrow \phi'(x) &= \frac{1}{\sqrt{2}}(\nu + \eta(x)) \\ A_\mu(x) \rightarrow B_\mu(x) &= A_\mu(x) - \frac{1}{e\nu}\partial_\mu\theta(x) \end{aligned} \quad (1.21)$$

³⁴² The kinetic term of the gauge field $F_{\mu\nu}$ is invariant under this transformation. If the gauge

³⁴³ transformations of Equation 1.21 are substituted into the Lagrangian (1.18) the effective

³⁴⁴ Lagrangian at the minimum of V is

$$\begin{aligned} \mathcal{L} &= \frac{1}{2}\partial_\mu\eta\partial^\mu\eta - \mu^2\eta^2 \\ &- \frac{1}{4}F_{\mu\nu}F^{\mu\nu} + \frac{1}{2}(e\nu)^2B_\mu B^\mu \\ &+ \frac{1}{2}e^2B_\mu B^\mu\eta(\eta + 2\nu) - \lambda\nu\eta^3 - \frac{\lambda}{4}\eta^4. \end{aligned} \quad (1.22)$$

³⁴⁵ The breaking of the original symmetry has dramatically altered the physical consequences of

³⁴⁶ the model. In its unbroken form, the model described by Equation 1.18 would produce two

³⁴⁷ real massive particles and one massless gauge boson mandated by local gauge invariance.

³⁴⁸ After symmetry breaking, the effective Lagrangian in Equation 1.22 contains a massive

³⁴⁹ scalar η with $m = \sqrt{2\mu^2}$ and a *massive* gauge boson B_μ with mass $m = \sqrt{2}e\nu$. By ac-

³⁵⁰ quiring a mass, the gauge boson B_μ has acquired the degree of freedom (as it can now

³⁵¹ be longitudinally polarized) previously associated to the second degree of freedom in the

⁵In the unitary gauge, the choice of gauge ensures that the mass matrix is diagonalized.

352 scalar ϕ field. This phenomenon, known as the “Higgs Mechanism,” is a simplified version
 353 of the techniques successfully used to unify the electromagnetic and weak forces that we
 354 will discuss in the next section.

355 §1.1.5 Electroweak Unification

356 In the 1960s, the ideas of local gauge invariance in field theories, spontaneous symme-
 357 try breaking, and the Higgs mechanism were combined by Glashow [7], Weinberg [8] and
 358 Salam [9] to form the unified theory of electroweak interactions, the nucleus of the Stan-
 359 dard Model. This model successfully unified the electromagnetic and weak interactions into
 360 a unified theory with a larger symmetry group. The reason for the empirically observed
 361 difference in scales between two interactions is due to the larger, unified symmetry group
 362 being broken. This broken symmetry creates heavy gauge bosons via the Higgs mechanism,
 363 whose large mass decreases the strength of “weak” interactions at low energy, as discussed in
 364 Section 1.1.2. The model successfully predicted the existence and approximate masses of the
 365 weak force carriers, the W^\pm and Z bosons. These particles were later observed [13, 14, 15, 16]
 366 with the predicted masses at the UA1 and UA2 experiments.

367 To provide a simple introduction to the mechanisms of the model, we will start with a
 368 model that includes only one family of leptons, the electron e and its associated neutrino
 369 ν_e . Following once again the treatment of [12], we describe the representation of the e and
 370 ν_e in the chosen symmetry group of the model. We then construct a locally gauge invariant
 371 Lagrangian with spontaneously broken symmetry, and examine the particle content of the
 372 resulting model.

The form of the charged current $J_\mu(x) = \bar{u}_{\nu_e} \gamma_\mu \frac{1-\gamma_5}{2} u_e$ in the weak interaction amplitudes (1.9) indicates that the left-handed electron and neutrino (remember that the $(1-\gamma_5)$ kills any right-handed spinors) can be combined into a doublet L of $SU(2)$.

$$L = \frac{1 - \gamma_5}{2} \begin{pmatrix} \nu_e \\ e^- \end{pmatrix} = \begin{pmatrix} \nu_e \\ e^- \end{pmatrix}_L \quad (1.23)$$

³⁷³ The operators that operate on “weak isospin,” the quantum of $SU(2)_L$, are

$$\tau^+ = \frac{\tau^1 + i\tau^2}{2} = \begin{pmatrix} 0 & 1 \\ 0 & 0 \end{pmatrix} \quad (1.24)$$

$$\tau^- = \frac{\tau^1 - i\tau^2}{2} = \begin{pmatrix} 0 & 0 \\ 1 & 0 \end{pmatrix}, \quad (1.25)$$

where the τ^i are the Pauli matrices. The weak currents J_μ^\pm can be written by combining Equations 1.23–1.25

$$J_\mu^\pm = \bar{L}\gamma_\mu\tau^\pm L. \quad (1.26)$$

³⁷⁴ Since τ^1 , τ^2 , and τ^3 are the generators of the $SU(2)$ group, we can complete the group

³⁷⁵ by adding a neutral current to the charged currents of Equation 1.26. The τ^3 generator is
³⁷⁶ diagonal, so the charge of the current is zero and no mixing of the fields occur:

$$\begin{aligned} J_\mu^3 &= \bar{L}\gamma_\mu\frac{\tau^3}{2}L \\ &= \bar{L}\gamma_\mu\frac{1}{2}\begin{pmatrix} 1 & 0 \\ 0 & -1 \end{pmatrix}L \\ &= \frac{1}{2}\bar{\nu}_e\gamma_\mu\nu_e - \frac{1}{2}\bar{e}_L\gamma_\mu e_L. \end{aligned} \quad (1.27)$$

³⁷⁷ Naively one might hope that the neutral current of Equation 1.27 would correspond to the
³⁷⁸ electromagnetic (photon) current of QED. However, this is impossible for two reasons. First,
³⁷⁹ the right-handed component e_R does not appear in the current, so this interaction violates
³⁸⁰ parity, a known symmetry of the electromagnetic interactions. Second, the current couples to
³⁸¹ neutrinos, which have no electric charge. Therefore, the “charge” corresponding to the $SU(2)$
³⁸² gauge symmetry generators $T^i = \int J_0^i(x)d^3x$ cannot be that of the QED, and the gauge
³⁸³ group must be enlarged to include an additional $U(1)$ symmetry. The generator of the new
³⁸⁴ symmetry must commute with the generators of the $SU(2)_L$ group. The symmetry cannot
³⁸⁵ be directly extended with $U(1)_{em}$ as the electromagnetic charge $Q = \int(e_L^\dagger e_L + e_R^\dagger e_R)d^3x$
³⁸⁶ does not commute with T^i . The solution is to introduce the “weak hypercharge” $\frac{Y}{2} = Q - T^3$,
³⁸⁷ which commutes the generators of $SU(2)_L$. Thus the symmetry group of the electroweak
³⁸⁸ model is $SU(2)_L \times U(1)_Y$.

³⁸⁹ The $SU(2)_L \times U(1)_Y$ gauge invariant Lagrangian is written

$$\begin{aligned}\mathcal{L} &= \bar{L}i\gamma^\mu(\partial_\mu - ig\frac{\vec{\tau}}{2} \cdot \vec{A}_\mu + \frac{i}{2}g'B_\mu)L \\ &+ \bar{R}i\gamma^\mu(\partial_\mu + \frac{i}{2}g'B_\mu)R \\ &- \frac{1}{4}F_{\mu\nu}^iF^{i\mu\nu} - \frac{1}{4}B_{\mu\nu}B^{\mu\nu}.\end{aligned}$$

³⁹⁰ As R is a singlet in $SU(2)$, it does not couple to the $SU(2)$ gauge bosons A_μ^i . For this
³⁹¹ Lagrangian to correspond to empirical observations at low energy, the $SU(2)_L \times U(1)_Y$
³⁹² must be broken. As $U(1)_{em}$ symmetry is observed to be good symmetry at all scales the
³⁹³ broken Lagrangian must be invariant under $U(1)_{em}$.

³⁹⁴ To accomplish the symmetry breaking, we introduce a new $SU(2)$ doublet of complex
³⁹⁵ Higgs fields ϕ that have hypercharge $Y = 1$, and contribute \mathcal{L}_S to the Lagrangian:

$$\begin{aligned}\phi &= \begin{pmatrix} \phi^+ \\ \phi^0 \end{pmatrix} \\ \mathcal{L}_S &= (D_\mu\phi)^\dagger(D^\mu\phi) - V(\phi^\dagger\phi),\end{aligned}$$

where D_μ is the gauge covariant derivative containing couplings to both the $SU(2)_L$ and
 $U(1)_Y$ gauge fields, and V has a form analogous to V in Equation 1.19. At this point we
also add $SU(2)_L \times U(1)_Y$ invariant “Yukawa” terms

$$\mathcal{L}_Y = -G_e(\bar{L}\phi R + \bar{R}\phi^\dagger L) + h.c. \quad (1.28)$$

³⁹⁶ to the Lagrangian which couple the fermions (L and R) to the Higgs field. After symmetry
³⁹⁷ breaking these terms will allow the fermions to acquire masses. By choosing the m^2 and λ
³⁹⁸ parameters of V appropriately, the new ϕ field acquires a non-zero VEV and the symmetry
³⁹⁹ is spontaneously broken.

At the minimum of V , the Higgs field satisfies $\phi^\dagger\phi = \frac{\nu^2}{2}$ and the Higgs fields has a
VEV of

$$\phi_{min} = \begin{pmatrix} 0 \\ v/\sqrt{2} \end{pmatrix}.$$

The new symmetry of the model can be confirmed by looking at the action of the different
symmetry generators on the VEV. If the generator acting on the vacuum state has a non-
zero value, then the corresponding symmetry is broken. It can then be seen that the original
symmetry generators T^+ , T^- , T^3 , and Y are all broken. The vacuum *is* invariant under Q ,

the generator of $U(1)_{em}$:

$$Q\phi_{min} = (T^3 + \frac{Y}{2}) \begin{pmatrix} 0 \\ v/\sqrt{2} \end{pmatrix} = 0,$$

400 so the broken Lagrangian contains the correct symmetry properties.

The gauge boson content of the electroweak interaction is obtained by parameterizing the Higgs field in the magnitude–phase notation of Equation 1.20 and using the unitary gauge (see Section 1.1.4), where the gauge transformation is chosen so Higgs field is real.

The Higgs scalar doublet is then

$$\phi' = \begin{pmatrix} 0 \\ \frac{1}{\sqrt{2}}(\nu + H(x)) \end{pmatrix} = \frac{1}{\sqrt{2}}(\nu + H(x))\chi.$$

The mass spectrum of the gauge bosons of the electroweak interaction (the photon, W^\pm , and Z) is determined by the interaction of the gauge field terms in the covariant derivative with the non-zero vacuum expectation value ν of the scalar Higgs field ϕ

$$(D_\mu \phi)' = (\partial_\mu - ig \frac{\vec{\tau}}{2} \cdot \vec{A}'_\mu - \frac{i}{2} g' B'_\mu) \frac{1}{\sqrt{2}}(\nu + H)\chi.$$

The terms in the expansion of the kinetic term of the Higgs field that are quadratic in ν^2 and a gauge boson field give the mass associated to that boson, and can be written as

$$\mathcal{L}_{mass} = \frac{\nu^2}{8}(g^2 A'_\mu{}^{1\mu} A'^{1\mu} + g^2 A'_\mu{}^{2\mu} A'^{2\mu} + (g A'_\mu{}^{3\mu} - g' B'_\mu)^2). \quad (1.29)$$

The $A'_\mu{}^{1\mu}$ and $A'_\mu{}^{2\mu}$ fields can be combined such that the first two terms in Equation 1.29 are equivalent to the mass term of a charged boson

$$W_\mu^\pm = \frac{A'_\mu{}^{1\mu} \mp i A'_\mu{}^{2\mu}}{2}.$$

401 This is the familiar W^\pm boson of β and muon decay, and has mass $M_W = \frac{1}{2}g\nu$. The third
402 term in Equation 1.29 can be written in matrix form and then diagonalized into mass
403 eigenstates

$$\begin{aligned} & \frac{\nu^2}{8} (A'_\mu{}^{3\mu} \ B'_\mu) \begin{pmatrix} g^2 & -gg' \\ -gg' & g'^2 \end{pmatrix} \begin{pmatrix} A'^{3\mu} \\ B'^\mu \end{pmatrix} \\ & \rightarrow \frac{\nu^2}{8} (Z_\mu \ A_\mu) \begin{pmatrix} g^2 + g'^2 & 0 \\ 0 & 0 \end{pmatrix} \begin{pmatrix} Z^\mu \\ A^\mu \end{pmatrix}, \end{aligned}$$

giving a massive Z boson with

$$M_Z = \frac{\nu}{2} \sqrt{g^2 + g'^2} \quad (1.30)$$

and the massless photon A_μ of QED. The mass of the Z is related to the mass of the W^\pm

by

$$M_Z \equiv \frac{M_W}{\cos \theta_W},$$

404 where θ_W is the “Weinberg angle,” which must be determined from experiment. As the
 405 Fermi contact interaction of Section 1.1.2 is an effective theory of the weak sector, the value
 406 of G_F obtained from β and muon decay experiments give clues to the masses of the W and
 407 Z .

$$M_W = \frac{1}{2} \left(\frac{e^2}{\sqrt{2} G_F} \right)^{(1/2)} \frac{1}{\sin \theta_W} \approx \frac{38 \text{ GeV}}{\sin \theta_W} > 37 \text{ GeV}$$

$$M_Z \approx \frac{76 \text{ GeV}}{\sin 2\theta_W} > 76 \text{ GeV}.$$

408 The discovery of the W [13, 14] and Z [15, 16] at the CERN SPS was a huge triumph for
 409 the electroweak model.

410 The model that is presented in this section assumes only one species of leptons, the
 411 electron and its associated neutrino. The electroweak model is trivially extended [12] to
 412 include the other species (μ, τ) of leptons and the three families of quarks. The masses of
 413 the fermions are determined by the Yukawa terms in Equation 1.28. Each particle species
 414 has a Yukawa term relating the Higgs VEV to its mass that is not constrained by the theory,
 415 and must be determined by experiment.

416 §1.1.6 Quantum Chromodynamics

417 After electroweak unification, the Standard Model is completed by the theory of Quantum
 418 Chromodynamics (QCD), which describes the interactions between quarks and gluons. QCD
 419 is a broad field and only a brief introduction to its motivations and the phenomenology
 420 relevant to the analysis presented in this thesis is contained in this section. The existence
 421 of quarks as composite particles of hadrons was first proposed by Gell–Man and Zweig to
 422 explain the spectroscopy of hadrons. QCD is an $SU(3)$ non–Abelian gauge theory which
 423 is invariant under *color* transformations. Color is the charge of QCD and comes in three
 424 types: red, green and blue. The gauge boson that carries the force of QCD is called the
 425 gluon, which is massless as the $SU(3)_c$ color symmetry is unbroken.

426 There are three marked differences between the photon of QED and the gluon of QCD.
 427 First, the gluon carries a color charge, while the photon is electrically neutral. This has the
 428 consequence that a gluon can couple to other gluons. Secondly, it is found that no colored

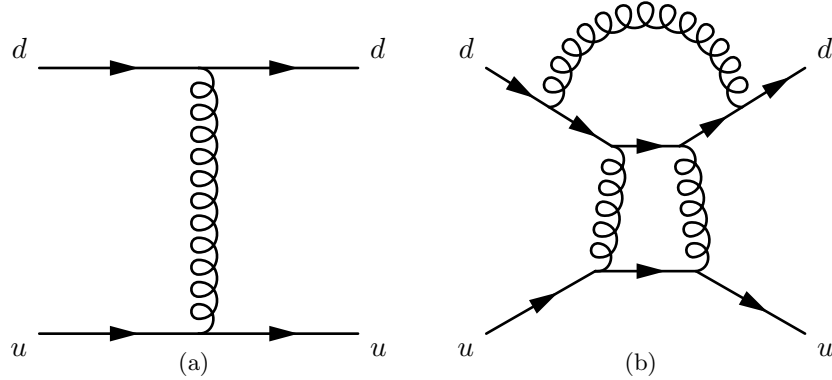


Figure 1.3: Feynman diagrams of a first–order (a) QCD interaction and a multi–loop (b) QCD interaction that have the same initial and final states. Each internal gluon propagator contributes a factor of g_s , the strong coupling constant, to the the amplitude. Since $g_s > 1$, multi–loop diagrams have a larger contribution than simpler diagrams.

object exists in nature. The corollary of this is that it is believed to be impossible for a single “bare” quark or gluon to be observed. The mechanism that gives rise to this effect is called “color confinement.” The strength of the strong force between two interacting colored objects increases with distance. If two colored objects in a hadron are pulled apart, the energy required to separate them will eventually be large enough to produce new (anti-)colored objects, resulting in two (or more) colorless hadrons. Finally, at low energy, QCD is non–perturbative. What this means in practice is that when computing an amplitude from a QCD Feynman diagram, additional gluon interactions contribute a value greater than one. The dominance of multi–loop diagrams is illustrated in Figure 1.1.6. Thus higher order diagrams with many internal loops cannot be ignored in QCD as is possible in the QED or Electroweak models. In practice what is done is to “factorize” QCD interaction amplitudes into a perturbative (high–energy) part and a non–perturbative part. The perturbative portion is calculable using the Feynman calculus; the non–perturbative must be estimated from parameterization functions that are experimentally measured.

The practical consequence of color confinement to a physicist studying electroweak phenomena at a high–energy particle physics experiment is the production of quark and gluon “jets,” which are high multiplicity sprays of particles observed in the detector. In a proton–proton collision, quarks and gluons can be knocked off the incident protons. These quarks and gluons immediately “hadronize,” surrounding themselves with additional hadrons, the majority of which are charged and neutral pions. Heavier quarks, such as the charm, beauty,

449 and top quarks undergo a flavor-changing weak decays, which can give rise to structure
 450 (leptons, sub-jets) within the jet. Furthermore, due to the relative strength of the strong
 451 interaction compared that of the electroweak, collision events involving only strong inter-
 452 actions are produced at rates many orders of magnitudes larger than that of electroweak
 453 interactions. This makes life difficult for physicists studying the electroweak force at hadron
 454 colliders. Sections 2.7, and Chapters 3 and 5 will discuss the techniques used to identify and
 455 remove QCD events from the data at different stages of the analysis.

456 §1.2 Beyond the Standard Model

457 The Standard model is one of the most successful theories of the natural world ever created.
 458 The predictions of the SM have been tested to many orders of magnitude and no experiment
 459 to date⁶ has found a result statistically incompatible with the Standard Model. However,
 460 there is a general consensus in the physics community that the Standard Model is not
 461 complete. It is believed that it is only an effective theory that is valid below some energy
 462 scale Λ . Above this energy, there must exist some other “new physics,” which unifies the
 463 forces of the Standard Model and correctly describes the natural world at all scales, while
 464 maintaining equivalence to the Standard Model at low energy. This concept is analogous to
 465 the relationship between the effective Fermi contact theory of Section 1.1.2 and the unified
 466 electroweak theory of Section 1.1.5. The size of the cutoff scale Λ is estimated [12] to be
 467 $\mathcal{O}(10^{15})$ GeV for a unified theory with $SU(5)$ symmetry and even larger, $\mathcal{O}(10^{19})$ GeV =
 468 M_{planck} if the theory is unified with gravity.

469 There are many compelling reasons that indicate that the Standard Model is incom-
 470 plete. One is the fact that the model does not include gravity, which has still not been
 471 successfully reformulated into a quantum mechanical theory. Another is that cosmological
 472 observations indicate the presences of massive amounts of “dark matter” in the universe.
 473 Dark matter is expected to be composed of a stable massive neutral particle which interacts
 474 very weakly with other matter; no Standard Model particle fits this description. Finally,
 475 there is the “hierarchy,” or fine-tuning problem. This problem strongly affects the Higgs sec-

⁶The Standard Model predicts that lepton number is a good quantum number and that the neutrinos are massless. It has recently been found that the neutrinos do have non-zero mass, and that they undergo oscillations between different neutrino species, violating lepton number.

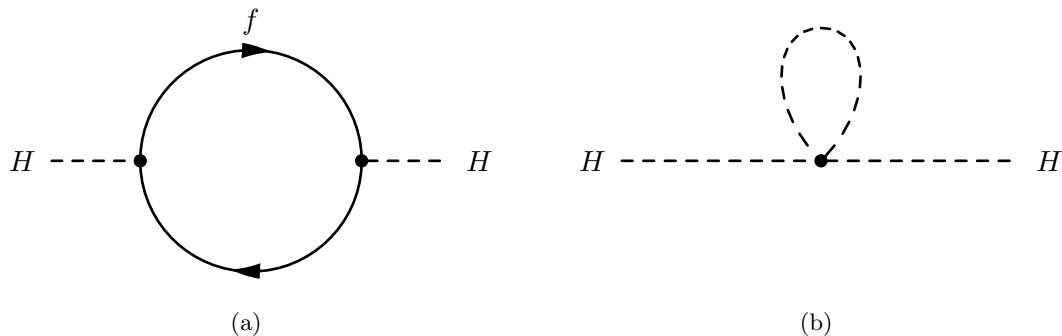


Figure 1.4: Feynman diagram of fermion (a) and scalar (b) loop corrections to Higgs mass.

476 tor, and motivated the development of Supersymmetry, which are the targets of the search
477 presented in this thesis. An short overview of the hierarchy problem and Supersymmetry
478 are presented in the next sections.

479 §1.2.1 The Hierarchy Problem

The enormous size of the cutoff scale Λ in the Standard Model causes a major theoretical problem in the Standard Model. During renormalization of the Standard Model, amplitudes with divergent integrals are cut off at Λ . These large constant terms are “absorbed” into the physical observables. The cutoff term appears directly in quantum corrections to the Higgs mass [17]. The Yukawa term $-\lambda_f H \bar{f} f$ coupling the fermion f to the Higgs H produces loop corrections to Higgs mass. The two types of corrections due to fermion loops and scalar loops are illustrated in Figure 1.4. The contribution [17] of the loop correction in Figure 1.4(a) to the Higgs mass is

$$m_H^2 = -\frac{|\lambda_f|^2}{8\pi^2} \Lambda^2 + \dots \quad (1.31)$$

The correction scales with Λ^2 , which is many orders of magnitude larger than the electroweak (M_W) scale. The physical mass of the Higgs is expected to have the same scale as M_W , $\mathcal{O}(100 \text{ GeV}/c^2)$. The fact that each fermion contributes a loop correction (Equation 1.31) requires that the “bare mass” of the Higgs to be tuned to the precision of $(M_W/\Lambda)^2 \approx 10^{-26}$ for the renormalized mass to be correct! This is the so-called fine-tuning problem: it is believed that in a natural theory there will be only one scale. The electroweak unification analogy is in Equation 1.11, where it was noticed that the difference between the QED and weak scale was due to the massive M_W propagator term, and that the fundamental scale

⁴⁸⁸ g of the intermediate weak boson theory was compatible with QED. The most promising
⁴⁸⁹ solution to the hierarchy problem is the introduction of a new, “super” symmetry.

⁴⁹⁰ §1.2.2 Supersymmetry

⁴⁹¹ Supersymmetry extends the Standard Model by positing that there exists a symmetry
⁴⁹² between the integer–spin bosons (γ, W^\pm, Z, H) and the half integer–spin fermions (quarks
⁴⁹³ and leptons). In Supersymmetry, every particle in the Standard Model has a “superpartner”
⁴⁹⁴ with a spin differs by $1/2$. All of the other quantum numbers (including mass) of the
⁴⁹⁵ superpartners are the same. The introduction of this symmetry immediately solves the
⁴⁹⁶ hierarchy problem. For every scalar loop correction (Figure 1.4(b)) to the Higgs mass there is
⁴⁹⁷ now a corresponding fermion loop correction (Figure 1.4(a)). As the fermion and the scalar
⁴⁹⁸ have the same quantum numbers (except for spin) it turns out that these two diagrams
⁴⁹⁹ have the same value, but *opposite* sign. Thus the large Λ^2 superpartner loop corrections to
⁵⁰⁰ the Higgs mass exactly cancel out the problematic Standard Model corrections. It is clear
⁵⁰¹ that if Supersymmetry exists, it must be broken. We have not observed a scalar charged
⁵⁰² particle with the same mass as the electron, for example. An excellent overview of possible
⁵⁰³ mechanisms that create spontaneous symmetry breaking in Supersymmetric models is given
⁵⁰⁴ in Chapter 6 of [17].

⁵⁰⁵ §1.2.3 The Minimal Supersymmetric Model

⁵⁰⁶ The simplest possible Supersymmetric extension to the Standard Model is the Minimal
⁵⁰⁷ Supersymmetric Model (MSSM). The model groups superpartner pairs into chiral (a left or
⁵⁰⁸ right–handed fermion field plus a complex scalar field) and gauge (a spin–1 vector boson and
⁵⁰⁹ a left or right–handed *gaugino* fermion) “supermultiplets.” As the weak interactions of the
⁵¹⁰ Standard Model fermions are chiral, they (and their superpartners) must belong in a chiral
⁵¹¹ supermultiplet. It is interesting to note that there is a different superpartner for the left and
⁵¹² right–handed components of the fermions, even though the superpartners are spin–0 and
⁵¹³ cannot have any handedness. It is found that there must be two Higgs supermultiplets for the
⁵¹⁴ MSSM to be viable. As there are now fermionic particles in the Higgs sector (the Higgsinos),
⁵¹⁵ if only one supermultiplet is introduced the MSSM suffers from non–renormalizable gauge

Names		spin 0	spin 1/2	$SU(3)_C, SU(2)_L, U(1)_Y$
squarks, quarks ($\times 3$ families)	Q	$(\tilde{u}_L \ \tilde{d}_L)$	$(u_L \ d_L)$	$(\mathbf{3}, \mathbf{2}, \frac{1}{6})$
	\bar{u}	\tilde{u}_R^*	u_R^\dagger	$(\bar{\mathbf{3}}, \mathbf{1}, -\frac{2}{3})$
	\bar{d}	\tilde{d}_R^*	d_R^\dagger	$(\bar{\mathbf{3}}, \mathbf{1}, \frac{1}{3})$
sleptons, leptons ($\times 3$ families)	L	$(\tilde{\nu} \ \tilde{e}_L)$	$(\nu \ e_L)$	$(\mathbf{1}, \mathbf{2}, -\frac{1}{2})$
	\bar{e}	\tilde{e}_R^*	e_R^\dagger	$(\mathbf{1}, \mathbf{1}, 1)$
Higgs, higgsinos	H_u	$(H_u^+ \ H_u^0)$	$(\tilde{H}_u^+ \ \tilde{H}_u^0)$	$(\mathbf{1}, \mathbf{2}, +\frac{1}{2})$
	H_d	$(H_d^0 \ H_d^-)$	$(\tilde{H}_d^0 \ \tilde{H}_d^-)$	$(\mathbf{1}, \mathbf{2}, -\frac{1}{2})$

Table 1.1: Chiral supermultiplets in the Minimal Supersymmetric Standard Model. The spin-0 fields are complex scalars, and the spin-1/2 fields are left-handed two-component Weyl fermions. Source: [17]

Names	spin 1/2	spin 1	$SU(3)_C, SU(2)_L, U(1)_Y$
gluino, gluon	\tilde{g}	g	$(\mathbf{8}, \mathbf{1}, 0)$
winos, W bosons	$\widetilde{W}^\pm \ \widetilde{W}^0$	$W^\pm \ W^0$	$(\mathbf{1}, \mathbf{3}, 0)$
bino, B boson	\tilde{B}^0	B^0	$(\mathbf{1}, \mathbf{1}, 0)$

Table 1.2: Gauge supermultiplets in the Minimal Supersymmetric Standard Model. Source: [17]

516 anomalies.⁷ By introducing an additional Higgs supermultiplet with opposite hypercharge,
 517 the anomaly is canceled. The scalar portion of the MSSM Higgs sector then contains two
 518 complex doublet fields $H_u = (H_u^+, H_u^0)$ (up-type) and $H_d = (H_d^0, H_d^-)$ (down-type). The
 519 complete chiral and gauge supermultiplets of the MSSM are enumerated in Tables 1.1
 520 and 1.2, respectively.

The superpotential (like the scalar potential of Section 1.1.3 but invariant under supersymmetric transformations) of the MSSM is then [17]

$$W_{\text{MSSM}} = \bar{u}\mathbf{y}_{\mathbf{u}}QH_u - \bar{d}\mathbf{y}_{\mathbf{d}}QH_d - \bar{e}\mathbf{y}_{\mathbf{e}}LH_d + \mu H_u H_d ,$$

521 where H_u , H_d , Q , L , \bar{u} , \bar{d} , and \bar{e} are the superfields defined in Table 1.1. The \mathbf{y} terms are
 522 Yukawa 3×3 matrices which act on the different families. It is important to note that the
 523 up-type quarks couple to the up-type Higgs H_u , while the down-type quarks and leptons

⁷A gauge anomaly is a linear divergence that occurs in diagrams containing a fermion loop with three gauge bosons (total) in the initial and final states. In the Electroweak model, the sum of the fermion contributions cancel the anomaly. Interestingly, the requirement of anomaly cancellation is only achieved in the SM is achieved only by requiring there be three types of color in QCD.

524 couple to the down-type Higgs. This feature has large phenomenological consequences,
 525 which are discussed in Section 1.3.2. The scalar portion of the W_{MSSM} potential defines the
 526 spontaneous symmetry breaking. Similar to the scalar potential V symmetry breaking of
 527 Section 1.1.3, the potential of V at the minimum is found⁸ to be

$$\begin{aligned} V = & \quad (|\mu|^2 + m_{H_u}^2)|H_u^0|^2 + (|\mu|^2 + m_{H_d}^2)|H_d^0|^2 \\ & - (bH_u^0H_d^0 + c.c.) + \frac{1}{8}(g^2 + g'^2)(|H_u^0|^2 - |H_d^0|^2)^2. \end{aligned} \quad (1.32)$$

Under suitable choices⁹ of the parameters in Equation 1.32, the up-type and down-type neutral Higgs fields acquire a VEV, ν_u and ν_d , respectively. The VEVs are related to the VEV of electroweak symmetry breaking (Equation 1.30) in the SM,

$$\nu_u^2 + \nu_d^2 = \nu^2 = \frac{2M_Z^2}{g^2 + g'^2} \approx (174 \text{ GeV})^2.$$

The ratio of the VEVs is expressed as

$$\tan \beta \equiv \frac{\nu_u}{\nu_d},$$

528 which is an important parameter of the MSSM. As there are two complex doublets, there are
 529 a total of eight degrees of freedom in the MSSM Higgs sector. After the symmetry breaking,
 530 three of the degrees of freedom are (like the Standard Model) eaten by the W^\pm and Z weak
 531 gauge bosons. The remaining five degrees of freedom create five massive Higgs bosons: two
 532 CP-even neutral scalars h^0 and H^0 , a CP-odd neutral scalar A^0 , and two (positive and
 533 negative) charged scalars H^\pm . The masses are of the different Higgs mass eigenstates are
 534 related to each other and $\tan \beta$ at tree level by

$$\begin{aligned} m_{h^0}^2 &= \frac{1}{2}(m_{A^0}^2 + m_Z^2 - \sqrt{(m_{A^0}^2 - m_Z^2)^2 + 4m_Z^2m_{A^0}^2 \sin^2(2\beta)}) \\ m_{H^0}^2 &= \frac{1}{2}(m_{A^0}^2 + m_Z^2 + \sqrt{(m_{A^0}^2 - m_Z^2)^2 + 4m_Z^2m_{A^0}^2 \sin^2(2\beta)}). \end{aligned} \quad (1.33)$$

It can be seen that the tree level mass m_{h^0} of Equation 1.33 is bounded from above by $m_{h^0} < m_Z |\cos(2\beta)| < 90 \text{ GeV}/c^2$. If this is true the model would have been excluded by the LEP experiment (see next section). However, there are important quantum corrections to m_{h^0} from the top-quark and top-squark loop diagrams which increase m_{h^0} . The Yukawa couplings in the MSSM depend on $\tan \beta$. The relationships for the most massive members

⁸A clever choice of the $SU(2)_L$ gauge has removed any contributions from the charged fields. The charged Higgs fields cannot have a VEV without breaking $U(1)_{em}$.

⁹See Chapter 7 of [17] for a detailed overview.

of each family are

$$m_t = y_t v \sin \beta, \quad m_b = y_b v \cos \beta, \quad m_\tau = y_\tau v \cos \beta.$$

- 535 The Yukawa couplings are free parameters determined by experimentally observed masses.
 536 This means that when $\tan \beta$ is large ($\beta \rightarrow \pi$), the Yukawa terms y for the b quarks and τ
 537 leptons must be enhanced to maintain the observed masses. The effect of $\tan \beta$ on the Higgs
 538 mass spectrum and couplings in the MSSM will be discussed further in Section 1.3.2.

539 §1.3 Searches for the Higgs boson

- 540 The discovery of the Higgs boson is one of the biggest prizes in science today. Dozens of
 541 experiments, thousands of scientists and billions of dollars (a human hierarchy problem)
 542 have been spent in efforts to discovery the Higgs. In this section we discuss how the Higgs
 543 and the MSSM could appear in modern colliders (with an emphasis on the LHC) and
 544 the current limits placed on the Higgs by the Large Electron–Positron Collider (LEP) and
 545 Tevatron experiments.

546 §1.3.1 Standard Model Higgs boson phenomenology

The phenomenology of the Higgs boson is strongly coupled to its relationship with mass. The coupling of the Higgs to the fermions is determined by the Yukawa terms (Equation 1.28) in the Lagrangian. Taking the electron as an example, after symmetry breaking, the Yukawa term is found to be

$$\mathcal{L}_e = -\frac{G_e}{\sqrt{2}}(\nu + H(x))\bar{e}e = -\frac{G_e\nu}{\sqrt{2}}\bar{e}e - \frac{G_e}{\sqrt{2}}H(x)\bar{e}e. \quad (1.34)$$

The value of G_e is a free parameter of the theory and is thus determined by the measurement of the electron mass and ν , the VEV of the Higgs field

$$\frac{G_e\nu}{\sqrt{2}} = \frac{m_e}{\nu}. \quad (1.35)$$

- 547 The left-hand side of Equation 1.35 is the same as the constant in the electron Higgs
 548 coupling term ($H(x)\bar{e}e$) in Equation 1.34. Therefore the coupling between the fermions
 549 and Higgs boson is proportional to their mass! This remarkable fact shapes the possible
 550 production modes and the branching fractions of Higgs decays.

- 551 The dominant modes of Higgs boson production depend on the type of experiment.
 552 In general, Higgs production is favored through high-mass intermediate states, due to the

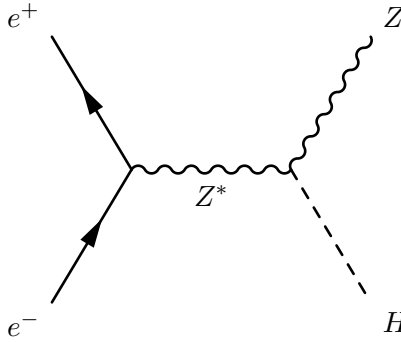


Figure 1.5: Higgstrahlung production diagram at e^+e^- colliders

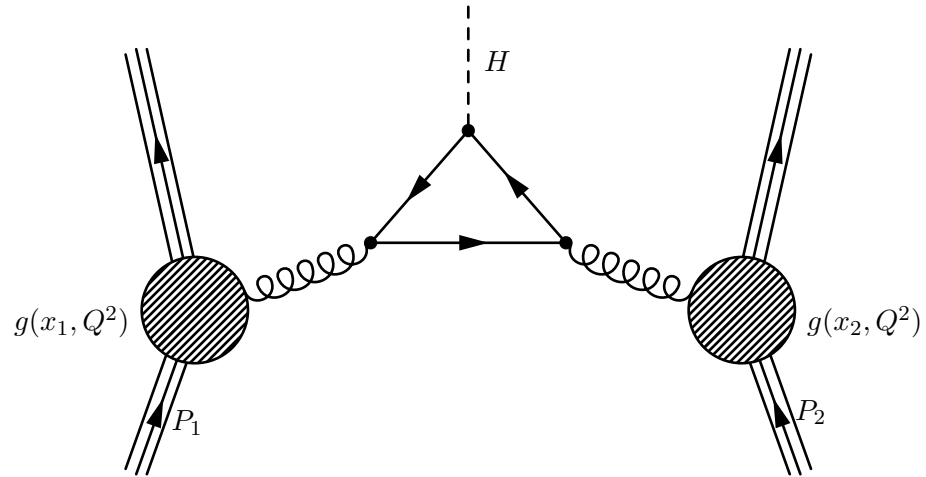


Figure 1.6: Gluon fusion Higgs production mechanism in a proton–proton collision. The Higgs mass coupling favors the heavy top quark in the central loop. Image credit: [18]

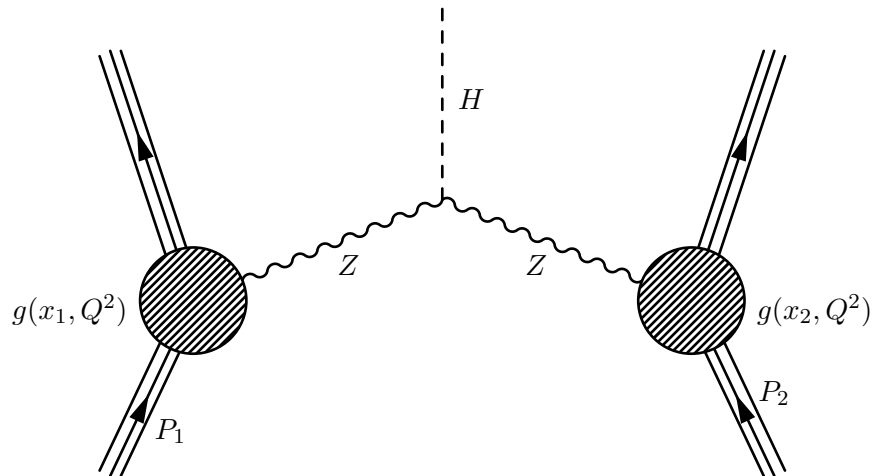


Figure 1.7: Vector boson fusion (VBF) Higgs production mechanism in proton–proton collisions. The VBF mechanism is notable for the lack of color–flow between the two incident protons, producing events with low jet activity in the central region.

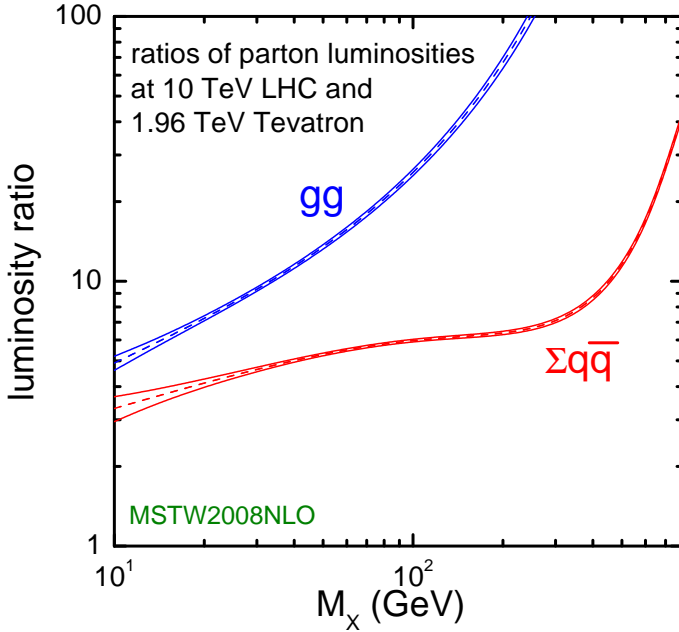


Figure 1.8: Ratio of the parton luminosity (the amount of luminosity contributed by the different species that compose the proton) of the LHC (at $\sqrt{s} = 10$ TeV) and the Tevatron. The large increase in gluon–gluon luminosity affects the favored production mechanisms of the Higgs boson.

mass² proportional coupling. At the Tevatron and LEP experiments, which will be introduced in the next section, the dominant SM Higgs production mode is “Higgstrahlung,” where a virtual W^\pm or Z gauge boson is produced and then radiates a Higgs boson. Higgstrahlung is illustrated in Figure 1.3.1. At the Large Hadron Collider, higher gluon luminosities (see Figure 1.8) result in the favored cross section being “gluon fusion,” (illustrated in Figure 1.3.1) where two gluons from the incident protons combine in a quark (dominated by the massive top quark) loop which then radiates a Higgs boson. Another important channel [19] is “vector boson fusion,” (Figure 1.3.1) where weak gauge bosons (W^\pm or Z) are radiated from the incoming quarks and fuse to produce a Higgs. This is a notable channel due to the lack of “color-flow” (gluons) between the two protons, producing an event with low central jet activity and two “tag-jets” in the forward and backward regions. The theoretical cross sections for the SM Higgs at the LHC are shown for the various production mechanisms in Figure 1.9.

The branching fractions of the different decay modes of the SM Higgs boson depend strongly on the mass of the Higgs boson. In general, the Higgs prefers (due to the Yukawa

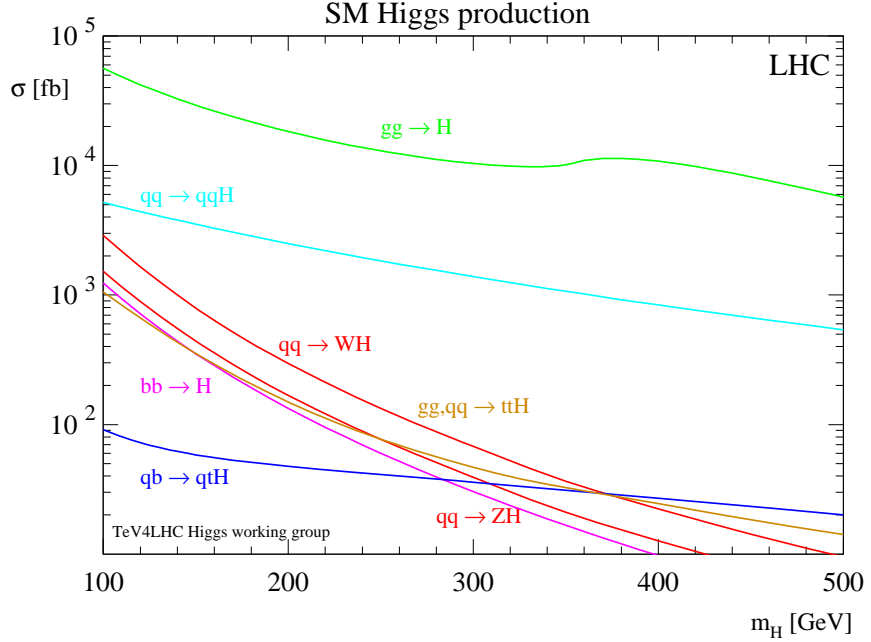


Figure 1.9: Cross section of the Standard Model Higgs boson versus the Higgs boson mass. The different curves give the contribution to the cross section from different production mechanisms. Source: [20].

568 couplings) to decay pairs of the particles with the highest mass possible. Below the threshold
 569 to decay to pairs of weak bosons ($M_H < 160 \text{ GeV}/c^2$), the Higgs decays predominantly
 570 to either b -quarks ($b\bar{b}$, 90%) or a pair of τ leptons ($\tau^+\tau^-$, $\approx 10\%$). Above the $W^\pm W^\mp$
 571 threshold, decays to vector bosons ($H \rightarrow W^\pm W^\mp$ and $H \rightarrow ZZ$) dominate. The dependence
 572 of branching fraction on M_H and the other rare decay modes are illustrated in Figure 1.10.
 573 For low mass Higgs, the $\tau^+\tau^-$ decay mode plays a particularly important role. The dominant
 574 decay mode $H \rightarrow b\bar{b}$ suffers from enormous backgrounds from QCD jet production. It
 575 is important to understand the magnitude of difference between expected Higgs boson
 576 production and the rates of various backgrounds. Figure 1.11 illustrates the cross sections
 577 for different SM processes at hadron colliders. The rate of Higgs production is many orders
 578 of magnitude ($\mathcal{O}(10^{-7})$) smaller than that of QCD production. It is important to therefore
 579 design searches to use handles that can reject the vast majority of the uninteresting events
 580 at hadron colliders.

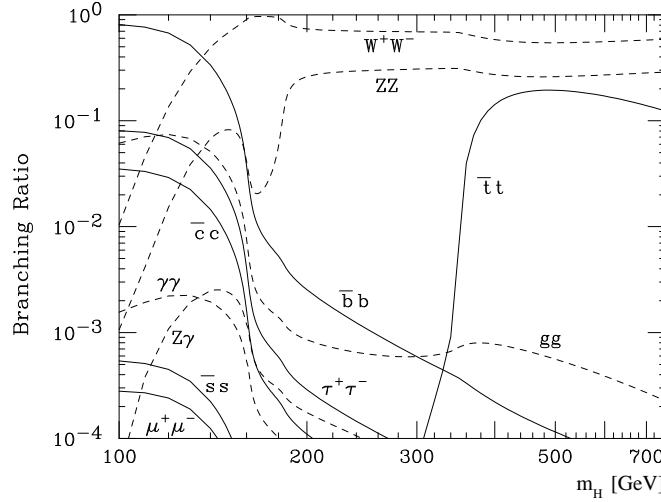


Figure 1.10: Branching fraction of the Standard Model Higgs bosons for different values of m_H . Source: [20].

581 §1.3.2 MSSM Higgs Phenomenology

582 The phenomenology of the Higgs sector of the MSSM is similar to the Standard Model in
 583 some respects, but differs in some key aspects which have important implications for final
 584 states involving τ leptons and b quarks. When the parameter $\tan\beta$ is large, the coupling
 585 factor between the Higgs and the down-type quarks and leptons (effectively the τ and b
 586 quark) is enhanced by $\tan\beta$. The gluon–gluon cross section is therefore increased by $\tan^2\beta$,
 587 where the top quark loop in Figure 1.3.1 is replaced by a ($\tan\beta$ enhanced) b quark loop.
 588 Additionally, MSSM Higgs production with associated b -quarks, illustrated in Figure 1.3.2,
 589 becomes an important production mode. At tree-level, the MSSM can be defined by the
 590 mass of the CP-odd Higgs m_{A^0} and $\tan\beta$. For a reasonably high $\tan\beta$, there is always one
 591 CP-even Higgs (h^0 or H^0) which is mass-degenerate with the A^0 . When $\tan\beta$ and m_{A^0}
 592 are both large, associated b production dominates the total cross section [22]. The cross
 593 sections of the different MSSM neutral Higgs bosons are shown in Figure 1.13. The $\tan\beta$
 594 enhancement of the MSSM Higgs coupling to the b quarks and τ leptons causes the branching
 595 fraction of all neutral MSSM Higgs states to be $H \rightarrow b\bar{b}$ (90%) and $H \rightarrow \tau^+\tau^-$ (10%) across
 596 the entire range of m_{A^0} . The enhanced production rate and the high branching fraction to
 597 τ leptons make the MSSM Higgs decaying to τ leptons an exciting and promising channel
 598 to search for Higgses and Supersymmetric physics at colliders.

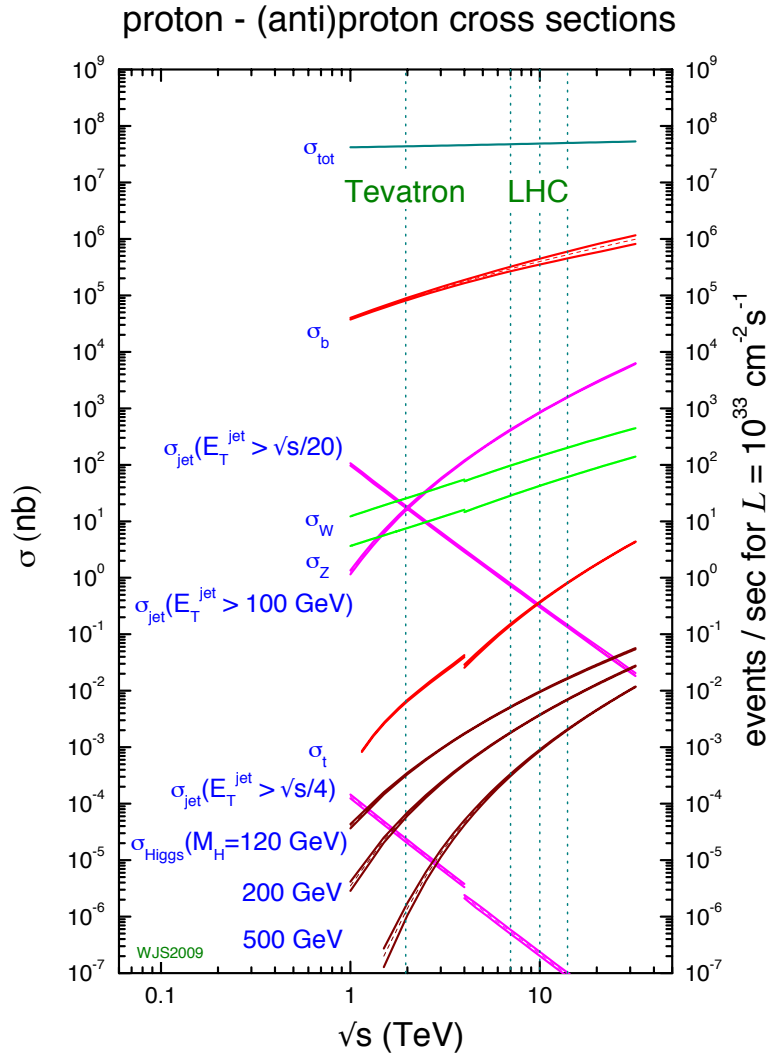


Figure 1.11: Cross sections of various processes at hadron colliders. The horizontal axis represents the center of mass energy of the collision. Of note is the vast difference in scales between Higgs production (maroon lines, $\mathcal{O}(10^{-2} \text{ nb})$) and the QCD cross section to produce $b\bar{b}$ pairs (red line, $\mathcal{O}(10^4 \text{ nb})$). Source: [21].

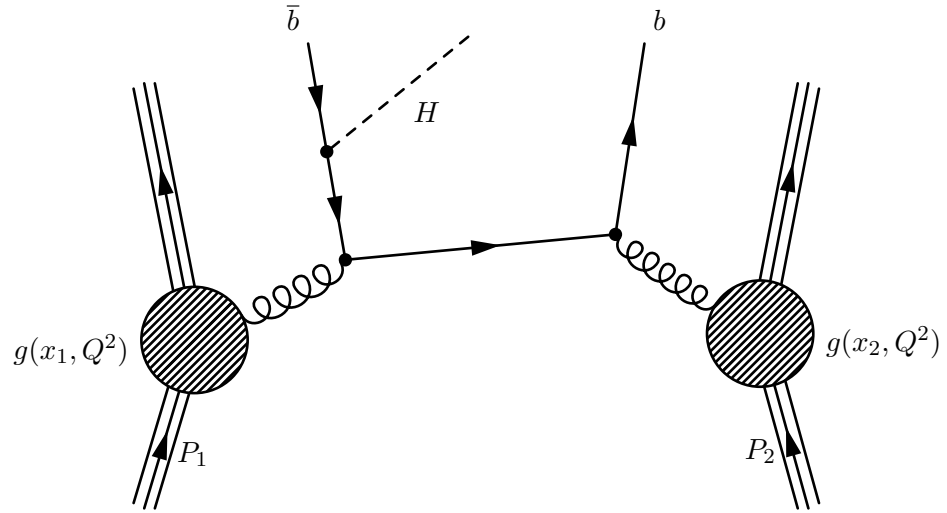


Figure 1.12: One possible diagram for an MSSM Higgs produced with associated b -quarks in a proton–proton collision.

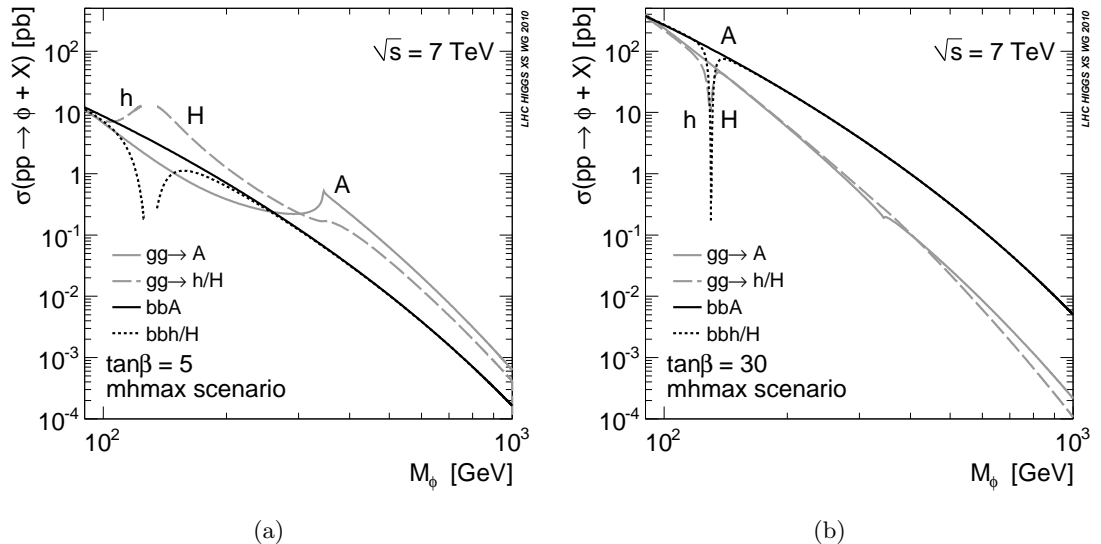


Figure 1.13: Cross sections for the different MSSM Higgs bosons versus m_{A^0} in the m_{hmax} benchmark scenario [23] scenario for $\tan\beta = 5$ (a) and $\tan\beta = 30$ (b). Source: [22]

Higgs Decay	Z Decay
$b\bar{b}$	$q\bar{q}$
$\tau^+\tau^-$	$q\bar{q}$
$b\bar{b}$	$t\bar{t}$
$b\bar{b}$	$\nu\bar{\nu}$
$b\bar{b}$	$\mu^+\mu^-$
$b\bar{b}$	e^+e^-

Table 1.3: Different channels used at LEP to search for Higgs bosons produced with the Higgstrahlung mechanism.

599 §1.3.3 Results from LEP and Tevatron

600 The LEP and Tevatron experiments have both set limits on the existence of the Standard
 601 Model and MSSM Higgs boson. Additionally, precision electroweak measurements give ad-
 602 ditional hints on the prospects for both models.

603 LEP was an e^+e^- collider at CERN and has effectively excluded the presence of a
 604 low (less than 114 GeV/c²) mass Higgs boson. The dominant SM Higgs production mode
 605 at LEP is Higgstrahlung, where the Higgs is produced in association with a Z boson (see
 606 Figure 1.3.1). The search at LEP utilized a number of different decay channels [20]. The
 607 decay channels used in the LEP search are summarized in Table 1.3.3.

608 The results using all channels from the four LEP experiments¹⁰ have been combined into
 609 a single limit, shown in Figure 1.14. The analysis sets a limit on the ratio $\xi^2 = (g_{HZZ}/g_{HZZ})^2$,
 610 the upper limit on the HZZ coupling divided by the predicted value of the Standard Model.
 611 For Higgs masses below 114 GeV/c², the ratio is below unity at the 95% confidence level,
 612 ruling out a Standard Model Higgs below that mass.

613 The Tevatron is a proton–antiproton collider with a center-of-mass energy of $\sqrt{s} = 1.96$ TeV ■
 614 There are two general purpose detectors at the Tevatron, CDF and DØ. The dominant Higgs
 615 production modes at the Tevatron are Higgstrahlung and gluon fusion (see Figure 1.3.1).
 616 For low mass ($m_H < 135$ GeV/c²) Higgs bosons the dominant channel at the Tevatron is the
 617 Higgstrahlung production mode and $H \rightarrow b\bar{b}$ decays. Large multi-jet backgrounds prevent

¹⁰ALEPH, DELPHI, L3, and OPAL

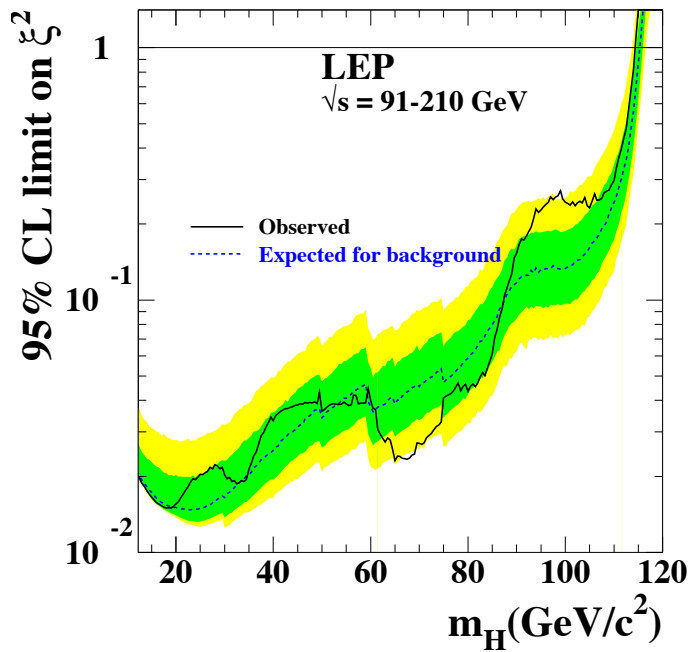


Figure 1.14: Combined LEP upper limit set on the quantity $\xi^2 = (g_{HZZ}/g_{HZZ})^2$ at 95% confidence level. Regions where the observed ratio is less than one exclude the Standard Model. The dashed line gives the expected limit for the null (background only) hypothesis, with the green and yellow bands representing the expected variance at one and two sigma, respectively, of the limit. The solid line is the observed limit from the combined LEP data. Reference: [20]

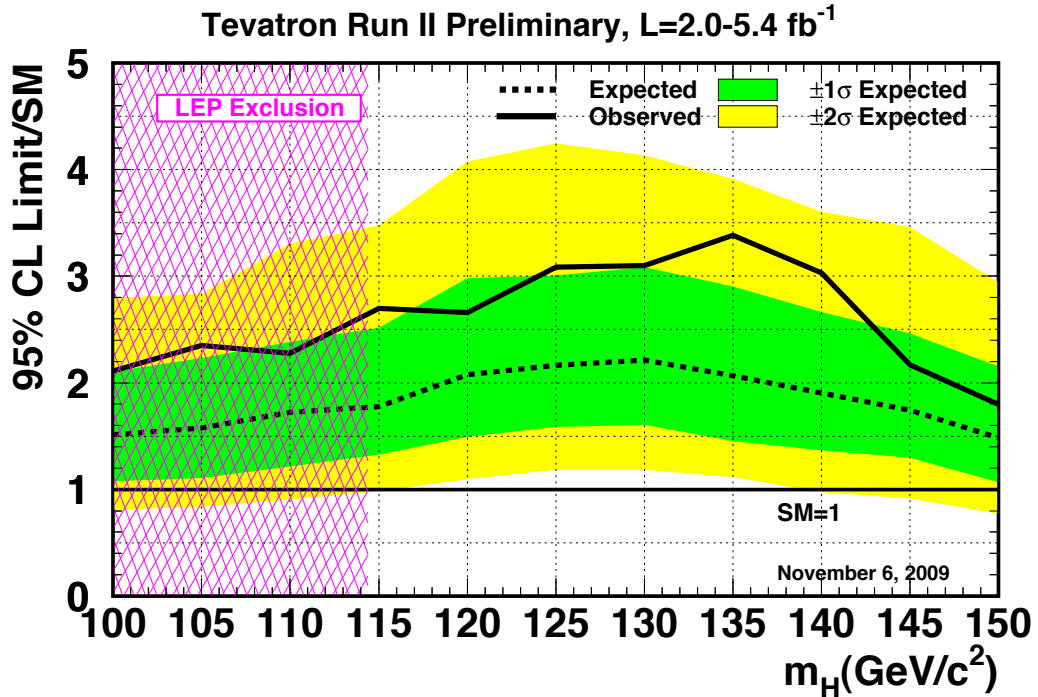


Figure 1.15: Combined CDF and DØ RunII upper limit on the cross section of a Standard Model–like Higgs boson. The LEP limit is shown in pink. Reference: [20]

the $H \rightarrow b\bar{b}$ decay mode from being useful for searching for Higgs bosons produced by gluon fusion. The $H \rightarrow \tau^+\tau^-$ and $H \rightarrow \gamma\gamma$ decays are additionally used in an inclusive search at low mass, but do not dominate the search sensitivity. The combined low-mass limit on the Standard Model Higgs from both Tevatron experiments is shown in Figure 1.15. The Tevatron currently sets an upper limit on the SM Higgs cross section of about 2.5 times the Standard Model expectation.

When ($m_H < 135$ GeV/ c^2) the $H \rightarrow W^+W^-$ decay mode becomes significant. Low di–boson backgrounds allow this decay mode to probe both the Higgstrahlung and gluon fusion production modes. The combined results of the CDF and DØ searches using the W^+W^- decay mode recently excluded (See Figure 1.16) a Standard Model Higgs with a mass between 162 and 166 GeV/ c^2 . This is the first exclusion in Standard Model Higgs mass parameter space since the LEP result.

Analyses at LEP and Tevatron have also addressed excluded regions of the MSSM. At LEP, the dominant production modes of the MSSM Higgs bosons are Higgstrahlung and

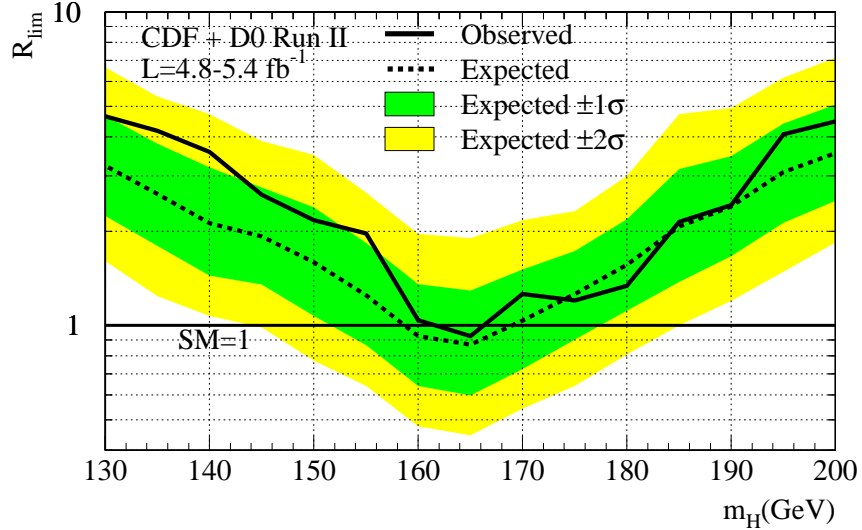


Figure 1.16: Combined CDF and DØ RunII upper limit on the cross section of a Standard Model–like Higgs boson using the $H \rightarrow W^+W^-$ decay mode. The Standard Model is excluded for Higgs boson masses between 162 and 166 GeV/c^2 . Reference: [20]

632 pair production, where $e^+e^- \rightarrow h^0A^0$ or H^0A^0 . For the Higgstrahlung production mode,
 633 the Standard Model search can be reinterpreted in terms of the MSSM. To address the pair
 634 production mode, searches were performed in the $e^+e^- \rightarrow h^0A^0 \rightarrow b\bar{b}b\bar{b}$ and $\tau^+\tau^-q\bar{q}$ decay
 635 modes. Finally, LEP is also sensitive to associated MSSM Higgs production at low m_{A^0} and
 636 high $\tan\beta$ to $e^+e^- \rightarrow \{\bar{\phi}\}$, where the associated fermions $\{\cdot\}$ are b –quarks or tau leptons.
 637 The combined limits from LEP in the $m_{A^0} - \tan\beta$ plane are shown in Figure 1.17.

638 At the Tevatron, CDF and DØ have set a combined limit on the MSSM using the
 639 inclusive $H \rightarrow \tau^+\tau^-$ channel. The analysis presented in this thesis is very similar to the
 640 approaches used at the Tevatron. Results from the Tevatron have excluded the MSSM for
 641 $\tan\beta$ greater than approximately 35 for MSSM Higgs mass $m_{A^0} < 200$ GeV/c^2 . The full
 642 exclusion plot for the m_h –max and “no mixing” MSSM benchmark scenarios are shown in
 643 Figure 1.18.

644 §1.4 The Physics of the Tau Lepton

645 As discussed in Sections 1.3.1 and 1.2.3, the τ lepton is an important probe of Higgs physics.
 646 The τ lepton has some unusual properties which make it particularly challenging at hadron
 647 colliders. With a mass of 1.78 GeV/c^2 , the τ lepton is heaviest of the leptons. The nominal

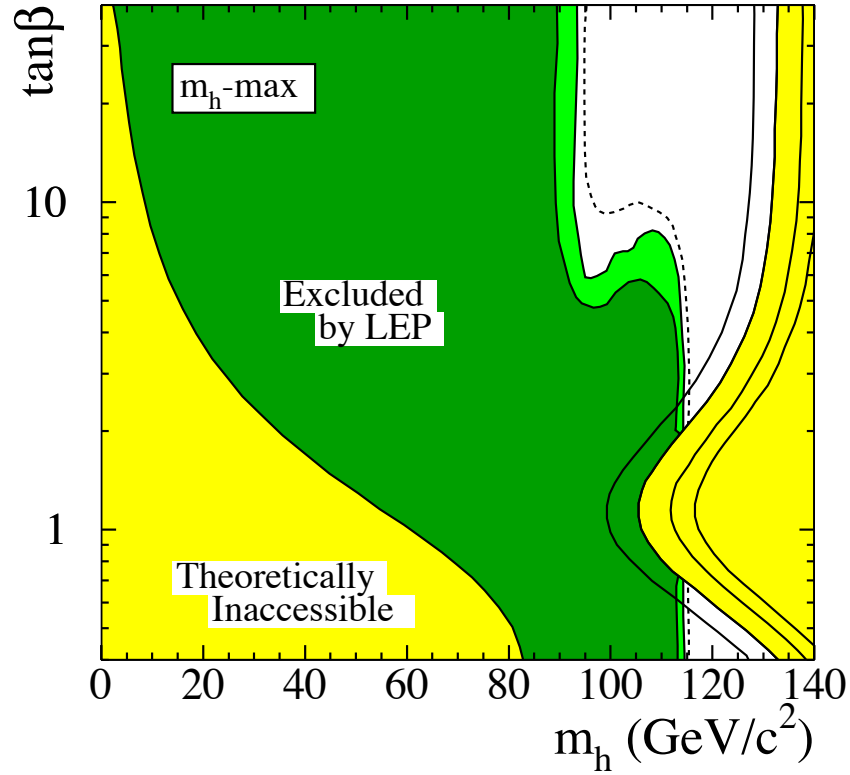


Figure 1.17: Combined LEP limits on the MSSM. The results are interpreted in the context of the m_h -max benchmark [23] scenario of the MSSM. Reference: [20]

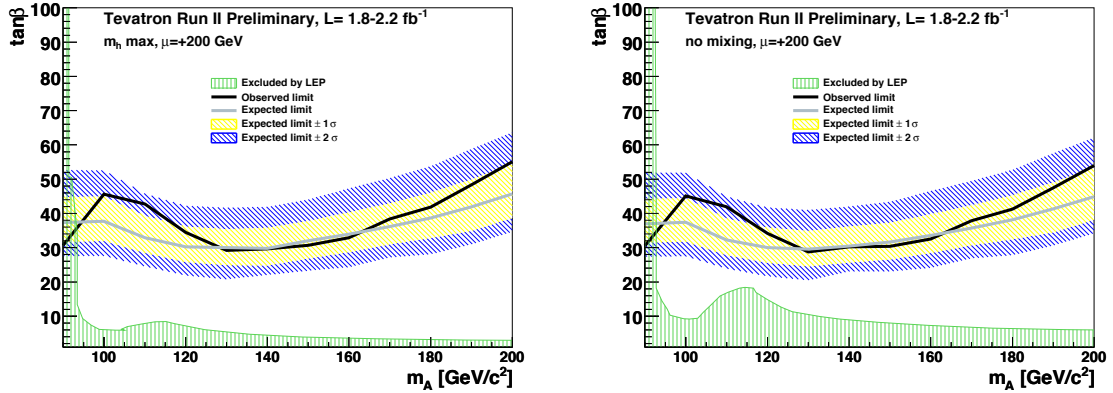


Figure 1.18: Combined Tevatron limits on the MSSM. The grey line and blue and yellow bands give the expected limit and its one and two sigma contours. The black line is the observed limit. The results are interpreted in the context of the m_h -max benchmark (left) and “no mixing” (right) MSSM scenarios. The limit from LEP is shown in green. Reference: [20]

Visible Decay Products	Resonance	Mass (MeV/ c^2)	Fraction [20]
Leptonic modes			
$e^- \nu_\tau \bar{\nu}_e$	-	0.5	17.8%
$\mu^- \nu_\tau \bar{\nu}_\mu$	-	105	17.4%
Hadronic modes			
$\pi^- \nu_\tau$	-	135	10.9%
$\pi^- \pi^0 \nu_\tau$	ρ	770	25.5%
$\pi^- \pi^0 \pi^0 \nu_\tau$	$a1$	1200	9.3%
$\pi^- \pi^- \pi^+ \nu_\tau$	$a1$	1200	9.0%
$\pi^- \pi^- \pi^+ \pi^0 \nu_\tau$	$a1$	1200	4.5%
Total			94.4%

Table 1.4: Resonances and branching ratios of the dominant decay modes of the τ lepton. The decay products listed correspond to a negatively charged τ lepton; the table is identical under charge conjugation.

648 decay distance $c\tau$ of the τ lepton is 87 μm , which in practice means that the τ will always
 649 decay before reaching the first layer of the detector. Tau decays can be effectively classified
 650 into two types. “Leptonic” decays consist of a τ decaying to a light lepton ($\ell = e, \mu$) and two
 651 neutrinos $\tau^+ \rightarrow \ell^+ \nu_\tau \bar{\nu}_\ell$. “Hadronic” decays consist of a low-multiplicity collimated group of
 652 hadrons, typically π^\pm and π^0 mesons. The hadronic decays of the τ lepton compose approx-
 653 imately 65% of the τ lepton branching fraction, with the remainder shared approximately
 654 equally by the leptonic decays. The branching fractions for the leptonic and most common
 655 hadronic decays are shown in Table 1.4.

656 The tau is also a challenging object in that the decay of the tau always includes neu-
 657 trinos. The associated neutrinos are weakly interacting and do not create a signal in any
 658 detector at CMS. The only sign that the neutrinos are there is an imbalance in the total
 659 transverse¹¹ energy in the event. This thesis will describe a novel way to reconstruct the
 660 neutrinos associated to tau decays in Chapter 4.

¹¹At proton colliders, the constituent quarks/gluons of the proton share the total proton momentum. As the total fraction of momentum carried by the parton involved in a hard collision is unknown, longitudinal momentum is not conserved.

A tau with produced with energy E travels on average

$$\gamma c\tau = \frac{E}{1.78 \text{ GeV}} 87 \text{ }\mu\text{m}$$

before decaying in the detector. These lengths are comparable to the resolution of the CMS tracker, therefore it is possible to reconstruct a vertex corresponding to a tau decay that is displaced with respect to the primary vertex. This can be used as an additional discriminant against QCD, which is expected to decay promptly. Furthermore, in Chapter 4 we will see it may be possible to use it when reconstructing the associated neutrinos.

666

Chapter 2

667

The Compact Muon Solenoid Experiment

668 The Compact Muon Solenoid (CMS) Experiment is a “general purpose” particle detector
 669 designed to measure collision events at the Large Hadron Collider (LHC), a proton–proton
 670 synchrotron located at the CERN laboratory in Geneva, Switzerland. The design goals of
 671 the CMS experiment are [24], in order of priority:

- 672 • Good muon identification and momentum resolution over a wide range of momenta
 and angles, good dimuon mass resolution ($\approx 1\%$ at 100 GeV/c 2), and the ability to
 determine unambiguously the charge of muons with $p < 1$ TeV/c;
- 675 • Good charged-particle momentum resolution and reconstruction efficiency in the in-
 ner tracker. Efficient triggering and offline tagging of τ ’s and b -jets, requiring pixel
 detectors close to the interaction region;
- 678 • Good electromagnetic energy resolution, good diphoton and dielectron mass resolution
 ($\approx 1\%$ at 100 GeV/c 2), wide geometric coverage, π^0 rejection, and efficient photon and
 lepton isolation at high luminosities;
- 681 • Good missing-transverse-energy and dijet-mass resolution, requiring hadron calorime-
 ters with a large hermetic geometric coverage and with fine lateral segmentation.

683 The detector uses a hermetic design that maximizes the solid-angle of the fiducial region to
 684 capture as much information about the collisions as possible. The general geometry of the
 685 detector is cylindrical. A cutaway diagram of the detector is shown in Figure 2.1. Each of
 686 the sub-detector components consists of “barrel” and “endcap” components. As its name
 687 suggests, the detector is centered around a four Tesla superconducting solenoid magnet.
 688 The individual sub-detectors of CMS are arranged in a manner that permits identification

689 of different species of particles. The central (closest to interaction point) sub-detectors are
 690 the charged particle tracking systems (the “tracker”). The tracker is designed to be a non–
 691 destructive instrument, which means that ideally that the momentum of particles are un–
 692 changed after passing through it. Outside of the tracker is the electromagnetic and hadronic
 693 calorimeters, which are abbreviated ECAL and HCAL, respectively. The calorimeters are
 694 destructive detector, and are designed such that visible incident particles are completely
 695 absorbed. The outer layers of CMS are designed to measure muons, the one¹ species of
 696 particle that is nearly immune to the stopping power of the calorimeter. The arrangement
 697 of destructive and non-destructive sub-detectors facilitates the identification of different
 698 types of particles. This concept is illustrated in Figure 2.1(b). In this chapter we give an
 699 brief overview of the LHC machine, and then describe the individual sub-detector systems
 700 of CMS.

701 §2.1 The Large Hadron Collider

702 The Large Hadron Collider is a proton–proton synchrotron, with a design collision energy
 703 of 14 TeV. At the time of this writing (and for the foreseeable future), the LHC is the
 704 world’s largest and highest energy particle accelerator. A synchrotron is a machine that
 705 accelerates beams of charged particles by using magnets to steer them in a circle through
 706 radio–frequency resonating cavities which accelerate the particles. As the LHC is a collider,
 707 there are two beams that are accelerated in opposite directions. The maximum beam energy
 708 of a synchrotron is determined by its radius and the maximum strength of the magnetic
 709 fields used to bend the path of the beam. The dipole magnets used by the LHC to steer the
 710 particles are superconducting niobium–titanium. To maintain them in a superconducting
 711 state, they are cooled using superfluid liquid helium to 1.9 Kelvin. To store the beam at the
 712 injection energy of 450 GeV, the magnetic dipole fields must be maintained at 1/2 Tesla. As
 713 the energy of each beam energy is increased to its (design) maximum of 7 TeV, the dipole
 714 fields are ramped to a maximum field of over 8 Tesla.

¹Neutrinos of course fulfill this requirement as well, but are so weakly interacting that they are effectively invisible.

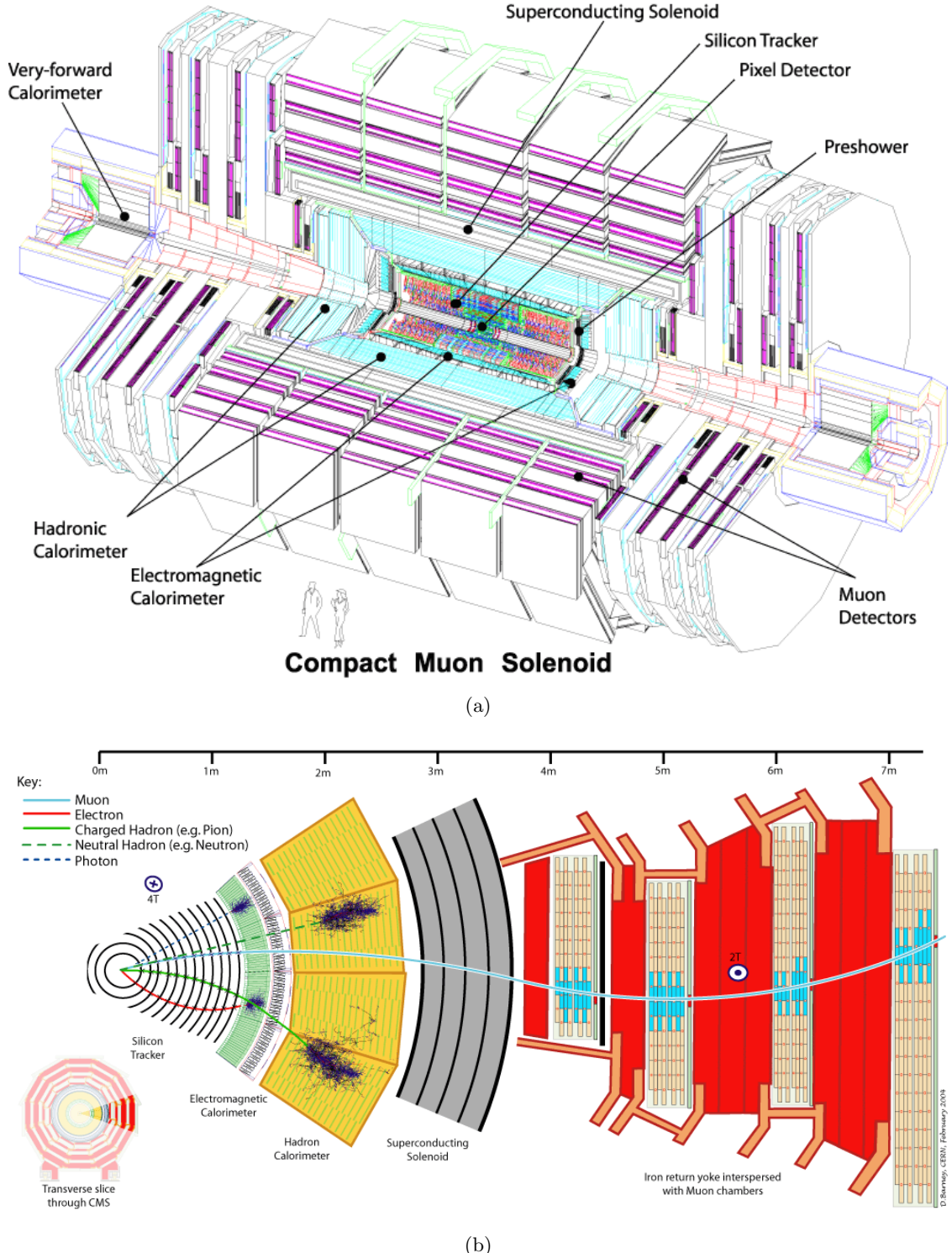


Figure 2.1: Figure (a), top, shows a schematic drawing of the CMS detector. The individual sub-detectors are labeled. Two humans are shown in the foreground for scale. Figure (b) shows a radial cross section of the detector and demonstrates how the (non-)destructiveness of different sub-detectors facilitates particle identification.

₇₁₅ §2.2 Solenoid Magnet

The four Tesla field of the CMS solenoid magnet is a critical factor in ability of CMS to precisely measure the particles produced in collisions at the LHC. The momentum of charged particles is measured in the tracking detector by examining the curvature of the particles path as it travels through the magnetic field. The radius of curvature r of a charged particle in a magnetic field is given by

$$r = \frac{p_{\perp}}{|qB|}, \quad (2.1)$$

₇₁₆ where q is the charge of the particle, B is strength of the magnetic field, and p_{\perp} is the
₇₁₇ component of the particle's relativistic momentum perpendicular to the direction of the
₇₁₈ magnetic field. From Equation 2.1, it is evident that the ability to measure high momentum
₇₁₉ charged particles (a critical goal of CMS) requires a high magnetic field. Even at very high
₇₂₀ particle energies where the resolution becomes poor, the strength of the magnetic field
₇₂₁ is still very important for identifying the bending direction of the particle; the direction
₇₂₂ corresponds to the particle's electric charge. Furthermore, the homogeneity of the magnetic
₇₂₃ field is important to minimize systematic errors in the measurement of tracks.

₇₂₄ The CMS solenoid is extremely large. The radial bore of the magnet is 6.3 meters; the
₇₂₅ magnet is 12.5 meters in length and weighs 220 tons. The large bore of the magnet allows
₇₂₆ the tracker and calorimeter systems to be located inside the solenoid. The internal windings
₇₂₇ of solenoid is arranged in four layers to increase the total field strength and are cooled by
₇₂₈ liquid helium to a temperature of 4.5 Kelvin. The windings are magnetically coupled to
₇₂₉ the support superstructure. This coupling allows the magnetic to heat uniformly during a
₇₃₀ “quench” event², reducing localized stresses. The nominal current at full field of the solenoid
₇₃₁ is 19.14 kA. The solenoid itself is surrounded by an iron return yoke with a total mass of
₇₃₂ 10,000 tons. The return yoke surrounding the solenoid minimizes the fringing field. The
₇₃₃ muon detector system is interspersed inside the yoke, and takes advantage of the return
₇₃₄ field in the yoke to measure the momentum and charge of muons.

²A quench event occurs when some part of the magnet is suddenly no longer in a superconducting state. The coil becomes resistive and the large current in the magnet creates large amounts of heat.

735 §2.3 Charged Particle Tracking Systems

736 The charged particle tracking system measures the trajectories of charged particles emerging
 737 from the event. The tracker measures the trajectory of a charged particle by measuring
 738 “hits” along the trajectory. Each hit corresponds to the global position of the trajectory
 739 on a given surface. The trajectory can then be reconstructed by a helix to the points.
 740 The tracker is designed to have a resolution that permits the reconstruction of “secondary
 741 vertices” in b –quark and τ lepton decays. To accomplish this, there are two types of tracking
 742 detectors in CMS. The “pixel detector” composes the inner layers (three in the barrel, two in
 743 the endcaps). The pixel detector is situated as close as possible (4.4 cm) to the interaction
 744 point and has a very high resolution. Outside of the pixel detector is the silicon strip tracker,
 745 with ten layers in the barrel and 12 layers in the endcaps. A secondary vertex occurs when a
 746 particle is semi-stable, traveling some non-negligible distance in the detector, but decaying
 747 before the first layer of the tracking system. The pixel and strip tracking detectors have a
 748 fiducial region which extends to a pseudorapidity of approximately $|\eta| \approx 2.5$.

749 Both the pixel and strip trackers are silicon based. The principle of operation is similar
 750 to that of a charged-coupled discharge (CCD) in a modern digital camera. The sensitive
 751 portion of the detector is a silicon chip that is arranged with diode junctions formed by
 752 a p –doped layer and an n –doped layer³. Each $p - n$ junction is electrically isolated from
 753 adjacent layers. The size of each junction region determines⁴ the spatial resolution of the
 754 sensor. In the pixel detector, each sensor region “pixel” is $100 \times 150 \mu\text{m}^2$. In the strip
 755 tracker, The rear side of the chip is mounted to read-out electronics. During operation, a
 756 high-voltage reverse bias is applied to each $p - n$ junction to achieve full depletion. When
 757 a charged particle passes through the detector, the diode-junction breaks down and the
 758 readout system registers the hit.

Fixme: right

acronym

759 The tracking system has been specifically designed for the high radiation environment
 760 around the interaction point. The detector is cooled to -27°C during operation to minimize

³The pixel detector actually uses a more complicated multi-layered scheme to improve radiation hardness. For details, see Section 3.2.2 of [24].

⁴Additionally, the size of the sensitive area needs to be small enough such that the hit occupancy during a typically LHC event is not too large, which would cause overlaps and spoil the ability to reconstruct tracks. The expected occupancy depends on the distance r^2 from the interaction. The expected occupancy in the pixel detector for LHC collisions is 10^{-4} .

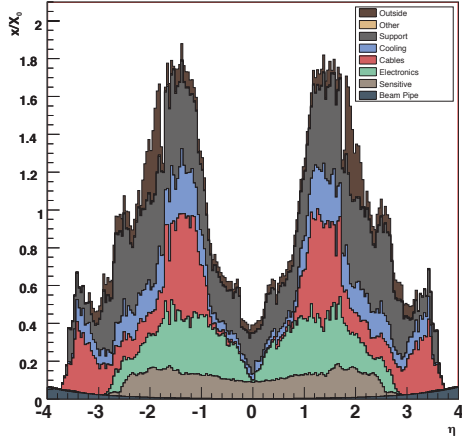


Figure 2.2: Material budget of the CMS tracker in units of radiation lengths X_0 versus pseudorapidity. The material budget is broken down into the contributions from the different components of the tracker. The amount of material is largest in the “transition region” between the barrel and endcap.

761 damage. Radiation exposure produced in LHC collisions can change behavior of the tracking
 762 detector in three ways. Over time, radiation can induce positive holes in oxide layers found
 763 in the read-out electrons which increase the signal-to-noise ratio. In the sensor mass itself,
 764 radiation damage changes the doping from n to p over time. The required voltage to deplete
 765 the sensor will thus increase over time. The readout electronics, bias voltage supplies, and
 766 cooling systems are designed to scale with the radiation damage and maintain a signal-to-
 767 noise ration of 10:1 or greater for 10 years of LHC operation. The final radiation effect is not
 768 an integrating effect. A “single event upset” is transient effect where an ionizing charged
 769 particle passes through the readout electronics and changes the state of the digital circuitry.

770 In the ideal case, the tracker would be a non-destructive instrument. However, charged
 771 particles can interact with the mass of the tracker (and its support infrastructure). These
 772 interactions limit the resolution of the tracker. The amount of matter in the tracker is
 773 referred to as the “material budget”. The material budget of the CMS tracker depends
 774 heavily on the pseudorapidity η and is illustrated in Figure 2.2. The relatively large ma-
 775 terial budget of the CMS tracker has two effects: charged particles can undergo “multiple
 776 scattering,” interacting with material in the tracker. This can cause “kinks” in the recon-
 777 structed track. Hadronic particles (charged and neutral) can undergo nuclear interactions,

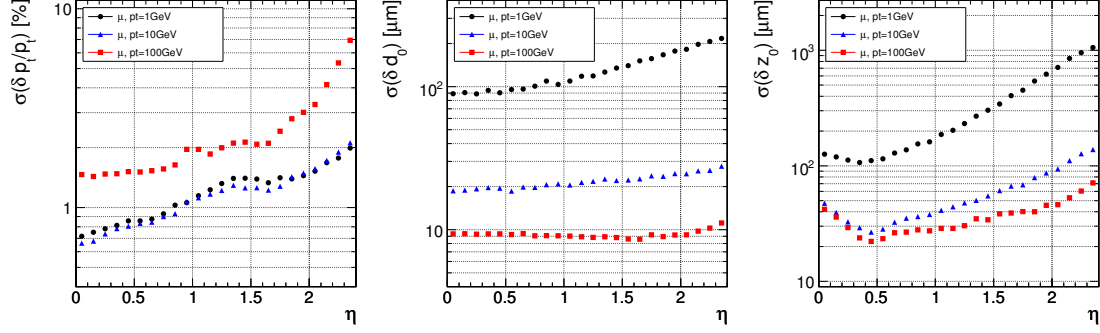


Figure 2.3: Expected resolutions of reconstructed transverse momentum (left), transverse impact parameter (center), and longitudinal impact parameter (right) versus absolute pseudorapidity $|\eta|$. The resolution is shown for three different cases of particle p_T , 1 GeV/c (black), 10 GeV/c (blue), and 100 GeV/c (red).

which are hard collisions between the incident particle and a nucleus in tracker material. This typically produces a spray of hadrons from the point of interaction. Finally, the material budget can cause ‘‘photon conversions.’’ A photon conversion occurs when a photon (which typically does not interact with the tracker) converts into an electron–positron pair while passing through material in the tracker.

The expected (from simulation) impact parameter and transverse momentum resolution of the tracker is shown in Figure 2.3. The momentum scale of the tracker has been measured [25] in 7 TeV 2010 CMS data using $J/\psi \rightarrow \mu^+\mu^-$ decays and is found to agree with the prediction from simulation within 5%. The impact parameter and vertex resolutions have also been measured [26] in data and found to be in excellent agreement with the simulation.

§2.4 Electromagnetic Calorimeter

The electromagnetic calorimeter (ECAL) of CMS is designed to measure the energy of particles which interact electromagnetically with high precision.⁵ The ECAL is a *scintillation* detector, and functions by counting the number of photons produced in an electromagnetic shower inside a crystal. Upon entering the crystal, a charged particle or photon will interact electromagnetically with the crystal, producing a shower of electrons and photons. The

⁵One of the design goals of the CMS experiment is to be able to conduct a search for Standard Higgs bosons decaying to pairs of photons. The branching fraction to photons is illustrated in Figure 1.10.

795 shower will expand until it consists entirely of photons. The crystal is optically clear, so
 796 these photons travel to the rear face of the crystal where they are then counted by a pho-
 797 tomultiplier. The number of detected photons can then be related to the energy that was
 798 deposited in the crystal. At 18°C, about 4.5 photoelectrons will be produced per MeV of de-
 799 posited energy. The ECAL has excellent solid angle coverage, extending to a pseudorapidity
 800 of $|\eta| = 3.0$.

801 The ECAL uses lead tungstate (PbWO_4) crystals as the scintillation medium. The
 802 crystals have a very large density, which allows the calorimeter to be relatively compact.
 803 To be able to correctly measure the energy of electrons and photons, an incident photon or
 804 electron must be completely stopped by interactions with the calorimeter. The quantities
 805 that determine if an electron or photon will be completely contained is the total depth of
 806 the crystal, the crystal density, and the radiation length property X_0 of the crystal. The
 807 radiation length X_0 is defined as the mean distance (normalized to material density) after
 808 which an electron will have lost $(1 - \frac{1}{e})$ of its energy. The PbWO_4 crystals of the CMS
 809 ECAL have a density of 8.28 g/cm² and a depth of 230 mm. A single crystal thus has a
 810 total radiation length of 25.8 X_0 , and will capture on average 99.9993% of the energy of an
 811 incident electron. The front face of the crystal is 22 mm × 22 mm, which corresponds to an
 812 $\eta - \phi$ area of 0.00174×0.00174 . The Molière radius of a material is the average radial profile
 813 size of an electromagnetic shower, and for PbWO_4 is 2.2 cm. The fact that the Molière
 814 radius is larger than the size of the individual crystals improves the spatial resolution of
 815 the measurement. As the shower is shared between multiple crystals, the relative amounts
 816 deposited in each crystal allows the true impact point to be determined with a resolution
 817 smaller than the individual crystal size.

818 The transparency of the CMS ECAL crystals change as they are exposed to radiation.
 819 However, at the working temperature of the ECAL (18°C), the crystal transparency will
 820 naturally return to its nominal value. The transparency of the crystals thus decreases during
 821 the course of a run of collisions, then increases during the following collision-less period.
 822 The changing transparency conditions need to be continuously monitored and corrected
 823 for to ensure a stable detector response. The transparency of the crystals are measured
 824 continuously using two lasers. One laser has wavelength $\lambda = 400$ nm which corresponds to

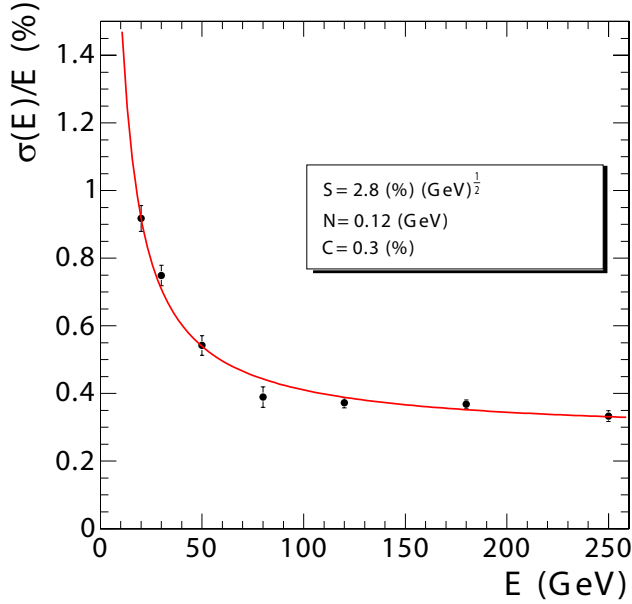


Figure 2.4: Energy resolution (in %) of the CMS ECAL measured at an electron test beam. The resolution depends on the incident energy of the electron. The points are fitted to function with the form given in Equation 2.2. The fitted parameters are given in the legend.

the color of light produced in the scintillations and is sensitive to changes in transparency.
 The other laser is in the near-infrared and is used to monitor the overall stability of the crystal. The lasers are synchronized to pulse between LHC bunch trains so the transparency can be continuously monitored while collisions are occurring.

The energy resolution of the ECAL is given by

$$\left(\frac{\sigma}{E}\right)^2 = \left(\frac{S}{\sqrt{E}}\right)^2 + \left(\frac{N}{E}\right)^2 + C^2, \quad (2.2)$$

where S is a stochastic noise term (due to photon counting statistics), N is a noise term, and C is a constant term. The parameters of Equation 2.2 have been measured at an electron test-beam (see Figure 2.4). The energy resolution is better than 1% for electron energies greater than 20 GeV.

§2.5 Hadronic Calorimeter

The hadronic calorimeter (HCAL) surrounds the CMS ECAL and is located within the coil of the CMS solenoid magnet. To ensure incident particles are completely contained within the calorimeter volume, in the barrel region the HCAL employs a “tail-catcher”, an extra

837 layer of calorimetry outside of the magnet. The hadronic calorimeter measures the energy
 838 of charged and neutral hadronic particles. The HCAL is a *sampling* calorimeter. Layers of
 839 plastic scintillating tiles are interspersed between brass absorber plates. An incident hadron
 840 produces a hadronic shower as it passes through the absorber. The particles in the shower
 841 produce light as they pass through the scintillating tiles. Measuring the light produced in
 842 each layer of tile allows the reconstruction of the radial profile of the shower which can be
 843 related to the deposited energy. The response of the scintillator tiles are calibrated using a
 844 radioactive source, either Cs¹³⁷ or Co⁶⁰. Small stainless tubes permit the radioactive sources
 845 to be moved into the center of the tile during calibration. The granularity of the HCAL is
 846 0.087 × 0.087 and 0.17 × 0.17 in $\eta - \phi$ in the barrel ($|\eta| < 1.6$) and endcap ($|\eta| > 1.6$),
 847 respectively.

848 The outer HCAL (HO), or “tail catcher” is designed to capture showers which begin
 849 late in the ECAL or HCAL and ensure they do not create spurious signals in the muon
 850 system (“punch through”). The HO is installed outside of the solenoid magnet in the first
 851 layer between the first two layers of the iron return yoke. The total depth of the HCAL,
 852 including the HO is then 11.8 interaction lengths.

853 The HCAL includes a specially designed forward calorimeter (HF). The design of the
 854 forward calorimeter is constrained by the extreme amount of radiation it is exposed to,
 855 particularly at the highest rapidities. The active material of the HF are quartz fibers. The
 856 fibers are installed inside grooves inside of a steel absorber. Charged particles created in
 857 showers in the absorber create light in the fibers, provided they have energy greater than
 858 the Cherenkov threshold. As Cherenkov light is created by
 859 the passage of charged particles through matter, the HF design is not sensitive to neutrons
 860 emitted by radionucleids that may be created in the absorber material during operation.
 861 The fibers are grouped into two sets: one set of fibers are installed over the full depth of
 862 the detector, the other only cover half the depth. A crude form of particle identification
 863 is possible, as showers created by electrons and photons will deposit the majority of the
 864 energy in the front of the detector.

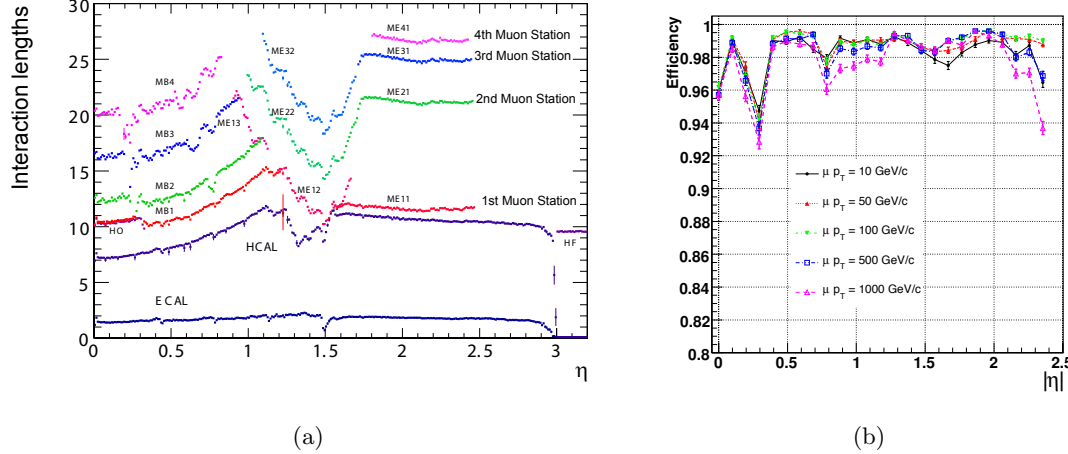


Figure 2.5: The left figure, (a), illustrates the number of interaction lengths versus pseudorapidity η of material that must be traversed before reaching the different layers of the muon system. On the right, (b) shows the efficiency versus η to reconstruct a “global” muon for different transverse momenta.

865 §2.6 Muon System

866 The ability to detect and measure muons is one of the most valuable tools an experimentalist
 867 has at a hadron collider experiment. Muons have particular properties that cause them to
 868 leave extremely unique signatures in the detectors.

869 • Muons are stable particles, for the typical energies and distances considered at a
 870 collider.

871 • Muons have non-zero charge, so their trajectories can be measured.

872 • Muons are heavy enough that they are “minimum ionizing particles,” in that they
 873 lose very little energy as they pass through material.

874 The approach to detecting muons is to build the detector to a thickness such that other
 875 particles (electrons, photons, hadrons) will not penetrate the outermost calorimeter. Any
 876 charged particle that is detected outside of this region can then be identified as a muon. At
 877 CMS, the muon detection systems are built into the magnet return yoke outside of the CMS
 878 calorimeters and magnet, giving them excellent protection (illustrated in Figure 2.5(a))
 879 against hadronic “punch-through.” The purity of particles that reach the muon system
 880 make it especially effective as a “trigger” of interesting physics. The CMS muon system

881 has the feature that it additionally can trigger on the transverse momenta of muons. The
 882 CMS muon system is composed of three types of detectors: drift tubes (DT), resistive plate
 883 chambers (RPC), and cathode strip chambers (CSC).

884 A drift tube detector is of a tube filled with a mixture of argon (85%) and carbon
 885 dioxide (15%) gas with a positively charged ($V = +3.6$ kV) wire running through the
 886 middle of the tube. When a charged particle passes through the tube, it ionizes some gas.
 887 The free electrons are then drawn to the positively charged wire inside the tube, creating a
 888 signal when reach it. The speed of the detector is limited by the “drift time,” the maximum
 889 amount of time it may take for an electron to reach a sensor wire. The precision of the
 890 spatial measurement can be increased by recording the time at which each wire records a
 891 signal and correlating the measurements across multiple tubes. The time resolution of the
 892 CMS DTs is on the order of a few nanoseconds, allowing the DT to provide a trigger on
 893 a given proton bunch crossing. The tubes in adjacent layers are offset by one half tube
 894 width to take advantage of this effect and ensure there are no gaps in the fiducial region. In
 895 CMS, the smallest unit of the DT system is the superlayer, which consists of four layers of
 896 tubes. A DT chamber consists of three or two superlayers. The tubes in the two superlayers
 897 farthest from the beam are oriented parallel to the beam and measured the bending of the
 898 muons in the magnetic field. The inner superlayer is oriented orthogonally to the beam and
 899 measures the longitudinal position of incident muons. There are four muon “stations” in
 900 the barrel which contain DT chambers. The stations correspond to available areas in the
 901 magnetic return yoke. In the barrel, the muon momentum resolution of the DTs is better
 902 than 95%.

903 Cathode strip chambers (CSCs) are used in the endcap muon system, providing cov-
 904 erage in the pseudorapidity range $0.9 < |\eta| < 2.4$. A cathode strip chamber consists of a
 905 chamber filled with inert gas that with a number of internal wires held at a high voltage. A
 906 number of cathode strips are installed perpendicular⁶ induced to the wires on the walls of
 907 the chamber. When a muon passes through the CSC, it ionizes some of the gas. The high
 908 voltage on a nearby wire causes this ionized gas to break down, forming a conductive pas-

⁶The wires are actually placed at an angle to the perpendicular to compensate for a shifting effect caused by the magnetic field Lorentz force.

909 sage in the gas and an “avalanche” current between the wire and a number of the cathode
 910 strips. The spatial position of the hit in two dimensions is found taking one coordinate from
 911 the wire and the other coordinate from the signal average of the cathode strips.

912 The CSCs in the CMS endcap are positioned such that a muon in the pseudorapidity
 913 range $1.2 < |\eta| < 2.4$ will cross three or four CSC detectors. The geometry of the CSC
 914 strips and wires is designed to provide a spatial $r - \phi$ resolution of 2 mm at the L1 trigger
 915 level and a final offline reconstruction resolution of 75 μm for the first layer and 150 μm for
 916 outer layers. The RMS of the response time for a CSC layer is about 11 ns, which is too
 917 long to correctly associate a signal in the CSCs to an LHC bunch crossing (25 ns) with
 918 high efficiency. By grouping the layers into chambers, and taking the shortest response, the
 919 correct bunch crossing can be identified with 98–99% efficiency.

920 The Resistive Plate Chamber (RPC) muon detectors ensure that the muon system can
 921 be used as a fast, first level trigger. The RPC detector consists of two gaps filled with gas
 922 (up and down) with a common set of strips between the two gaps. The strips are oriented
 923 parallel to the beam line to permit measurement of the transverse momentum of the muons.

924 §2.7 Trigger System

925 At the LHC, proton bunch crossings (collisions) occur every 25 ns. This corresponds to
 926 an interaction rate of 40 MHz. At this high rate, and with the huge number of channels
 927 in the CMS detector, the front-end bandwidth readout from the detector is over 1 Pb/s.
 928 Due to bandwidth and storage requirements, the rate at which events are permanently
 929 recorded must be reduced by more than a factor of a million. This reduction is achieved
 930 by CMS trigger system. As only a fraction of the total events can be stored, and the rate
 931 of diffractive and common QCD multi-jet production is many orders of magnitude larger
 932 than “interesting” new physics (see Figure 1.11). The trigger must therefore be designed to
 933 select “interesting” events. A typical requirement applied at the trigger level might be the
 934 presence of a high- p_{T} muon, an isolated ECAL deposit, or a large deposit of energy in the
 935 event.

936 The CMS trigger consists of two stages: a fast Level-1 (L1) trigger and a High-Level
 937 Trigger (HLT). The L1 trigger system is built on custom, typically reprogrammable elec-

tronics and interfaces directly to the detector subsystems. The L1 trigger has access to information from the muon and calorimeter systems. The L1 does not have access to the full granularity of the muon system and calorimeters but must make the decision based on coarse segments. The design acceptance rate of the L1 trigger is 100 kHz. The trigger typically operates at a nominal rate of 30 kHz. The maximum latency of the L1 is 3.2 μ s, requiring that the output from detector electronics be passed through memory pipelines to ensure that no bunch crossings go unanalyzed. The High-Level Trigger (HLT) runs on a farm of about 1000 commercial compute nodes and processes events that are accepted by the L1 trigger. An HLT decision (“path”) has the ability to reconstruct tracks and do a full regional unpacking of the recorded hits in a regions of the calorimeter. Each HLT path has a strict rate budget, as the total rate of the HLT is required to be less than 100 Hz. The triggers used at CMS change as the conditions change. To limit the total rate to 100 Hz as the luminosity increases, trigger paths must either increase their thresholds, or apply a “prescale.” When a prescale is applied, a fraction of events passing the trigger are thrown away randomly.

The CMS trigger is a deep subject and a complete description is beyond the scope of this thesis. A detailed description can be found in [27]. The triggers used in the analysis presented in this thesis will be briefly described. Two types of trigger selections were applied to the 2010 datasets used in this analysis. During the initial period of low luminosity running, single muon triggers were used. As the luminosity increased, the p_T threshold of the trigger was increased. In some cases, an “isolated muon” HLT trigger was required, in which a veto was applied on muons with associated energy deposits in the calorimeter. In the final period of data taking, two “cross-triggers” were used. These required the presence of both a muon and a hadronic tau decay in the event. The triggers used in this analysis in the different 2010 run periods are enumerated in Table 5.1.

The muon component of all the triggers used in this analysis is based on the “L1 seed trigger” L1_SingleMu7, which nominally selects event which contain a muon with $p_T > 7$ GeV/c. The L1 muon trigger decision is determined by the Global Muon Trigger (GMT), which combines information from the DT, CSC, and RPC sub-detectors, and is able to trigger muons up to a pseudorapidity of $|\eta| < 2.1$. Each sub-detector has a “local trigger,”

968 which can reconstruct tracks in the muon system. For the drift tubes, the Bunch Track
969 Identifiers (BTI), a custom integrated circuit, searches for aligned hits in the associated
970 DT chamber. The CSCs and RPCs employ similar strategies to detect local muon tracks.
971 The sub-detectors send the GMT the charge, p_T , η , ϕ , and a quality code of up to four
972 local muons. The measurements from the sub-detectors are combined and a final decision
973 is made by the GMT.

Chapter 3

974

975 Tau Identification: The Tau Neural Classi- 976 fier

977 High tau identification performance is important for the discovery potential of many possible
 978 new physics signals at the Compact Muon Solenoid (CMS). The Standard Model background
 979 rates from true tau leptons are typically the same order of magnitude as the expected signal
 980 rate in many searches for new physics. The challenge of doing physics with taus is driven
 981 by the rate at which objects are incorrectly tagged as taus. In particular, quark and gluon
 982 jets have a significantly higher production cross-section and events where these objects
 983 are incorrectly identified as tau leptons can dominate the backgrounds of searches for new
 984 physics using taus. Efficient identification of hadronic tau decays and low misidentification
 985 rate for quarks and gluons is thus essential to maximize the significance of searches for new
 986 physics at CMS.

987 Tau leptons are unique in that they are the only type of leptons which are heavy enough
 988 to decay to hadrons. The hadronic decays compose approximately 65% of all tau decays, the
 989 remainder being split nearly evenly between $\tau^- \rightarrow \mu^- \bar{\nu}_\mu \nu_\tau$ and $\tau^- \rightarrow e^- \bar{\nu}_e \nu_\tau$. The hadronic
 990 decays are typically composed of one or three charged pions and zero to two neutral pions.
 991 The neutral pions decay almost instantaneously to pairs of photons.

992 In this chapter, we describe a technique to identify hadronic tau decays. Tau decays
 993 to electrons and muons are difficult to distinguish from prompt production of electrons and
 994 muons in pp collisions. Analyses that use exclusively use the leptonic (e, μ) decays of taus
 995 typically require that the decays be of opposite flavor. With the Tau Neural Classifier, we
 996 aim to improve the discrimination of true hadronic tau decays from quark and gluon jets
 997 using a neural network approach.

998 §3.1 Geometric Tau Identification Algorithms

999 The tau identification strategies used in previously published CMS analyses are fully de-
 1000 scribed in [28]. A summary of the basic methods and strategies is given here. There are
 1001 two primary methods for selecting objects used to reconstruct tau leptons. The CaloTau
 1002 algorithm uses tracks reconstructed by the tracker and clusters of hits in the electromag-
 1003 netic and hadronic calorimeter. The other method (PFTau) uses objects reconstructed by
 1004 the CMS particle flow algorithm, which is described in [29]. The particle flow algorithm
 1005 provides a global and unique description of every particle (charged hadron, photon, elec-
 1006 tron, etc.) in the event; measurements from sub-detectors are combined according to their
 1007 measured resolutions to improve energy and angular resolution and reduce double counting.
 1008 All of the tau identification strategies described in this thesis use the particle flow objects.

1009 Both methods typically use an “leading object” and an isolation requirement to reject
 1010 quark and gluon jet background. Quark and gluon jets are less collimated and have a higher
 1011 constituent multiplicity and softer constituent p_T spectrum than a hadronic tau decay of
 1012 the same transverse momentum. The “leading track” requirement is applied by requiring a
 1013 relatively high momentum object near the center of the jet; typically a charged track with
 1014 transverse momentum greater than 5 GeV/c within $\Delta R < 0.1$ about the center of the jet
 1015 axis. The isolation requirement exploits the collimation of true taus by defining an isolation
 1016 annulus about the kinematic center of the jet and requiring no detector activity about a
 1017 threshold in that annulus. This approach yields a misidentification rate of approximately 1%
 1018 for QCD backgrounds and a hadronic tau identification efficiency of approximately 50% [28].

1019 §3.2 Decay Mode Tau Identification: Motivation

1020 The tau identification strategy described previously can be extended by looking at the dif-
 1021 ferent hadronic decay modes of the tau individually. The dominant hadronic decays of taus
 1022 consist of a one or three charged π^\pm mesons and up to two π^0 mesons and are enumerated
 1023 in Table 1.4. The majority of these decays proceed through intermediate resonances and
 1024 each of these decay modes maps directly to a tau final state multiplicity. Each intermediate
 1025 resonance has a different invariant mass (see Figure 3.1). This implies that the problem of

hadronic tau identification can be re-framed from a global search for collimated hadrons satisfying the tau mass constraint into a ensemble of searches for single production of the different hadronic tau decay resonances. The Tau Neural Classifier algorithm implements this approach using two complimentary techniques: a method to reconstruct the decay mode and an ensemble of neural network classifiers used to identify each decay mode resonance and reject quark and gluon jets with the same final state topology.

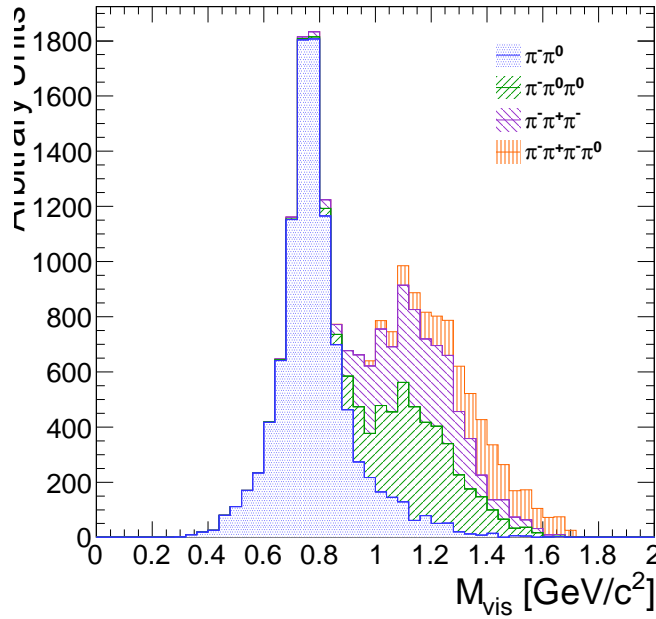


Figure 3.1: The invariant mass of the visible decay products in hadronic tau decays. The decay mode $\tau^- \rightarrow \pi^- \nu_\tau$ is omitted. The different decay modes have different invariant masses corresponding to the intermediate resonance in the decay.

§3.3 The Tau Neural Classifier

The Tau Neural Classifier (TaNC) algorithm reconstructs the decay mode of the tau-candidate and then feeds the tau-candidate to a discriminator associated to that decay mode to make the classification decision. Each discriminator therefore maps to a reconstructed decay mode in a one-to-one fashion. To optimize the discrimination for each of the different decay modes, the TaNC uses an ensemble of neural nets. Each neural net corresponds to one of the dominant hadronic decay modes of the tau lepton. These selected

hadronic decays constitute 95% of all hadronic tau decays. Tau–candidates with reconstructed decay modes not in the set of dominant hadronic modes are immediately tagged as background.

§3.3.1 Decay Mode Reconstruction

The major task in reconstructing the decay mode of the tau is determining the number of π^0 mesons produced in the decay. A π^0 meson decays almost instantaneously to a pair of photons. The photon objects are reconstructed using the particle flow algorithm [29]. The initial collection of photon objects considered to be π^0 candidates are the photons in the signal cone described by using the “shrinking–cone” tau algorithm, described in [28].

The reconstruction of photons from π^0 decays present in the signal cone is complicated by a number of factors. To suppress calorimeter noise and underlying event photons, all photons with minimum transverse energy less than 0.5 GeV are removed from the signal cone, which removes some signal photons. Photons produced in secondary interactions, pile-up events, and electromagnetic showers produced by signal photons that convert to electron–positron pairs can contaminate the signal cone with extra low transverse energy photons. Highly boosted π^0 mesons may decay into a pair of photons with a small opening angle, resulting in two overlapping showers in the ECAL being reconstructed as one photon. The π^0 meson content of the tau–candidate is reconstructed in two stages. First, photon pairs are merged together into candidate π^0 mesons. The remaining un–merged photons are then subjected to a quality requirement.

Photon Merging

Photons are merged into composite π^0 candidates by examining the invariant mass of all possible pairs of photons in the signal region. Only π^0 candidates (photon pairs) with a composite invariant mass less than 0.2 GeV/c are considered. The combination of the high granularity of the CMS ECAL and the particle flow algorithm provide excellent energy and angular resolution for photons; the π^0 mass peak is readily visible in the invariant mass spectrum of signal photon pairs (see figure 3.3.1). The π^0 candidates that satisfy the invariant mass requirement are ranked by the difference between the composite invariant mass of the photon pair and the invariant mass of the π^0 meson given by the PDG [20]. The

1068 best pairs are then tagged as π^0 mesons, removing lower-ranking candidate π^0 s as necessary
 1069 to ensure that no photon is included in more than one π^0 meson.

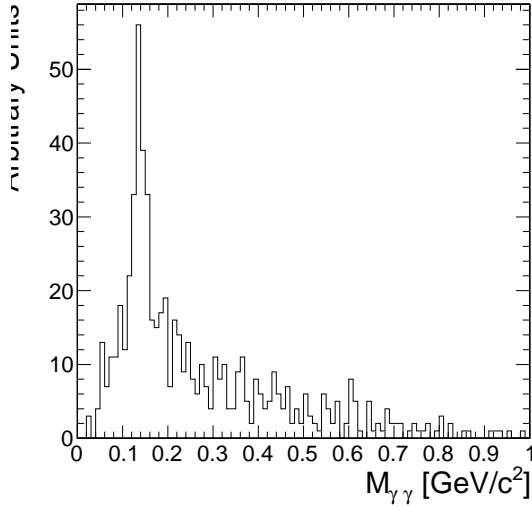


Figure 3.2: Invariant mass of the photon pair for reconstructed tau-candidates with two reconstructed photons in the signal region that are matched to generator level $\tau^- \rightarrow \pi^- \pi^0 \nu_\tau$ decays.

1070 Quality Requirements

1071 Photons from the underlying event and other reconstruction effects cause the number of
 1072 reconstructed photons to be greater than the true number of photons expected from a given
 1073 hadronic tau decay. Photons that have not been merged into a π^0 meson candidate are
 1074 recursively filtered by requiring that the fraction of the transverse momentum carried by
 1075 the lowest p_T photon be greater than 10% with respect to the entire (tracks, π^0 candidates,
 1076 and photons) tau-candidate. In the case that a photon is not merged but meets the minimum
 1077 momentum fraction requirement, it is considered a π^0 candidate. This requirement removes
 1078 extraneous photons, while minimizing the removal of single photons that correspond to a
 1079 true π^0 meson (see Figure 3.3). A mass hypothesis with the nominal [20] value of the π^0
 1080 is applied to all π^0 candidates. All objects that fail the filtering requirements are moved to
 1081 the isolation collection.

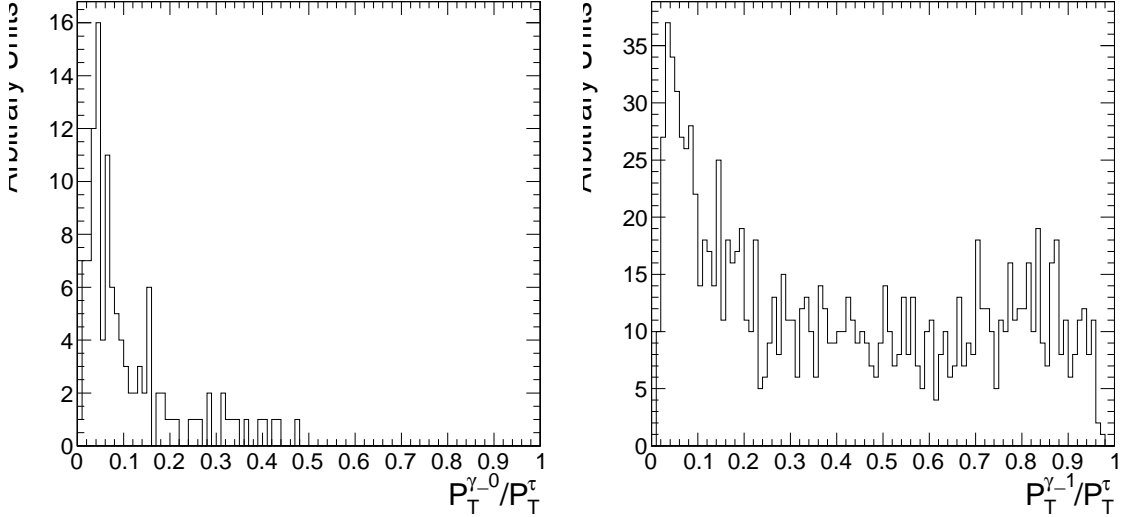


Figure 3.3: Fraction of total τ -candidate transverse momenta carried by the photon for reconstructed taus containing a single photons for two benchmark cases. On the left, the reconstructed tau-candidate is matched to generator level $\tau^- \rightarrow \pi^- \nu_\tau$ decays, for which no photon is expected. On the right, the reconstructed tau-candidate is matched to generator level $\tau^- \rightarrow \pi^- \pi^0 \nu_\tau$ decays and the photon is expected to correspond to a true π^0 meson. The requirement on the p_T fraction of the lowest p_T photon improves the purity of the decay mode reconstruction.

1082 Performance

1083 The performance of the decay mode reconstruction can be measured for tau-candidates that
 1084 are matched to generator level hadronically decaying tau leptons by examining the correla-
 1085 tion of the reconstructed decay mode to the true decay mode determined from the Monte
 1086 Carlo generator level information. Figure 3.4 compares the decay mode reconstruction per-
 1087 formance of a naive approach where the decay mode is determined by simply counting
 1088 the number of photons to the performance of the photon merging and filtering approach
 1089 described in Section 3.3.1. The correlation for the merging and filtering algorithm is much
 1090 more diagonal, indicating higher performance. The performance is additionally presented for
 1091 comparison in tabular form in Table 3.3.1 (merging and filtering approach) and Table 3.3.1
 1092 (naive approach).

1093 The performance of the decay mode reconstruction is dependent on the transverse
 1094 momentum and η of the tau-candidate and is shown in Figure 3.5. The p_T dependence
 1095 is largely due to threshold effects; high multiplicity decay modes are suppressed at low

1096 transverse momentum as the constituents are below the minimum p_T quality requirements.
 1097 In the forward region, nuclear interactions and conversions from the increased material
 1098 budget enhances modes containing π^0 mesons.

True decay mode	Reconstructed Decay Mode					
	$\pi^- \nu_\tau$	$\pi^- \pi^0 \nu_\tau$	$\pi^- \pi^0 \pi^0 \nu_\tau$	$\pi^- \pi^+ \pi^- \nu_\tau$	$\pi^- \pi^+ \pi^- \pi^0 \nu_\tau$	Other
$\pi^- \nu_\tau$	14.8%	1.6%	0.4%	0.1%	0.0%	0.7%
$\pi^- \pi^0 \nu_\tau$	6.0%	17.1%	9.0%	0.1%	0.1%	5.5%
$\pi^- \pi^0 \pi^0 \nu_\tau$	0.9%	3.8%	4.2%	0.0%	0.1%	5.9%
$\pi^- \pi^+ \pi^- \nu_\tau$	0.8%	0.3%	0.1%	9.7%	1.6%	6.2%
$\pi^- \pi^+ \pi^- \pi^0 \nu_\tau$	0.1%	0.2%	0.1%	1.7%	2.7%	4.5%

Table 3.1: Decay mode correlation table for the selected dominant decay modes for the naive approach. The percentage in a given row and column indicates the fraction of hadronic tau decays from $Z \rightarrow \tau^+ \tau^-$ events that are matched to a generator level decay mode given by the row and are reconstructed with the decay mode given by the column. Entries in the “Other” column are immediately tagged as background.

True decay mode	Reconstructed Decay Mode					
	$\pi^- \nu_\tau$	$\pi^- \pi^0 \nu_\tau$	$\pi^- \pi^0 \pi^0 \nu_\tau$	$\pi^- \pi^+ \pi^- \nu_\tau$	$\pi^- \pi^+ \pi^- \pi^0 \nu_\tau$	Other
$\pi^- \nu_\tau$	16.2%	1.0%	0.1%	0.1%	0.0%	0.3%
$\pi^- \pi^0 \nu_\tau$	10.7%	21.4%	3.6%	0.2%	0.1%	1.9%
$\pi^- \pi^0 \pi^0 \nu_\tau$	1.8%	7.1%	4.4%	0.1%	0.0%	1.5%
$\pi^- \pi^+ \pi^- \nu_\tau$	0.9%	0.2%	0.0%	11.5%	0.6%	5.4%
$\pi^- \pi^+ \pi^- \pi^0 \nu_\tau$	0.1%	0.3%	0.0%	3.2%	2.9%	2.7%

Table 3.2: Decay mode correlation table for the selected dominant decay modes for the merging and filtering approach. The percentage in a given row and column indicates the fraction of hadronic tau decays from $Z \rightarrow \tau^+ \tau^-$ events that are matched to a generator level decay mode given by the row and are reconstructed with the decay mode given by the column. Entries in the “Other” column are immediately tagged as background.

1099 §3.3.2 Neural Network Classification

1100 Neural Network Training

1101 The samples used to train the TaNC neural networks are typical of the signals and back-
 1102 grounds found in common physics analyses using taus. The signal-type training sample is

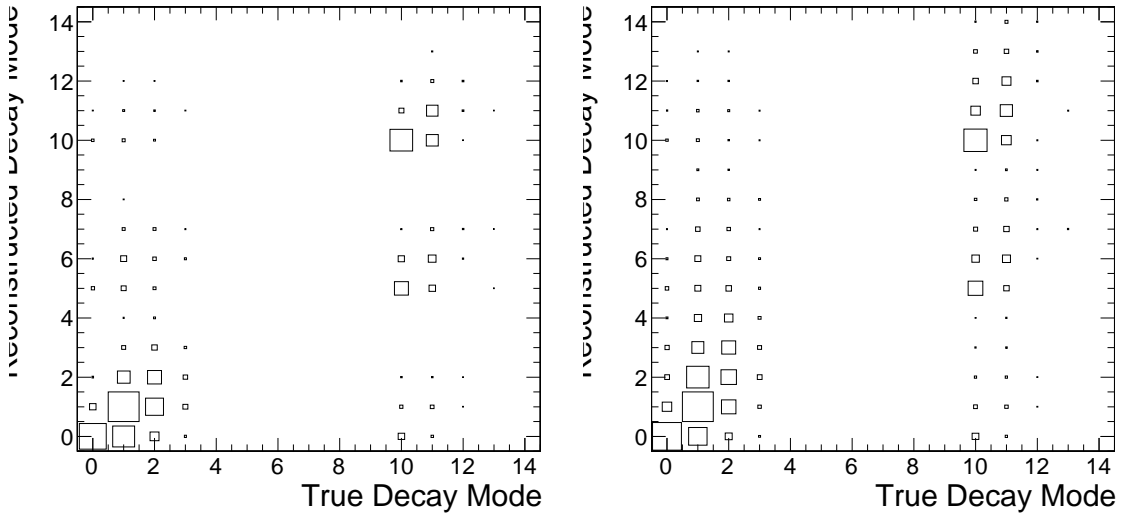


Figure 3.4: Correlations between reconstructed tau decay mode and true tau decay mode for hadronic tau decays in $Z \rightarrow \tau^+\tau^-$ events. The correlation when no photon merging or filtering is applied is shown on the right, and the correlation for the algorithm described in Section 3.3.1 is on the right. The horizontal and vertical axis are the decay mode indices of the true and reconstructed decay mode, respectively. The decay mode index N_{DM} is defined as $N_{DM} = (N_{\pi^\pm} - 1) \cdot 5 + N_{\pi^0}$. The area of the box in each cell is proportional to the fraction of tau-candidates that were reconstructed with the decay mode indicated on the vertical axis for the true tau decay on the horizontal axis. The performance of a decay mode reconstruction algorithm can be determined by the spread of the reconstructed number of π^0 mesons about the true number (the diagonal entries) determined from the generator level Monte Carlo information. If the reconstruction was perfect, the correlation would be exactly diagonal.

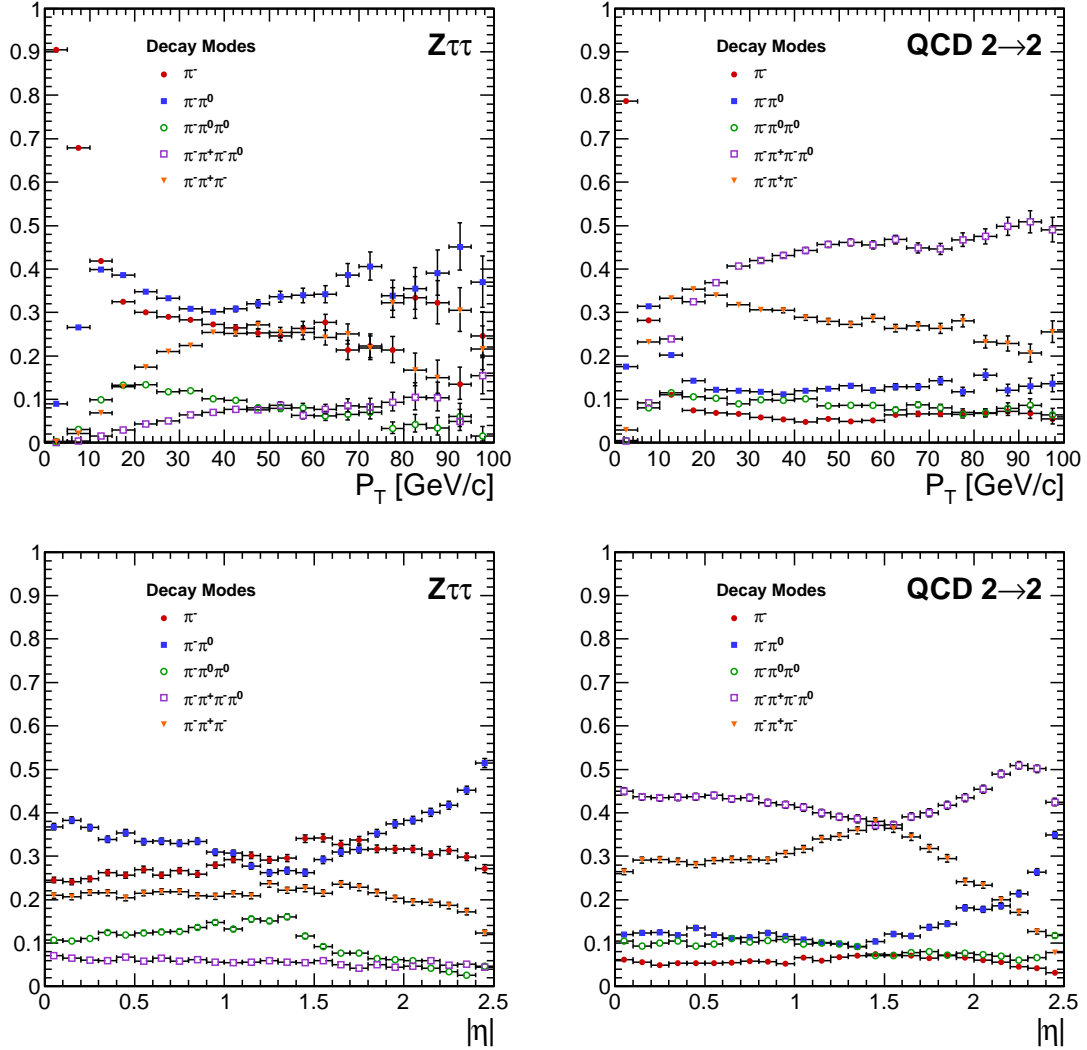


Figure 3.5: Kinematic dependence of reconstructed decay mode for tau-candidates in $Z \rightarrow \tau^+\tau^-$ (left) and QCD di-jets (right) events versus transverse momentum (top) and pseudo-rapidity (bottom). Each curve is the probability for a tau-candidate to be reconstructed with the associated decay mode after the leading pion and decay mode preselection has been applied.

1103 composed of reconstructed tau–candidates that are matched to generator level hadronic tau
 1104 decays coming from simulated $Z \rightarrow \tau^+ \tau^-$ events. The background training sample consists
 1105 of reconstructed tau–candidates in simulated QCD $2 \rightarrow 2$ hard scattering events. The QCD
 1106 p_T spectrum is steeply falling, and to obtain sufficient statistics across a broad range of p_T
 1107 the sample is split into different \hat{p}_T bins. Each binned QCD sample imposes a generator
 1108 level cut on the transverse momentum of the hard interaction. During the evaluation of
 1109 discrimination performance the QCD samples are weighted according to their respective
 1110 integrated luminosities to remove any effect of the binning.

1111 The signal and background samples are split into five subsamples corresponding to
 1112 each reconstructed decay mode. An additional selection is applied to each subsample by
 1113 requiring a “leading pion”: either a charged hadron or gamma candidate with transverse
 1114 momentum greater than 5 GeV/c. A large number of QCD training events is required as
 1115 both the leading pion selection and the requirement that the decay mode match one of the
 1116 dominant modes given in Table 1.4 are effective discriminants. For each subsample, 80% of
 1117 the signal and background tau–candidates are used for training the neural networks, with
 1118 half (40%) used as a validation sample used to ensure the neural network is not over-trained.
 1119 The number of signal and background entries used for training and validation in each decay
 1120 mode subsample is given in Table 3.3.2.

1121 The remaining 20% of the signal and background samples are reserved as a statisti-
 1122 cally independent sample to evaluate the performance of the neural nets after the training
 1123 is completed. The TaNC uses the Multi-layer Perceptron (MLP) neural network implemen-
 1124 tation provided by the TMVA software package, described in [30]. The MLP classifier is a
 1125 feed-forward artificial neural network. There are two layers of hidden nodes and a single
 1126 node in the output layer. The hyperbolic tangent function is used for the neuron activation
 1127 function.

The neural networks used in the TaNC have two hidden layers and single node in the
 output layers. The number of nodes in the first and second hidden layers are chosen to be
 $N + 1$ and $2N + 1$, respectively, where N is the number of input observables for that neural
 network. According to the Kolmogorov’s theorem [31], any continuous function $g(x)$ defined

	Signal	Background
Total number of tau-candidates	874266	9526176
Tau-candidates passing preselection	584895	644315
Tau-candidates with $W(p_T, \eta) > 0$	538792	488917
Decay Mode	Training Events	
π^-	300951	144204
$\pi^-\pi^0$	135464	137739
$\pi^-\pi^0\pi^0$	34780	51181
$\pi^-\pi^-\pi^+$	53247	155793
$\pi^-\pi^-\pi^+\pi^0$	13340	135871

Table 3.3: Number of events used for neural network training and validation for each selected decay mode.

on a vector space of dimension d spanned by x can be represented by

$$g(x) = \sum_{j=1}^{j=2d+1} \Phi_j \left(\sum_{i=1}^d \phi_i(x) \right) \quad (3.1)$$

for suitably chosen functions for Φ_j and ϕ_i . As the form of Equation 3.1 is similar to the topology of a two hidden-layer neural network, Kolmogorov's theorem suggests that *any* classification problem can be solved with a neural network with two hidden layers containing the appropriate number of nodes.

The neural network is trained for 500 epochs. At ten epoch intervals, the neural network error is computed using the validation sample to check for over-training (see Figure 3.6).

The neural network error E is defined [30] as

$$E = \frac{1}{2} \sum_{i=1}^N (y_{ANN,i} - \hat{y}_i)^2 \quad (3.2)$$

where N is the number of training events, $y_{ANN,i}$ is the neural network output for the i th training event, and y_i is the desired (-1 for background, 1 for signal) output the i th event.

No evidence of over-training is observed.

The neural networks use as input observables the transverse momentum and η of the tau-candidates. These observables are included as their correlations with other observables can increase the separation power of the ensemble of observables. For example, the opening angle in ΔR for signal tau-candidates is inversely related to the transverse momentum,

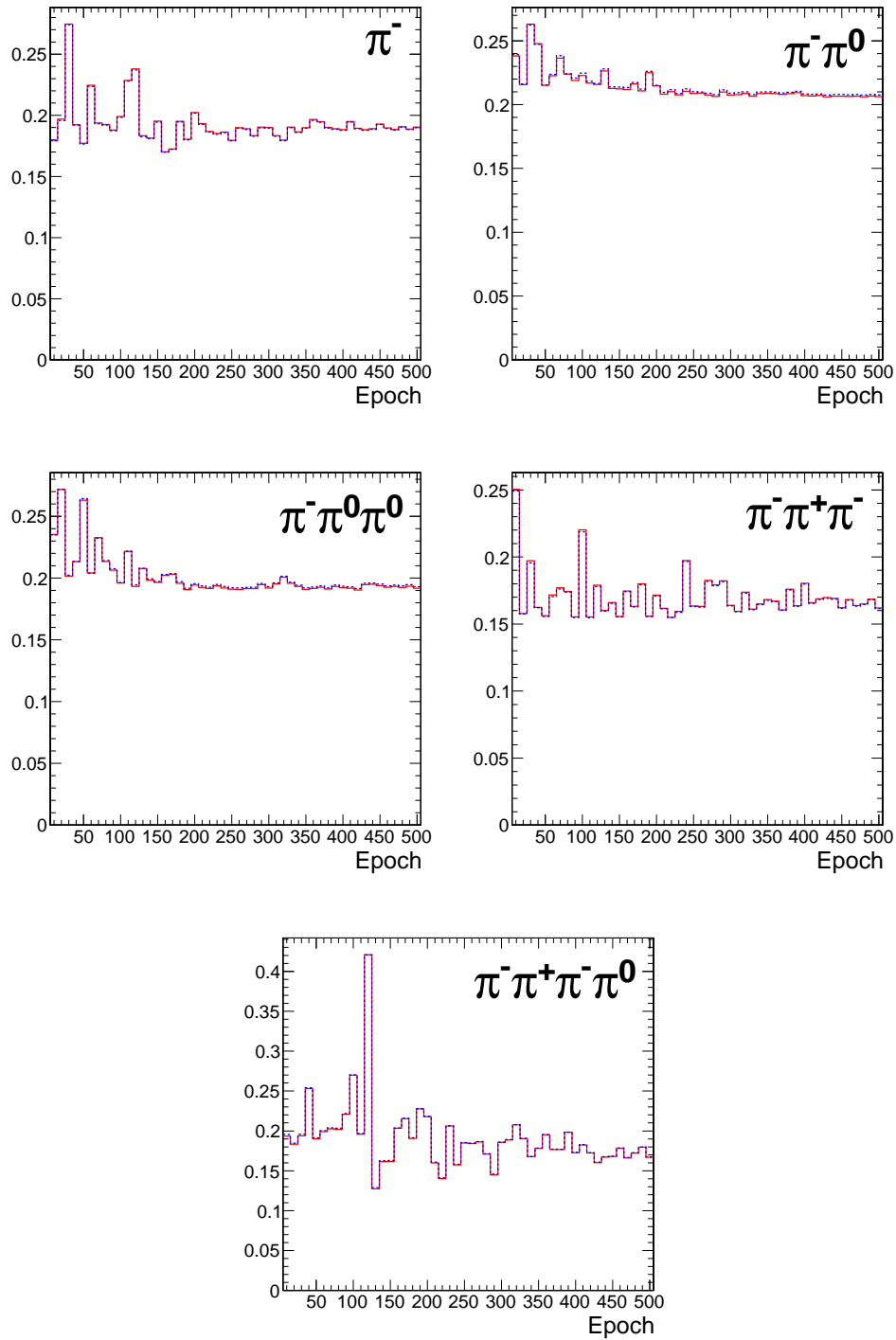


Figure 3.6: Neural network classification error for training (solid red) and testing (dashed blue) samples at ten epoch intervals over the 500 training epochs for each decay mode neural network. The vertical axis represents the classification error, defined by equation 3.2. N.B. that the choice of hyperbolic tangent for neuron activation functions results in the desired outputs for signal and background to be 1 and -1, respectively. This results in the computed neural network error being larger by a factor of four than the case where the desired outputs are (0, 1). Classifier over-training would be evidenced by divergence of the classification error of the training and testing samples, indicating that the neural net was optimizing about statistical fluctuations in the training sample.

1139 while for background events the correlation is very small [32]. In the training signal and
 1140 background samples, there is significant discrimination power in the p_T spectrum. However,
 1141 it is desirable to eliminate any systematic dependence of the neural network output on p_T
 1142 and η , as in practice the TaNC will be presented with tau-candidates whose $p_T - \eta$ spectrum
 1143 will be analysis dependent. The dependence on p_T and η is removed by applying a p_T and
 1144 η dependent weight to the tau-candidates when training the neural nets.

The weights are defined such that in any region in the vector space spanned by p_T and η where the signal sample and background sample probability density functions are different, the sample with higher probability density is weighted such that the samples have identical $p_T - \eta$ probability distributions. This removes regions of $p_T - \eta$ space where the training sample is exclusively signal or background. The weights are computed according to

$$W(p_T, \eta) = \text{less}(p_{sig}(p_T, \eta), p_{bkg}(p_T, \eta))$$

$$w_{sig}(p_T, \eta) = W(p_T, \eta)/p_{sig}(p_T, \eta)$$

$$w_{bkg}(p_T, \eta) = W(p_T, \eta)/p_{bkg}(p_T, \eta)$$

1145 where $p_{sig}(p_T, \eta)$ and $p_{bkg}(p_T, \eta)$ are the probability densities of the signal and background
 1146 samples after the “leading pion” and dominant decay mode selections. Figure 3.7 shows the
 1147 signal and background training p_T distributions before and after the weighting is applied.

1148 Discriminants

1149 Each neural network corresponds to a different decay mode topology and as such each
 1150 network uses different observables as inputs. However, many of the input observables are
 1151 used in multiple neural nets. The superset of all observables is listed and defined below.
 1152 Table 3.4 maps the input observables to their associated neural networks. In three prong
 1153 decays, the definition of the “main track” is important. The main track corresponds to the
 1154 track with charge opposite to that of the total charge of the three tracks. This distinction is
 1155 made to facilitate the use of the “Dalitz” observables, allowing identification of intermediate
 1156 resonances in three-body decays. This is motivated by the fact that the three prong decays
 1157 of the tau generally proceed through $\tau^- \rightarrow a1^- \nu_\tau \rightarrow \pi^- \rho^0 \nu_\tau \rightarrow \pi^- \pi^+ \pi^- \nu_\tau$; the oppositely
 1158 charged track can always be identified with the ρ^0 decay.

1159 **ChargedOutlierAngleN**

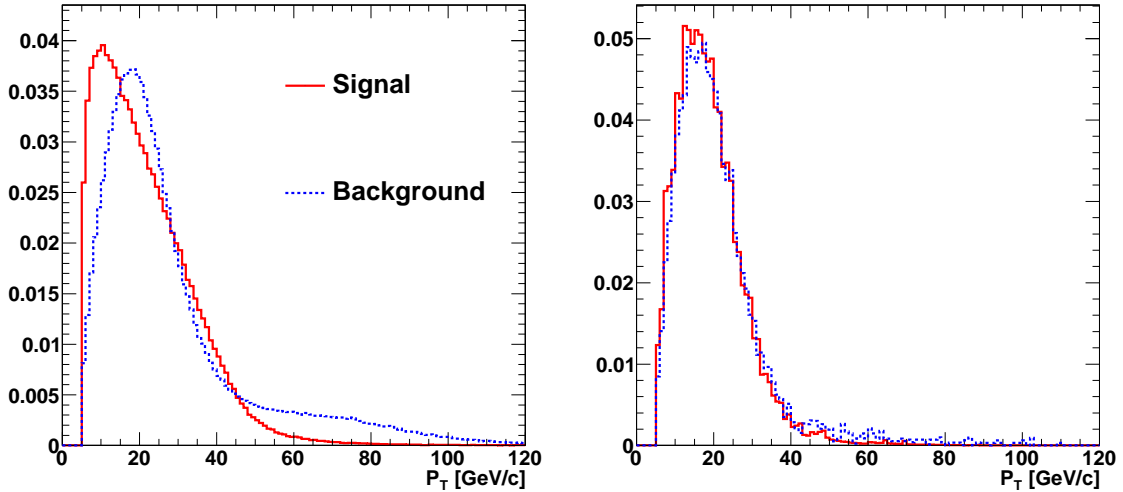


Figure 3.7: Transverse momentum spectrum of signal and background tau-candidates used in neural net training before (left) and after (right) the application of $p_T - \eta$ dependent weight function. Application of the weights lowers the training significance of tau-candidates in regions of $p_T - \eta$ phase space where either the signal or background samples has an excess of events.

1160 ΔR between the Nth charged object (ordered by p_T) in the isolation region and the
1161 tau-candidate momentum axis. If the number of isolation region objects is less than
1162 N, the input is set at one.

1163 **ChargedOutlierPtN**

1164 Transverse momentum of the Nth charged object in the isolation region. If the number
1165 of isolation region objects is less than N, the input is set at zero.

1166 **DalitzN**

1167 Invariant mass of four vector sum of the “main track” and the Nth signal region
1168 object.

1169 **Eta**

1170 Pseudo-rapidity of the signal region objects.

1171 **InvariantMassOfSignal**

1172 Invariant mass of the composite object formed by the signal region constituents.

1173 **MainTrackAngle**

1174 ΔR between the “main track” and the composite four–vector formed by the signal
 1175 region constituents.

1176 **MainTrackPt**

1177 Transverse momentum of the “main track.”

1178 **OutlierNCharged**

1179 Number of charged objects in the isolation region.

1180 **OutlierSumPt**

1181 Sum of the transverse momentum of objects in the isolation region.

1182 **PiZeroAngleN**

1183 ΔR between the Nth π^0 object in the signal region (ordered by p_T) and the tau–
 1184 candidate momentum axis.

1185 **PiZeroPtN**

1186 Transverse momentum of the Nth π^0 object in the signal region.

1187 **TrackAngleN**

1188 ΔR between the Nth charged object in the signal region (ordered by p_T) and the
 1189 tau–candidate momentum axis, exclusive of the main track.

1190 **TrackPtN**

1191 Transverse momentum of the Nth charged object in the signal region, exclusive of the
 1192 main track.

1193 Neural Network Performance

1194 The classification power of the neural networks is unique for each of the decay modes.
 1195 The performance is determined by the relative separation of the signal and background
 1196 distributions in the parameter space of the observables used as neural network inputs. A
 1197 pathological example is the case of tau–candidates with the reconstructed decay mode of
 1198 $\tau^- \rightarrow \pi^- \nu_\tau$. If there is no isolation activity, the neural net has no handle with which it

1199 can separate the signal from the background. The neural net output for tau-candidates in
 1200 the testing sample (independent of the training and validation samples) for each of the five
 1201 decay mode classifications is shown in Figure 3.8.

1202 When a single neural network is used for classification, choosing an operating point is
 1203 relatively straightforward: the requirement on neural network output is tuned such that the
 1204 desired purity is attained. However, in the case of the TaNC, multiple neural networks are
 1205 used. Each network has a unique separation power (see Figure 3.9) and each neural network
 1206 is associated to a reconstructed decay mode that composes different relative fractions of the
 1207 signal and background tau-candidates. Therefore, a set of five numbers is required to define
 1208 an “operating point” (the signal efficiency and background misidentification rate) in the
 1209 TaNC output. All points in this five dimensional cut-space map to an absolute background
 1210 fake-rate and signal efficiency rate. Therefore there must exist a 5D “performance curve”
 1211 which for any attainable signal efficiency gives the lowest fake-rate. A direct method to
 1212 approximate the performance curve is possible using a Monte Carlo technique.

1213 The maximal performance curve can be approximated by iteratively sampling points in
 1214 the five-dimensional cut space and selecting the highest performance points. The collection
 1215 of points in the performance curve are ordered by expected fake rate. During each iteration,
 1216 the sample point is compared to the point before the potential insertion position of the
 1217 sample in the ordered collection. The sample point is inserted into the collection if it has
 1218 a higher signal identification efficiency than the point before it. The sample point is then
 1219 compared to all points in the collection after it (i.e. those with a larger fake rate); any point
 1220 with a lower signal efficiency than the sample point is removed. After the performance curve
 1221 has been determined, the set of cuts are evaluated on an independent validation sample
 1222 to ensure that the measured performance curve is not influenced by favorable statistical
 1223 fluctuations being selected by the Monte Carlo sampling. The performance curves for two
 1224 different transverse momentum ranges are shown in Figure 3.10.

The 5D performance curve can also be parameterized by using the probability for a tau-candidate to be identified for a given decay mode. An artificial neural network maps a point in the space of input observables to some value of neural network output x . The neural network training error is given by Equation 3.2. A given point in the vector space

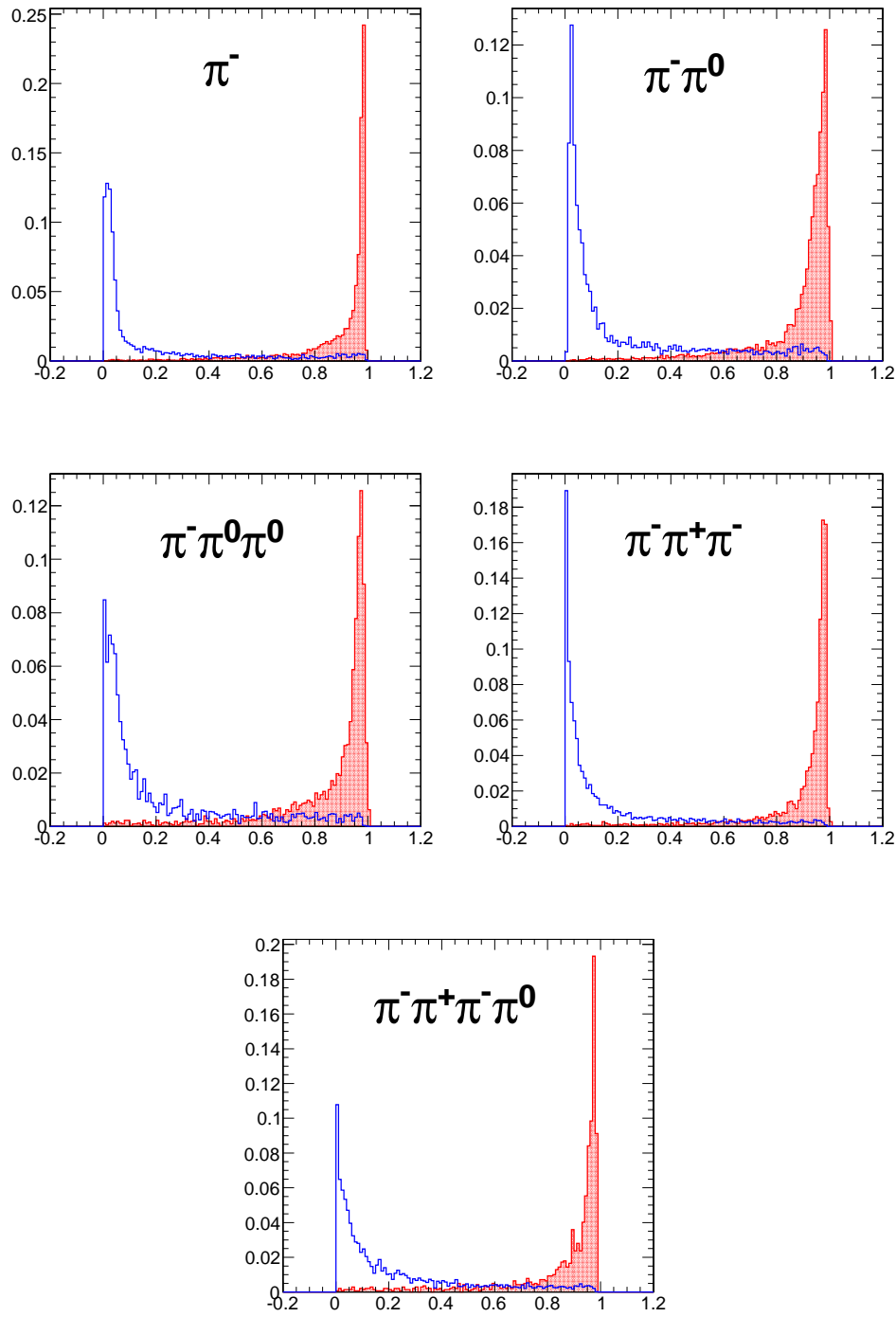


Figure 3.8: Neural network output distributions for the five reconstructed tau–candidate decay modes used in the TaNC for $Z \rightarrow \tau^+\tau^-$ events (red) and QCD di-jet events (blue).

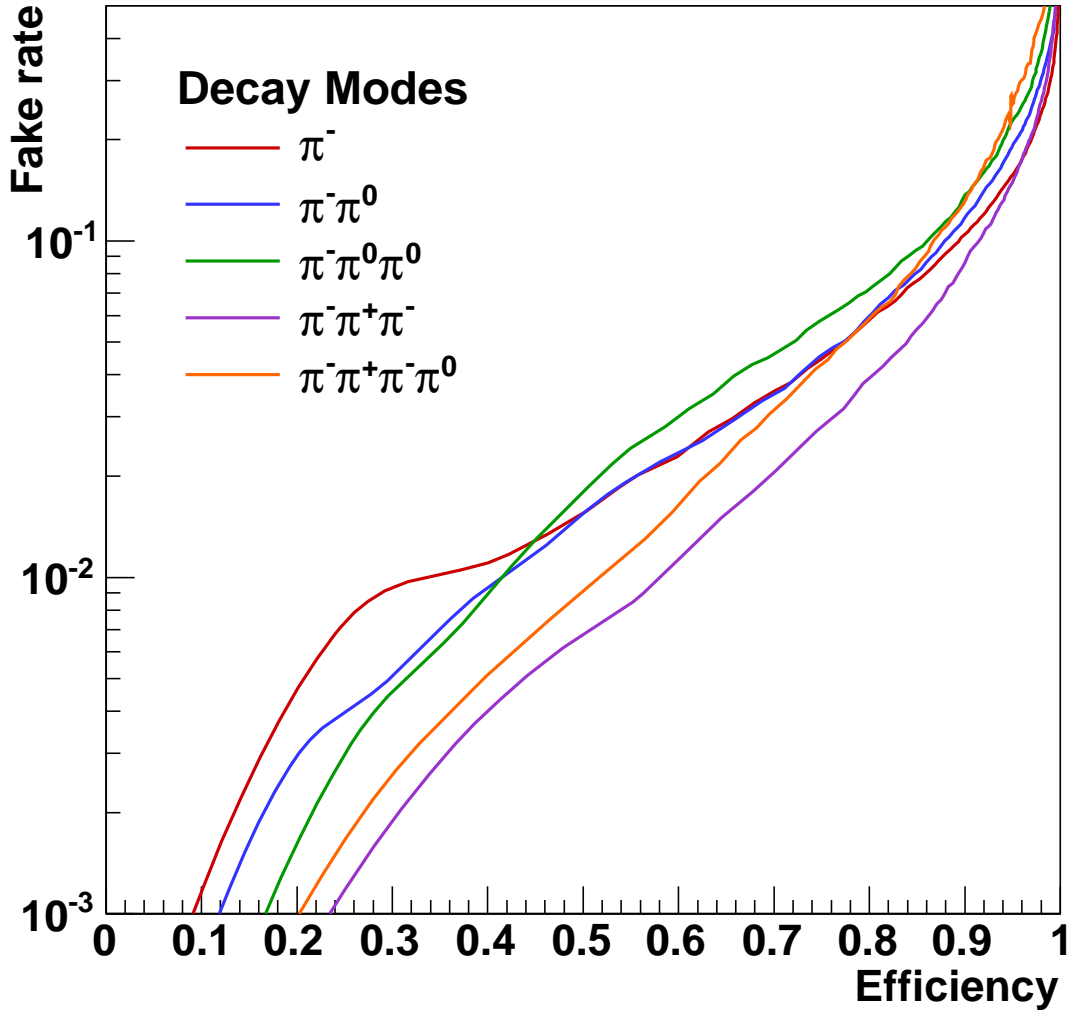


Figure 3.9: Performance curves for the five neural networks used by the TaNC for tau-candidates with transverse momentum greater than 20 GeV/c. Each curve represents the signal efficiency (on the horizontal axis) and background misidentification rate (vertical axis) for a scan of the neural network selection requirement for a single neural network. The efficiency (or misidentification rate) for each neural network performance curve is defined with respect to the preselected tau-candidates that have the reconstructed decay mode associated with that neural network. Each neural network has a different ability so separate signal and background as each classifier uses different observables as inputs.

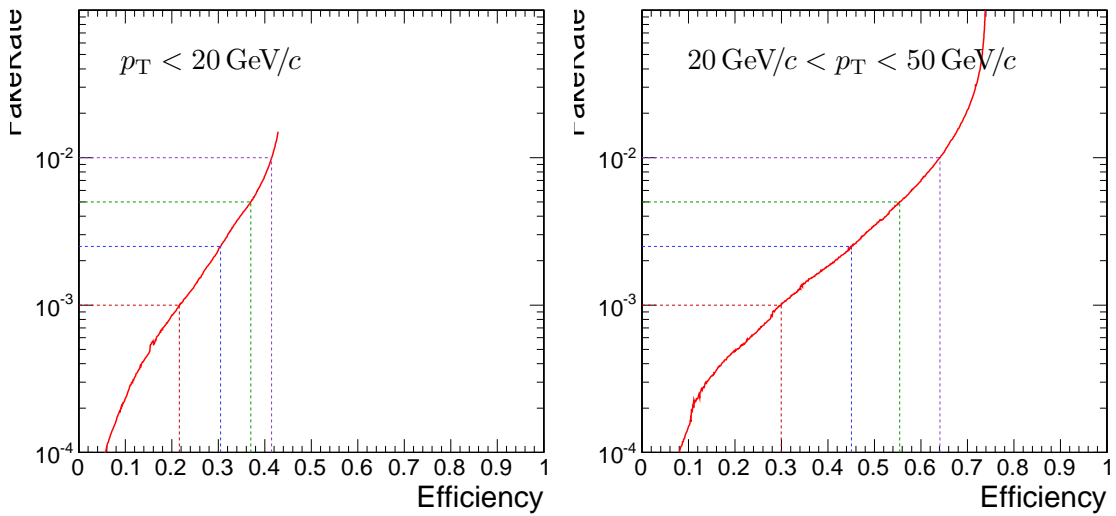


Figure 3.10: Tau Neural Classifier performance curves for tau-candidates with $p_T < 20 \text{ GeV}/c$ (left) and $20 < p_T < 50 \text{ GeV}/c$ (right). The vertical axis represents the expected fake-rate of QCD jets and the horizontal axis the expected signal efficiency for hadronic tau decays. The performance curve for the low transverse momentum range is worse due to leading pion selection. While both true taus and QCD are removed by this cut, the selection preferentially keeps the QCD tau-candidates with low multiplicities, which increases the number of QCD tau-candidates passing the decay mode selection.

spanned by the neural network input observables (denoted as “feature space”) contributes to the neural network training error E by

$$E' = (1 - x)^2 \cdot \rho^\tau + x^2 \cdot \rho^{QCD}$$

1225 where $\rho^\tau(\rho^{QCD})$ denotes the training sample density of the τ signal and QCD–jet background at that point in feature space.

The value x assigned by the neural network to this region in feature space should satisfy the requirement of minimal error:

$$\begin{aligned} \frac{\partial E'}{\partial x} &= 0 \\ 0 &= -2(1 - x) \cdot \rho^\tau + 2x \cdot \rho^{QCD} \\ x &= \frac{\rho^\tau}{\rho^\tau + \rho^{QCD}} \end{aligned} \tag{3.3}$$

$$\begin{aligned} \rho^{QCD} &= \frac{1}{x} - 1 \\ \frac{\rho^{QCD}}{\rho^\tau} &= \frac{1}{x} - 1 \end{aligned} \tag{3.4}$$

1227 The ratio $\frac{\rho^{QCD}}{\rho^\tau}$ corresponds to the ratio of the normalized probability density functions of
1228 signal and background input observable distributions, i.e. $\int \rho^\tau d\vec{x} = 1$.

In the case of multiple neural networks, one can derive a formula that maps the output x_j of the neural network corresponding to decay mode j according to the “prior probabilities” $p_j^\tau(p_j^{QCD})$ for true τ lepton hadronic decays (quark and gluon jets) to pass the preselection criteria and be reconstructed with decay mode j . By substituting $\rho^s \rightarrow \rho^s p_j^s$ for $s \in \{\tau, QCD\}$ in Equation 3.3, the output x_j can be related to $p_j^\tau(p_j^{QCD})$ by

$$x'_j = \frac{\rho^\tau \cdot p_j^\tau}{\rho^\tau \cdot p_j^\tau + \rho^{QCD} \cdot p_j^{QCD}} = \frac{p_j^\tau}{p_j^\tau + \frac{\rho^{QCD}}{\rho^\tau} \cdot p_j^{QCD}} \tag{3.5}$$

Substituting Equation 3.4 into Equation 3.5 yields the transformation of the output x_j of the neural neural network corresponding to any selected decay mode j to a single discriminator output x'_j which for a given point on the optimal performance curve should be independent of j .

$$x'_j = \frac{p_j^\tau}{p_j^\tau + \left(\frac{1}{x_j} - 1\right) \cdot p_j^{QCD}} \tag{3.6}$$

1229 In this manner a single number (the “transform cut”) given by Equation 3.6 can be used
1230 to specify any point on the performance curve. The training sample neural network output
1231 after the transformation has been applied is shown in Figure 3.12. The performance curve

1232 for the cut on the transformed output is nearly identical to the optimal performance curve
 1233 determined by the Monte Carlo sampling technique.

1234 The discriminator output of the TaNC algorithm is a continuous quantity, enabling
 1235 analysis specific optimization of the selection to maximize sensitivity. For the convenience
 1236 of the user, four operating point benchmark selections are provided in addition to the
 1237 continuous output. The four operating points are chosen such that for tau-candidates with
 1238 transverse momentum between 20 and 50 GeV/c, the expected QCD di-jet fake rate will be
 1239 0.1%, 0.25%, 0.50% and 1.0%, respectively.

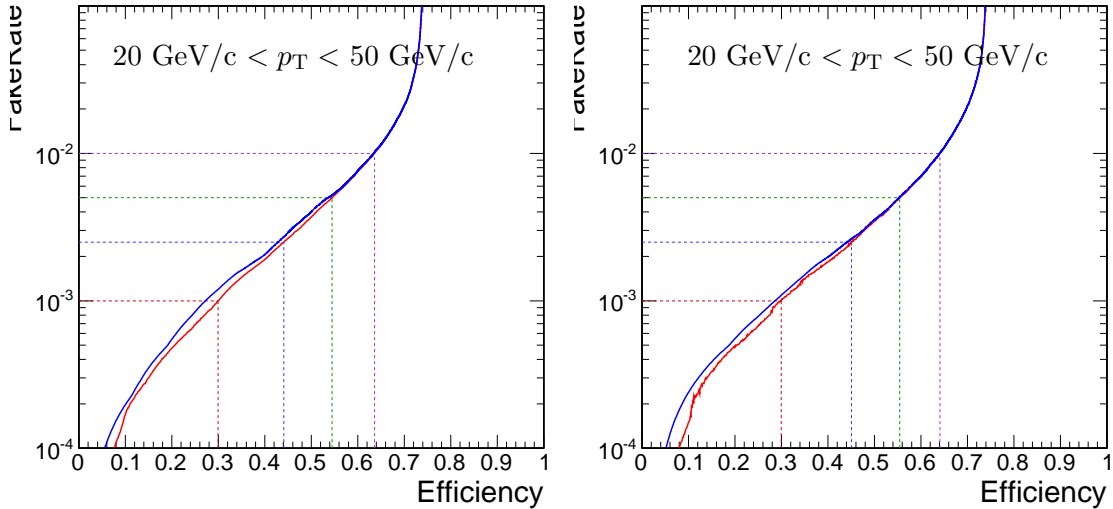


Figure 3.11: Tau Neural Classifier performance curves for tau-candidates with $20 < p_T < 50 \text{ GeV}/c$. The figure on the left compares the optimal performance curve determined by the Monte Carlo sampling method (red) to the performance curve obtained by scanning the ‘‘transform cut’’ (blue) defined in Equation 3.6 from zero to one. The figure on the right is the same set of cuts (and cut transformation values) applied on an independent sample to remove any biases introduced by the Monte Carlo sampling. The four dashed lines indicate the performance for the four benchmark points.

1240 §3.4 Summary

1241 The Tau Neural classifier introduces two complimentary new techniques for tau lepton
 1242 physics at CMS: reconstruction of the hadronic tau decay mode and discrimination from
 1243 quark and gluon jets using neural networks. The decay mode reconstruction strategy pre-
 1244 sented in Section 3.3.1 significantly improves the determination of the decay mode. This

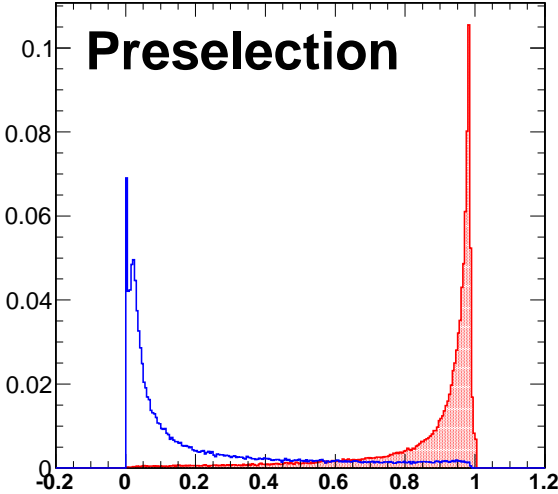


Figure 3.12: Transformed TaNC neural network output for tau-candidates with transverse momentum between 20 and 50 GeV/c that pass the pre-selection criteria. The neural network output for each tau-candidate has been transformation according to Equation 3.6. The decay mode probabilities ρ_i^{bkg} , ρ_i^{signal} are computed using the entire transverse momentum range of the sample.

1245 information has the potential to be useful in studies of tau polarization and background
1246 estimation.

1247 The Tau Neural classifier tau identification algorithm significantly improves tau dis-
1248 crimination performance compared to isolation-based approaches [28] used in previous CMS
1249 analyses. Figure 3.13 compares the performance of the “shrinking cone” isolation tau-
1250 identification algorithm [28] to the performance of the TaNC for a scan of requirements
1251 on the transformed neural network output. The signal efficiency and QCD di-jet fake rate
1252 versus tau-candidate transverse momentum and pseudo-rapidity for the four benchmark
1253 points and the isolation based tau identification are show in Figure 3.14. For tau-candidates
1254 with transverse momentum between 20 and 50 GeV/c, the TaNC operating cut can be cho-
1255 sen such that the two methods have identical signal efficiency; at this point the TaNC
1256 algorithm reduces the background fake rate by an additional factor of 3.9. This reduction
1257 in background will directly improve the significance of searches for new physics using tau
1258 leptons at CMS.

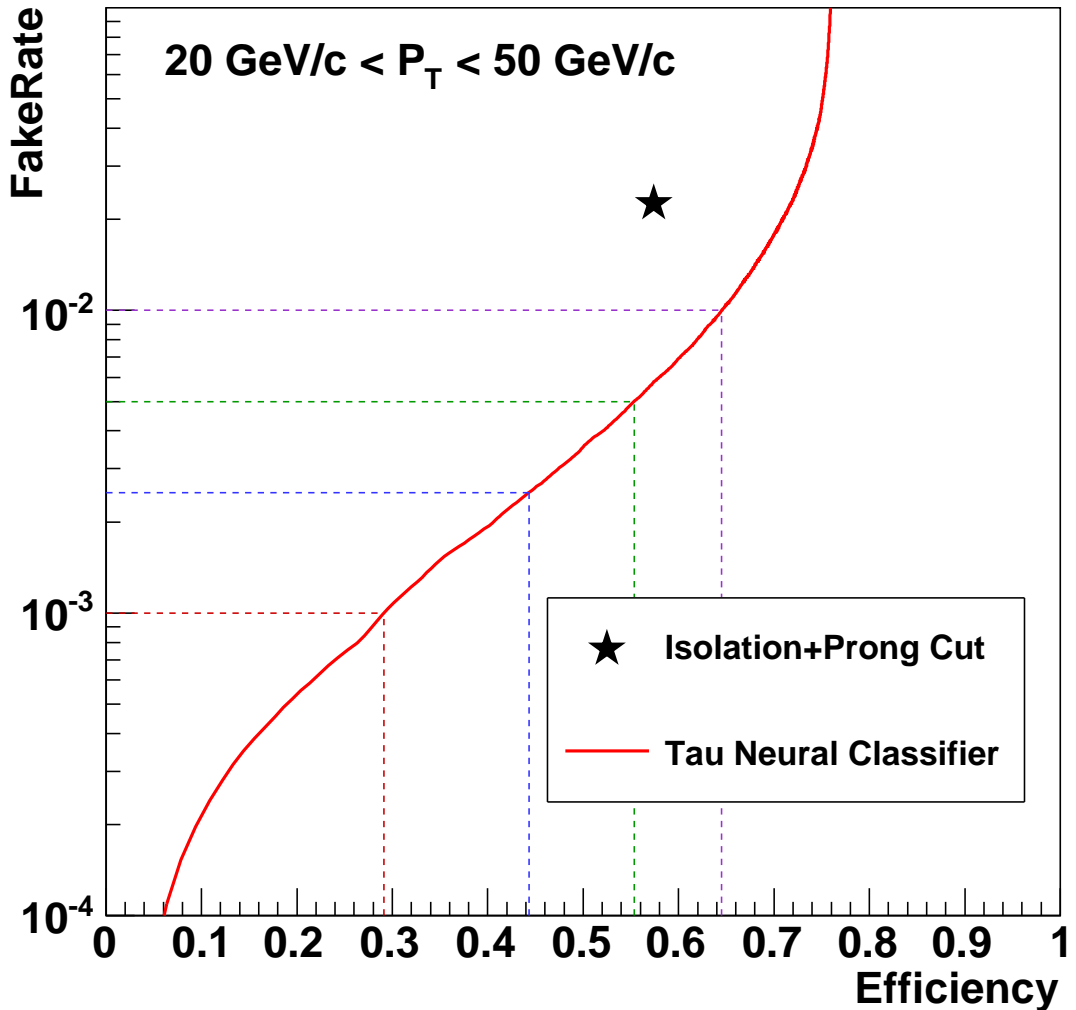


Figure 3.13: Performance curve (red) of the TaNC tau identification for various requirements on the output transformed according to Equation 3.6. The horizontal axis is the efficiency for true taus with transverse momentum between 20 and 50 GeV/c to satisfy the tau identification requirements. The vertical axis gives the rate at which QCD di-jets with generator-level transverse momentum between 20 and 50 GeV/c are incorrectly identified as taus. The performance point for the same tau-candidates using the isolation based tau-identification [28] used in many previous CMS analyses is indicated by the black star in the figure. An additional requirement that the signal cone contain one or three charged hadrons (typical in a final physics analysis) has been applied to the isolation based tau-identification to ensure a conservative comparison.

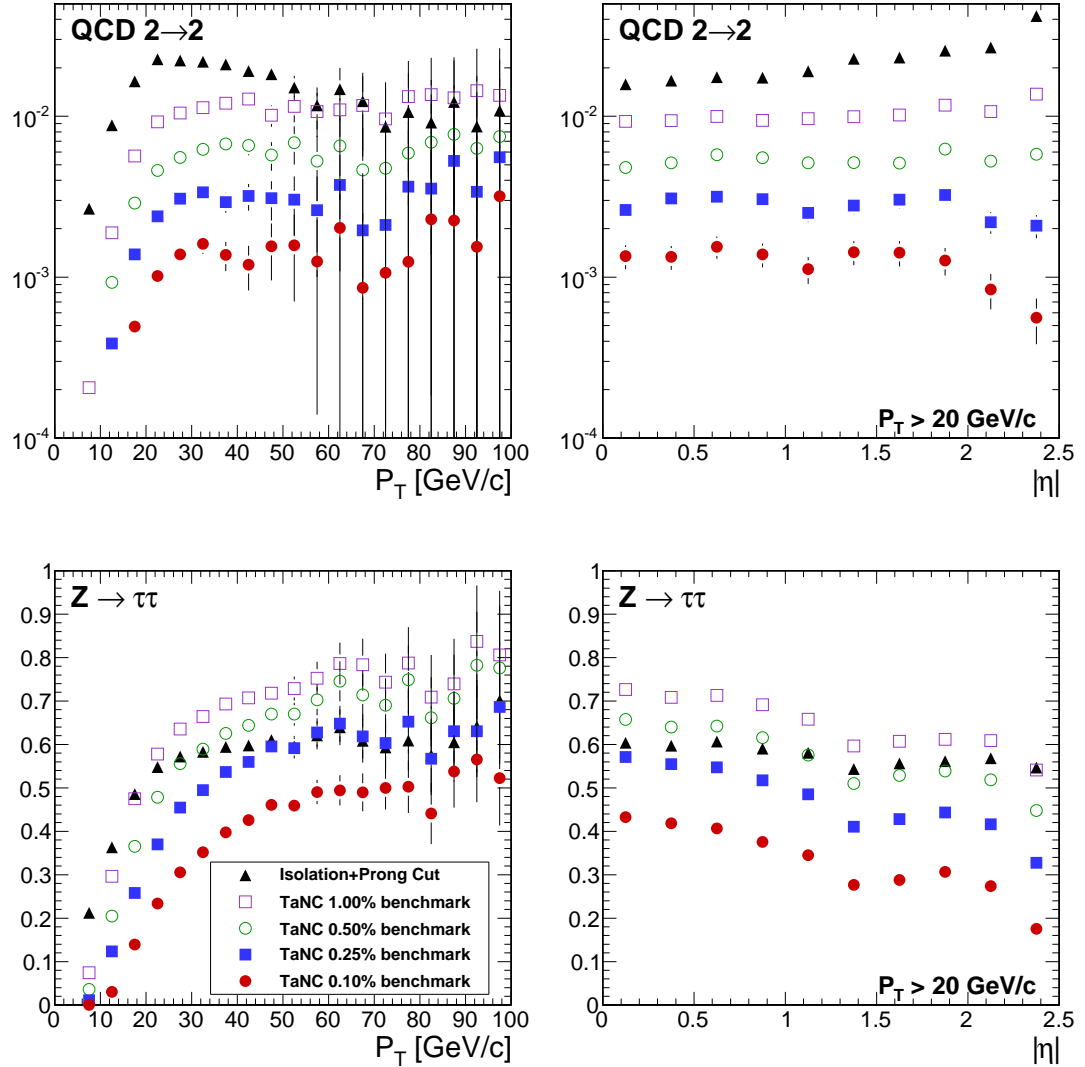


Figure 3.14: Comparison of the identification efficiency for hadronic tau decays from $Z \rightarrow \tau^+\tau^-$ decays (bottom row) and the misidentification rate for QCD di-jets (top row) versus tau-candidate transverse momentum (left) and pseudo-rapidity (right) for different tau identification algorithms. The efficiency (fake-rate) in a given bin is defined as the quotient of the number of true tau hadronic decays (generator level jets) in that bin that are matched to a reconstructed tau-candidate that passes the identification algorithm divided by the number of true tau hadronic decays (generator level jets) in that bin. In the low transverse momentum region both the number of tau-candidates in the denominator and the algorithm acceptance vary rapidly with respect to p_T for both signal and background; a minimum transverse momentum requirement of 20 GeV/c is applied to the pseudorapidity plots to facilitate interpretation of the plots.

1259 §3.5 HPS+TaNC: A Hybrid Algorithm

1260 The techniques used in the TaNC have been hybridized with techniques used by the “Hadrons
 1261 plus Strips” (HPS) algorithm [33]. The combined algorithm is referred to “Hadrons plus
 1262 Strips and Tau Neural Classifier” (HPS + TaNC) identification algorithm. The algorithm
 1263 combines the HPS methods of constructing the signal components of the tau candidate
 1264 and the discrimination methods of the TaNC algorithm. Both algorithms are based on re-
 1265 constructing individual tau lepton hadronic decay modes, which has been demonstrated to
 1266 improve the tau identification performance significantly with respect to previously used cone
 1267 isolation based algorithms [34]. The HPS + TaNC algorithm first reconstructs the hadronic
 1268 decay mode of the tau, and applies different discriminants based on the reconstructed de-
 1269 cay mode. Identification of hadronic tau decays by the HPS + TaNC algorithm proceeds in
 1270 two stages: first, the hadronic decay mode of the tau is reconstructed and then different
 1271 discriminators are applied, based on the reconstructed decay mode. In the decay mode re-
 1272 construction particular attention is paid to the reconstruction of neutral pions, which are
 1273 expected for the majority of hadronic decay modes.

1274 §3.5.1 Decay mode reconstruction

1275 The decay mode reconstruction algorithm is seeded by particle-flow jets reconstructed by
 1276 the anti- k_T algorithm [35]. In order to reconstruct the decay mode, the algorithm needs to
 1277 merge photon candidates into candidate π^0 mesons. The π^0 candidates are reconstructed by
 1278 two algorithms which are executed concurrently. The “combinatorial” π^0 algorithm produces
 1279 a π^0 candidate for every possible pair of photons within the jet. The “strips” algorithm clus-
 1280 ters photons strips in $\eta - \phi$. The results of both algorithms are combined and then “cleaned”,
 1281 resolving multiple hypotheses. The quality of a π^0 candidate is determined according to the
 1282 following categorical rankings:

- 1283 • The π^0 candidate is in the ECAL barrel region ($|\eta| < 1.5$) and has invariant mass
 1284 $|m_{\gamma\gamma} - m_{\pi^0}| < 0.05 \text{ GeV}/c^2$.
- 1285 • The π^0 candidate is in the ECAL endcap region ($|\eta| > 1.5$) and has invariant mass
 1286 $m_{\gamma\gamma} < 0.2 \text{ GeV}/c^2$.

- 1287 • The π^0 candidate contains two or more photons within an $\eta - \phi$ strip of size 0.05×0.20 .
- 1288 • Photons not satisfying any of the other categories are considered as unresolved π^0
- 1289 candidates in case they have $p_T > 1.0$ GeV/c.

1290 The symbol m_{π^0} denotes the nominal neutral pion mass [20]. The size of the invariant mass

1291 windows in the ECAL endcap and barrel regions is motivated by the resolution of the π^0

1292 mass (illustrated in Figure 3.15) measured during the commissioning of the particle-flow

1293 algorithm in early CMS data [36]. Multiple π^0 candidates in the same category are ranked

1294 in quality according to the difference of the reconstructed photon pair mass to the nominal

1295 π^0 mass. After the π^0 candidates are ranked, the highest ranked candidate is selected for

1296 the final collection. The photon constituents of the highest ranked candidate are removed

1297 from remaining π^0 candidates not yet selected for the final collection in order to prevent

1298 photons from entering more than one π^0 candidate. The rank of remaining π^0 candidates

1299 is reevaluated and the π^0 candidate with the next highest rank is selected for the output

 collection. The process is repeated until no more π^0 candidates are remaining.

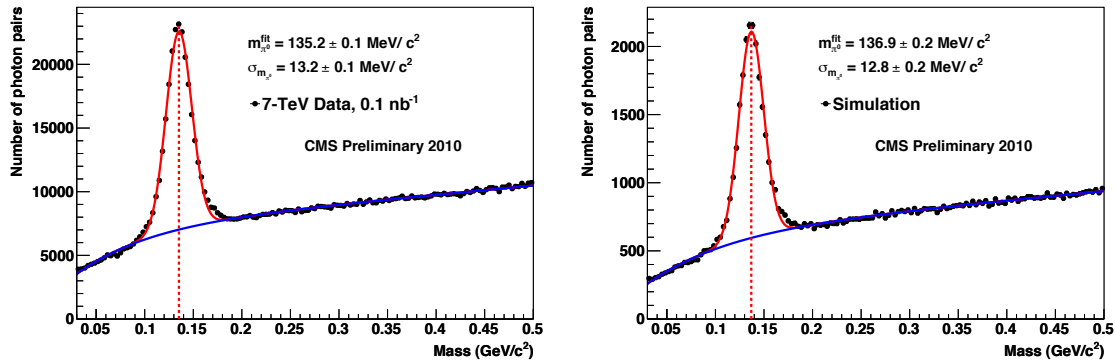


Figure 3.15: Invariant mass distribution of photon pairs reconstructed by the particle-flow in 2010 CMS minimum bias events (left), and predicted by the simulation (right). A clear resonant pick corresponding to the π_0 meson is visible above the combinatoric background. Reference: [36]

1300

1301 Once the final collection of π^0 candidates is determined, tau reconstruction in the

1302 HPS + TaNC algorithm proceeds by building tau candidates from reconstructed π^0

1303 candidates and charged hadrons reconstructed by the particle-flow algorithm. A combinatoric

1304 approach is again employed for the tau candidate building. A tau candidate hypothesis is

1305 built for every combination of jet constituents (π^0 candidates plus charged hadrons) which
 1306 has a multiplicity consistent with a hadronic tau decay. The tau candidates are ranked anal-
 1307 ogous to the ranking utilized for the π^0 reconstruction, but with the following categorical
 1308 rankings:

- 1309 • In each decay mode category, the tau candidate with the highest neural network
 1310 output is selected.
- 1311 • The tau candidate has unit charge.
- 1312 • The tau candidate passes the “lead pion” criteria, requiring that there is a photon or
 1313 charged pion candidate with $p_T > 5$ GeV/c.
- 1314 • The tau candidate passes the HPS invariant mass and collimation¹ requirements.

1315 In case multiple tau candidates satisfy all four categorical requirements, the tau candidate
 1316 with the highest energy sum of charged and neutral pions is selected as the highest ranking
 1317 one.

1318 §3.5.2 Hadronic tau discrimination

1319 The final level of discrimination is performed by an ensemble of neural networks, with each
 1320 neural network corresponding to a specific decay mode, analogously to the method used
 1321 original TaNC algorithm (Section 3.3.2). The inputs of each neural network are different and
 1322 correspond to the observables (invariant mass, Dalitz masses) available for its associated
 1323 decay mode. The neural networks are trained on samples simulated $Z \rightarrow \tau^+\tau^-$ events
 1324 (“signal”) and QCD di-jet events selected in the 7 TeV data collected by CMS in 2010
 1325 (“background”). All of the tau hypothesis from a given jet reconstructed in data are used
 1326 for training. The $Z \rightarrow \tau^+\tau^-$ signal sample is generated by PYTHIA [37] which has been
 1327 interfaced to TAUOLA [38] for the purpose of generating the decays of the tau leptons using
 1328 the full matrix element information. After generation, the events passed through the “full”
 1329 GEANT [39] based simulation of the CMS detector. Only tau candidates which have been

¹The invariant mass of the signal candidates is required to be compatible with the resolution for that decay mode. The collimation selection requires the maximum ΔR between any two signal candidates to be less than $2.8/E_T$, where E_T is the total transverse energy of the signal candidates. A full description is available in [33].

1330 reconstructed in a decay mode matching the true decay mode of the tau on generator
 1331 level enter the signal training sample. The neural network implementation, network layout,
 1332 and training strategies are the same as in the original TaNC algorithm described in this
 1333 chapter. To account for differences in the input signal purity and separation power of the
 1334 neural networks between decay modes, the outputs of each neural network are transformed
 1335 according to the method described in Section 3.3.2. Multiple working-points corresponding
 1336 to different purities are provided. The “loose” working point corresponds to an approximate
 1337 fake-rate of 1%, and has slightly higher signal efficiency performance at high p_T than the
 1338 corresponding HPS isolation-only working point.

1339 §3.6 Electron and Muon Rejection

1340 Additional discriminators must be applied to prevent electrons and muons from being iden-
 1341 tified as hadronic tau decays. This is especially important for removing $Z \rightarrow e^+e^-$ and
 1342 $Z \rightarrow \mu^+\mu^-$ contributions when selecting events with two taus and requiring one of them to
 1343 decay leptonically and the other hadronically. The electron and muon discrimination algo-
 1344 rithms and performance are described in detail in [28]. A cursory overview of the techniques
 1345 used are given here. Muon removal is achieved with high purity by requiring that no track in
 1346 the signal collection of the tau candidate is matched to a segment² in the muon system. The
 1347 rejections of true electrons is more difficult. Electrons leave no signal in the muon system
 1348 and produce Bremsstrahlung photons as they travel through the magnetic field. The most
 1349 significant difference from a true hadronic tau is that an electron is not expected to deposit
 1350 any energy in the hadronic calorimeter. Electrons are thus rejected by requiring that there
 1351 is a HCAL energy deposit with a magnitude that is greater than 10% of the momentum of
 1352 the leading track in the tau.

²A track reconstructed in the DT or CSC sub-detectors.

Input observable	Neural network				
	$\pi^- \nu_\tau$	$\pi^- \pi^0 \nu_\tau$	$\pi^- \pi^0 \pi^0 \nu_\tau$	$\pi^- \pi^+ \pi^- \nu_\tau$	$\pi^- \pi^+ \pi^- \pi^0 \nu_\tau$
ChargedOutlierAngle1	•	•	•	•	•
ChargedOutlierAngle2	•	•	•	•	•
ChargedOutlierPt1	•	•	•	•	•
ChargedOutlierPt2	•	•	•	•	•
ChargedOutlierPt3	•	•	•	•	•
ChargedOutlierPt4	•	•	•	•	•
Dalitz1			•	•	•
Dalitz2			•	•	•
Eta	•	•	•	•	•
InvariantMassOfSignal		•	•	•	•
MainTrackAngle		•	•	•	•
MainTrackPt	•	•	•	•	•
OutlierNCharged	•	•	•	•	•
OutlierSumPt	•	•	•	•	•
PiZeroAngle1		•	•		•
PiZeroAngle2			•		
PiZeroPt1		•	•		•
PiZeroPt2			•		
TrackAngle1				•	•
TrackAngle2				•	•
TrackPt1				•	•
TrackPt2				•	•

Table 3.4: Input observables used for each of the neural networks implemented by the Tau Neural Classifier. The columns represents the neural networks associated to various decay modes and the rows represent the superset of input observables (see Section 3.3.2) used in the neural networks. A dot in a given row and column indicates that the observable in that row is used in the neural network corresponding to that column.

Chapter 4

Mass Reconstruction: The Secondary Vertex Fit

1353 The dominant background in the search for a Higgs decaying to a $\tau^+\tau^-$ pair are Standard
 1354 Model $Z \rightarrow \tau^+\tau^-$ events. The most “natural” observable to discriminate between a Higgs
 1355 signal and the Z background is the invariant mass of the di-tau system, utilizing the fact
 1356 that the Z resonance is well known ($m_Z = 91.1876 \pm 0.0021$ GeV/ c^2) and has a narrow width
 1357 ($\Gamma_Z = 2.4952 \pm 0.0023$ GeV) [20]. The experimental complication in this approach is due to
 1358 the neutrinos produced in the tau lepton decays, which escape detection and carry away an
 1359 unmeasured amount of energy, making it difficult to reconstruct the tau lepton four-vectors.
 1360 In this chapter we give an overview of techniques used in previous literature [19, 40, 41] to
 1361 construct an observable related to the tau pair mass. We then introduce a new algorithm,
 1362 called the Secondary Vertex (SV) fit. The SVfit reconstructs the “full” tau pair mass, and
 1363 provides increased performance with respect to techniques previously used in the literature.

1364 §4.1 Existing mass reconstruction algorithms

1365 The simplest observable related to the $\tau^+\tau^-$ mass is one can construct that is sensitive to
 1366 new particle content is the invariant mass of the visible (reconstructible) decay products
 1367 associated with each tau decays. This quantity, referred in this document as the “Visible
 1368 Mass,” has the advantages of simplicity and lack of exposure to systematic errors associ-
 1369 ated with the reconstruction of the E_T^{miss} . However, no attempt is made to reconstruct the
 1370 neutrinos in the event. The reconstructed mass is thus systematically smaller than mass of
 1371 the resonance which produced the tau leptons. The visible mass is typically on the order of
 1372 1/2 of the resonance mass, depending on the kinematic requirements applied to the visible
 1373 products of the tau decays.

The Collinear Approximation is a technique previously used [19] to reconstruct the full $\tau^+\tau^-$ mass. In an event with two tau decays, there are a total of six¹ unknowns associated with the missing energy: the three components of the momentum of each neutrino. The Collinear Approximation makes the assumption that the neutrinos have the same direction as their associated visible decay products. This assumption reduces the number of unknown quantities to two, corresponding to the total energy of each neutrino. These two unknowns can be solved for by using the two components of the reconstructed missing transverse energy, which in the ideal case corresponds to the transverse component of the vector sum of the two neutrino's four momentum. The characteristic equation of the Collinear Approximation is

$$\begin{pmatrix} E_x^{\text{miss}} \\ E_y^{\text{miss}} \end{pmatrix} = \begin{pmatrix} \cos \phi_1 & \cos \phi_2 \\ \sin \phi_1 & \sin \phi_2 \end{pmatrix} \begin{pmatrix} E_1 \\ E_2 \end{pmatrix} \quad (4.1)$$

where $(E_x^{\text{miss}}, E_y^{\text{miss}})$ are the two components of the reconstructed missing transverse energy, $\phi_{1(2)}$ is the azimuthal angle of the visible component of the first (second) tau decay, and $E_{1(2)}$ is the reconstructed energy of neutrino of the first (second) tau decay. E_1 and E_2 can be extracted by inverting the matrix on the right hand side of Equation 4.1.

$$\begin{pmatrix} E_1 \\ E_2 \end{pmatrix} = \frac{1}{\sin(\phi_2 - \phi_1)} \begin{pmatrix} \sin \phi_2 & -\cos \phi_2 \\ -\sin \phi_1 & \cos \phi_1 \end{pmatrix} \begin{pmatrix} E_x^{\text{miss}} \\ E_y^{\text{miss}} \end{pmatrix} \quad (4.2)$$

The Collinear Approximation suffers from two problems. The approximation can fail (yielding unphysical negative energies for the reconstructed neutrinos) when the missing transverse energy is mis-measured. The events with unphysical solutions must be removed from the analysis, leading to a dramatic reduction in acceptance (on the order of 50% in this analysis). Improvements to the collinear approximation algorithm have recently been made which aim to recover part of the events with unphysical solutions [42]. But even with these improvements, no physical solution is still found for a large fraction of signal events. Additionally, the method is numerically sensitive when the two τ lepton are nearly back-to-back in azimuth. In these cases the $\sin(\phi_2 - \phi_1)^{-1}$ term in Equation 4.2 is very large

¹Technically, there is an extra unknown for each leptonic tau decay, which has two associated neutrinos. This is a small effect compared to the overall resolution of the collinear approximation.

1386 and small mis-measurements of the missing transverse energy can produce a large tail on
 1387 the reconstructed mass. This tail is particularly large for low-mass resonances. The large
 1388 tail for high mass is predominantly due to the fact (discussed in Section 4.4.2) that the
 1389 kinematic requirements² applied on the visible decay products preferentially selects events
 1390 where the visible decay products carry the majority of the energy of the original τ lepton,
 1391 reducing the amount of true missing energy in the event.

1392 §4.2 The Secondary Vertex fit

1393 A novel algorithm is presented in the following, which succeeds in finding a physical solution
 1394 for every event. As an additional benefit, the new algorithm is found to improve the di-tau
 1395 invariant mass resolution, making it easier to separate the Higgs signal from the $Z \rightarrow \tau^+\tau^-$
 1396 background.

1397 The novel Secondary Vertex fit (SVfit) algorithm for di-tau invariant mass reconstruc-
 1398 tion that we present in the following utilizes a likelihood maximization to fit a $\tau^+\tau^-$ in-
 1399 variant mass hypothesis for each event. The likelihood is composed of separate terms which
 1400 represent probability densities of:

- 1401 • tau decay kinematics
- 1402 • matching between the momenta of neutrinos produced in the tau decays and the
 1403 reconstructed missing transverse momentum
- 1404 • a regularization “ p_T -balance” term which accounts for the effects on the di-tau in-
 1405 variant mass of acceptance cuts on the visible tau decay products
- 1406 • the compatibility of tau decay parameters with the position of reconstructed tracks
 1407 and the known tau lifetime of $c\tau = 87 \mu\text{m}$ [20].

1408 The likelihood is maximized as function of a set of parameters which fully describe the tau
 1409 decay.

²The kinematic requirements on the visible decay products are necessary to reduce backgrounds and maintain compatibility with un-prescaled event triggers. This topic is discussed in detail in Chapter 5.

1410 §4.3 Parametrization of tau decays

1411 The decay of a tau with visible four-momentum p_{vis} measured in the CMS detector (“laboratory”) frame can be parametrized by three variables. The invisible (neutrino) momentum
 1412 is fully determined by these parameters.

1414 The “opening-angle” θ is defined as the angle between the boost direction of the tau
 1415 lepton and the momentum vector of the visible decay products in the rest frame of the
 1416 tau. The azimuthal angle of the tau in the lab frame is denoted as $\bar{\phi}$ (we denote quantities
 1417 defined in the laboratory frame by a overline). A local coordinate system is defined such
 1418 that the \bar{z} -direction lies along the visible momentum and $\bar{\phi} = 0$ lies in the plane spanned
 1419 by the momentum vector of the visible decay products and the proton beam direction. The
 1420 third parameter, $m_{\nu\nu}$, denotes the invariant mass of the invisible momentum system.

Given θ , $\bar{\phi}$ and $m_{\nu\nu}$, the energy and direction of the tau lepton can be computed by means of the following equations: The energy of the visible decay products in the rest frame of the tau lepton is related to the invariant mass of the neutrino system by:

$$E^{vis} = \frac{m_\tau^2 + m_{vis}^2 - m_{\nu\nu}^2}{2m_\tau} \quad (4.3)$$

1421 Note that for hadronic decays, $m_{\nu\nu}$ is a constant of value zero, as only a single neutrino is
 1422 produced. Consequently, the magnitude of P^{vis} depends on the reconstructed mass of the
 1423 visible decay products only and is a constant during the SVfit.

The opening angle $\bar{\theta}$ between the tau lepton direction and the visible momentum vector in the laboratory frame is determined by the rest frame quantities via the (Lorentz invariant) component of the visible momentum perpendicular to the tau lepton direction:

$$\begin{aligned} p_\perp^{vis} &= \bar{p}_\perp^{vis} \\ \Rightarrow \sin \bar{\theta} &= \frac{p^{vis} \sin \theta}{\bar{p}^{vis}} \end{aligned} \quad (4.4)$$

Substituting the parameters $m_{\nu\nu}$ and θ into Equations 4.3 and 4.4, the energy of the tau is obtained by solving for the boost factor γ in the Lorentz transformation between the tau rest frame and laboratory frame of the visible momentum component parallel to the

tau direction:

$$\bar{p}^{vis} \cos \bar{\theta} = \gamma \beta E^{vis} + \gamma p^{vis} \cos \theta$$

$$\Rightarrow \gamma = \frac{E^{vis}[(E^{vis})^2 + (\bar{p}^{vis} \cos \bar{\theta})^2 - (p^{vis} \cos \theta)^2]^{1/2} - p^{vis} \cos \theta \bar{p}^{vis} \cos \bar{\theta}}{(E^{vis})^2 - (p^{vis} \cos \theta)^2},$$

$$E^\tau = \gamma m_\tau$$

1424 The energy of the tau lepton in the laboratory frame as function of the measured visible
 1425 momentum depends on two of the three parameters only - the rest frame opening angle θ and
 1426 the invariant mass $m_{\nu\nu}$ of the neutrino system. The direction of the tau lepton momentum
 1427 vector is not fully determined by θ and $m_{\nu\nu}$, but is constrained to lie on the surface of a
 1428 cone of opening angle $\bar{\theta}$ (given by Equation 4.4), the axis of which is given by the visible
 1429 momentum vector. The tau lepton four-vector is fully determined by the addition of the
 1430 third parameter $\bar{\phi}$, which describes the azimuthal angle of the tau lepton with respect to the
 1431 visible momentum vector. The spatial coordinate system used is illustrated in Figure 4.1.

1432 §4.4 Likelihood for tau decay

The probability density functions for the tau decay kinematics are taken from the kinematics review of the PDG [20]. The likelihood is proportional to the phase-space volume for two-body ($\tau \rightarrow \tau_{had}\nu$) and three-body ($\tau \rightarrow e\nu\nu$ and $\tau \rightarrow \mu\nu\nu$) decays. For two-body decays the likelihood depends on the decay angle θ only:

$$d\Gamma \propto |\mathcal{M}|^2 \sin \theta d\theta$$

For three-body decays, the likelihood depends on the invariant mass of the neutrino system also:

$$d\Gamma \propto |\mathcal{M}|^2 \frac{((m_\tau^2 - (m_{\nu\nu} + m_{vis})^2)(m_\tau^2 - (m_{\nu\nu} - m_{vis})^2))^{1/2}}{2m_\tau} m_{\nu\nu} dm_{\nu\nu} \sin \theta d\theta \quad (4.5)$$

1433 In the present implementation of the SVfit algorithm, the matrix element is assumed to be
 1434 constant, so that the likelihood depends on the phase-space volume of the decay only ³.

1435 §4.4.1 Likelihood for reconstructed missing transverse momentum

1436 Momentum conservation in the plane perpendicular to the beam axis implies that the
 1437 vectorial sum of the momenta of all neutrinos produced in the decay of the tau lepton pair

³The full matrix elements for tau decays may be added in the future, including terms for the polarization of the tau lepton pair, which is different in Higgs and Z decays [43].

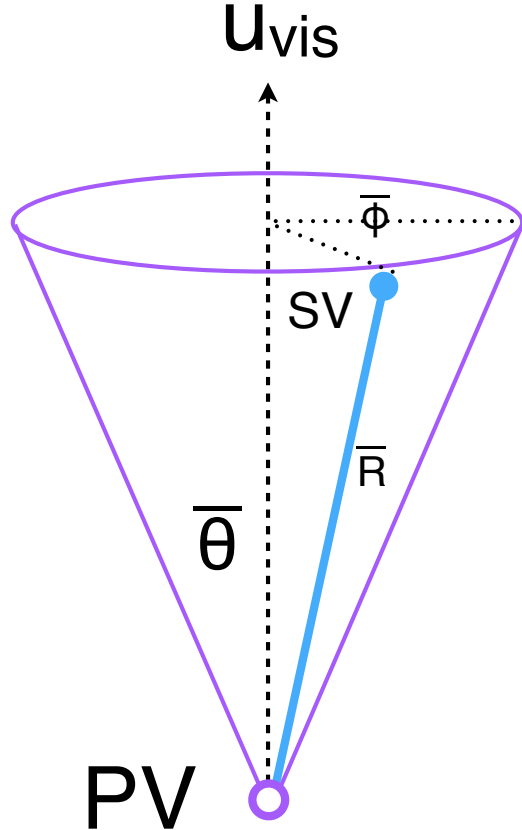


Figure 4.1: Illustration of the coordinate system used by the SVfit to describe the decays of tau leptons.

1438 matches the reconstructed missing transverse momentum. Differences are possible due to
1439 the experimental resolution and finite p_T of particles escaping detection in beam direction
1440 at high $|\eta|$.

The E_T^{miss} resolution is measured in $Z \rightarrow \mu^+\mu^-$ events selected in the 7 TeV data collected by CMS in 2010. Corrections are applied to the distribution of E_T^{miss} in the Monte Carlo simulated events to match the resolution measured in data. The uncertainty on this correction factor is taken as a “shape systematic.” The treatment of this correction and its corresponding uncertainty are described in Chapters 7 and 8. The momentum vectors of reconstructed E_T^{miss} and neutrino momenta given by the fit parameters are projected in direction parallel and perpendicular to the direction of the $\tau^+\tau^-$ momentum vector. For both components, a Gaussian probability function is assumed. The width and mean values

of the Gaussian in parallel (“||”) and perpendicular (“ \perp ”) direction are:

$$\sigma_{\parallel} = \max(7.54(1 - 0.00542 \cdot q_T), 5.)$$

$$\mu_{\parallel} = -0.96$$

$$\sigma_{\perp} = \max(6.85(1 - 0.00547 \cdot q_T), 5.)$$

$$\mu_{\perp} = 0.0,$$

¹⁴⁴¹ where q_T denotes the transverse momentum of the tau lepton pair.

¹⁴⁴² §4.4.2 Likelihood for tau lepton transverse momentum balance

The tau lepton transverse momentum balance likelihood term represents the probability density $p(p_T^{\tau}|M_{\tau\tau})$ of the tau transverse momentum, given the condition that the tau is produced in the decay of a resonance of mass $M_{\tau\tau}$. The likelihood is constructed by parametrizing the shape of the tau lepton p_T distribution in simulated Higgs $\rightarrow \tau^+\tau^-$ events as a function of the Higgs mass. The functional form of the parametrization is taken to be the sum of two terms. The first term, denoted by $p^*(p_T|M)$, is derived by assuming an isotropic two-body decay, that is

$$dp^* \propto \sin \theta d\theta.$$

Performing a variable transformation from θ to $p_T \sim \frac{M}{2} \sin \theta$, we obtain

$$\begin{aligned} p^*(p_T|M) &= \frac{dp}{dp_T} = \frac{dp}{d\cos \theta} \left| \frac{d\cos \theta}{dp_T} \right| \\ &\propto \left| \frac{d}{dp_T} \sqrt{1 - \left(2 \frac{p_T}{M}\right)^2} \right| \\ &= \frac{1}{\sqrt{\left(\frac{M}{2p_T}\right)^2 - 1}}. \end{aligned} \tag{4.6}$$

The first term of the p_T -balance likelihood is taken as the convolution of Equation 4.6 with a Gaussian of width s . The second term is taken to be a Gamma distribution with scale parameter θ and shape parameter k , in order to account for tails in the p_T distribution of the tau lepton pair. The complete functional form is thus given by

$$p(p_T|M) \propto \int_0^{\frac{M}{2}} p^*(p'_T|M) e^{-\frac{(p_T-p'_T)^2}{2s^2}} dp'_T + a\Gamma(p_T, k, \theta). \tag{4.7}$$

Numerical values of the parameters s , θ and k are determined by fitting the PDF in Equation 4.7 to the tau lepton p_T distribution in simulated Higgs $\rightarrow \tau^+\tau^-$ events. The relative

weight a of the two terms is also determined in the fit. Replacing the integrand in Equation 4.7 by its Taylor expansion so that the integration can be carried out analytically, keeping polynomial terms up to fifth order, and assuming the fit parameters to depend at most linearly on the Higgs mass, we obtain the following numerical values for the parameters:

$$\begin{aligned}s &= 1.8 + 0.018 \cdot M_{\tau\tau} \\k &= 2.2 + 0.0364 \cdot M_{\tau\tau} \\\theta &= 6.74 + 0.02 \cdot M_{\tau\tau} \\a &= 0.48 - 0.0007 \cdot M_{\tau\tau}.\end{aligned}$$

The motivation for the p_T -balance likelihood is to add a “regularization” term which compensates for the effect of p_T cuts applied on the visible decay products of the two tau leptons. In particular for tau lepton pairs produced in decays of resonances of low mass, the visible p_T cuts significantly affect the distribution of the visible momentum fraction $x = E_{vis}/E_\tau$. The effect is illustrated in Figures 4.3 and 4.4. If no attempt would be made to compensate for this effect, Equations 4.4 and 4.5 would yield likelihood values that are too high at low x , resulting in the SVfit to underestimate the energy of visible decay products (overestimate the energy of neutrinos) produced in the tau decay, resulting in a significant tail of the reconstructed mass distribution in the high mass region. The $\tau^+\tau^-$ invariant mass distribution reconstructed with and without the p_T -balance likelihood term is shown in Figure 4.2. A significant improvement in resolution and in particular a significant reduction of the non-Gaussian tail in the region of high masses is seen.

§4.4.3 Secondary vertex information

The parametrization of the tau decay kinematics described in section 4.3 can be extended to describe the production and decay of the tau. As the flight direction of the tau is already fully determined by the parameters θ , $\bar{\phi}$ and $m_{\nu\nu}$, the position of the secondary (decay) vertex is hence fully determined by addition of a single parameter for the flight distance, r . The tau lifetime $c\tau = 87 \mu\text{m}$ is large enough to allow the displacement of the tau decay vertex from the primary event vertex to be resolved by the CMS tracking detector. The resolution provided by the CMS tracking detector is utilized to improve the resolution on

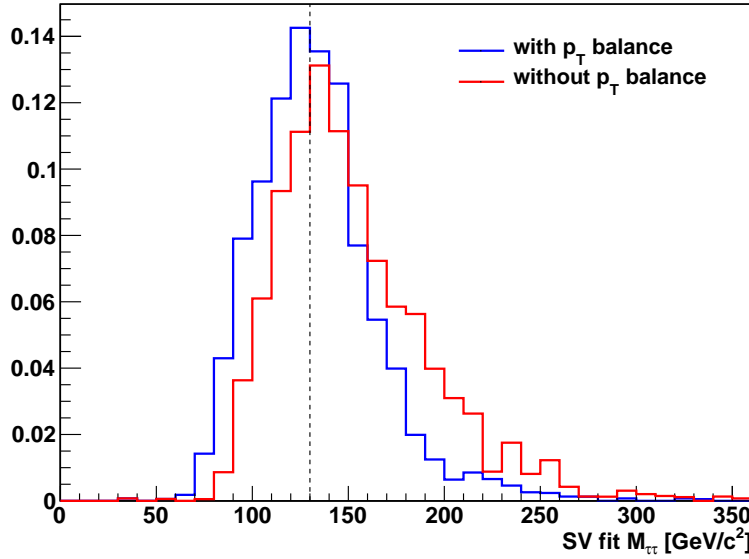


Figure 4.2: Distribution of di-tau invariant mass reconstructed by the SVfit algorithm in simulated Higgs events with $m_{A^0} = 130 \text{ GeV}/c^2$. The SVfit algorithm is run in two configurations, with (blue) and without (red) the p_T -balance likelihood term included in the fit.

1463 the $\tau^+\tau^-$ invariant mass reconstructed by the SVfit algorithm. The likelihood term based on
 1464 the secondary vertex information is based on the compatibility of the decay vertex position
 1465 with the reconstructed tracks of charged tau decay products. Perhaps surprisingly, it turns
 1466 out that the flight distance parameter R is sufficiently constrained even for tau decays into
 1467 a single charged hadron, electron or muon.

The parameter R can be constrained further by a term which represents the probability for a tau lepton of momentum P to travel a distance d before decaying:

$$p(d|P) = \frac{m_\tau}{P c \tau} e^{-\frac{m_\tau d}{P c \tau}}$$

1468 The likelihood terms for the secondary vertex fit have been implemented in the SVfit
 1469 algorithm. In the analysis presented in this note, the decay vertex information is not used,
 1470 however, because of systematic effects arising from tracker (mis-)alignment which are not
 1471 yet fully understood.

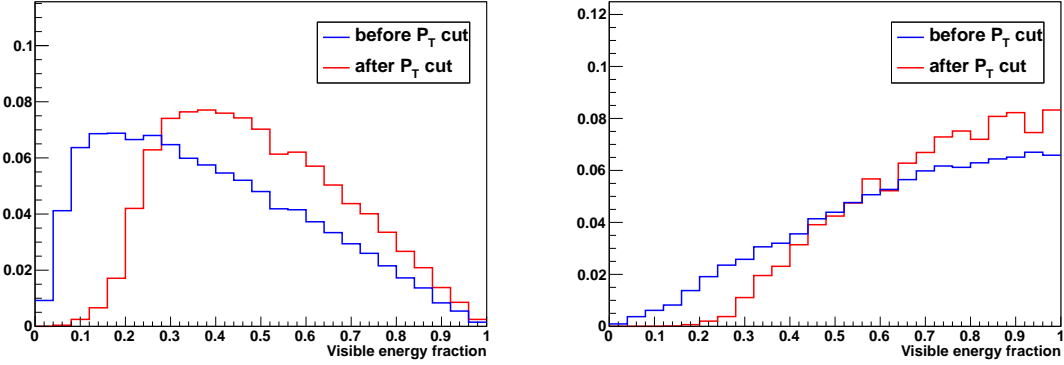


Figure 4.3: Normalized distributions of the fraction of total tau decay energy carried by the muon (left) and hadronic constituents (right) in simulated Higgs events with $m_{A^0} = 130 \text{ GeV}/c^2$. The distribution is shown before (blue) and after (red) the requirement on the p_T of the visible decay products described in Chapter 5.

1472 §4.5 Performance

1473 The tau pair mass reconstructed by the Secondary Vertex fit (“SVfit mass”) provides
 1474 the observable with the largest separation between signal Higgs events and the dominant
 1475 $Z \rightarrow \tau^+ \tau^-$ background. The mean of the SVfit mass is located at the true mass of the di-tau
 1476 pair. The SVfit algorithm has a higher acceptance and better resolution than the Collinear
 1477 Approximation algorithm. The SVfit always finds a physical solution, improving on the effi-
 1478 ciency of the collinear approximation by a factor of two. Additionally, it has a much better
 1479 resolution. The collinear approximation reconstructed mass distribution has a large tail at
 1480 high mass due to events with poorly measured E_T^{miss} . The shape of the SVfit distribution
 1481 is nearly Gaussian. The comparison is illustrated in Figure 4.5. Previous searches for Higgs
 1482 bosons decaying to tau leptons [40] have in general used the “visible mass” as the observ-
 1483 able used to search for new resonances. The SVfit method has the obvious difference that it
 1484 reconstructs the “full” tau pair mass, which is the most natural observable corresponding
 1485 to a particle decaying to tau leptons. In addition, the relative resolution⁴ of the SV fit is
 1486 superior to that of the visible mass. This feature is illustrated in Figure 4.6. In Figure 4.6,
 1487 the visible mass distribution is scaled by an arbitrary number such that the scaled mean
 1488 of the distribution matches the true mass of the tau pair (and the SVfit mass). The width

⁴We define this metric of performance as the variance of a distribution divided by its mean.

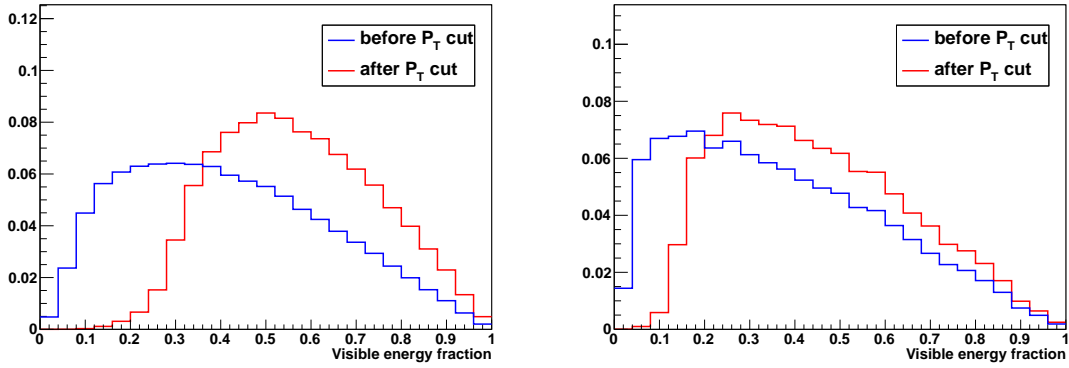


Figure 4.4: Normalized distributions of the fraction of total tau decay energy carried by the muon in simulated $Z \rightarrow \tau^+\tau^-$ (left) and Higgs events with $m_{A^0} = 200$ GeV/c^2 (right). The distribution is shown before (blue) and after (red) the requirement that the p_T of the muon be greater than 15 GeV/c .

of the SVfit distribution is smaller than that of the scaled visible mass distribution, indicating better performance. The increase in relative resolution allows a “bump,” due to the presence of signal events, to be more easily distinguished from the $Z \rightarrow \tau^+\tau^-$ background. This increases the power of the search for the new signal.

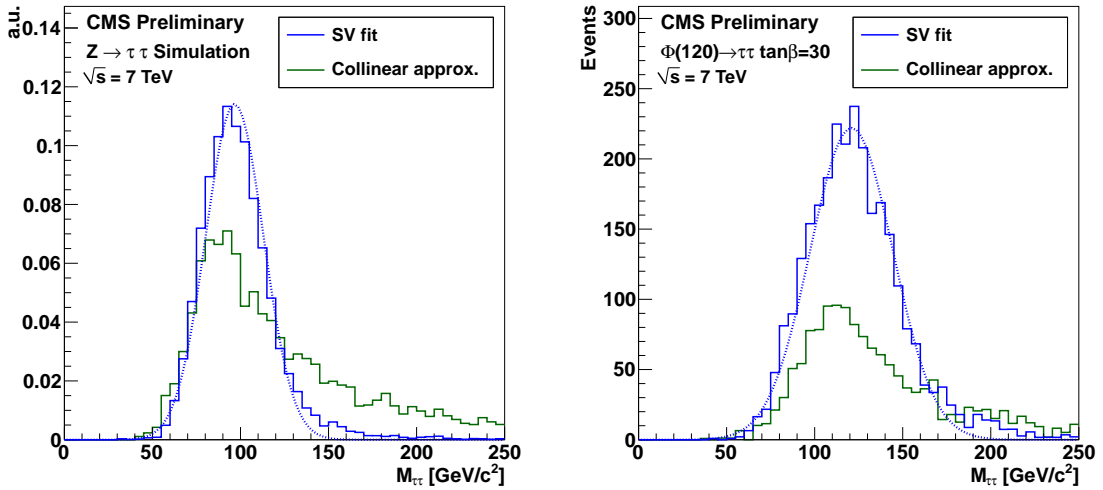


Figure 4.5: Comparison of the reconstructed tau pair mass spectrum in $Z \rightarrow \tau^+\tau^-$ (left) and MSSM $H(120) \rightarrow \tau^+\tau^-$ (right) events after the selections described in chapter 5. The mass spectrum reconstructed by the Secondary Vertex fit is shown in blue, the result of the collinear approximation algorithm is given in green. In the left plot, both distributions are normalized to unity, illustrating the improvement in resolution (shape) provided by the SVfit. In the right plot, the distributions are normalized to an (arbitrary) luminosity, illustrating the loss of events that occurs due to unphysical solutions in the application of the collinear approximation.

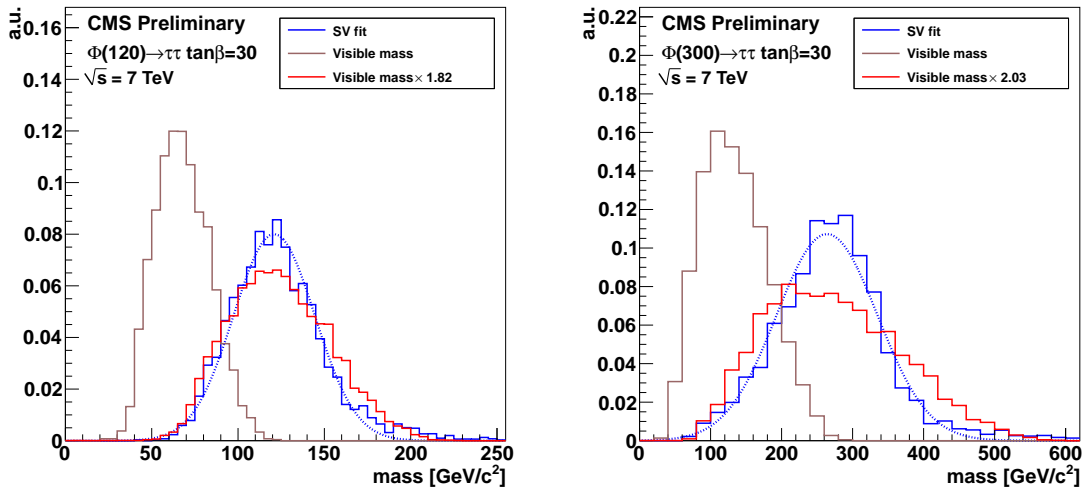


Figure 4.6: Comparison of the invariant mass of the muon and τ_{jet} (the “visible mass”) with the full $\tau^+\tau^-$ mass reconstructed by the SVfit. The spectrum is shown for two simulated MSSM Higgs samples, with $m_{A^0} = 120 \text{ GeV}/c^2$ (left), and $m_{A^0} = 200 \text{ GeV}/c^2$ (right). To illustrate that relative resolution of the SVfit is superior to that of the visible mass, the visible mass is also shown scaled up such that the mean of the two distributions are identical.

1493

Chapter 5

1494

Analysis Selections

1495 The selections applied to data in this analysis are designed to maximize the significance of
 1496 Higgs signal events in the final set of selected events. This analysis presented in this thesis
 1497 is an inclusive analysis, meaning that no preference is given to any single Higgs production
 1498 mechanism. The analysis looks specifically at the channel in which one tau decays to a
 1499 muon and the other decays to hadrons. Therefore the first step in the analysis selection is
 1500 to find High Level Trigger selection that is highly efficient for the signal and is not highly
 1501 prescaled¹. After the trigger selection, events are required to contain at least a good muon
 1502 and a good tau. Vetoos on extra leptons are applied to reduce backgrounds from di-muon
 1503 events. Finally, kinematic and charge selections on the are applied to the event to reduce
 1504 $W + \text{jets}$ and QCD backgrounds.

1505

§5.1 High Level Trigger

1506 As only data which passes the HLT is recorded, it is thus critical that an appropriate trig-
 1507 ger path is found. The events in this analysis are triggered by a combination of muon and
 1508 muon + tau-jet “cross-channel” triggers. For the muon triggers, the HLT paths with low-
 1509 est p_T thresholds are used as long as the path remained unprescaled (see Table 5.1). The
 1510 muon + tau-jet “cross-channel” trigger paths increase the trigger efficiency for events con-
 1511 taining muons of transverse momenta close to the $p_T^\mu > 15$ GeV/c cut threshold. The trigger
 1512 efficiency is measured in data via the tag-and-probe technique. Details of the muon trigger
 1513 efficiency measurement are given in Section 7.1. Monte Carlo simulated events are required

¹If a trigger has high background rates, it may exceed its rate budget with increasing luminosity. When this happens, it is generally “prescaled,” and some fraction of the events that pass this trigger are randomly thrown it away to reduce the rate. In general, it is better to use an unprescaled trigger with lower efficiency than a prescaled trigger.

Trigger path	run-range
HLT_Mu9	132440 - 147116
HLT_IsoMu9	147196 - 148058
HLT_Mu11	147196 - 148058
HLT_Mu15	147196 - 149442
HLT_IsoMu13	148822 - 149182
HLT_IsoMu9_PFTau15	148822 - 149182
HLT_Mu11_PFTau15	148822 - 149182

Table 5.1: Muon and muon + tau–jet “cross–channel” trigger paths utilized to trigger events in different data–taking periods.

1514 to pass the HLT_Mu9 trigger path. Weights are applied to simulated events to account for the
 1515 difference between the simulated HLT_Mu9 efficiency and the combined efficiency of the set
 1516 HLT_Mu9, HLT_IsoMu9, HLT_Mu11, HLT_IsoMu13, HLT_Mu15, HLT_IsoMu9_PFTau15
 1517 and HLT_Mu11_PFTau15 used to trigger the data.

1518 §5.2 Particle Identification

1519 §5.2.1 Muons

1520 Muon candidates are required to be reconstructed as global and as tracker muons, meaning
 1521 that a full track is reconstructed in the muon system and is well matched to a track in the
 1522 silicon strip and pixel trackers. Additionally, they are required to pass the “Vector Boson
 1523 Task Force” (VBTF) muon identification criteria developed for the $Z \rightarrow \mu^+ \mu^-$ cross–section
 1524 measurement [44]:

- 1525 • ≥ 1 Pixel hits
- 1526 • ≥ 10 hits in silicon Pixel + Strip detectors
- 1527 • ≥ 1 hit(s) in muon system
- 1528 • ≥ 2 matched segments

- 1529 • $\chi^2/DoF < 10$ for global track fit
- 1530 • transverse impact parameter of “inner” track $d_{\text{IP}} < 2$ mm with respect to beam-spot

1531 In order to reduce background contributions from muons originating from heavy quark
 1532 decays in QCD multi-jet events, muons are required to be isolated. Isolation is computed
 1533 as the p_{T} sum of charged and neutral hadrons plus photons reconstructed by the CMS
 1534 particle-flow algorithm [29] within a cone of size $\Delta R_{iso} = 0.4$ around the muon direction
 1535 divided by the muon p_{T} . The innermost region of size $\Delta R_{veto} = 0.08$ (0.05) is excluded
 1536 from the computation of the isolation p_{T} sum with respect to neutral hadrons (photons),
 1537 in order to avoid energy deposits in the electromagnetic and hadronic calorimeters which
 1538 are due to the muon to enter the sum. In order to reduce pile-up effects, particles entering
 1539 the isolation p_{T} sum are required to have transverse momenta $p_{\text{T}} > 1.0$ GeV/c. Charged
 1540 particles are additionally required to originate from the same vertex as the muon. The
 1541 muons are required to be isolated with respect to charged hadrons of $p_{\text{T}} > 1.0$ GeV/c and
 1542 photons of $p_{\text{T}} > 1.5$ GeV/c as reconstructed by the particle-flow algorithm [29] in a cone
 1543 of size $\Delta R = 0.4$ around the direction of the muon. The distribution of the muon isolation
 1544 discriminant is shown in Figure 5.1(a).

1545 §5.2.2 Hadronic Taus

1546 Hadronic decays of taus are identified by the HPS + TaNC hybrid algorithm described in
 1547 Section 3.5. The “loose” working point is used, corresponding to an expected QCD fake-rate
 1548 of about 1%. $Z \rightarrow \mu^+ \mu^-$ background contributions are largely due to muons which failed
 1549 to get reconstructed as global muons (thus failing the muon identification requirement) and
 1550 are misidentified as tau-jet candidates. These muons are typically isolated and have a large
 1551 chance to pass the hadronic tau ID discriminators. To reject these events, hadronic taus are
 1552 additionally required to pass an anti-muon veto described in Section 3.6.

1553 §5.2.3 Missing Transverse Energy

1554 The missing transverse energy $E_{\text{T}}^{\text{miss}}$, in the event is reconstructed based on the vectorial
 1555 momentum sum of particle candidates reconstructed by the particle-flow algorithm [29, 45].
 1556 In the ideal case, the $E_{\text{T}}^{\text{miss}}$ corresponds to the vector sum of the transverse components of

Background	Cross Section (pb)
QCD Heavy Flavor	84679 ³
$W \rightarrow \mu\nu + \text{jets}$	10435
$Z \rightarrow \mu\mu + \text{jets}$	1666
$t\bar{t} + \text{jets}$	158

Table 5.2: The different backgrounds to the analysis presented in this thesis that include misidentified hadronic taus.

1557 all neutrinos in the event. The E_T^{miss} resolution in simulated $Z \rightarrow \mu^+\mu^-$ events is found
 1558 to be smaller (better) than in the data. The reconstructed E_T^{miss} in the simulated events is
 1559 “smeared” by a correction factor such that the data and simulation are in agreement. The
 1560 “Z-recoil” E_T^{miss} correction procedure is described in Section 7.4.

1561 §5.3 Event Selections

1562 The selections applied to the analysis are designed to reject large fractions of the background
 1563 while maintaining a high efficiency for identifying signal Higgs events. The backgrounds
 1564 can be divided into two classifications: “fake” backgrounds, in which there is at least one
 1565 misidentified hadronic tau decay, and the irreducible $Z \rightarrow \tau^+\tau^-$ background, which cannot²
 1566 be distinguished from the potential presence of a Higgs boson of the same mass. Strategies
 1567 for dealing with the irreducible Z background will be discussed in the Chapter 9. The
 1568 different fake backgrounds, their cross section, and the basic removal strategies are outlined
 1569 in Table 5.2.

1570 Events are selected by requiring a muon of $p_T^\mu > 15$ GeV/c within $|\eta_\mu| < 2.1$ and a tau-
 1571 jet candidate of $p_T^{\tau-\text{jet}} > 20$ GeV/c within $|\eta_{\tau-\text{jet}}| < 2.3$. The η requirement on the muon
 1572 ensures that it is within the fiducial region of the muon trigger system. The η requirement
 1573 on the hadronic tau ensures it is well within the fiducial region of the tracker ($|\eta| < 2.5$)
 1574 and minimizes exposure to large QCD backgrounds in the very forward region.

²Due to the differences in spin between the Z (spin 1) and the Higgs (spin 0), in the future it may be possible to separate the two using spin correlations of the two tau decays.

1575 The muon and tau–jet candidate are required to be of opposite charge, as the Higgs is
 1576 neutral and charge is conserved. The muon is required to be pass the identification criteria
 1577 described in Section 5.2.1. The tau-jet candidate is required to pass the “loose” TaNC tau
 1578 identification discriminator.

1579 Additional event selection criteria are applied to reduce contributions of specific back-
 1580 ground processes. In order to reject $Z \rightarrow \mu^+ \mu^-$ background, a dedicated discriminator
 1581 against muons is applied [28]. Remaining di-muon background is suppressed by reject-
 1582 ing events which have a track of $p_T > 15$ GeV/c and for which the sum of energy deposits
 1583 in ECAL plus HCAL is below $0.25 \cdot P$ within a cylinder of radius 15 cm (ECAL) and
 1584 25 cm (HCAL), respectively. Contamination from $Z \rightarrow \tau^+ \tau^-$ events in which the recon-
 1585 structed tau–jet candidate is due to a $\tau \rightarrow e \nu \nu$ decay is reduced by applying a dedicated
 1586 tau ID discriminator against electrons.

The $t\bar{t}$ and $W + \text{jets}$ backgrounds are suppressed by cuts on the transverse mass of the $\mu - E_T^{\text{miss}}$ system and the P_ζ variable. The transverse mass (M_T) cut is defined as the quantity

$$M_T = p_T^\mu E_T^{\text{miss}} \sqrt{1 - \cos \Delta\phi},$$

1587 where $\Delta\phi$ is the angle between the muon and the reconstructed E_T^{miss} in the transverse
 1588 plane. The M_T quantity is much higher in events $W \rightarrow \mu\nu$ decays than in signal Higgs
 1589 events. In $W \rightarrow \mu\nu$ decays, the neutrino expected to be produced in the opposite to the
 1590 muon in azimuth. In signal events, there are three neutrinos produced, with the majority
 1591 (two) of the neutrinos being associated to the $\tau \rightarrow \mu\nu\nu$ decay. Accordingly, we expect
 1592 that the E_T^{miss} is on average collinear with the muon in signal events. The M_T distribution
 1593 immediately before the M_T cut is applied is illustrated in Figure 5.1(b) for the different
 1594 background sources and 2010 data.

1595 The P_ζ variable is another quantity with discriminant power against $W + \text{jets}$ and
 1596 $t\bar{t}$ backgrounds. The observable has been introduced in the search for $H \rightarrow \tau^+ \tau^-$ events
 1597 performed by the CDF collaboration [46]. The observable is motivated by the fact that in
 1598 $\tau^+ \tau^-$ signal events all neutrinos are produced in direction very close of the visible decay
 1599 products of one of the two tau leptons. It is therefore expected that the direction of the
 1600 missing transverse energy vector in these events point in a direction somewhere between

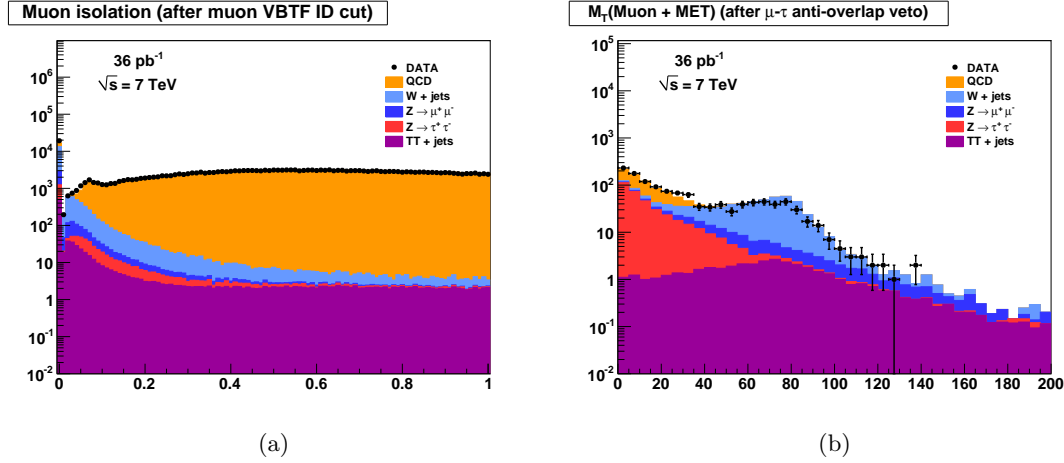


Figure 5.1: Distributions of the muon isolation (a) and M_T (b) discriminant variables. The muon isolation discriminant rejects the QCD background at a high rate. The M_T cut is designed to reject $W + \text{jets}$ and $t\bar{t} + \text{jets}$ backgrounds. The distributions shown are computed immediately before the corresponding selection is applied.

1601 the visible τ -lepton decay products. This event topology is not preferred in $W + \text{jets}$, $t\bar{t}$
 1602 and QCD background events. The observable is computed as difference of the projections:

$$P_\zeta = \vec{P}_T^{vis_1} + \vec{P}_T^{vis_2} + E_T^{\text{miss}}$$

1603 on the axis ζ bisecting the directions $\vec{P}_T^{vis_1}$ and $\vec{P}_T^{vis_2}$ of the visible τ lepton decay products
 1604 in the transverse plane (see Figure 5.2(a) for an illustration). The distribution of P_ζ after
 1605 the M_T selection has been applied is shown in Figure 5.2(b). The complete set of event
 1606 selection criteria applied are summarized in Table 5.3.

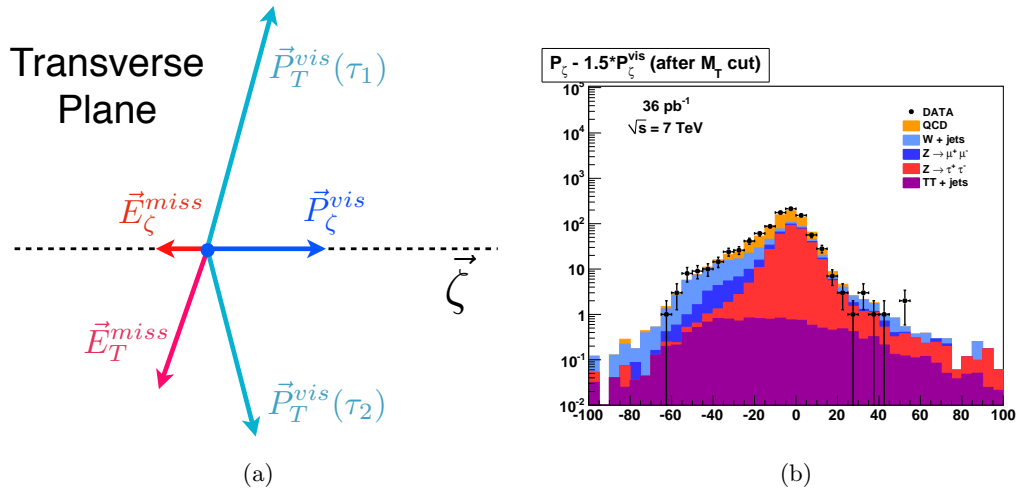


Figure 5.2: The vector quantities used in construction of the quantity $P_\zeta - 1.5 \cdot P_\zeta^{\text{vis}}$ are illustrated in Figure (a). Image credit: [46] The distribution of the P_ζ variable in the different background sources and 2010 data after the M_T cut has been applied is shown at right in (b).

Requirement	
Trigger	HLT Mu9 for MC <i>cf.</i> table 5.1 for Data
Vertex	reconstructed with beam-spot constraint:
Muon	$-24 < z_{vttx} < +24 \text{ cm}$, $ \rho < 2 \text{ cm}$, $N_{\text{DOF}} > 4$ reconstructed as global Muon with: $p_T > 15 \text{ GeV}/c$, $ \eta < 2.1$, VBF Muon ID passed, isolated within $\Delta R = 0.4$ cone with respect to charged hadrons of $p_T > 1.0 \text{ GeV}/c$ and neutral electromagnetic objects of $E_T > 1.5 \text{ GeV}$
Tau-jet Candidate	reconstructed by HPS + TaNC combined Tau ID algorithm TaNC “medium” Tau ID discriminator and discriminators against electrons and muons passed, calorimeter muon rejection passed
Muon + Tau-jet	$\text{charge}(\text{Muon}) + \text{charge}(\text{Tau-jet}) = 0$, $\Delta R(\text{Muon}, \text{Tau-jet}) > 0.5$
Kinematics	$M_T(\text{Muon-MET}) < 40 \text{ GeV}$ $P_\zeta - 1.5 \cdot P_\zeta^{\text{vis}} > -20 \text{ GeV}$

Table 5.3: Event selection criteria applied to select $H \rightarrow \tau^+ \tau^- \rightarrow \mu \tau_{had}$ events.

1607

Chapter 6

1608

Data–Driven Background Estimation

1609 For the result of this analysis to be reliable, it is of paramount importance that the back-
 1610 grounds be well understood. The CMS experiment has adopted a policy that if possible, all
 1611 background processes should be measured in a “data–driven” way. By requiring that the
 1612 background comes from data, biases due to incorrectly modeling the background processes
 1613 in simulation can be minimized or eliminated. In general, the data–driven methods also have
 1614 the advantage that they are independent of the uncertainty on the integrated luminosity.
 1615 This analysis measures the backgrounds using two complementary methods, the “Template
 1616 Method” and the “Fake–rate method.” In both cases, predictions are made about back-
 1617 grounds in the signal region using measurements obtained in background enriched control
 1618 regions of the data.

1619 The Template Method fits the sum of background shape templates to the M_{vis} spec-
 1620 trum of events selected in the final analysis and is described in Section 6.3. The results of
 1621 Template Method presented in this chapter cannot be used directly in the final result of this
 1622 analysis, as the final likelihood fit (see Chapter 8) implicitly performs a template fit of the
 1623 background shapes. Nonetheless, we present the results here as an additional cross–check
 1624 of the simulation performance, and to give an overview of the method.

1625 The Fake–rate Method is based on applying probabilities for quark and gluon jets to
 1626 be misidentified as hadronic tau decays to events passing all event selection criteria except
 1627 the tau identification requirements. The probabilities with which jets fake hadronic tau
 1628 signatures are measured in data. Contrary to the Template Method, the Fake–rate Method
 1629 estimates the sum of the contributions of backgrounds that contain incorrectly identified
 1630 taus. The Fake–rate method is detailed in Section 6.2. The two methods are complementary
 1631 as the Template Method uses only information about the different visible mass distribution

1632 shapes of the backgrounds, while the Fake–rate method uses only information about the
 1633 hadronic tau fake–rate.

1634 §6.1 Background Enriched Control Regions

1635 The criteria applied to select events in the background enriched control regions for the Tem-
 1636 plate Method is based on the work described in [47]. With respect to that work, the muon
 1637 isolation criteria applied to select $Z \rightarrow \mu^+ \mu^-$, $W + \text{jets}$, $t\bar{t} + \text{jets}$ and QCD background
 1638 enriched control samples has been changed to relative isolation with respect to charged
 1639 hadrons and neutral electromagnetic objects reconstructed by the particle–flow algorithm.
 1640 The selection of the enriched backgrounds is accomplished by disabling or inverting specific
 1641 selections of Chapter 5 that were implemented to reject the given background. The selection
 1642 of control regions used to measure the fake–rates for different types of background processes
 1643 are very similar to the selections used for the Template Method. The details of the fake–rate
 1644 measurement selections may be found in [48].

1645 All control regions are selected from the 2010 CMS muon primary datasets using single
 1646 muon HLT trigger paths. The set of triggers and run–ranges used to select events in the
 1647 background enriched control samples is the same as for the analysis (see Table 5.1). The
 1648 Monte Carlo simulated events used for comparison with the control region selections are
 1649 required to pass the HLT_Mu9 trigger path and are weighted according to the description
 1650 in Chapter 7 to account for the difference in efficiency between HLT_Mu9 and the trigger
 1651 paths required to have passed in the data.

1652 QCD di–jet events containing a muon (originating from the leptonic decay of a b or
 1653 c quark) are selected by applying an anti–isolation requirement on the jet containing a
 1654 muon. $W + \text{jets}$ and $t\bar{t} + \text{jets}$ are selected by requiring an isolated muon, and inverting the
 1655 transverse mass (M_T) and P_ζ selections. Tau–jet candidates considered in the $Z \rightarrow \mu^+ \mu^-$
 1656 sample where the reconstructed tau–jet candidate is faked by a misidentified muon and in
 1657 the $t\bar{t} + \text{jets}$ control sample are required to pass the “loose” TaNC discriminator. For the
 1658 Template Method, the $Z \rightarrow \mu^+ \mu^-$ sample where the reconstructed tau–jet candidate is faked
 1659 by a misidentified quark or gluon jet, the $W + \text{jets}$ and the QCD enriched control samples
 1660 have a loose hadronic tau “preselection” applied. The tau–jet candidates are required to

1661 pass the “very loose”, but fail the “loose” TaNC discriminator. The criteria applied to select
 1662 events in the different background enriched control samples are summarized in Table 6.1.
 1663 The goal of the background enriched selection process is to select different background
 1664 processes with high purity. A highly pure background control sample improves the stability
 1665 of inferences about the signal region made using information in the enriched control region.
 1666 The purity of the control regions (estimated using simulation) are summarized in Table 6.2.
 1667

1668 The number of events observed in the different control samples is compared to the
 1669 Monte Carlo expectation in Table 6.2. Except for the contribution of $Z \rightarrow \mu^+ \mu^-$ events
 1670 in which the reconstructed tau–jet candidate is due to a misidentified quark or gluon jet,
 1671 good agreement between data and Monte Carlo simulation is observed. Differences observed
 1672 between data and simulation will be accounted for as systematic uncertainties.

1673 The distributions of visible and “full” $\tau^+ \tau^-$ invariant mass reconstructed by the SVfit
 1674 algorithm (see Chapter 4) observed in the background enriched control regions is compared
 1675 to the Monte Carlo simulation in Figures 6.1 and 6.2. The template for the $W +$ jets back-
 1676 ground has been corrected for the bias on the $M_{vis}^{\mu\tau_{had}}$ shape caused by the $M_T^{\mu E_T^{\text{miss}}} <$
 1677 $50 \text{ GeV}/c^2$ and $P_\zeta - 1.5 \cdot P_\zeta^{\text{vis}} > -20 \text{ GeV}$ requirements applied in the final analysis via the
 1678 reweighting procedure described in [47]. In the $t\bar{t} +$ jets enriched control region a peak at the
 1679 Z mass is observed in data, which is not modeled by the Monte Carlo samples considered.
 1680 The peak could be due to $Z \rightarrow \mu^+ \mu^-$ events produced in association with b quarks. On
 1681 the other hand, the contribution from $t\bar{t} +$ jets events to that sample seems to be overesti-
 1682 mated. The origin of the Z mass peak merits further investigation, but overall the $t\bar{t} +$ jets
 1683 is a negligible background contribution.

1684 §6.2 The Fake–rate Method

1685 The probabilities with which quark and gluon jets get misidentified as tau–jets may be
 1686 utilized to obtain an estimate of background contributions in physics analyses. As an il-
 1687 lustrative example and in order to demonstrate the precision achievable with the method,
 1688 we introduce the method in the context of a “closure test,” using a simulated samples,

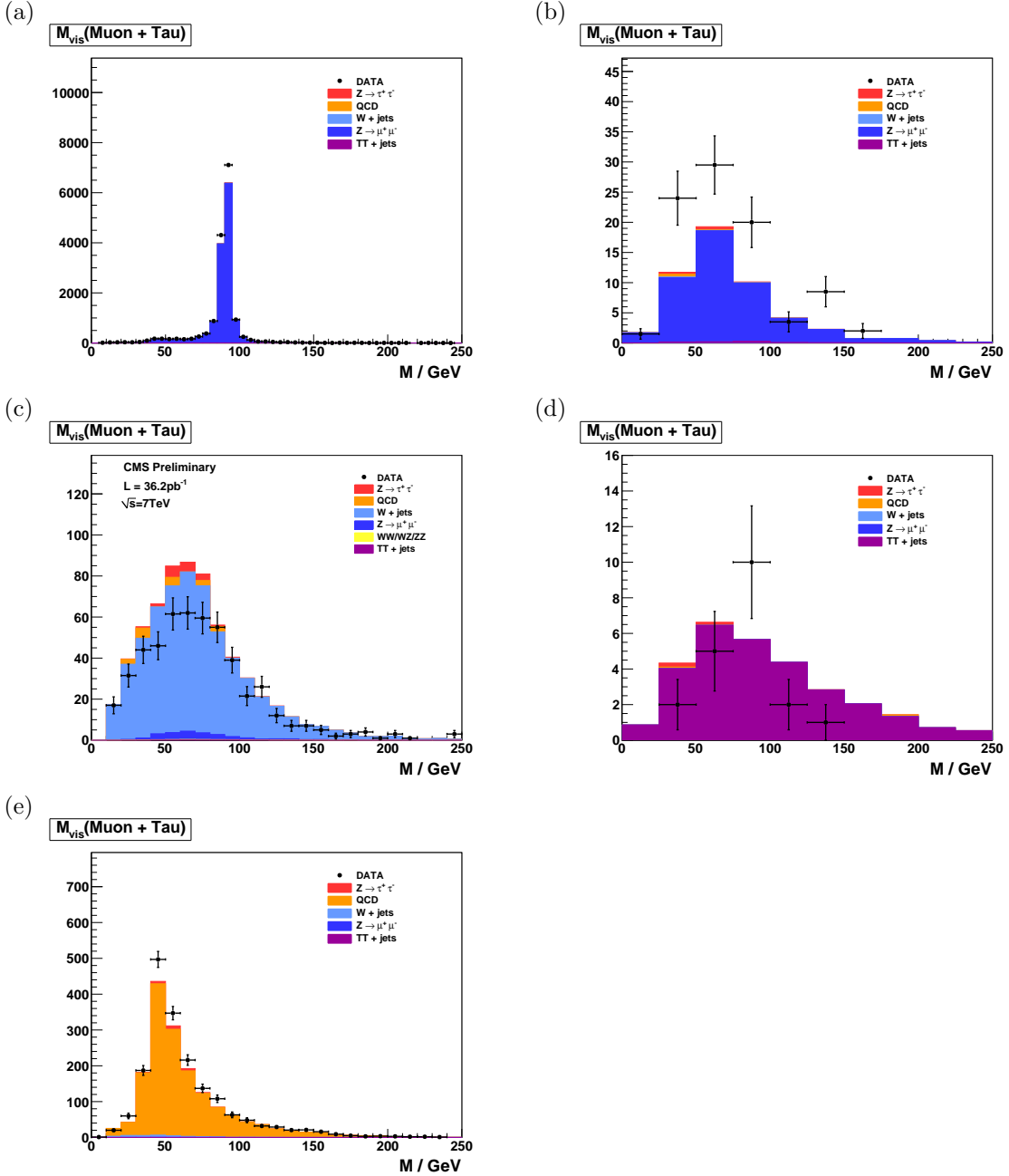


Figure 6.1: Distribution of visible mass of muon plus the tau–jet candidate reconstructed in the background enriched control samples for $Z \rightarrow \mu^+ \mu^-$ (a) and (b), $W + \text{jets}$ (c), $t\bar{t} + \text{jets}$ (d) and QCD multi-jet (e) backgrounds. In (a) reconstructed tau–jet candidates are expected to be dominantly due to misidentified muons, while in (b) they are expected to be mostly due to misidentified misidentified quark or gluon jets.

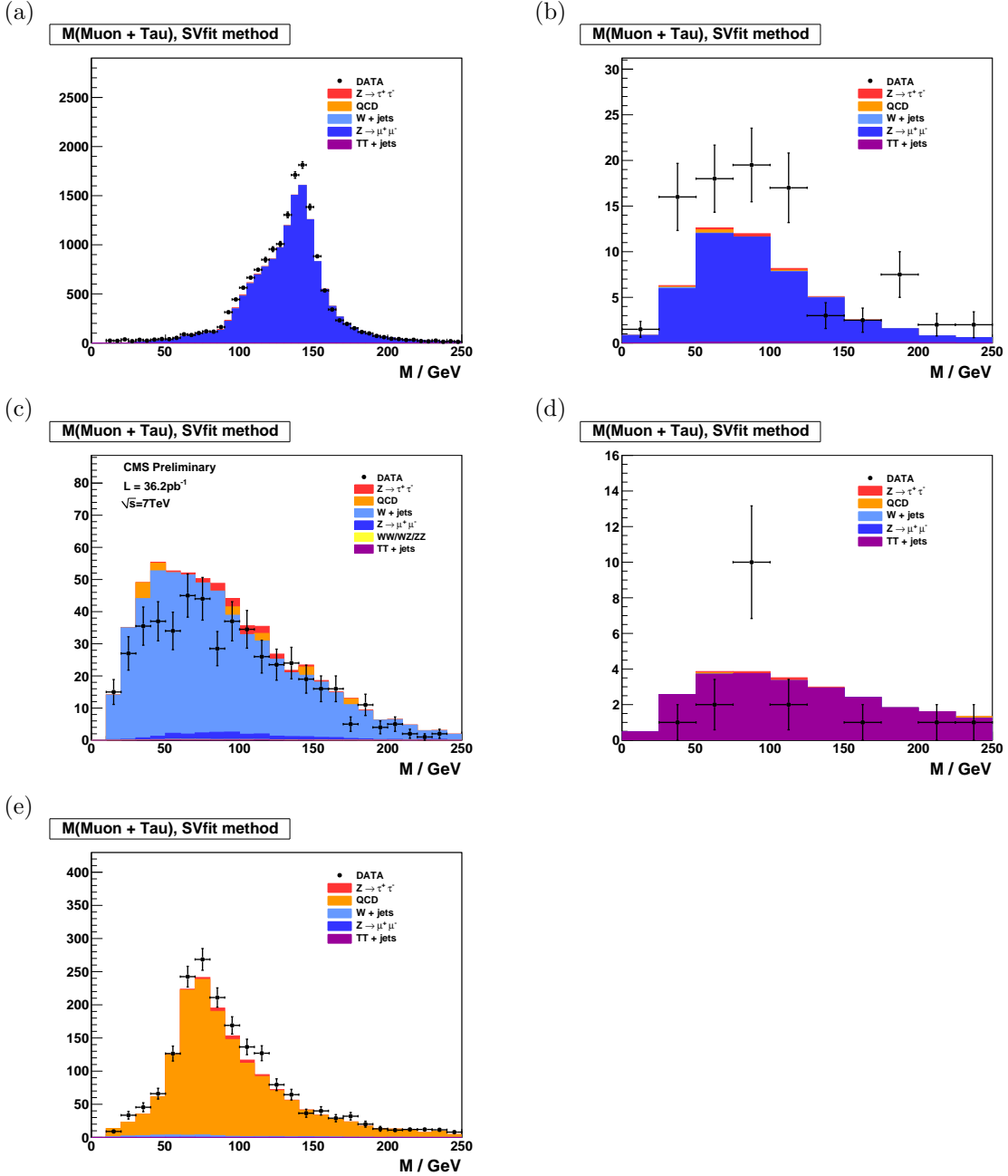


Figure 6.2: Distribution of “full” invariant mass reconstructed by the SVfit algorithm in the background enriched control samples for $Z \rightarrow \mu^+\mu^-$ (a) and (b), $W + \text{jets}$ (c), $t\bar{t} + \text{jets}$ (d) and QCD multi-jet (e) backgrounds. In (a) reconstructed tau-jet candidates are expected to be dominantly due to misidentified muons, while in (b) they are expected to be mostly due to misidentified misidentified quark or gluon jets.

1689 a simple method of computing the fake–rate, and a simpler¹ hadronic tau identification
 1690 algorithm. The closure test demonstrates that the method is self–consistent, and that the
 1691 fake–rate technique can be used to estimate the contributions of QCD, $W + \text{jets}$, $t\bar{t} + \text{jets}$
 1692 and $Z \rightarrow \mu^+\mu^-$ backgrounds. The analysis selections used in the closure test are almost
 1693 identical to the selections used in this analysis. Exact details of the selections can be found
 1694 in reference analysis [44]. The method is then extended to use fake–rates measured in data,
 1695 a multivariate method of computing the fake–rates, and the HPS + TaNC tau identification
 1696 algorithm used in this analysis.

1697 §6.2.1 Parameterization of Fake–rates

1698 Efficiencies and fake–rates of the tau identification algorithm based on requiring no tracks
 1699 of $p_T > 1$ GeV/ c and ECAL energy deposits of $p_T > 1.5$ GeV/ c reconstructed within
 1700 an “isolation cone” of size $\Delta R_{iso} = 0.5$ and outside of a “shrinking signal cone” of size
 1701 $\Delta R_{sig} = 5.0/E_T$ as it is used in the $Z \rightarrow \tau^+\tau^- \rightarrow \mu + \tau$ -jet analysis [44] are displayed
 1702 in Figure 6.3. In order to account for the visible p_T and η dependence, we parametrize
 1703 the fake–rates in bins of transverse momentum and pseudo–rapidity. As we will show in
 1704 Section 6.2.3, the parametrization of the fake–rates by p_T and η makes it possible to not
 1705 only estimate the total number of background events contributing to physics analyses, but
 1706 to model the distributions of kinematic observables with a precision that is sufficient to
 1707 extract information on the background shape.

We add a third quantity, the E_T -weighted jet–width R_{jet} , to the parametrization in order to account for differences between the fake–rates of quark and gluon jets, which on average have differing widths and different fake–rates. The jet width quantity R_{jet} is defined as

$$R_{jet} = \sqrt{E(\eta^2) + E(\phi^2)}$$

1708 where $E(\eta^2)$, $E(\phi^2)$ is the second η , ϕ moment of the jet constituents, weighted by con-
 1709 stituent transverse energy. Analyses performed by the CDF collaboration [40, 49, 46] found
 1710 that systematic uncertainties on background estimates obtained from the fake–rate method
 1711 are reduced in case differences between quark and gluon jets are accounted for in this way.

¹The closure test uses the “shrinking cone” tau identification algorithm, which is described briefly in Section 3.1. A full description can be found in [28].

1712 §6.2.2 Measurement of Fake–rates

Efficiencies and fake–rates are obtained by counting the fraction of tau–jet candidates passing all tau identification cuts and discriminators in a given bin² of p_T^{jet} , η_{jet} and R_{jet} :

$$P_{fr} \left(p_T^{jet}, \eta_{jet}, R_{jet} \right) := \frac{N_{jets} \left(p_T^{jet}, \eta_{jet}, R_{jet} | \text{tau ID passed} \right)}{N_{jets} \left(p_T^{jet}, \eta_{jet}, R_{jet} | \text{preselection passed} \right)} \quad (6.1)$$

1713 The pre–selection in the denominator of Equation 6.1 in general refers to p_T and η cuts,
 1714 which are applied with thresholds matching those applied on the final analysis level, but
 1715 may include loose tau identification criteria (which may be applied e.g. already during event
 1716 skimming). It is critical that the selection used in the denominator be identical to that of
 1717 the final analysis to ensure the fake–rates are not biased by different selections.

1718 Different sets of fake–rates are determined for the highest p_T and for the second highest
 1719 p_T jet in QCD di–jet events, for jets in a QCD event sample enriched by the contribution
 1720 of heavy quarks and gluons by requiring the presence of a muon reconstructed in the final
 1721 state, and for jets in “electroweak” events selected by requiring a W boson in the final state.

1722 §6.2.3 Application of Fake–rates

1723 Knowledge of the tau identification efficiencies and fake–rates as function of the parameters
 1724 p_T^{jet} , η_{jet} and R_{jet} as defined by Equation 6.1 is utilized to obtain an estimate for the con-
 1725 tributions of background processes to physics analyses involving tau lepton hadronic decays
 1726 in the final state. The basic idea is to replace tau identification cuts and discriminators by
 1727 appropriately chosen weights.

1728 Application of the fake–rate technique consists of two stages. The first stage consists of
 1729 loosening the tau identification cuts and discriminators and applying only the preselection
 1730 requirements defined by the denominator of Equation 6.1, in order to obtain an event
 1731 sample dominated by contributions of background processes. After disabling the selections
 1732 on hadronic tau identification, the relative contributions of the backgrounds are expected
 1733 to increase by the inverse of the (average) fake–rate, typically by a factor $\mathcal{O}(100)$. In the
 1734 second stage, weights are applied to all events in the background dominated control sample,
 1735 according to the probabilities $P_{fr} \left(p_T^{jet}, \eta_{jet}, R_{jet} \right)$ for jets to fake the signature of a hadronic

²The example presented in the closure tests bins the fake–rate calculation in bins of the parameterization variables. In Section 6.2.6 we describe a more robust multivariate method to compute the fake–rates.

1736 tau decay. After application of the weights, an estimate for the total number of background
 1737 events passing the tau identification cuts and discriminators and thus contributing to the
 1738 final analysis sample is obtained.

1739 The fake–rate technique works best if all background contributions to the analysis arise
 1740 from misidentification of quark and gluon jets as hadronic tau decays. Corrections to the
 1741 estimate obtained from the fake–rate technique are needed in case of background processes
 1742 contributing to the final analysis sample which either produce genuine tau leptons in the
 1743 final state (e.g. $t\bar{t} + \text{jets}$) or in which tau–jet candidates are due to misidentified electrons
 1744 or muons (e.g. $Z \rightarrow \mu^+\mu^-$, $Z \rightarrow e^+e^-$), as the latter may fake signatures of hadronic tau
 1745 decays with very different probabilities than quark and gluon jets.

1746 In the “simple” fake–rate method described in detail in the next section, the correc-
 1747 tions are taken from Monte Carlo simulations. Corrections based on Monte Carlo are needed
 1748 also to compensate for signal contributions to the background dominated control sample.
 1749 An alternative to Monte Carlo based corrections is to utilize additional information con-
 1750 tained in the background dominated control sample. The modified version is described in
 1751 Section 6.2.5. It has been used to estimate background contributions in searches for Higgs
 1752 boson production with subsequent decays into tau lepton pairs performed by the CDF col-
 1753 laboration in TeVatron Run II data [40, 49, 46]. We will refer to the modified version as
 1754 “CDF–type” method in the following.

1755 §6.2.4 “Simple” weight method

In the “simple” method all tau–jet candidates within the background dominated event sample are weighted by the probabilities of quark and gluon jets to fake the signature of a hadronic tau decay:

$$w_{jet}^{simple} \left(p_T^{jet}, \eta_{jet}, R_{jet} \right) := P_{fr} \left(p_T^{jet}, \eta_{jet}, R_{jet} \right) \quad (6.2)$$

1756 These weights are applied to all jets in the background dominated control sample which
 1757 pass the preselection defined by the denominator of Equation 6.1. Note that the weights
 1758 defined by Equation 6.2 can be used to estimate the contributions of background processes
 1759 to distributions of tau–jet related observables. They cannot be used as event weights.

In order to compare distributions of event level quantities or per-particle quantities for particles of types different from tau leptons decaying hadronically, event weights need to be defined. Neglecting the small fraction of background events in which multiple tau-jet candidates pass the complete set of all tau identification cuts and discriminators, event weights can be computed by summing up the per-jet weights defined by Equation 6.2 over all tau-jet candidates in the event which pass the preselection:

$$W_{\text{event}}^{\text{simple}} := \sum w_{\text{jet}}^{\text{simple}} \quad (6.3)$$

A bit of care is needed in case one wants to compare distributions of observables related to “composite particles” the multiplicity of which depends on the multiplicity of tau-jet candidates in the event (e.g. combinations of muon + tau-jet pairs in case of the $Z \rightarrow \tau^+ \tau^- \rightarrow \mu + \tau\text{-jet}$ analysis). Per-particle weights need to be computed for such “composite particles”, depending on $p_{\text{T}}^{\text{jet}}$, η_{jet} , R_{jet} of its tau-jet candidate constituent, according to:

$$w_{\text{comp-part}}^{\text{simple}}(p_{\text{T}}^{\text{jet}}, \eta_{\text{jet}}, R_{\text{jet}}) := w_{\text{jet}}^{\text{simple}}(p_{\text{T}}^{\text{jet}}, \eta_{\text{jet}}, R_{\text{jet}}) \quad (6.4)$$

Different estimates are obtained for the fake-rate probabilities determined for the high-
1760 est and second highest p_{T} jet in QCD di-jet events, jets in a muon enriched QCD sample
1761 and jets in $W + \text{jets}$ events. The arithmetic average of the four estimates of the closure test
1762 together with the difference between the computed average and the minimum/maximum
1763 value is given in Table 6.3.

We take the average value as “best” estimate of the background contribution and
1765 the difference between the average and the minimum/maximum estimate as its systematic
1766 uncertainty. We obtain a value of $\mathcal{O}(15\%)$ for the systematic uncertainty and find that
1767 the true sum of QCD, $W + \text{jets}$, $t\bar{t} + \text{jets}$ and $Z \rightarrow \mu^+ \mu^-$ background contributions agrees
1768 well with the “best” estimate obtained by the fake-rate method within the systematic
1769 uncertainty.
1770

Note that the estimate for the sum of background contributions which one obtains
1771 in case one applies the “simple” fake-rate weights defined by Equation 6.3 to a back-
1772 ground dominated control sample selected in data is likely to overestimate the true value
1773 of background contributions by a significant amount. The reason is that contributions of
1774 $Z \rightarrow \tau^+ \tau^-$ events with true taus are non-negligible. In fact, genuine tau contributions to
1775

1776 the background dominated control sample are expected to be 14.9% and since the per-
 1777 jet weights computed by Equation 6.2 are larger on average in signal than in background
 1778 events, the signal contribution increases by the weighting and amounts to 37.1% of the sum
 1779 of event weights computed by Equation 6.3 and given in Table 6.3.

1780 The contribution of the $Z \rightarrow \tau^+ \tau^-$ signal needs to be determined by Monte Carlo
 1781 simulation and subtracted from the estimate obtained by applying the “simple” fake–rate
 1782 method to data, in order to get an unbiased estimate of the true background contributions.

1783 §6.2.5 “CDF–type” weights

1784 Instead of subtracting from the estimate obtained for the sum of background contributions a
 1785 correction determined by Monte Carlo simulation, the genuine tau contribution contribution
 1786 to the background dominated event sample selected in data can be corrected for by adjusting
 1787 the weights, based solely on information contained in the analyzed data sample, avoiding
 1788 the need to rely on Monte Carlo based corrections.

1789 In the “CDF–type” method, additional information, namely whether or not tau–jet
 1790 candidates pass or fail the tau identification cuts and discriminators, is drawn from the data.
 1791 The desired cancellation of signal contributions is achieved by assigning negative weights to
 1792 those tau–jet candidates which pass all tau identification cuts and discriminators, i.e. to a
 1793 fair fraction of genuine hadronic tau decays, but to a small fraction of quark and gluon jets
 1794 only. The small reduction of the background estimate by negative weights assigned to quark
 1795 and gluon jets is accounted for by a small increase of the positive weights assigned to those
 1796 tau–jet candidates for which at least one of the tau identification cuts or discriminators
 1797 fails. In this way, an unbiased estimate of the background contribution is maintained.

To be specific, the “CDF–type” weights assigned to tau–jet candidates are computed
 as:

$$w_{jet}^{CDF}(p_T^{jet}, \eta_{jet}, R_{jet}) := \begin{cases} \frac{P_{fr}(p_T^{jet}, \eta_{jet}, R_{jet}) \cdot \varepsilon(p_T^{jet}, \eta_{jet}, R_{jet})}{\varepsilon(p_T^{jet}, \eta_{jet}, R_{jet}) - P_{fr}(p_T^{jet}, \eta_{jet}, R_{jet})} & \text{all tau ID passed} \\ \frac{P_{fr}(p_T^{jet}, \eta_{jet}, R_{jet}) \cdot (1 - \varepsilon(p_T^{jet}, \eta_{jet}, R_{jet}))}{\varepsilon(p_T^{jet}, \eta_{jet}, R_{jet}) - P_{fr}(p_T^{jet}, \eta_{jet}, R_{jet})} & \text{otherwise} \end{cases} \quad (6.5)$$

1798 For the derivation of Equation 6.5 for the “CDF–type” weights assigned to tau–jet candi-
 1799 dates, we will use the following notation: Let n_τ (n_{QCD}) denote the total number of tau–jets
 1800 (quark and gluon jets) in a certain bin of transverse momentum p_T^{jet} , pseudo–rapidity η_{jet}

1801 and jet-width R_{jet} and n_τ^{sel} (n_{QCD}^{sel}) denote the number of tau-jets (quark and gluon jets)
 1802 in that bin which pass all tau identification cuts and discriminators. By definition of the
 1803 tau identification efficiency $\varepsilon := \varepsilon(p_T^{jet}, \eta_{jet}, R_{jet})$ and fake-rate $f := f(p_T^{jet}, \eta_{jet}, R_{jet})$:

$$\begin{aligned} n_\tau^{sel} &= \varepsilon \cdot n_\tau \\ n_{QCD}^{sel} &= f \cdot n_{QCD}. \end{aligned} \quad (6.6)$$

Depending on whether or not a given tau-jet candidate passes all tau identification cuts and discriminators or not, we will assign a weight of value w_{passed} or w_{failed} to it. The values of the weights w_{passed} and w_{failed} shall be adjusted such that they provide an unbiased estimate of the background contribution:

$$w_{passed} \cdot f \cdot n_{QCD} + w_{failed} \cdot (1 - f) \cdot n_{QCD} \equiv n_{QCD}^{sel} = f \cdot n_{QCD} \quad (6.7)$$

while averaging to zero for genuine hadronic tau decays:

$$w_{passed} \cdot \varepsilon \cdot n_\tau + w_{failed} \cdot (1 - \varepsilon) \cdot n_\tau \equiv 0.$$

The latter equation yields the relation:

$$w_{passed} = -\frac{1 - \varepsilon}{\varepsilon} \cdot w_{failed}, \quad (6.8)$$

1804 associating the two types of weights. By inserting relation 6.8 into Equation 6.7 we obtain:

$$\begin{aligned} &-\frac{1 - \varepsilon}{\varepsilon} \cdot w_{failed} \cdot f \cdot n_{QCD} + w_{failed} \cdot (1 - f) \cdot n_{QCD} = f \cdot n_{QCD} \\ \Rightarrow &\left(\frac{-f + \varepsilon \cdot f + \varepsilon - f \cdot \varepsilon}{\varepsilon} \right) \cdot w_{failed} = f \\ \Rightarrow &w_{failed} = \frac{f \cdot \varepsilon}{\varepsilon - f} \end{aligned}$$

and

$$w_{passed} = -\frac{f \cdot (1 - \varepsilon)}{\varepsilon - f} \quad (6.9)$$

1805 which matches exactly Equation 6.5 for the ‘‘CDF-type’’ weights applied to tau-jet candidates given in Section 6.2.5.

1807 Event weights and the weights assigned to ‘‘composite particles’’ are computed in the
 1808 same way as for the ‘‘simple’’ weights, based on the weights assigned to the tau-jet candidates:

$$\begin{aligned} W_{event}^{CDF} &:= \Sigma w_{jet}^{CDF} \\ w_{comp-part}^{CDF}(p_T^{jet}, \eta_{jet}, R_{jet}) &:= w_{jet}^{CDF}(p_T^{jet}, \eta_{jet}, R_{jet}), \end{aligned} \quad (6.10)$$

1810 where the sums extend over all jets in the background dominated control sample which pass
 1811 the preselection defined by the denominator of Equation 6.1.

1812 The effect of the negative weights to compensate the positive weights in case the “CDF–
 1813 type” fake–rate method is applied to signal events containing genuine hadronic tau decays is
 1814 shown in Table 6.4 and illustrated in Figure 6.4. As expected, positive and negative weights
 1815 do indeed cancel in the statistical average.

1816 Figures 6.5, 6.6 and 6.7 demonstrate that an unbiased estimate of the background
 1817 contribution by the “CDF–type” weights is maintained. Overall, the estimates obtained
 1818 are in good agreement with the contributions expected for different background processes,
 1819 indicating that the adjustment of negative and positive weights works as expected for the
 1820 background as well.

1821 Results obtained by the “CDF–type” fake–rate method in the closure test are sum-
 1822 marized in Table 6.4, in which the total number of background events estimated by Equa-
 1823 tion 6.10 is compared to the true background contributions. The “best” estimate of the
 1824 background contribution obtained from the “CDF–type” method is again taken as the
 1825 arithmetic average of the estimates obtained by applying the fake–rate probabilities for
 1826 the highest and second highest p_T jet in QCD di–jet events, jets in a muon enriched QCD
 1827 sample and jets in $W + \text{jets}$ events. Systematic uncertainties are taken from the difference
 1828 between the computed average value and the minimum/maximum estimate. We obtain a
 1829 value of $\mathcal{O}(15 - 20\%)$ for the systematic uncertainty of the “CDF–type” method, slightly
 1830 higher than the systematic uncertainty obtained for the “simple” method. The small in-
 1831 crease of systematic uncertainties is in agreement with our expectation for fluctuations of
 1832 the jet–weights in case weights of negative and positive sign are used.

1833 §6.2.6 k–Nearest Neighbor Fake–rate Calculation

1834 For the fake–rate method to give correct results, care must be taken that the measured
 1835 fake–rate is well defined in all of the regions of phase space where it will be used. In the
 1836 closure test described above, the computation of the fake–rate was accomplished by binning
 1837 the numerator (tau ID passed) and denominator (tau ID passed and failed) distributions
 1838 in the three dimensions of the parameterizations. This method has the disadvantage that
 1839 the determination of the optimal binning is extremely difficult to determine, and that any

1840 bins with no entries in the denominator distribution caused the fake–rate to be undefined
 1841 in those regions.

To overcome these problems, the fake–rate parameterization is implemented by adapting a multivariate technique known as a k –Nearest Neighbor classifier (k NN). A k NN classifier is typically used to classify events by populating (“training”) an n –dimensional space with signal and background events. The probability for a given point x in the space to be “signal–like” is determined by finding the k nearest neighbors and computing the ratio

$$p_{sig} = \frac{n_{sig}}{n_{sig} + n_{bkg}}, \quad (6.11)$$

1842 where n_{sig} , n_{bkg} are the observed number of signal and background events, respectively. By
 1843 construction, $k = n_{sig} + n_{bkg}$. The principle of operation is illustrated in Figure 6.8.

1844 The classification feature of a k NN can be trivially adapted to parameterize an efficiency
 1845 (fake–rate) such that it is defined everywhere. Examining the form of Equation 6.11, it is
 1846 clear that by replacing n_{sig} with n_{passed} and n_{bkg} with n_{failed} , p_{sig} is equivalent to the tau–
 1847 fake rate. We thus “train” the k NN with tau–candidates which pass the tau identification as
 1848 signal events and those which fail as background events. The resulting classifier is a function
 1849 which returns the expected fake–rate for any point in the space of the parameterization.
 1850 The choice of k must be optimized. When k is low, the small number of neighbors causes
 1851 large counting fluctuations in the fake rate. If k is too large, the k NN effectively averages
 1852 over a large area of the space of the variables³. For the training statistics available in the
 1853 2010 data, $k = 20$ is found to be the optimal choice.

1854 §6.2.7 Results of Fake–Rate Background Estimation

1855 An independent estimate of the background contributions to the analysis presented in this
 1856 thesis is obtained by applying the fake–rate method in a manner analogous to the closure
 1857 test. Fake–rates in QCD multi–jet events (light quark enriched sample), QCD events con-
 1858 taining muons (heavy quark and gluon enriched sample) and $W +$ jets events are measured
 1859 in data [34, 48] and applied to events which pass all the event selection criteria listed in
 1860 Table 5.3, with the exceptions of

³In the limit $k \rightarrow \inf$, the k NN output reduces to a single number. In this extreme case, all information about the dependence of the fake–rate on the variables is lost.

- 1861 • the “loose” HPS + TaNC discriminator, and
 1862 • the requirement that the tau have unit charge.

1863 No assumption is made on the composition of $Z \rightarrow \mu^+ \mu^-$, $W + \text{jets}$, $t\bar{t} + \text{jets}$ and QCD
 1864 backgrounds contributing to the event sample selected by the analysis. Differences between
 1865 fake–rates obtained for QCD multi–jet, QCD muon enriched and $W + \text{jets}$ background
 1866 events are attributed as systematic uncertainties of the fake–rate method. Per jet and per
 1867 event weights have been computed by the “simple” and “CDF-type” weights as described in
 1868 the closure test and the results are found to be compatible within statistical and systematic
 1869 uncertainties. In the following, we present results for “CDF-type” weights. The “CDF-type”
 1870 weights have the advantage that the background estimate obtained does not change, whether
 1871 there is MSSM Higgs $\rightarrow \tau^+ \tau^-$ signal present in the data or not.

1872 Tau identification efficiencies need to be known when using “CDF-type” weights. Ded-
 1873 icated studies have checked the tau identification efficiencies in data [48]. Statistical and
 1874 systematic uncertainties of these studies are still sizeable at present, on the order of 20–30%.
 1875 No indication has been found, however, that the Monte Carlo simulation does not correctly
 1876 model hadronic tau decays in data. For the purpose of computing fake–rate weights via
 1877 the “CDF-type” method, tau identification efficiencies are taken from the Monte Carlo
 1878 simulation of hadronic tau decays in $Z \rightarrow \tau^+ \tau^-$ events. Systematic uncertainties on the
 1879 background estimate obtained by the fake–rate method are determined by varying the tau
 1880 identification efficiencies by $\pm 30\%$ relative to the value obtained from the Monte Carlo
 1881 simulation.

1882 The results of applying the fake–rate method to the mu + tau channel are summarized
 1883 in Table 6.5. The background prediction has been corrected for the expected⁴ contribution
 1884 of $13.1^{+2.8}_{-0.6}$ events from $Z \rightarrow \mu^+ \mu^-$ background events in which the reconstructed tau–jet is
 1885 due to a misidentified muon. The obtained estimate is in good agreement with the Monte
 1886 Carlo expectation.

1887 As an additional cross–check of the method, a sample of events containing a muon
 1888 plus a tau–jet of like–sign charge is selected in data and compared to the background

⁴The contribution of $Z \rightarrow \mu^+ \mu^-$ is estimated using a simulated sample.

1889 prediction obtained by applying the fake–rate method to the like–sign sample. The like–sign
 1890 sample is expected to be dominated by the contributions of $W + \text{jets}$ and QCD background
 1891 processes and allows to verify the fake–rate method in a practically signal free event sample.
 1892 The background estimate obtained by the fake–rate method is compared to the number of
 1893 events observed in the like–sign data sample in Table 6.6. The number of events expected
 1894 in the like–sign control sample from Monte Carlo simulation is indicated in the caption. All
 1895 numbers are in good agreement.

1896 The fake–rate method does not only allow to estimate the total number of background
 1897 events, but allows to model the distributions of background processes as well. The capability
 1898 to model distributions is illustrated in Figure 6.9, which shows good agreement between the
 1899 distributions observed in the like-sign data sample and the predictions obtained by the
 1900 fake–rate method for the distributions of muon plus tau–jet visible mass and of the “full”
 1901 invariant mass reconstructed by the SVfit algorithm.

Fixme: THIS
*IS FROM
 THE HPS
 NOTE!*

1902 §6.3 Template method

1903 Shape templates for the $\mu + \tau_{had}$ visible mass M_{vis} are obtained from data, using a set of
 1904 dedicated control regions which are chosen to select a high purity sample of one particular
 1905 background process each. The number of events selected in each control region and com-
 1906 parisons to the predictions from Monte Carlo simulations are summarized in Table 6.2. The
 1907 template M_{vis} shapes obtained from data in the background enriched control regions are
 1908 compared to the signal region shapes obtained by Monte Carlo simulation in Figure 6.10.
 1909 The M_{vis} spectrum observed in the final analysis is fitted to the sum of these templates. Es-
 1910 timates for background yields are obtained from the normalization factor of each template,
 1911 determined by the fit. Further details of the method can be found in [47] and [50].

1912 The TaNC (Section 3.3, [51]) discriminators used in [50] are replaced by the correspond-
 1913 ing discriminators of the HPS + TaNC algorithm (Section 3.5, [33]). The $Z/\gamma^* \rightarrow \tau^+\tau^-$ sig-
 1914 nal shape is obtained via the $Z/\gamma^* \rightarrow \mu^+\mu^-$ embedding technique [52]. The $\mu + \tau_{had}$ visible
 1915 mass spectrum observed in the final analysis is compared to the sum of template shapes
 1916 scaled by the normalization factors determined by the fit in Figure 6.11. The corresponding
 1917 estimates for background contributions are summarized in Table 6.7.

Requirement	$Z \rightarrow \mu^+ \mu^-$			Enriched background process		
	Muon fake	Jet fake	$W + \text{jets}$	$t\bar{t} + \text{jets}$	$W + \text{jets}$	QCD
Muon rel. iso.	< 0.15	< 0.1	< 0.1	< 0.1	< 0.1	> 0.10 $\&$ < 0.30
Muon Track IP	-	-	-	-	-	-
Tau TaNC discr.	-	1	1	medium passed	1	1
Tau 1 3-Prong	-	-	-	-	-	-
Charge(Tau) = ± 1	-	-	-	-	-	-
Tau μ -Veto	inverted	applied	applied	applied	applied	applied
Charge(Muon+Tau)	applied	-	-	-	-	-
M_T (Muon-MET)	-	< 40 GeV	-	-	-	< 40 GeV
$P_\zeta - 1.5 \cdot P_\zeta^{vis}$	> -20 GeV	-	-	-	-	> -20 GeV
global Muons	< 2	-	< 2	< 2	< 2	< 2
central Jet Veto	-	-	2	-	-	-
b-Tagging	-	-	-	3	-	-

¹ vloose passed $\&$ loose failed ² no Jets of $E_T > 20$ GeV within $|\eta| < 2.1$ (other than the τ -jet candidate) ³ min. two Jets of $E_T > 40$ GeV, at least one of which was at least of which with “TrackCountingHighEff” discriminator > 2.5

Table 6.1: Criteria to select events in different background enriched control samples. Hyphens indicate event selection criteria which are not applied.

Enriched Selection	Data	Σ_{SM}	Contribution from				Purity
			$Z \rightarrow \tau^+ \tau^-$	$Z \rightarrow \mu^+ \mu^-$	$W + \text{jets}$	$t\bar{t} + \text{jets}$	
$Z \rightarrow \mu^+ \mu^-$							
Muon fake	15156	17109.8	331.6	16586.6	55.1	80.4	35.0
Jet fake	85	62.7	2.5	55.5	0.5	1.4	2.4
$W + \text{jets}$	514	642.4	17.9	22.9	581.7	0.8	16.7
$t\bar{t} + \text{jets}$	26	39.7	0.7	< 0.1	0.6	38.4	< 1.0
QCD	2510	2571.8	16.6	0.8	9.3	1.6	2543.4
							98.9%

Table 6.2: Number of events observed in the different background enriched control samples compared to Monte Carlo expectations. Σ_{SM} denotes the sum of $Z \rightarrow \tau^+ \tau^-$, $Z \rightarrow \mu^+ \mu^-$, $W + \text{jets}$ and QCD processes. The expected purity of each control sample is computed as the ratio of contribution of the enriched process to Σ_{SM} .

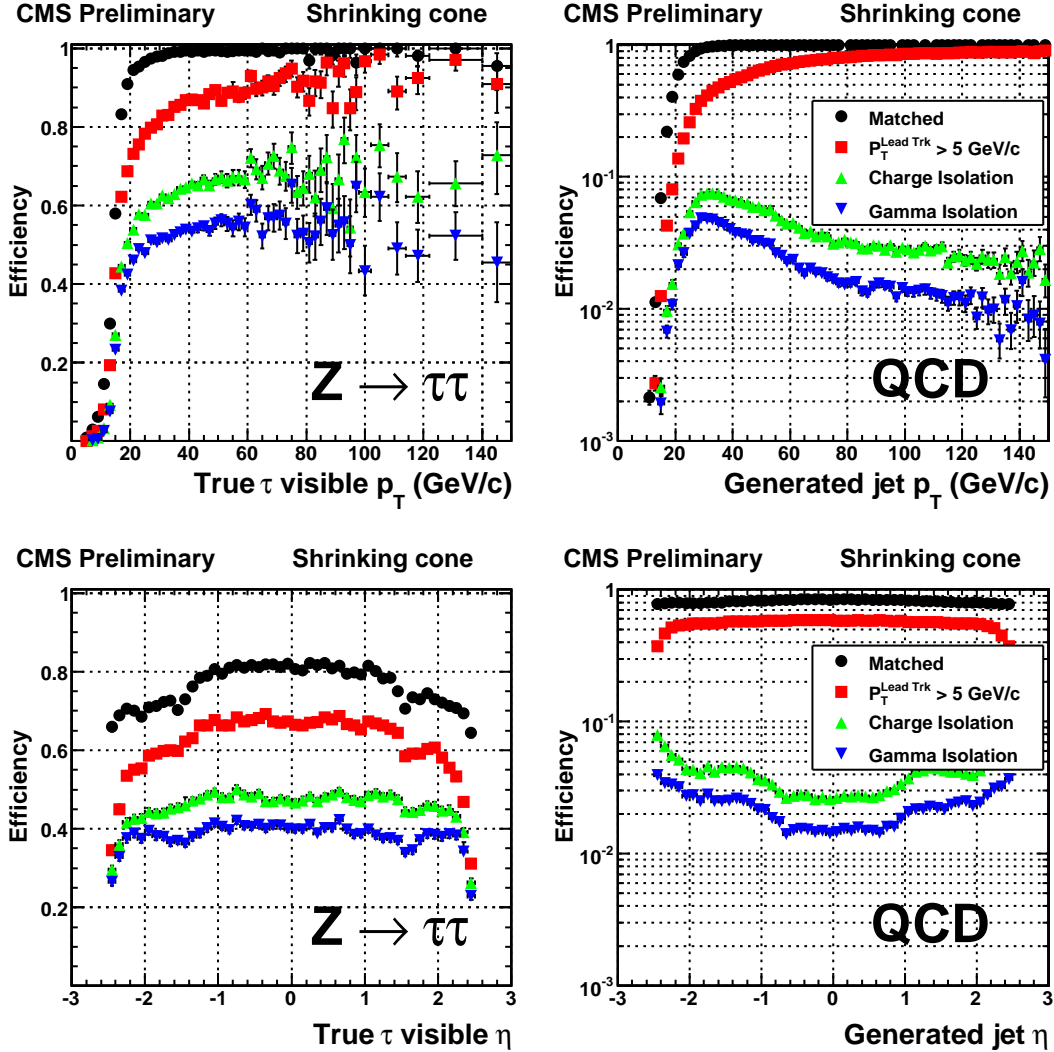


Figure 6.3: Cumulative efficiencies (left) and fake-rates (right) of successively applied tau identification cuts of the “shrinking signal cone” particle-flow based tau identification algorithm described in [28] as function of p_T^{jet} (top) and η^{jet} (bottom) of tau-jet candidates. The efficiencies/fake-rates for the complete set of tau identification criteria are represented by the blue (downwards facing) triangles.

Background Process	Expectation	Estimate obtained by applying weights of type:			Average fake-rate estimate
		QCD lead jet	QCD second jet	QCD μ -enriched	
W+jets	163.0 ± 7.1	157.2 ± 2.8	140.9 ± 2.7	129.9 ± 2.5	177.9 ± 3.2
QCD	246.4 ± 31.8	269.2 ± 14.0	246.5 ± 14.3	219.7 ± 11.8	300.8 ± 15.2
t <bar>t>+jets</bar>	12.2 ± 0.6	14.3 ± 0.3	12.6 ± 0.3	11.6 ± 0.3	16.5 ± 0.3
Z → $\mu^+ \mu^-$	68.6 ± 2.9	58.2 ± 1.3	51.2 ± 1.2	48.5 ± 1.1	65.8 ± 1.4
Σ Background	490.4 ± 32.7	499.9 ± 14.4	451.2 ± 14.6	409.7 ± 12.1	561.1 ± 15.6
Z → $\tau^+ \tau^-$	—	284.3 ± 3.7	269.0 ± 3.9	256.5 ± 3.3	325.3 ± 4.2

Table 6.3: Number of events from W+jets, QCD, tt>+jets and Z → $\mu^+ \mu^-$ background processes expected to pass all selection criteria of the Z → $\tau^+ \tau^- \rightarrow \mu^+ \tau^-$ cross-section analysis compared to the estimates obtained by weighting events in the background dominated control sample with the “simple” fake-rate weights defined by Equation 6.3.

Background Process	Expectation	Estimate obtained by applying weights of type:				Average fake-rate estimate
		QCD lead jet	QCD second jet	QCD μ -enriched	$W + \text{jets}$	
$W + \text{jets}$	163.0 ± 7.1	163.2 ± 3.8	140.6 ± 3.4	128.0 ± 3.1	188.3 ± 4.2	$155.0^{+33.6}_{-27.3}$
QCD	246.4 ± 31.8	300.5 ± 19.5	266.1 ± 19.0	236.0 ± 16.4	335.1 ± 20.4	$284.4^{+55.5}_{-52.0}$
$t\bar{t} + \text{jets}$	12.2 ± 0.6	13.1 ± 0.3	11.5 ± 0.3	10.2 ± 0.3	15.4 ± 0.4	$12.6^{+2.8}_{-2.4}$
$Z \rightarrow \mu^+\mu^-$	68.6 ± 2.9	52.7 ± 1.4	46.7 ± 1.4	41.9 ± 1.2	60.3 ± 1.6	$50.4^{+10.1}_{-8.6}$
Σ Background	490.4 ± 32.7	529.5 ± 19.9	464.9 ± 19.3	416.1 ± 16.8	599.1 ± 20.9	$502.4^{+99.4}_{-88.4}$
$Z \rightarrow \tau^+\tau^-$	–	0.3 ± 2.4	-10.6 ± 2.5	3.8 ± 2.0	-10.8 ± 2.8	$-4.3^{+8.4}_{-7.2}$

Table 6.4: Number of events from $W + \text{jets}$, QCD, $t\bar{t} + \text{jets}$ and $Z \rightarrow \mu^+\mu^-$ background processes expected to pass all selection criteria of the closure test compared to the estimates obtained by weighting events in the background dominated control sample with the “CDF-type” fake-rate weights defined by Equation 6.10.

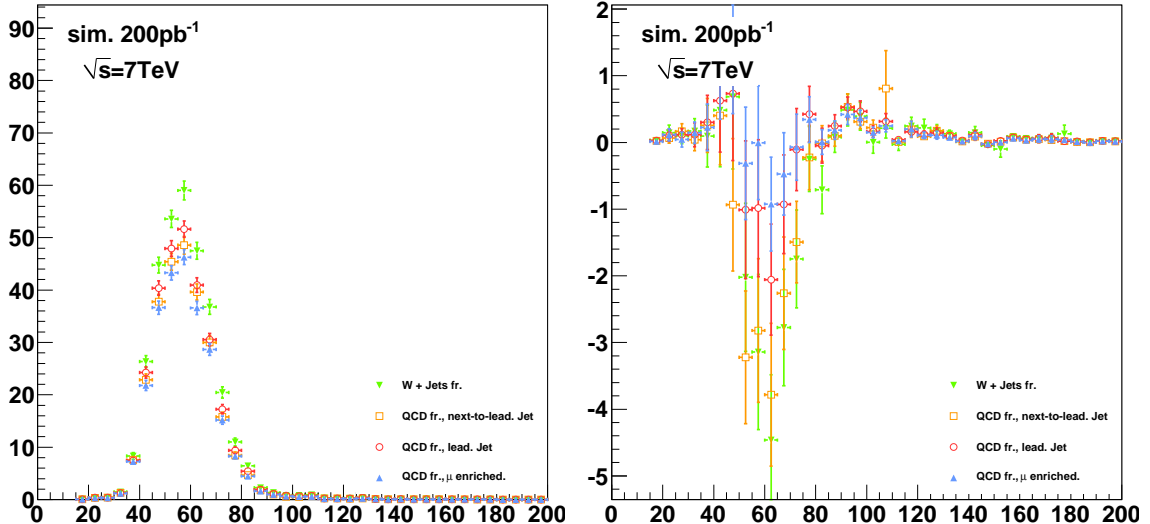


Figure 6.4: Distributions of visible invariant mass of muon plus tau-jet in $Z \rightarrow \tau^+\tau^-$ signal events weighted by “simple” weights computed according to Equation 6.4 (left) and “CDF-type” weights computed according to Equation 6.10 (right). The signal contribution to the background estimate computed by the “simple” method is non-negligible and needs to be corrected for. The “CDF-type” weights achieve a statistical cancellation of positive and negative weights, such that the total signal contribution averages to zero, avoiding the need for Monte Carlo based corrections.

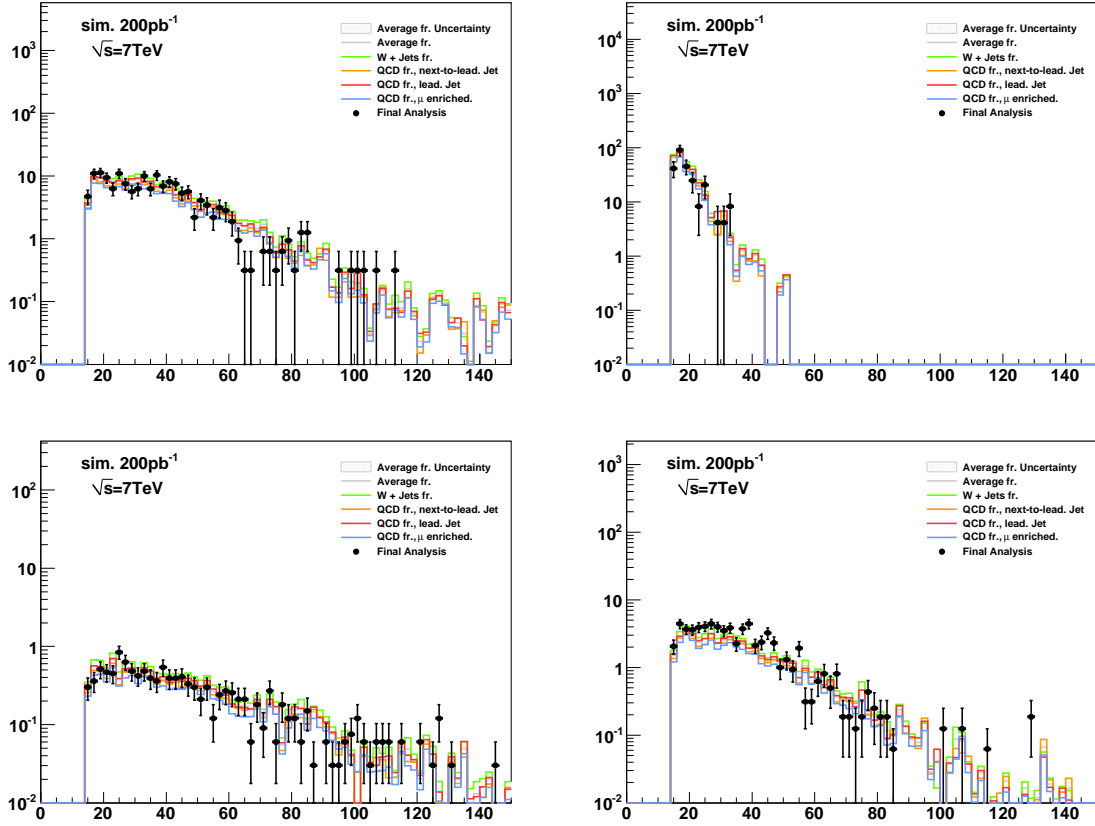


Figure 6.5: Distributions of muon transverse momentum in $W + \text{jets}$ (top left), QCD (top right), $t\bar{t} + \text{jets}$ (bottom left) and $Z \rightarrow \mu^+\mu^- \rightarrow \mu + \tau\text{-jet}$ cross-section analysis [44] compared to the estimate obtained from the “CDF method” fake-rate technique, computed according to Equation 6.10. The expected contribution of background processes is indicated by points. Lines of different colors represent the estimates obtained by applying fake-rate weights determined for different compositions of light quark, heavy quark and gluon jets, as described in Section 6.2.1. The maximum (minimum) estimate is interpreted as upper (lower) bound. The difference between the bounds is taken as systematic uncertainty on the estimate obtained from the “CDF-type” fake-rate method and is represented by the gray shaded area.

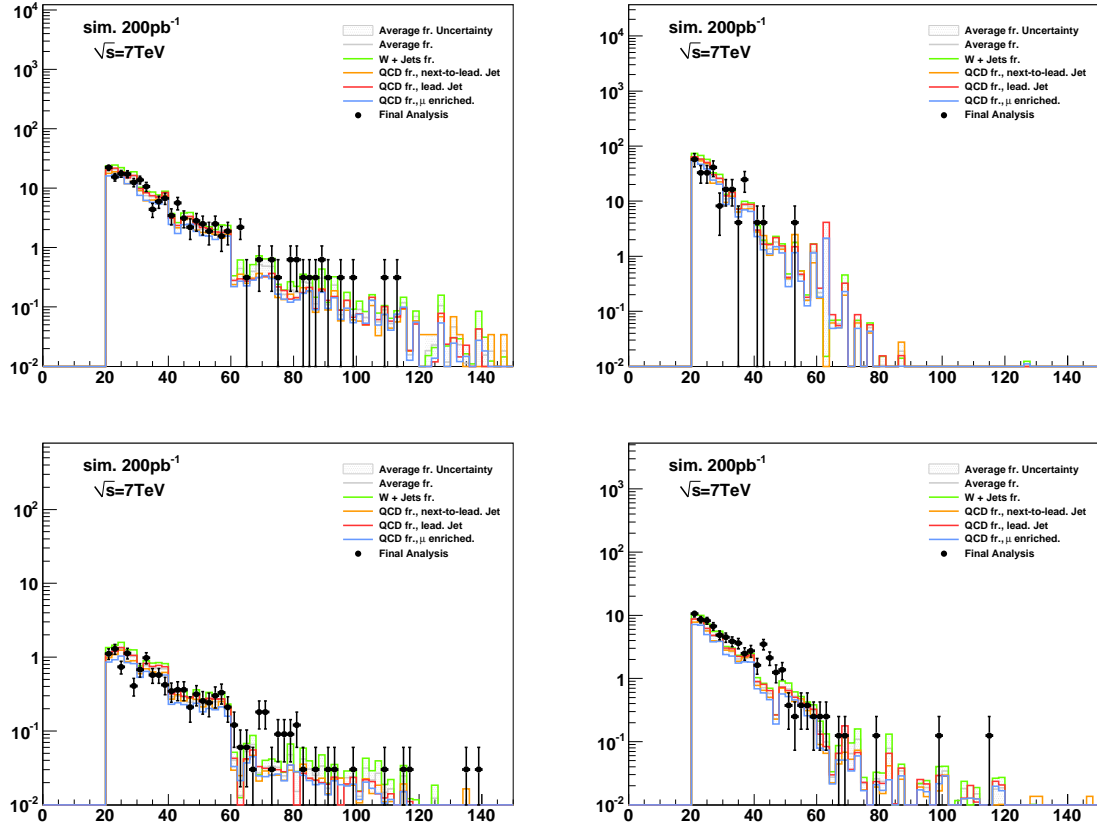


Figure 6.6: Distributions of transverse momenta of the tau–jet candidates in $W + \text{jets}$ (top left), QCD (top right), $t\bar{t} + \text{jets}$ (bottom left) and $Z \rightarrow \mu^+ \mu^-$ (bottom right) background events which pass all selection criteria of the $Z \rightarrow \tau^+ \tau^- \rightarrow \mu + \tau$ -jet cross-section analysis compared to the estimate obtained from the fake–rate technique, computed according to Equation 6.5. The expected contribution of background processes is indicated by points. Lines of different colors represent the estimates obtained by applying fake–rate weights determined for different compositions of light quark, heavy quark and gluon jets, as described in Section 6.2.1. The maximum (minimum) estimate is interpreted as upper (lower) bound. The difference between the bounds is taken as systematic uncertainty on the estimate obtained from the “CDF–type” fake–rate method and is represented by the gray shaded area.

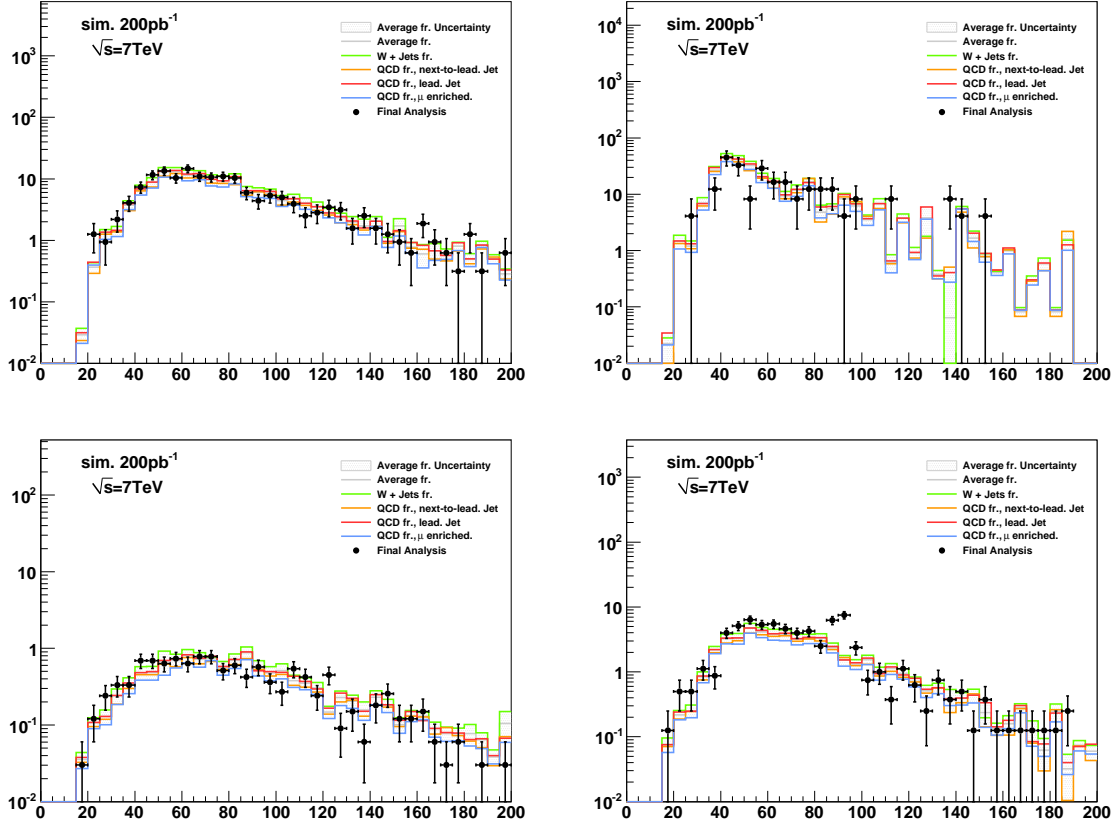


Figure 6.7: Distributions of the visible invariant mass of muon plus tau-jet in $W + \text{jets}$ (top left), QCD (top right), $t\bar{t} + \text{jets}$ (bottom left) and $Z \rightarrow \mu^+ \mu^-$ (bottom right) background events which pass all selection criteria of the closure test analysis compared to the estimate obtained from the fake-rate technique, computed according to Equation 6.10. The expected contribution of background processes is indicated by points. Lines of different colors represent the estimates obtained by applying fake-rate weights determined for different compositions of light quark, heavy quark and gluon jets, as described in Section 6.2.1. The maximum (minimum) estimate is interpreted as upper (lower) bound. The difference between the bounds is taken as systematic uncertainty on the estimate obtained from the “CDF-type” fake-rate method and is represented by the gray shaded area.

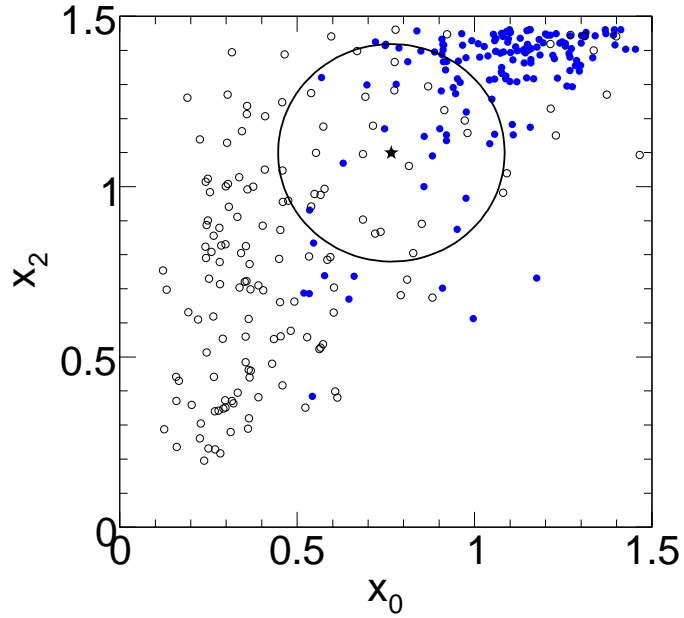


Figure 6.8: Example of the operation of a k NN classifier. The closest $k = 50$ neighbors (those inside the circle) to a test point (indicated by the star marker) are selected. The probability that the star marker is a signal event is given the number of signal neighbors (blue markers) in the circle divided by k . Image credit: [30]

Events weighted by:	Estimate
QCD lead jet	$202.1^{+14.9}_{-74.8}$
QCD second jet	$198.0^{+22.8}_{-79.3}$
QCD μ -enriched	$213.3^{+17.7}_{-82.6}$
$W + \text{jets}$	$232.8^{+21.1}_{-95.0}$
N_{bgr} estimate	$236.1^{+24.1}_{-65.9}$

Table 6.5: Estimate for background contributions obtained by weighting events passing all selection criteria listed in Table 5.3 except for the requirement for tau-jet candidates to pass the “medium” tight TaNC discriminator and have unit charge by fake-rates measured in QCD multi-jet, QCD muon enriched and $W + \text{jets}$ data samples.

Events weighted by:	Estimate
QCD lead jet	$191.7^{+2.3}_{-17.9}$
QCD second jet	$185.1^{+6.0}_{-21.1}$
QCD μ -enriched	$194.7^{+2.0}_{-20.5}$
$W + \text{jets}$	$208.9^{+0.5}_{-14.4}$
Fake-rate estimate	$201.8^{+14.2}_{-18.9}$
Observed	223

Table 6.6: Number of events observed in like-sign control region compared to the estimate obtained by fake-rate method.

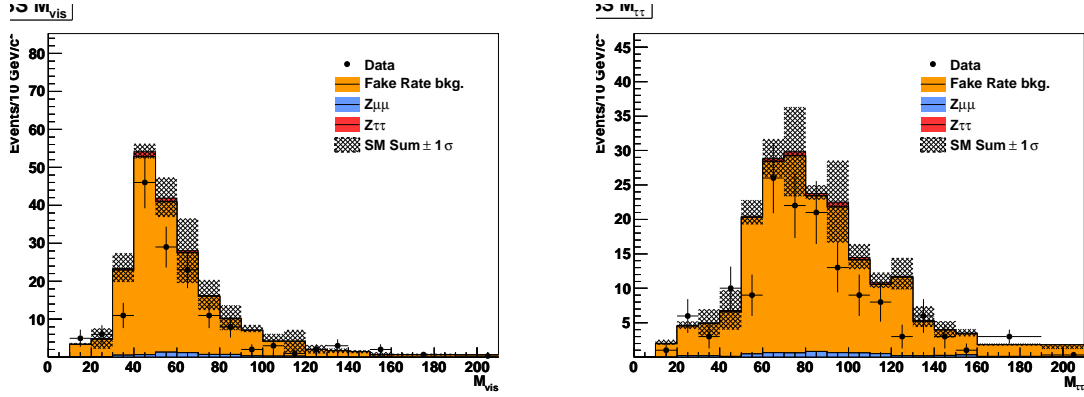


Figure 6.9: Distribution of visible mass (left) and “full” invariant mass reconstructed by the SVfit algorithm (right) observed in the like-sign charge control region compared to the background estimate obtained by the fake-rate method.

Process	Estimate
$Z \rightarrow \mu^+ \mu^-$	
Muon fake	5.7 ± 6.0
Jet fake	< 14.5
$W + \text{jets } t\bar{t} + \text{jets}$	7.6 ± 6.9
QCD	141.3 ± 40.4
N_{bgr} estimate	226.5 ± 33.1

Table 6.7: Estimated contributions of individual background processes to the signal region, obtained via the template method. As the shapes are very similar, the normalization factors for QCD and $W + \text{jets}$ background processes are anti-correlated. As a consequence, the sum of background contributions is determined by the fit more precisely than the individual contributions.

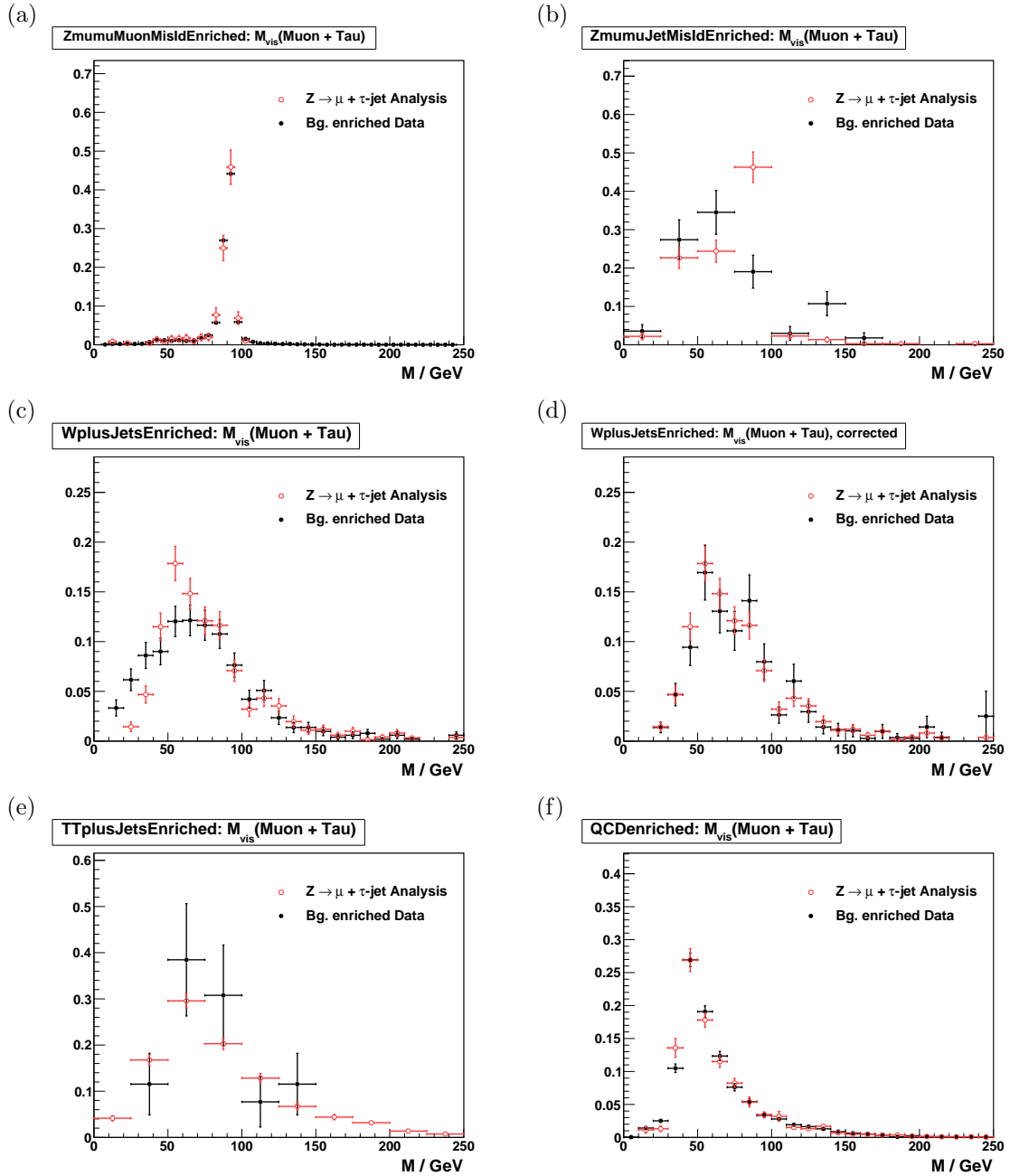


Figure 6.10: $\mu + \tau_{had}$ shape templates obtained from $Z \rightarrow \mu^+\mu^-$ (a) and (b), $W + \text{jets}$ before (c) and after (d) the bias correction explained in Section 6.3, $t\bar{t} + \text{jets}$ (e) and QCD multi-jet (f) backgrounds enriched control regions compared to the expected distribution of the enriched background process to the signal region, predicted by Monte Carlo simulations. In (a) reconstructed tau-jet candidates are expected to be dominantly due to misidentified muons, while in (b) they are expected to be mostly due to misidentified quark or gluon jets.

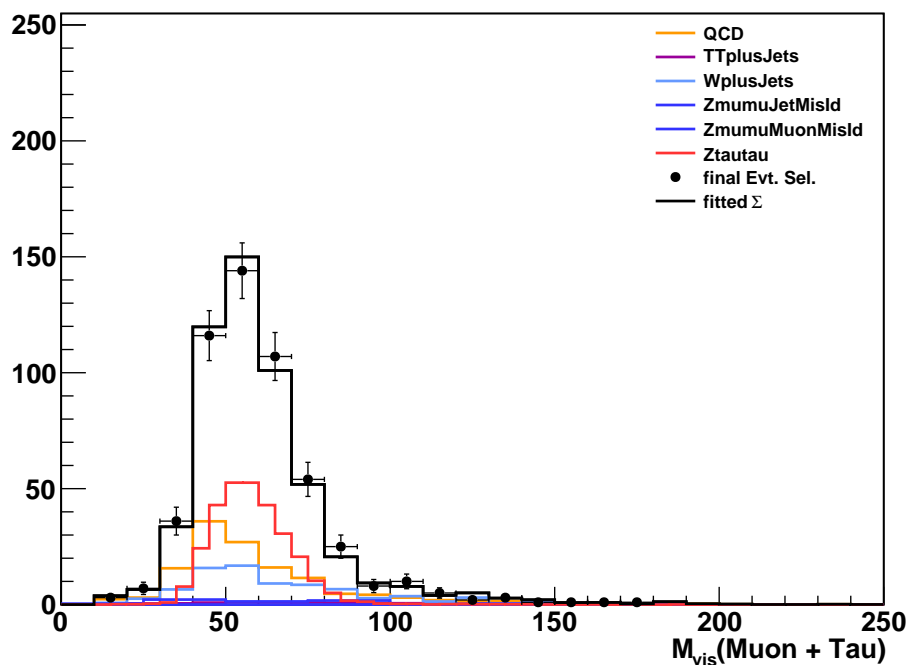


Figure 6.11: M_{vis} distribution of events selected by the $Z/\gamma^* \rightarrow \tau^+\tau^- \rightarrow \mu + \tau_{had}$ cross-section analysis compared to the sum of shape templates for signal and background processes scaled by the normalization factors determined by the fit.

1918

Chapter 7

1919

Monte Carlo Corrections

1920 One of the most important goals of the analysis is to minimize the effect of potentially
 1921 incorrect simulation effects on the final result. While the simulated CMS events have been
 1922 observed to match the 2010 data with surprising results, it is nonetheless critical to measure
 1923 in real data phenomenon which can have significant effects on the analysis whenever possible.
 1924 In practice, these measurements are used to apply a correction factor to the corresponding
 1925 measurement obtained from Monte Carlo. This measured correction factor has an associ-
 1926 ated uncertainty, and is taken into account as a systematic uncertainty. The application of
 1927 systematic uncertainties is described in the next chapter.

1928 The corrections measured and used in this analysis can be divided into two categories,
 1929 efficiency corrections and scale corrections. Identification efficiency corrections scale the
 1930 expected yield (due to a given identification selection) up or down. Scale corrections sys-
 1931 tematically scale the energy of a particle (or E_T^{miss}) up or down. In this analysis we apply
 1932 efficiency corrections for the High Level Trigger muon requirement, all stages of muon iden-
 1933 tification, and the hadronic tau identification. We apply a momentum scale correction to
 1934 the muon and tau legs, and to the resolution of the E_T^{miss} . Finally, events are simulated with
 1935 overlapping “pile-up”¹ events. The simulated events are weighted such that the number of
 1936 pile-up events in the simulation matches that observed in the data.

1937 §7.1 Muon Identification Efficiency

1938 The identification efficiencies associated with the muon are measured in $Z \rightarrow \mu^+ \mu^-$ events
 1939 using the “tag and probe” technique [44]. $Z \rightarrow \mu^+ \mu^-$ events are selected from the Muon

¹A pile-up event occurs when there are multiple interactions in one bunch proton bunch crossing. Pile-up increases with the instantaneous luminosity provided by the collider.

1940 7 TeV CMS 2010 datasets² by requiring that the events pass the “loose” Vector Boson Task
 1941 Force (VBTF) event selections [44]. In the selected events, we define the “tag” muons as
 1942 those that have transverse momentum greater than 15 GeV/c and pass the VBTF muon
 1943 selection. The tag muons are further required to pass the “combined relative isolation” de-
 1944 scribed in the VBTF paper. We finally require that the tag muon be matched to an HLT
 1945 object corresponding to the run-dependent requirements listed in Table 5.1. The trigger
 1946 match requirement ensures that the event would be recorded independently of the probe
 1947 muon. After the tag and probe muon pairs have been collected, we compare the muon identi-
 1948 fication performance in the probe collection in events selected in data to the performance in
 1949 simulated $Z \rightarrow \mu^+ \mu^-$ events. The selection of events and tag muon in the simulated sample
 1950 is the same as the data sample, with the notable exception that the only HLT requirement
 1951 applied in MC is that the tag muon is matched to an HLT_Mu9 object. Any difference in ef-
 1952 ficiency between the HLT_Mu9 path and the paths used to select the data (in the tag–probe
 1953 measurement and in the analysis) will be considered implicitly in the correction factor.

1954 The efficiencies for the muon selections applied in this analysis are measured using
 1955 the “probe” objects. We measure the following marginal efficiencies, each relative to the
 1956 previous requirement:

- 1957 • Efficiency of global probe muons to satisfy VBTF muon identification selections.
- 1958 • Efficiency of global probe muons passing the VBTF muon identification selection to
1959 satisfy the isolation criteria described in Section 5.2.1.
- 1960 • Efficiency of probe muons passing the offline analysis selection defined in Chapter 5
1961 to pass the HLT selection.

1962 In each case, the invariant mass spectrum of the tag–probe pair is fitted with a Crystal
 1963 Ball function for the signal ($Z \rightarrow \mu^+ \mu^-$) events and an exponential for the background.
 1964 The fit is done for two cases; where the probe fails the selection and the where it passes.
 1965 The method is illustrated in Figure 7.1. The signal yield N is extracted from each fit and
 1966 the efficiency is computed as $N_{\text{pass}}/(N_{\text{pass}} + N_{\text{fail}})$. Each efficiency is measured in both the

²/Mu/Run2010A-Sep17ReReco²/RECO and /Mu/Run2010B-PromptReco-v2/RECO

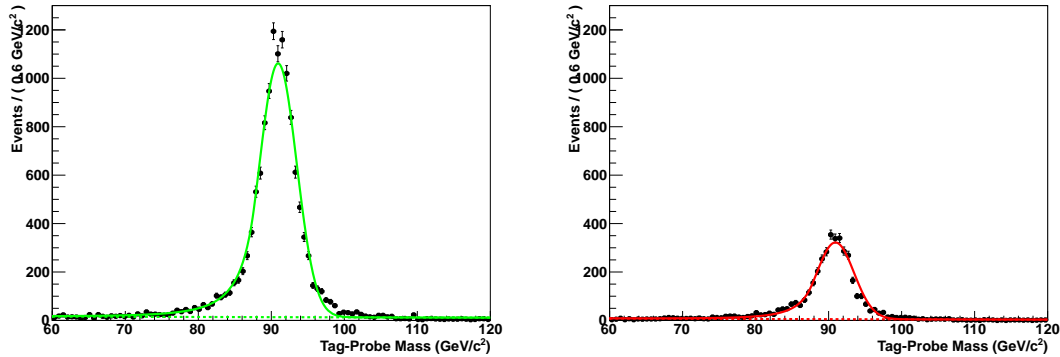


Figure 7.1: The tag–probe dimuon invariant mass spectrum in events in which the probe muon passed (left) and failed (right) the muon isolation requirement. The solid line gives the result of a simultaneous fit of the signal ($Z \rightarrow \mu^+ \mu^-$ events) and background. The fitted background contribution is shown as the dotted line. The muon isolation efficiency is then extracted from the number of signal events in the passing and failing bins.

1967 data and the simulation. The results of the measurements are shown in Table 7.1. In the
 1968 final analysis, the simulated events are weighted by the fractional difference to the measured
 1969 values; the statistical uncertainty on the weight is taken as the sum in quadrature of the
 1970 statistical uncertainties for the data and simulation efficiency measurements. The uncer-
 1971 tainty on this measurement is taken as systematic uncertainty in the final measurement.
 1972

1973 The correction for the trigger efficiency needs to take into account the differences in
 1974 the HLT selections applied during different operating periods (see Table 5.1). To determine
 1975 the overall correction factor, we measure the trigger efficiency in data for each of the op-
 1976 erating periods and compare it to the simulated efficiency of the HLT_Mu9 selection. The
 1977 overall efficiency in data is taken as the average of the three periods, weighted by integrated
 1978 luminosity.

1979 The efficiency of the “cross–triggers” used in the run–range period 148822 – 149182
 1980 (period C) cannot be measured in $Z \rightarrow \mu^+ \mu^-$ events as they require a reconstructed PFTau
 1981 object at the trigger level. A single muon trigger (HLT_Mu15) is also used in period C.
 1982 The contribution of the cross–triggers is taken as a correction to the single muon trigger
 1983 period C efficiency. The “muon leg” of the cross–triggers have the same requirements as
 1984 the single muon triggers used in the run–range 147196 – 148058 (period B). The “cross–

Muon selection	Efficiency		Ratio	Corection
	Data	Simulation		
VBTF identification	$99.2^{+0.1\%}_{-0.1\%}$	$99.1^{+0.1\%}_{-0.1\%}$	$1.001^{+0.001}_{-0.001}$	1.0
Particle Isolation	$76.8^{+0.4\%}_{-0.4\%}$	$78.3^{+0.3\%}_{-0.3\%}$	$0.981^{+0.006}_{-0.006}$	0.98
Trigger	$95.0^{+0.5\%}_{-0.5\%}$	$96.5^{+0.1\%}_{-0.2\%}$	$0.984^{+0.006}_{-0.006}$	0.98

Table 7.1: Efficiency of the various global muon selections applied in the analysis measured in data and simulated $Z \rightarrow \mu^+\mu^-$ events. The “correction” column gives the event weight correction applied to the simulated events in the final analysis. The efficiency for each selection is the marginal efficiency with respect to the selection in the row above it.

trigger” contribution is estimated as the difference between the efficiency in period B and the single-muon period C efficiency multiplied by a correction factor of $0.9 \pm 10\%$ to account for the τ leg efficiency. In the case that the measured single-muon period C efficiency is larger than the period B efficiency (due to statistical fluctuations and improvements in the trigger system), the period B efficiency is increased by 2%.

§7.2 Hadronic Tau Identification Efficiency

The hadronic tau identification efficiency has been measured in 2010 7 TeV CMS data. The most straight forward to measure the tau ID efficiency would be to use a resonance which decays to taus and has a known cross section. One could then measure the tau ID efficiency in by comparing the observed yield N_{obs} in data with that expected from the known cross section, according to the cross section equation,

$$\varepsilon = \frac{N_{\text{obs}} - N_{\text{bkg}}}{\mathcal{L} \times \mathcal{A} \times \sigma \times \text{BR}_\tau}.$$

The only suitable resonance for this method is $Z \rightarrow \tau^+\tau^-$. This method has been applied³ in the CMS $Z \rightarrow \tau^+\tau^-$ cross section analysis ??, and measured a tau identification simulation to data correction factor of 0.960 ± 0.067 .

³Actually, a slightly more complicated method is used. The analysis uses three decay channels, and the $Z \rightarrow \tau^+\tau^-$ cross section and tau identification correction factors are fitted simultaneously. The central value of the $Z \rightarrow \tau^+\tau^-$ cross section is driven by the $Z \rightarrow \tau^+\tau^- \rightarrow e\mu$ channel, which is independent of the hadronic tau identification.

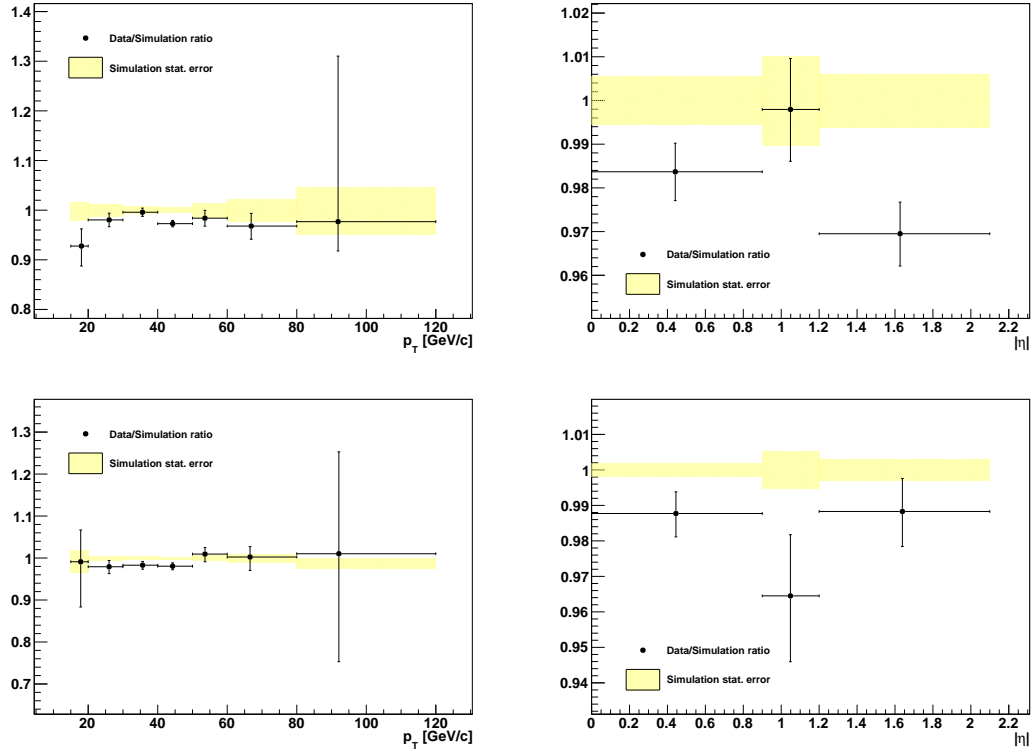


Figure 7.2: Ratio of muon isolation efficiency (top) and HLT trigger efficiency (bottom) measured in data compared to simulated $Z \rightarrow \mu^+\mu^-$ events. The correction factors are measured in bins of p_T (left) and η . In the analysis, the correction factors are taken to be flat.

Unfortunately, this method cannot be used in this analysis. The measurement using the Z resonance operates on the assumption there is no new physics contribution to the events in the Z bump. In the case that there was a Higgs signal at $m_{A^0} = 90$ GeV/ c^2 , it would be indistinguishable from the Z and would appear as an increase of N_H in the observed yield. The analysis would be completely insensitive to a Higgs boson on the Z peak, and cause the efficiency to be overestimated by a factor

$$\delta\varepsilon = \frac{N_H}{\mathcal{L} \times \mathcal{A} \times \sigma \times \text{BR}_\tau}.$$

The solution to this problem is to use a “tag and probe” approach analogous to the 1994 muon efficiency measurement of Section 7.1. The tag and probe method is only sensitive to 1995 the shapes of the distributions, and is independent of a Higgs contribution to the Z peak. 1996 This measurement has been performed by the CMS Tau Physics Object Group [48]. A 1997 loose hadronic tau preselection is applied to events which pass the selections (excluding the 1998

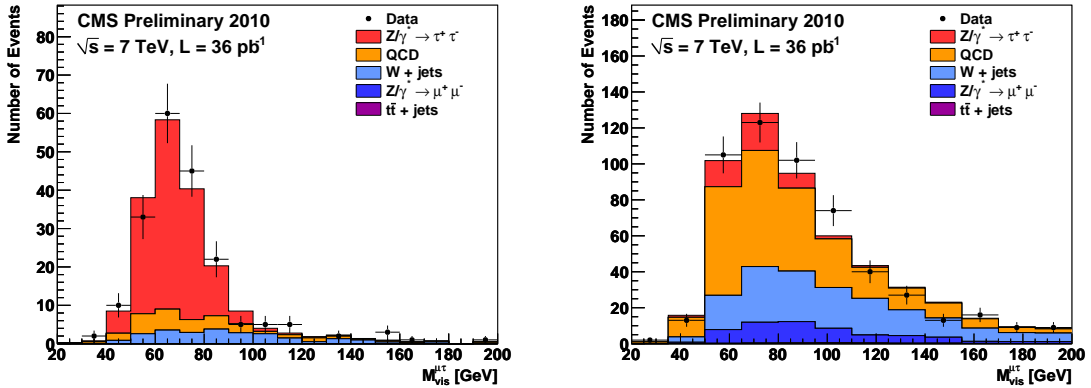


Figure 7.3: Visible mass spectrum of preselected events used to measure the hadronic tau identification efficiency in 2010 CMS 7 TeV data. The figure on the left (right) shows the preselected events that pass (fail) the hadronic tau identification. The different colors indicate the fitted yields of the different signal and background contributions. Reference: [48].

hadronic tau identification) of the CMS EWK $Z \rightarrow \tau^+\tau^-$ cross section measurement [53].
 The preselected sample is then split into two categories, those that pass the hadronic tau identification and those that fail. The signal and background yields in each category are fitted using the Template Method described in Section 6.3. An illustrative example of the fits for the yields is shown in Figure 7.3. The hadronic tau identification efficiency can then be computed using the relative size of the true tau yields in the passing and failing categories. The efficiency is measured [48] for the loose HPS + TaNC tau identification in the 2010 CMS dataset and is found to be 1.06 ± 0.30 .

§7.3 Muon and Tau Momentum Scale

Muons are one of the best measured objects at CMS. The momentum scale of CMS muons has been measured [54] using the J/ψ , $\psi(2S)$ and Υ di-muon resonant decays. The muon momentum resolution is found to be 3% or better for muons with $p_T < 100$ GeV/ c . We apply the muon momentum correction using the ‘‘MuSICleFit’’ algorithm described in [54]. The muon momentum correction and uncertainty varies as a function of muon p_T and η . The effect of the muon momentum correction uncertainty is a small effect in this analysis compared to the τ and E_T^{miss} scale uncertainties.

2015 The uncertainty on the jet energy scale is determined from an analysis of the p_T balance
 2016 between photons and jets in $\gamma + \text{jets}$ events [55]. The jet energy scale uncertainties are
 2017 determined by the JetMET group are applied to tau-jets as well as other jets in the event.
 2018 The tau energy scale correction factor is taken to be 1.0 with an uncertainty of 3%. The QCD
 2019 jet energy scale has been measured to within 3% uncertainty. In the future, the energy scale
 2020 of the tau is expected to be determined to a much better precision, as the neutral hadronic
 2021 activity of a hadronic tau decay is expected to be zero. The jet energy scale of 3% can be
 2022 confidently considered [48] an upper limit⁴, and is used in this analysis as the tau energy
 2023 scale uncertainty.

2024 §7.4 Missing Transverse Energy Correction

2025 In practice, the resolution of the reconstructed missing transverse energy is poor as it is
 2026 sensitive to the mis-measurement of any object in the event. Furthermore, a fraction of the
 2027 particles produced in the hard collision can be produced in the very forward region, outside
 2028 of the fiducial region of the calorimeters. The resolution of the E_T^{miss} reconstruction can be
 2029 measured in $Z \rightarrow \mu^+ \mu^-$ events. The true E_T^{miss} in such events is expected to be zero. The
 2030 E_T^{miss} resolution in simulated $Z \rightarrow \mu^+ \mu^-$ events is found to be smaller (better) than in the
 2031 data.

2032 The E_T^{miss} resolution depends on the “recoil” of the Z boson. The reason for this effect
 2033 is that for events where the Z is produced nearly at rest, the associated recoil products have
 2034 very small transverse momentum and are produced at very high pseudorapidity. The E_T^{miss}
 2035 is corrected using a procedure called a “Z-recoil” correction, as described in [56]. The reso-
 2036 lution of the E_T^{miss} is measured in $Z \rightarrow \mu^+ \mu^-$ events in simulation and data. The difference
 2037 in the reconstructed E_T^{miss} resolution in both samples is parameterized by the magnitude of
 2038 the transverse momenta of the particles recoiling against the Z .⁵ The reconstructed E_T^{miss}
 2039 in the simulated $Z \rightarrow \tau^+ \tau^-$, $Z \rightarrow \mu^+ \mu^-$, and $W + \text{jets}$ samples is “smeared” by a random

⁴The tau energy scale was roughly measured using the invariant mass of the hadronic decay products and shown to be compatible with 1.0, within 3%.

⁵The “recoil” particles are defined as all those not identified as Z decay products. This definition is equivalent to the total decay product transverse momentum q_T added reconstructed E_T^{miss} .

amount in each event such that the final resolution matches the observed resolution in the data.

Z -recoil corrections are determined as described in [56] and applied to simulated $Z \rightarrow \tau^+\tau^-$, $Z \rightarrow \mu^+\mu^-$ and $W + \text{jets}$ events, in order to correct for residual differences in E_T^{miss} response and resolution between data and Monte Carlo simulation [57]. The corrections are obtained by an unbinned maximum likelihood fit (in data and simulation) of the transverse recoil vector $\vec{u}_T = -(\vec{q}_T + E_T^{\text{miss}})$ as function of the transverse momentum \vec{q}_T of the Z -boson in directions parallel and perpendicular to the Z -boson transverse momentum vector.

Two additionally types of corrections are applied to the simulated E_T^{miss} , “clustered” and “unclustered.” The overall correction factor from these two effects is taken to be unity. However, the uncertainty on these two correction factors is used as a systematic uncertainty when setting the final limit. The clustered E_T^{miss} correction varies the scale of all jets with $p_T > 10$ GeV/ c in the event and recomputes the shifted E_T^{miss} . The unclustered E_T^{miss} correction varies the energy scale of all jets/particles in the event with $p_T < 10$ GeV/ c . The scale uncertainty is 3% for the clustered correction and 10% for the unclustered correction.

§7.5 Pile-up Event Weighting

The average number of pile-up interactions in the event can effect almost all aspects of the analysis. In general, increasing pile-up lowers particle identification efficiencies and lowers E_T^{miss} resolution. It is therefore important that the distribution of pile-up events in the simulation matches the distribution found in the data. Differences in the number of pile-up interactions between the data (averaged over the analyzed run-range) and pile-up Monte Carlo samples produced for “BX156”⁶ pile-up conditions are corrected for by reweighting Monte Carlo simulated events according to the number of reconstructed event vertices, in order to match the distribution measured in a $W \rightarrow \mu\nu$ dataset triggered by the HLT_Mu15 High Level Trigger path. Vertices considered for this purpose are required to pass $-24 < z_{vtx} < +24$ cm, $|\rho| < 2$ cm, nDoF > 4 . In addition, the total transverse momenta of all tracks fitted to the vertex is required to exceed 10 GeV/ c , assuming that

⁶The BX156 name comes from the fact that the pile-up scenario used in this simulation corresponds to an LHC configuration with 156 bunches.

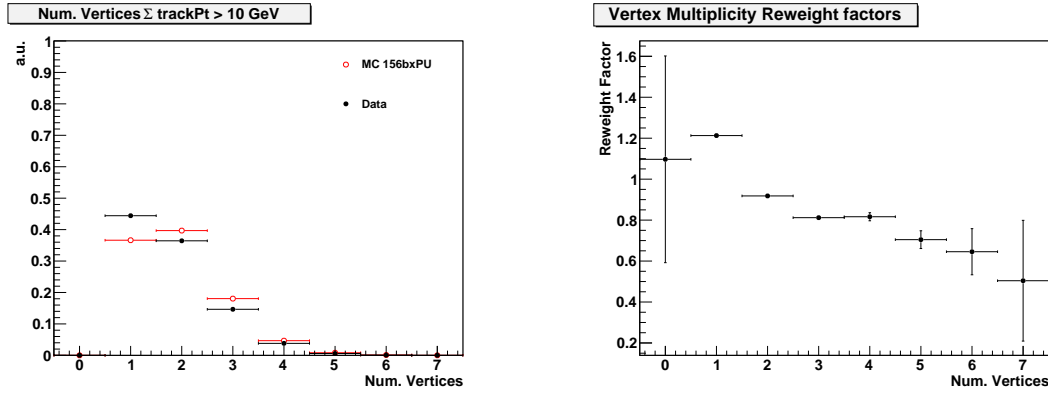


Figure 7.4: Vertex multiplicity distribution measured in the analyzed data-taking period compared to Monte Carlo simulation with “BX156” pile-up conditions (left) and resulting Monte Carlo reweighting factors (right).

2067 “softer” vertices have little or no effect on the “hard” event to pass event selection criteria.
 2068 The average vertex multiplicity distribution measured in data is compared to Monte Carlo
 2069 simulation with “BX156” pile-up conditions in Figure 7.4. Both distributions are similar,
 2070 resulting in Monte Carlo reweighting factors close to unity.

2071

Chapter 8

2072 Systematics and Limit Extraction

2073 In this chapter we discuss the systematic uncertainties affecting the search for the Higgs
 2074 boson and the statistical techniques used to establish an upper limit on the Higgs $\rightarrow \tau^+\tau^-$
 2075 branching ratio times cross section ($\sigma \times \text{BR}_\tau$). The limit can be interpreted as the largest¹
 2076 signal presence that could exist in the data and still be consistent with the null hypothesis.
 2077 The limit on $\sigma \times \text{BR}_\tau$ is roughly independent of the theoretical model². In the conclusion,
 2078 we will interpret the $\sigma \times \text{BR}_\tau$ limit result in the context of the MSSM theory.

Proper determination of systematic uncertainties is one of the most challenging and important components in performing a measurement correctly. A systematic uncertainty is the effect of the uncertainty of some ancillary measurement (or assumption) that is used in the computation of the final result. An instructive example of how a systematic uncertainty can affect the final result is a counting experiment measuring the cross section of some signal particle in the presence of background. The formula for the cross section times the branching fraction is

$$\sigma \times BR = \frac{N_{sig}}{\mathcal{L} \cdot \mathcal{A} \cdot \epsilon} = \frac{N_{obs} - N_{bkg}}{\mathcal{L} \cdot \mathcal{A} \cdot \epsilon}, \quad (8.1)$$

where N_{obs} is the number of events observed in data, N_{bkg} is the estimated number of background events in the observed data sample, \mathcal{L} is the integrated luminosity, and $\mathcal{A} \cdot \epsilon$ is the acceptance times efficiency of the signal. All of the quantities in Equation 8.1 (with the exception of the observed count N_{obs}) have some uncertainty which will effect the final measurement. Consider a situation where the expected number of background events is determined by fitting some sideband spectrum, and the fitted result has some error δN_{bkg} .

¹At some stated level of statistical confidence; the convention for limits in experimental high energy physics is 95%.

²Provided that the width of the Higgs bosons in the given model is smaller than the resolution of the SVfit mass resolution.

The total relative effect of this error can be obtained by error propagation

$$\frac{\delta(\sigma \times BR)}{\sigma \times BR} = \frac{\partial(\sigma \times BR)}{\partial N_{bkg}} \frac{1}{\sigma \times BR} \delta N_{bkg} = \frac{-\delta N_{bkg}}{N_{obs} - N_{bkg}}. \quad (8.2)$$

It is interesting to examine Equation 8.2 in two scenarios. In the limit that N_{obs} is large compared to N_{bkg} , the effect of the error on the background estimate δN_{bkg} does not affect the final result. In contrast, in a scenario when the data is dominated by background events, the relative error on the signal measurement due to the background estimation approaches infinity. The sensitivity of a measurement to a systematic uncertainty on a parameter depends on the context in which that parameter is used.

Experimental systematic uncertainties relevant for MSSM Higgs $\rightarrow \tau^+ \tau^-$ search presented in this thesis are classified in three categories: normalization uncertainties on the signal and $Z \rightarrow \tau^+ \tau^-$ background (events with true taus), normalization uncertainties on contributions from background with fake taus, and shape uncertainties. Normalization uncertainties on events with true taus are due to lepton reconstruction, identification, isolation and trigger efficiencies. These terms are equivalent to the efficiency ϵ and acceptance terms \mathcal{A} of Equation 8.2 and affect the expected yield of MSSM Higgs $\rightarrow \tau^+ \tau^-$ signal and $Z \rightarrow \tau^+ \tau^-$ background events. The uncertainties on these effects are obtained by measuring the effect in data and simulation, according to the procedures of Chapter 7, and calculating a correction factor. The uncertainty associated with the measurement of the correction factor is the systematic uncertainty. The normalization uncertainties are assumed to be uncorrelated with the shapes of visible and SVfit mass distributions which are used to extract the MSSM Higgs $\rightarrow \tau^+ \tau^-$ signal contribution in the analyzed dataset. Uncertainties on the shapes of the distributions are described by “morphing” systematics. These are due to uncertainties on the momentum/energy scale of identified electrons, muons, tau and other jets in the event. As the SVfit mass reconstruction algorithm uses the missing transverse energy, the shape of the SVfit distribution is sensitive to systematic uncertainties on the overall scale E_T^{miss} measurement. The “morphing” systematics affect the shapes of signal as well as background contributions. Normalization uncertainties on background contributions are estimated from the level of agreement between data and Monte Carlo simulation in background dominated control regions.

2106 §8.1 Signal normalization uncertainties

2107 The signal normalization uncertainties are due to imperfect knowledge of how improperly
 2108 modeled effects in the simulation could affect the acceptance model, the probability that
 2109 a given signal event will pass one of the selections (detailed in Chapter 5). The general
 2110 procedure to quantify these uncertainties is to measure the effect in some control region
 2111 in both the data and Monte Carlo. The ratio of data to Monte Carlo then gives a correc-
 2112 tion factor which is applied to the simulation. An uncertainty on the measurement of the
 2113 effect in control region (in the data, simulation, or both) is then taken as the systematic
 2114 uncertainties. The signal normalization uncertainties affecting this analysis on muon trig-
 2115 ger, reconstruction, identification and isolation efficiencies are taken from the tag and probe
 2116 analysis of $Z \rightarrow \mu^+ \mu^-$ events presented in Section 7.1. A very conservative estimate of 30%
 2117 is taken for the uncertainty on the tau reconstruction and identification efficiency. The tau
 2118 identification uncertainty measurement is discussed briefly in 7.2. The dependency of the
 2119 Higgs signal extraction on the tau identification efficiency has been studied, the result being
 2120 that uncertainties on the tau identification efficiency affect the limit on cross-section times
 2121 branching ratio for MSSM Higgs $\rightarrow \tau^+ \tau^-$ production by a few percent only. An uncertainty
 2122 of 11% is attributed to the luminosity measurement [58].

2123 §8.2 Background normalization uncertainties

2124 Uncertainties on the normalization of background processes are obtained from the study
 2125 of background enriched control regions presented in Chapter 6. The main fake tau back-
 2126 grounds in this analysis are QCD multi-jet and $W + \text{jets}$ events. These backgrounds are
 2127 produced copiously enough for the backgrounds to be studied in control regions dominated
 2128 by a single background process with a purity exceeding 90% and an event statistics exceed-
 2129 ing the expected contribution of that background to the analysis by more than one order of
 2130 magnitude. Both backgrounds are found to be well modeled by the Monte Carlo simulation.
 2131 The overall background yields used in the final fit are measured in the background enriched
 2132 control regions, and cross-checked using the Fake-rate and Template methods. For a de-
 2133 tailed discussion of the measurements, see Chapter 6. An uncertainty of 10% is attributed

2134 to the contribution of QCD and $W + \text{jets}$ backgrounds to the analysis. The cross-section
 2135 for $t\bar{t} + \text{jets}$ production makes it difficult to select a high purity sample of $t\bar{t} + \text{jets}$ events of
 2136 high event statistics. From the study of the 19 events selected in the $t\bar{t} + \text{jets}$ background
 2137 enriched control sample we assume an uncertainty on the $t\bar{t} + \text{jets}$ background contribution
 2138 in the analysis of 30%. The $Z \rightarrow \mu^+ \mu^-$ background has been studied with large statistical
 2139 precision in two separate control regions, and is dominated by events in which the recon-
 2140 structed tau-jet candidate is either due to a misidentified quark or gluon jet or due to a
 2141 misidentified muon. Good agreement between data and Monte Carlo simulation is found
 2142 in both cases. Sizeable uncertainties on the $Z \rightarrow \mu^+ \mu^-$ background contribution arise due
 2143 to the extrapolation from the background enriched control regions to the data sample con-
 2144 sidered in the analysis, however: the contribution of $Z \rightarrow \mu^+ \mu^-$ background events to the
 2145 analysis is due to events in which one of the two muons produced in the Z decay either
 2146 escapes detection or fakes the signature of a hadronic tau decay. Both cases may be difficult
 2147 to model precisely in the Monte Carlo simulation. The non-observation of a Z mass peak in
 2148 the mu + tau visible mass distribution studied with the fake-rate method on the other hand
 2149 sets a limit on possible contributions from $Z \rightarrow \mu^+ \mu^-$ background events. Conservatively,
 2150 we assume an uncertainty of 100% on both types of $Z \rightarrow \mu^+ \mu^-$ background contributions.

2151 §8.3 Shape uncertainties

2152 Shape uncertainties on the distributions of visible and “full” invariant mass reconstructed by
 2153 the SVfit algorithm are estimated by varying the electron energy and muon momentum scale,
 2154 the energy scale of tau-jets and other jets in the event and varying the missing transverse
 2155 energy in Monte Carlo simulated events. After each variation the complete event is re-
 2156 reconstructed and passed through the event selection. Shifted visible and “full” invariant
 2157 mass shapes are obtained for each variation from the events passing all event selection
 2158 criteria. The difference between shifted shapes and the “nominal” shapes obtained from
 2159 Monte Carlo simulated events with no variation of energy or momentum scale or of the
 2160 missing transverse energy applied is then taken as shape uncertainty.

2161 The systematic uncertainties on the muon and tau energy scales have been provided
 2162 by the muon and tau CMS Physics Object Groups and are described in Section 7.3. The

modelling of missing transverse energy in different types of background events has been studied in the background enriched control regions described in Chapter 6. No significant deviations between data and Monte Carlo simulation have been found. Uncertainties due to missing transverse energy are estimated by varying the “clustered” and “unclustered” energy scales, described in Section 7.4 and recomputing the total E_T^{miss} .

§8.4 Theory uncertainties

The signal and background normalization as well as the shape uncertainties are all experimental uncertainties in nature. Additional theoretical uncertainties arise from imprecise knowledge of parton-distribution functions (PDFs) and of the exact dependency of signal cross-sections and branching ratios on $\tan \beta$ and m_{A^0} . The PDFs describe how the energy of the protons is shared between the quarks and gluons. Since the longitudinal boost of the hard collisions depends on the PDFs, the signal acceptance is sensitive to errors in the PDFs. The uncertainties on the signal acceptance due to PDF uncertainties are estimated using tools developed by the CMS Electroweak working group [59]. The acceptance is computed with respect to MSSM Higgs $\rightarrow \tau^+ \tau^-$ decays that have muons of $p_T^\mu > 15$ GeV/c and $|\eta_\mu| < 2.1$, jets produced in hadronic tau decays with visible $p_T^{\text{vis}} > 20$ GeV/c and $|\eta_{\text{vis}}| < 2.3$ on generator level. Acceptance values are computed for the central value and 44 eigenvectors of the CTEQ66 PDF set [60]. The systematic uncertainty on the signal acceptance is computed following the PDF4LHC recommendations [61, 62].

The effect of Monte Carlo normalization, shape and theory uncertainties on the signal efficiency times acceptance is summarized in Table 8.1.

§8.5 Limit Extraction Method

The search for a new signal is performed by examining the observed distribution of the reconstructed di-tau mass $m_{\tau\tau}$ as reconstructed by the SVfit algorithm. An “bump” in this spectrum would indicate the presence of a new particle. To make a statement about the presence of a bump with confidence, the shape under a potential bump must be well described. The background shape is decomposed into the combination of shapes from the different background sources, which we refer to here as “templates.” The data and the

Source	Effect
Normalization uncertainties	
Trigger	0.981 ± 0.006
Muon identification	1.001 ± 0.001
Muon isolation	0.984 ± 0.006
Tau-jet identification	1.00 ± 0.30
Shape uncertainties	
Muon momentum scale	$\ll 1\%$
Tau-jet energy scale	$1 - 4\%^1$
Jet energy scale (JES)	$< 1\%^2$
E_T^{miss} (Z -recoil correction)	1%
Theory uncertainties	
PDF	2% ³

¹ decreasing with m_A

² number quoted for $gg \rightarrow A/H$ and $b\bar{b} \rightarrow A/H$ sample as a whole;

in the subsample of events with b-tagged jets the effect of the JES uncertainty is 4%

³ with small dependence on m_A

Table 8.1: Effect of normalization uncertainties on the $gg \rightarrow A/H$ and $b\bar{b} \rightarrow A/H$ signal efficiency times acceptance.

²¹⁹¹ templates for each background distribution is binned in the observable $m_{\tau\tau}$ variable. The
²¹⁹² normalization of each template represents the total yield expected for that source.

We can then define a likelihood for any configuration of our templates given the observed data. The likelihood is a “binned Poisson likelihood,” which is defined as the product of the Poisson probability in each bin. The Poisson probability $P(n|\mu)$ is the probability to observe n events given an expectation of μ events. The Poisson probability is given by the expression

$$P(k|\mu) = \frac{\mu^k e^{-\mu}}{k!}. \quad (8.3)$$

²¹⁹³ The total likelihood for observed data given some configuration of templates is then simply

2194 the product of the Poisson probabilities (Equation 8.3) in each of the N_{bin} bins:

$$\mathcal{L} = \prod_{i=1}^{N_{bin}} \frac{\mu_i^{n_i} e^{-\mu_i}}{n_i!}, \quad (8.4)$$

2195 where the expected number of events μ_i in the bin i is the sum of the number of events

2196 from all sources

$$\mu_i = \sum_{j=1}^{N_{source}} \mu_{ji}.$$

2197 The number of expected events in a source, in turn, can be written

$$\mu_{ji} = L \sigma_j \epsilon_{ji} \quad (8.5)$$

2198 where L is the integrated luminosity, σ_j is the cross section for source j , and ϵ_{ji} is the
2199 efficiency for source j in bin i .

2200 We incorporate the systematic uncertainties of the analysis by introducing a set of
2201 “nuisance parameters” $\vec{\beta}$ into the likelihood function. As the name suggests, we are not
2202 interested in the actual value of the nuisance parameters. Each nuisance parameter pa-
2203 rameterizes some phenomenon in the analysis. The shape templates (which can be defined
2204 purely in terms of σ_j and ϵ_{ji} in Equation 8.5) are now interpreted as functions of the set
2205 of nuisance parameters $\vec{\beta}$. Existing knowledge about the value of the nuisance parameter is
2206 introduced by extending the likelihood function with a constraint $\mathcal{G}(\vec{\beta})$ that expresses the
2207 knowledge about the nuisance parameters. The templates μ_{ji} can depend on the nuisance
2208 parameters in two ways. Normalization uncertainties introduce multiplicative nuisance fac-
2209 tors on the yield of some (sub)set of the sources defined by Equation 8.5. As an example,
2210 consider a simplified situation where there are only two sources: $Z \rightarrow \tau^+ \tau^-$ and $W + \text{jets}$
2211 events. Both sources are sensitive to the efficiency of the muon trigger. Only the $Z \rightarrow \tau^+ \tau^-$
2212 sample is sensitive to the efficiency of the hadronic tau identification algorithm, as the
2213 fake-rate in $W + \text{jets}$ is measured in data. We would then introduce two multiplicative nui-
2214 sance parameters, β_μ and β_τ , which respectively correspond to the two uncertainties. The
2215 expected number of events in the i th bin is then given by a modified form of Equation 8.5

$$\mu_i = L \beta_\mu \sigma^W \epsilon_i^W + L \beta_\mu \beta_\tau \sigma^Z \epsilon_i^Z. \quad (8.6)$$

2216 From Equation 8.6, we can see that β_μ affects both sources but β_τ only affects the $Z \rightarrow \tau^+ \tau^-$
2217 source.

The shape uncertainties discussed in Section 8.3 are incorporated using a technique

$(1 - \alpha)\%$	$m = 1$	$m = 2$	$m = 3$
68.27	1.00	2.30	3.53
90.00	2.71	4.61	6.25
95.00	3.84	5.99	7.82
99.00	6.63	9.21	11.34

Table 8.2: Correspondence between a confidence level defined by $(1 - \alpha)\%$ and the corresponding interval in $2\Delta \ln \mathcal{L}$. The $2\Delta \ln \mathcal{L}$ interval is different depending the number m of parameters which are being simultaneously estimated.

called “vertical template morphing.” For each source, different templates are created for three different values of the morphing parameter, corresponding to -1, 0, and +1 standard deviation shifts in the nuisance parameter. To determine the number of expected events in the i th bin as a function of the morphing parameter, we interpret quadratically between the i th bin values of the three templates, and extrapolate linearly beyond them. The overall likelihood then, including nuisance parameters, can be written as

$$\mathcal{L} = \prod_{i=1}^{N_{bin}} \frac{[\mu_i(\vec{\beta})]^{n_i} e^{-\mu_i(\vec{\beta})}}{n_i!} \times \prod_{m=1}^{N_\beta} \mathcal{G}(\beta_m). \quad (8.7)$$

In Equation 8.7, we have introduced the assumption that the nuisance parameters are uncorrelated.

We wish to determine if the data is compatible with a new signal. To test for the presence of a bump, we examine the likelihood as a function of the signal cross-section. If the presence of a signal is unambiguous, one can simply determine the likelihood as a function of the cross-section. If the signal is known to be non-zero, confidence intervals about the maximum likelihood can be constructed by examining the change in the logarithm $2\Delta \ln \mathcal{L}$ of the likelihood. The Frequentist interpretation of the confidence level $(1 - \alpha)$ is that if the experiments were repeated N times, the interval corresponding to $(1 - \alpha)$ would fail “cover” the *true* value of the observable in $\alpha \times N$ of the experiments. The correspondence between confidence levels and intervals in $2\Delta \ln \mathcal{L}$ is given in Table 8.2. Since the mass of a potential Higgs boson is unknown, we repeat this process for different signal masses. If there is not a significant signal, we can set upper bounds on the signal cross-section using one of several methods, which will be discussed below.

Fixme: Did I mix this up?

At this point, the likelihood still depends on the nuisance parameters. There are two methods of removing the dependence on the nuisance parameters, “marginalization” and “profiling.” Marginalization is the process of integrating the likelihood of Equation 8.7 over the entire range of all nuisance parameters. This effectively averages the effect of the different uncertainties into the marginalized likelihood function. The profiling method maximizes the likelihood in terms of the nuisance parameters. In the profiling method, the “profile likelihood” is created by maximizing the likelihood with respect to all of the nuisance parameters. One way to interpret the profiling method is that the values of nuisance parameters are being measured *in situ*, constrained by the observed data. While not a strictly Bayesian treatment, the profile likelihood method has been shown to give almost identical results to marginalization.

An interesting situation relating to the profiling of the nuisance parameters arises in this analysis in the context of the hadronic tau identification uncertainty. As discussed in Chapter 7, the Higgs–insensitive measurement of the tau identification efficiency has a high uncertainty of 30%. If the bump at the $Z \rightarrow \tau^+\tau^-$ resonance can be considered to Higgs free, the tau identification efficiency can be measured to a much greater precision, approximately 7% [53, 48]. When profiling the likelihood (as a function of cross section) for a Higgs with a mass $m_{A^0} > m_Z$, the likelihood contains the information that there is no Higgs contribution to the Z resonance. This fact enables the profiling process to constrain the systematic uncertainty on the tau identification efficiency to the 7% level using the size of the Z resonance. Conversely, when the likelihood is evaluating the likelihood of the presence of a Higgs signal with $m_{A^0} = m_Z$, the likelihood cannot distinguish between a potential presence of Higgs events in the Z bump or a systematic undershoot of the tau identification efficiency in the simulation. In this case the profiling processing has no power to constrain the systematic to a value lower than the initial 30% value.

In the absence of the signal, or even in the presence of one, we can determine a upper 95% CL bound on the cross-section of the signal using the profile likelihood. In one method we simply use Bayes’ Theorem to convert the likelihood to a posterior density in the signal cross-section, and integrate to find the point below which 95% of the probability lies. The

Bayesian posterior PDF is computed as

$$\mathcal{P}(\sigma_H | \bar{x}, m_H) = \frac{\mathcal{L}(\bar{x} | \sigma_H m_H) \mathcal{P}(\sigma_H)}{\int \mathcal{L}(\bar{x} | \sigma'_H m_H) \mathcal{P}(\sigma'_H) d\sigma'_H}. \quad (8.8)$$

2257 The left hand side of Equation 8.8 represents the probability density for a given signal cross
 2258 section, given the observed data \bar{x} and the assumed value m_H for the Higgs mass. We refer
 2259 to this method as the “Bayesian” method of setting limits.

2260 In the other method, which is referred to as the “Delta Log Likelihood” (DLL) method,
 2261 we compute two likelihoods. The first likelihood is computed for the “null hypothesis” case.
 2262 The likelihood is profiled (maximized) assuming that no signal is present. We then construct
 2263 the profile likelihood for increasing values of the signal yield. The upper limit is achieved
 2264 when the logarithm of the profile likelihood is 1.92 units less than the value of the null
 2265 hypothesis profile likelihood.

2266 In general the limits computed by the Bayesian and DLL methods are similar. However,
 2267 the effect of upward or downward statistical fluctuations in the observed data affect the two
 2268 methods in different ways. When the data fluctuates low, the DLL method will produce
 2269 a more stringent limit than the DLL method. When the data fluctuates high, creating an
 2270 apparent signal, the Bayesian method will (correctly) set a more stringent limit.

2271 In the results presented below we use nuisance parameters corresponding to the sys-
 2272 tematic errors summarized in Table 8.3.

Fixme: Get
MET scale,
how to split
between type
1 and type2?

Source	Method	Magnitude
Muon ID/trigger	Multiplicative	20%
Z cross section	Multiplicative	5%
Jet to τ fake rate	Multiplicative	20%
$\mu \rightarrow \tau$ fake rate	Multiplicative	100%
W +jets cross section	Multiplicative	10%
$t\bar{t}$ cross section	Multiplicative	40%
integrated luminosity	Multiplicative	11%
Tau energy scale	Morphing	3%
Missing E_T scale	Morphing	3%
Muon p_T scale	Morphing	neg.
EM energy scale	Morphing	neg.

Table 8.3: Summary of systematic uncertainties represented by nuisance parameters in the likelihood, their representation method and magnitudes.

2273

Chapter 9

2274

Results

2275

§9.1 Selected Events

2276 In the 36 pb^{-1} of 7 TeV data collected by CMS in 2010, the analysis selection criteria
 2277 described in Chapter 5 selects a total of 573 events. The expected yields from each of
 2278 the background sources, computed by the Template method (Section 6.3) and verified by
 2279 the Fake-rate method (Section 6.2) are shown in Table 9.1. The total expectation from the
 2280 Standard Model background is 577. The data agrees extremely well with the SM background
 2281 expectation considering the expected statistical variance of the observed data (24 events), as
 2282 well as the uncertainty on the integrated luminosity¹ and the tau identification uncertainty.

2283

2284 The distributions of the visible mass and SVfit mass in the final selected events are
 2285 shown in Figure 9.3. Excellent agreement is seen between the shapes of the distributions. The
 2286 p_T spectrum of the transverse momentum are sensitive to mis-modeling of the kinematics
 2287 and composition of the various background sources. Control plots showing the transverse
 2288 momenta of the muon and visible hadronic tau in the final analysis selection are shown
 2289 in Figure 9.1. The η and ϕ distributions of the muon and tau objects are sensitive to
 2290 detector effects, and the presence of cosmic muons. For example, muons from cosmic events
 2291 will preferentially be produced in the $\phi = 0$ direction. Spurious candidates resulting from
 2292 poorly model noise in one of the CMS subdetectors will in general be localized in $\eta - \phi$. The
 2293 η and ϕ distributions of the muon and tau candidates are shown in Figure 9.2 and show
 2294 excellent agreement.

¹The uncertainty on the CMS luminosity measurement was 11% at the time this analysis was performed. The measurement was later improved, and at the time of this writing the uncertainty on CMS 2010 integrated luminosity is 4% [58]. The improved luminosity measurement is not expected to change the results of this analysis significantly.

Process	Events in 36 pb ⁻¹
$t\bar{t} + \text{jets}$	6.6
$W + \text{jets}$	25.6
$Z \rightarrow \mu^+ \mu^-$	10.6
QCD	166.2
$Z \rightarrow \tau^+ \tau^-$	368.1
Standard Model sum	577.1
Data	573

Table 9.1: Number of Higgs $\rightarrow \tau^+ \tau^- \rightarrow \mu + \tau_{had}$ candidate events passing the selection criteria described in Chapter 5.

2295 The expected yields from an MSSM Higgs boson signal for $\tan \beta = 30^2$ are summarized
 2296 in . The contributions from the gluon fusion production mode and the associated b –quark
 2297 production modes are given separately. The yields are divided into the exclusive categories of
 2298 events containing a b –tagged jet and those without. For a Higgs mass of $m_{A^0} = 160$ GeV/ c^2 ,
 2299 a total of 17 events are expected at $\tan \beta = 30$.

Fixme:

Get cite

2300 §9.2 Limits on Higgs Production

2301 We compute upper limits on the cross section times the branching ratio using the Bayesian
 2302 method described in Section 8.5. We compute an expected limit in the same manner as an
 2303 observed limit, but with simulated data generated in “toy” experiments. A large number
 2304 of pseudo–data sets are generated using the null hypothesis templates using Monte Carlo
 2305 techniques. The nuisance parameters are sampled within their constraints in the generation
 2306 of the pseudo–date. The pseudo–data sets are expected to have the same statistical sen-
 2307 sitivity as the observed dataset. Upper limits are then computed using the pseudo–data.
 2308 The process is repeated many times, and the spread of the obtained upper limits deter-
 2309 mines the expected upper limit band. The expected nominal upper limit, and the ± 1 , and
 2310 ± 2 confidence limits are shown in Table 9.3. The observed limit on the MSSM computed

²Details of the relationship between the MSSM Higgs cross section and $\tan \beta$ are discussed in detail in Section 9.3.

from the 573 events selected in this analysis is given in the right column of Table 9.3. The observed limit is compatible with the expected limit, within 1.5 standard deviations. The trend of the expected and observed limits versus the Higgs mass using both observables are shown in Figure 9.4. The use of the SVfit reconstructed mass as the observable increases the power of the limit significantly. The limit trend has some interesting features. When the Higgs mass is close to the mass of the Z resonance, the analysis have little power to set a limit on the presence of the Higgs. This is due to the large uncertainty on the tau identification efficiency. Essentially, when $m_{A^0} = m_Z$, the Higgs yield in the Z bump would have be larger than 30% of the $Z \rightarrow \tau^+\tau^-$ yield for the profile likelihood to be able to recognize an excess of events. Below this value, the profile likelihood can simple shift the tau identification efficiency scale factor up by 30% and “eat” any potential excess of signal.

§9.3 Interpretation in the MSSM

The limits on the cross section times branching ratio are roughly model independent,³ and could be applied to set limits on the parameter space of a number of models. In this thesis, we interpret the results in the context of the MSSM. Specifically, we exclude a region in the $\tan\beta - m_{A^0}$ parameters space of the MSSM. To find the upper limit band on $\tan\beta$, we find the minimum value of $\tan\beta$ which provides the cross section and branching ratio product found in the corresponding row in Table 9.3.

The mapping between m_{A^0} and $\tan\beta$ and the Higgs cross section is provided by the LHC Higgs Cross Section working group [63]. The cross sections and branching ratios have been computed for the h^0 , H^0 , and A^0 MSSM Higgs states in both the ggA and qqA production modes, for a grid of points in $\tan\beta - m_{A^0}$ space. In order to combine the ggA and qqA production modes, what we call our signal cross-section is the sum of the cross-section times branching ratio for both modes, assuming $\tan\beta = 30$. Additionally, as discussed in Section 1.2.3, the MSSM Higgs sector consists of two Higgs doublets, yielding five physical Higgs bosons. This search is sensitive to the three neutral Higgs particles the

³This assumption is only valid if the shape of the sum of all new physics contributions are also model independent, on the scale of the experimental resolution. For the values of $\tan\beta$ this analysis is sensitive to, this is a valid approximation in the MSSM. In a model where the width of the Higgs boson resonance was larger than the resolution of the SVfit method, the limits of Table 9.3 would not be valid.

2337 h^0, H^0 , and A^0 . The relative contributions of the three Higgs types depends on the mass
 2338 m_{A^0} of the CP-odd Higgs. An observed signal will have contributions from at least two
 2339 Higgs states. For $m_{A^0} \leq 130$ GeV/c², the A^0 and h^0 are approximately degenerate in mass
 2340 and width. In this region the H^0 has a very small relative cross section and a constant
 2341 mass of $m_{H^0} \approx 130$ GeV/c². For $m_{A^0} \geq 130$ GeV/c², the h_0 reaches a limiting mass of
 2342 ≈ 130 GeV/c², and the H^0 and A^0 become mass degenerate.

2343 The region in $\tan\beta - m_{A^0}$ MSSM parameter space excluded by this analysis at 95%
 2344 CL is shown in Figure 9.3. The limit is compared to the combined result from Run II of
 2345 the Tevatron (this result is discussed in detail in Section 1.3.3). The result of this analysis
 2346 sets a stronger limit than the Tevatron for large values of m_{A^0} . In the low m_{A^0} region, the
 2347 analysis suffers due to the large tau identification efficiency uncertainty. This effect can be
 2348 mitigated by using the $e - \mu$ channel. The combined CMS result uses this approach, and
 2349 will be discussed briefly in the conclusion.

Fixme:

check this!

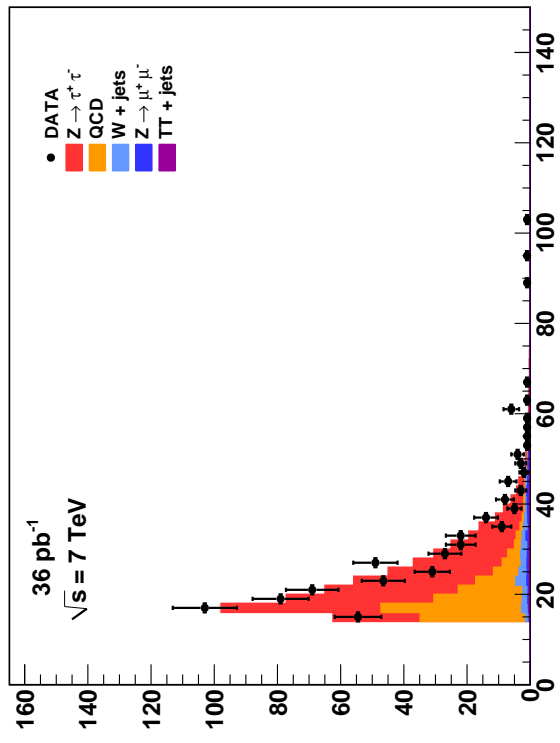
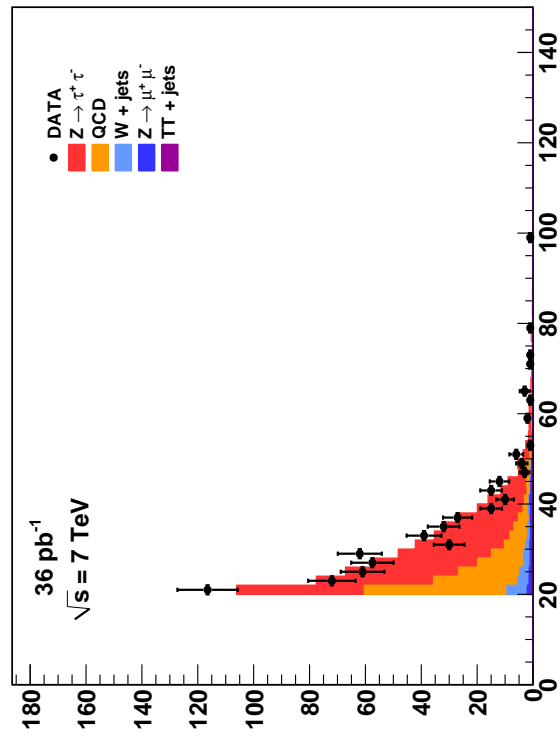
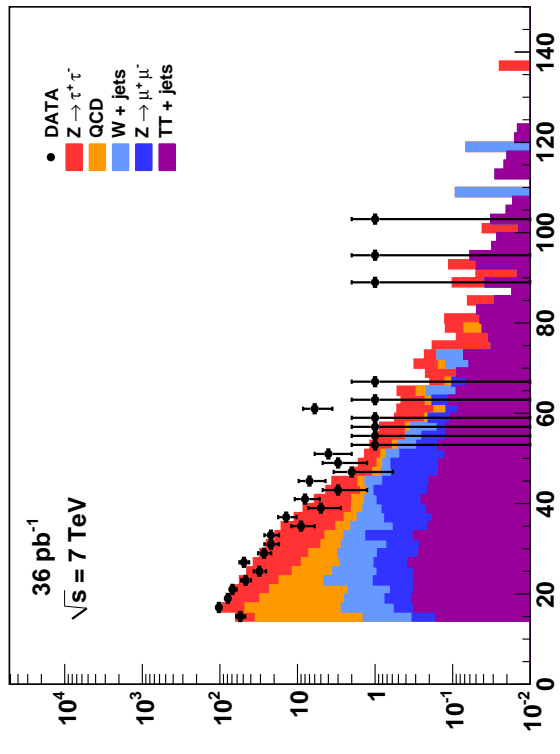
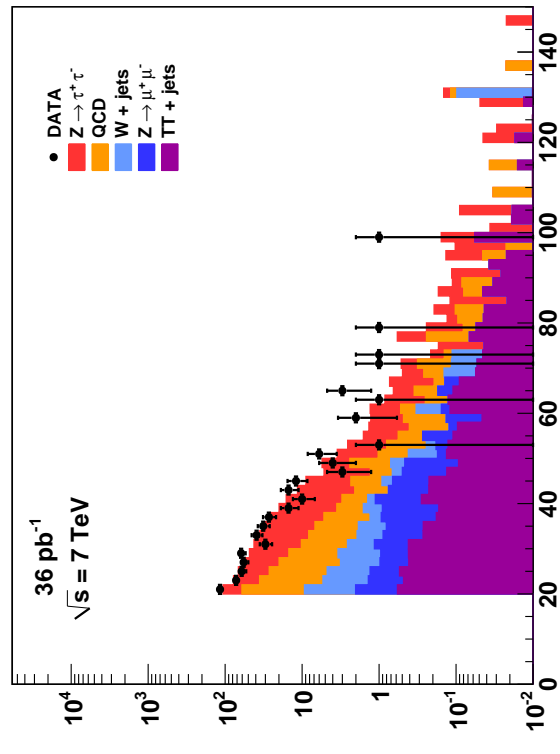
Muon (final event sample)**Tau (final event sample)****Muon (final event sample)****Tau (final event sample)**

Figure 9.1: Distribution of the transverse momentum of the muon (top) and hadronic tau in $Higgs \rightarrow \tau^+ \tau^- \rightarrow \mu + \tau_{had}$ candidate events passing the selection criteria described in Chapter 5. The distributions are shown in linear (logarithmic scale on the left (right)).

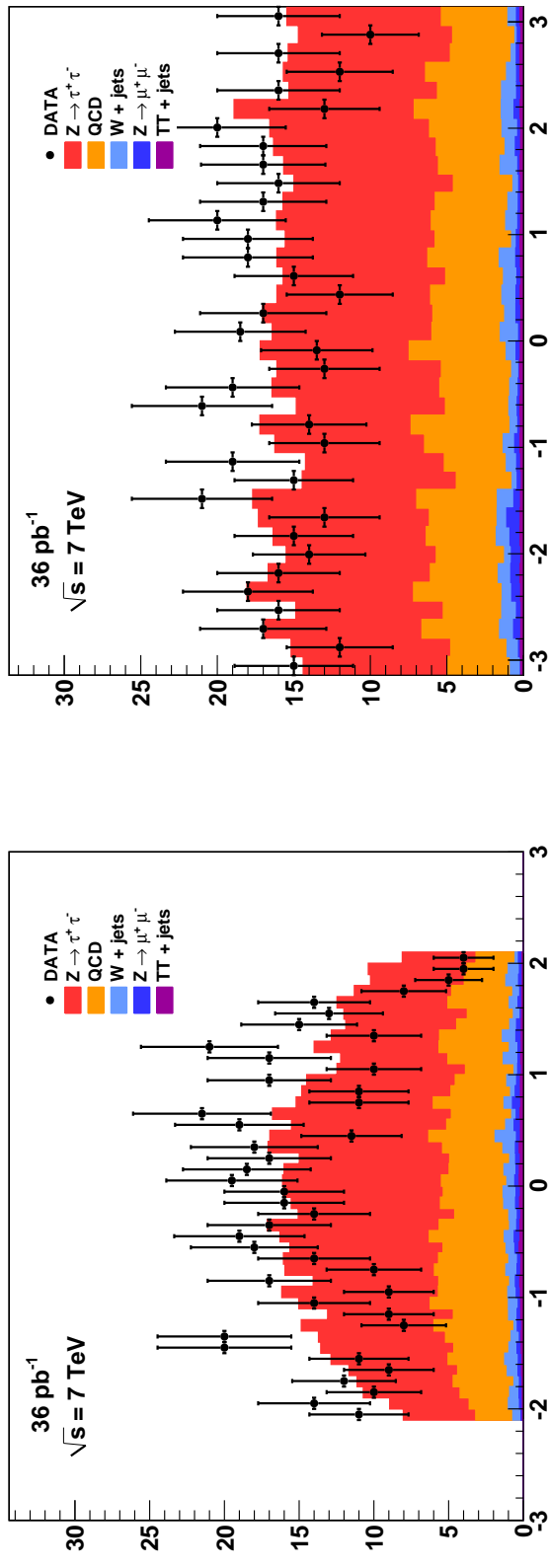
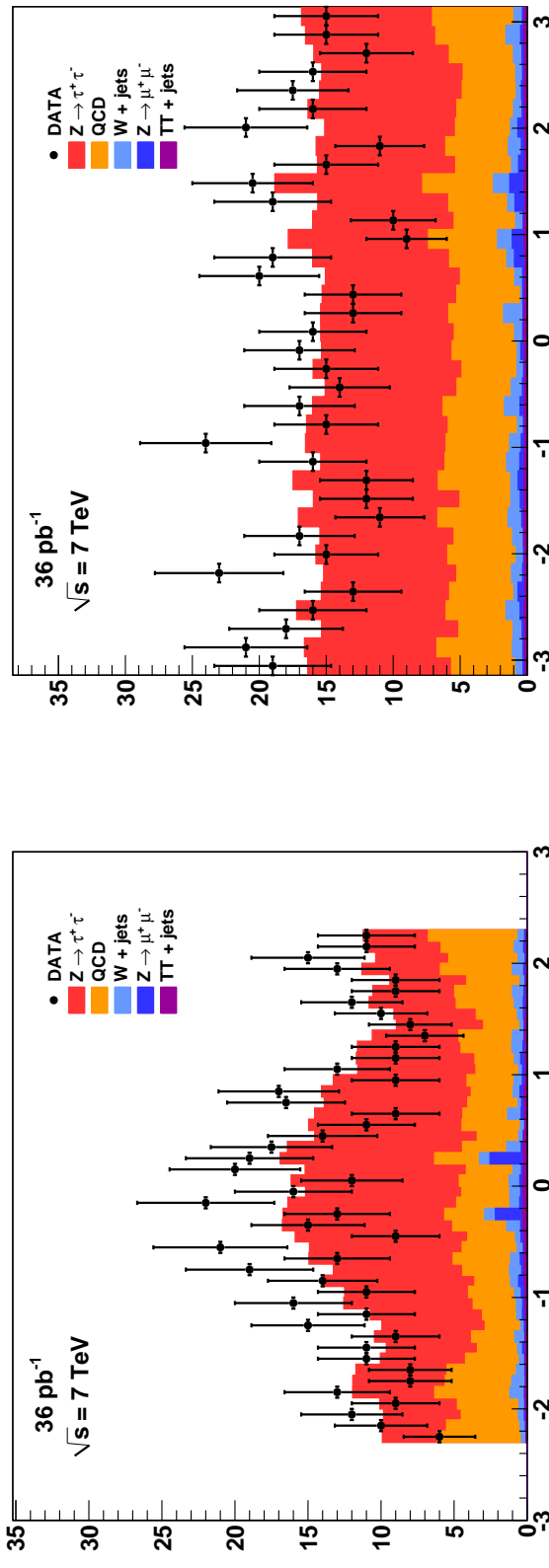
Muon (final event sample)**Tau (final event sample)**

Figure 9.2: Distribution of the η (left) and ϕ (right) of the muon (top) and hadronic tau (bottom) in Higgs $\rightarrow \tau^+\tau^- \rightarrow \mu + \tau_{had}$ candidate events passing the selection criteria described in Chapter 5.

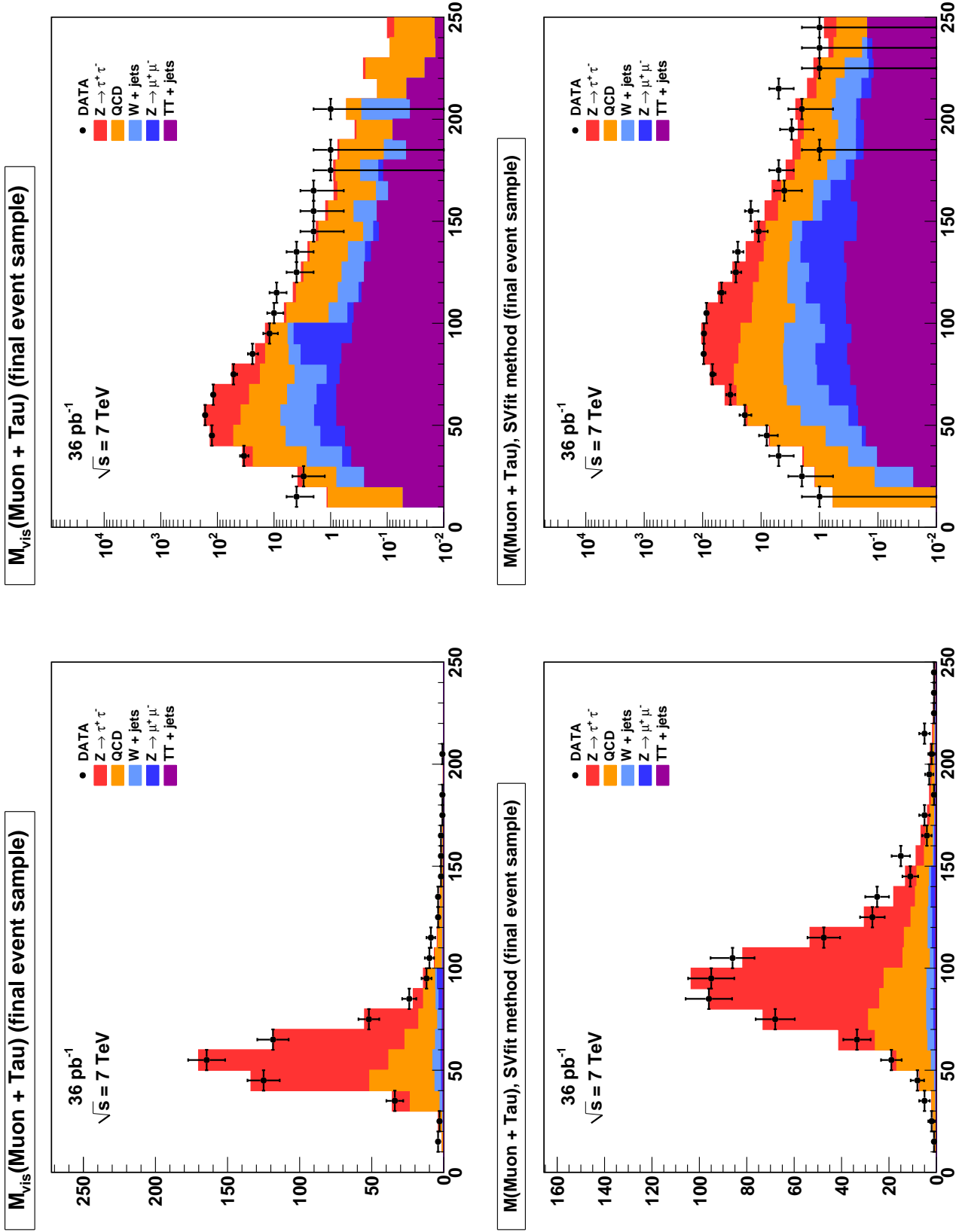


Figure 9.3: Distribution of visible (top) and “full” $\tau^+\tau^-$ invariant mass reconstructed by the SVfit algorithm (bottom) in $Higgs \rightarrow \tau^+\tau^- \rightarrow \mu + \tau_{had}$ candidate events passing the selection criteria described in Chapter 5. The distributions are shown in linear (logarithmic) scale on the left (right).

Process	Events without b -tag	Events with b -tag
Gluon fusion production		
A90	37.21	0.86
A100	27.40	0.40
A120	14.39	0.14
A130	11.81	0.18
A160	4.46	0.09
A200	1.51	0.03
A250	0.47	0.01
A300	0.15	0.0
A350	0.06	0.44
Associated b -quark production		
bbA90	33.07	5.50
bbA100	30.18	4.77
bbA120	21.91	4.02
bbA130	18.34	3.35
bbA160	10.35	2.10
bbA200	4.85	1.29
bbA250	2.11	0.55
bbA300	0.97	0.26
bbA350	0.41	0.13

Table 9.2: Number of Higgs signal event expected to pass the selection criteria described in Section 5. The expected signal yield is given for MSSM parameter $\tan \beta = 30$, using the cross sections provided by the LHC Higgs Cross Section working group.

Secondary Vertex Fit 95% CL Upper Limit (pb)						
Mass (GeV/c ²)	Expected $\sigma_H \times B_\tau$ (pb)					Observed $\sigma_H \times B_\tau$ (pb)
	-2 σ	-1 σ	Median	+1 σ	+2 σ	
90	329.2	429.2	621.9	862.9	999.1	394.7
120	30.1	41.6	59.8	82.0	116.6	86.5
130	20.7	27.6	40.5	55.6	79.4	59.9
160	10.3	13.2	19.0	26.2	35.8	28.3
200	6.3	8.3	11.2	15.8	20.2	16.4
250	4.0	5.6	7.6	10.6	14.5	12.9
300	2.9	4.0	5.7	7.8	11.1	9.4
Visible Mass 95% CL Upper Limit (pb)						
	90	120	130	160	200	250
90	376.2	523.3	688.2	980.9	998.8	573.8
120	37.0	52.1	75.4	109.2	164.1	82.6
130	26.2	35.9	52.2	74.6	117.5	64.2
160	14.3	18.3	25.1	35.2	55.1	41.2
200	8.9	11.9	16.6	22.4	32.8	31.1
250	5.9	8.1	11.5	15.9	22.3	18.1
300	4.2	5.8	8.4	11.7	15.9	10.8

Table 9.3: Expected 95% CL upper limit bands and the observed limit using the Bayesian prescription. The limit is computed using both the SVfit mass (top) as well as the visible mass (bottom) as the search observable. Use of the SVfit mass significantly improves the strength of the limit considerably.

Higgs State	Included when		
	$m_{A^0} < 130$ GeV/c ²	$m_{A^0} = 130$ GeV/c ²	$m_{A^0} > 130$ GeV/c ²
A^0	yes	yes	yes
H^0	yes	yes	no
h^0	no	yes	yes

Table 9.4: Logic for determining the MSSM Higgs cross section for a given mass of the CP-odd A^0 Higgs. In some regions of parameter space, the contributions of one of the CP-even Higgs particles is ignored.

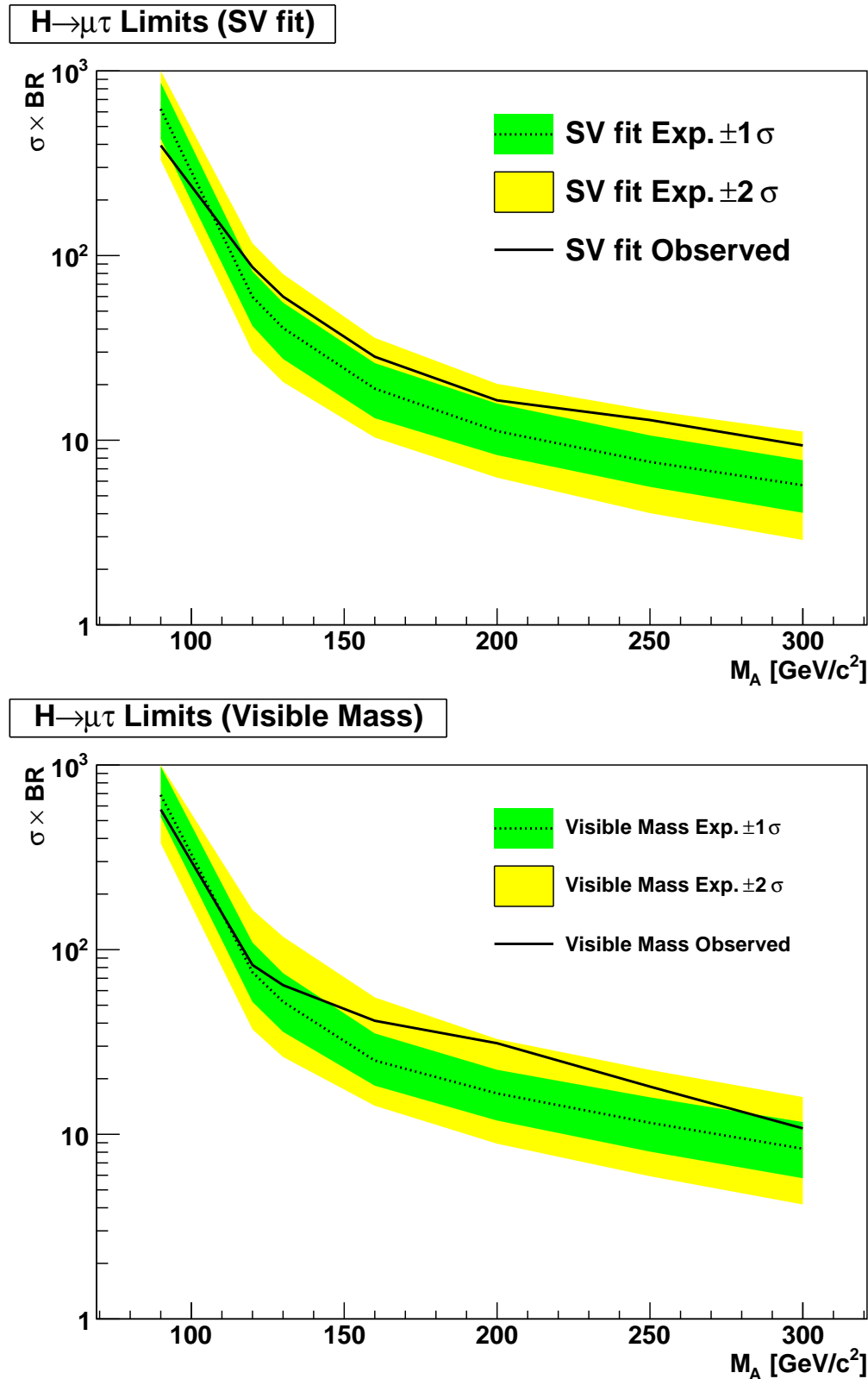


Figure 9.4: Observed and expected limits on the cross section times branching ratio of a Higgs boson versus Higgs mass. The top plot gives the limit computed using the SVfit mass as the observable, the bottom plot gives the limit computed using the visible mass. The dashed line gives the nominal expected limit. The green and yellow bands give the $+1$ and $+2$ standard deviations on the expected limit.

Figure 9.5: Region of MSSM $\tan \beta - m_{A^0}$ parameter space excluded by this analysis. THIS PLOT IS NOT DONE YET

2350 Conclusions

2351 This analysis has presented a search for MSSM Higgs bosons in the 2010 7 TeV CMS data
 2352 set. Two new experimental methods, the TaNC tau identification algorithm, and the SVfit
 2353 mass reconstruction method have been introduced in this thesis. Both methods increased
 2354 the sensitive of the Higgs search. The search was performed using 36 pb^{-1} of data. The
 2355 expected event yield from Standard Model sources is 577 events. In total, 573 events were
 2356 selected; the observed is compatible with the Standard Model. No signal-like excess of
 2357 events is observed. We set an upper limit on the production of Higgs bosons, and interpret
 2358 this limit in the context of the MSSM.

2359 The analysis presented in this thesis was part of a larger study [1] performed by the
 2360 CMS collaboration searching for the MSSM Higgs boson decaying to tau leptons. The CMS
 2361 analysis used three channels, the $H \rightarrow \tau\tau \rightarrow e - \tau_h$, $H \rightarrow \tau\tau \rightarrow e - \mu$, and the $\mu - \tau_h$
 2362 channel. The $\mu - \tau_h$ channel search presented in this thesis is very similar to the CMS result.
 2363 While not as pure as the $\mu - \tau$ channel, the inclusion of the high-statistics $e - \tau$ channel
 2364 increases the sensitivity of the CMS analysis. The $e - \mu$ channel has low statistics, but is
 2365 not sensitive to the systematic uncertainty on the hadronic tau identification. The region of
 2366 the MSSM parameter space excluded by combined CMS result is illustrated in Figure 9.3.
 2367 At the time of this writing, the CMS result described in [1] sets the most stringent limits
 2368 on the MSSM using a direct search.

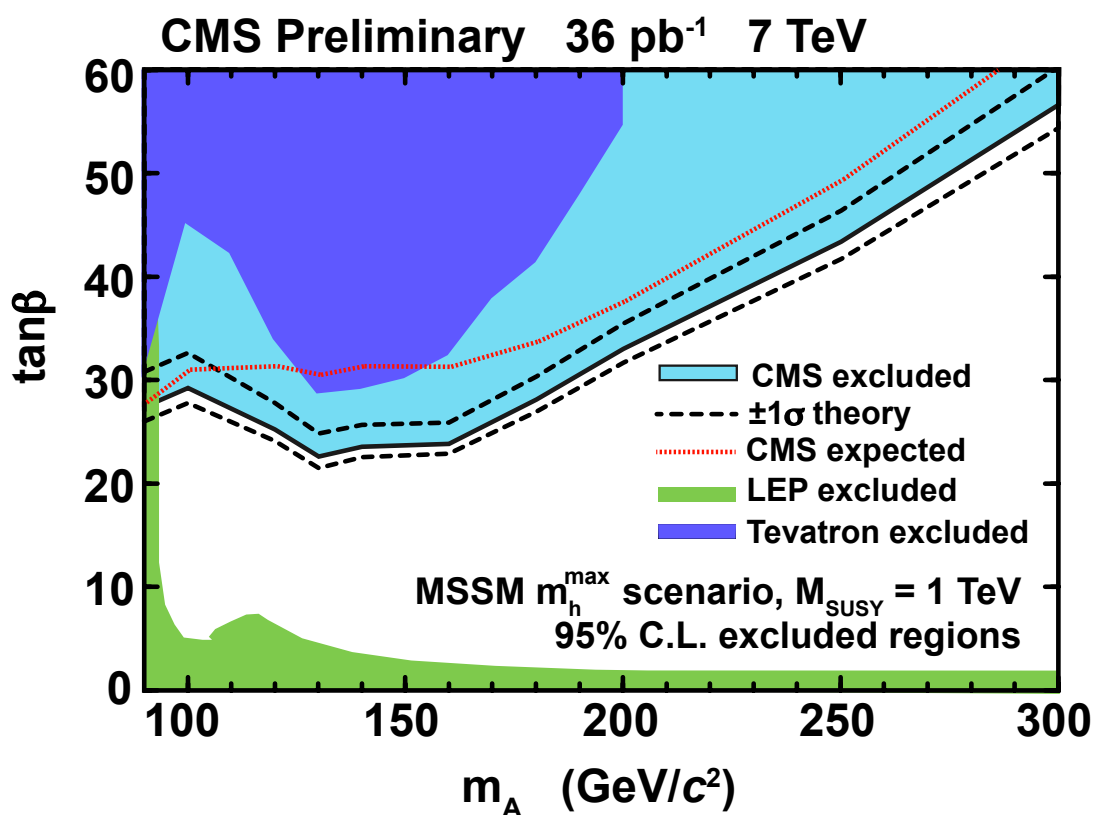


Figure 9.6: Region of MSSM $\tan\beta - m_{A^0}$ parameter space excluded by the CMS combined analysis [1].

2369 Bibliography

- 2370 [1] CMS Collaboration, “Search For Neutral MSSM Higgs Boson Production via Decays
2371 to Tau Pairs in pp Collisions at $\sqrt{s} = 7$ TeV”, *to be published* (2011).
- 2372 [2] J. Goldstone, “Field Theories with Superconductor Solutions”, *Nuovo Cim.* **19**
2373 (1961) 154–164. doi:10.1007/BF02812722.
- 2374 [3] J. Goldstone, A. Salam, and S. Weinberg, “Broken Symmetries”, *Phys. Rev.* **127**
2375 (Aug, 1962) 965–970. doi:10.1103/PhysRev.127.965.
- 2376 [4] F. Englert and R. Brout, “Broken Symmetry and the Mass of
2377 Gauge Vector Mesons”, *Phys. Rev. Lett.* **13** (Aug, 1964) 321–323.
2378 doi:10.1103/PhysRevLett.13.321.
- 2379 [5] P. W. Higgs, “Broken Symmetries and the Masses of Gauge Bosons”, *Phys. Rev.*
2380 *Lett.* **13** (Oct, 1964) 508–509. doi:10.1103/PhysRevLett.13.508.
- 2381 [6] G. S. Guralnik, C. R. Hagen, and T. W. B. Kibble, “Global Conservation
2382 Laws and Massless Particles”, *Phys. Rev. Lett.* **13** (Nov, 1964) 585–587.
2383 doi:10.1103/PhysRevLett.13.585.
- 2384 [7] S. Glashow, “Partial Symmetries of Weak Interactions”, *Nucl.Phys.* **22** (1961) 579–
2385 588. doi:10.1016/0029-5582(61)90469-2.
- 2386 [8] S. Weinberg, “A Model of Leptons”, *Phys.Rev.Lett.* **19** (1967) 1264–1266.
2387 doi:10.1103/PhysRevLett.19.1264.
- 2388 [9] A. Salam, “Weak and Electromagnetic Interactions”, Originally printed in
2389 *Svartholm: Elementary Particle Theory, Proceedings Of The Nobel Symposium
2390 Held 1968 At Lerum, Sweden*, Stockholm 1968, 367–377.
- 2391 [10] D. Griffiths, “Introduction to Elementary Particles”. Wiley-VCH, 2004.
- 2392 [11] E. Fermi, “An attempt of a theory of beta radiation. 1”, *Z. Phys.* **88** (1934) 161–
2393 177. doi:10.1007/BF01351864.
- 2394 [12] S. M. T. Morii, C.S. Lim, “The Physics of the Standard Model and Beyond”. World
2395 Scientific, 2004.
- 2396 [13] UA1 Collaboration, “Experimental observation of isolated large transverse energy
2397 electrons with associated missing energy at $\sqrt{s} = 540$ GeV”, *Phys. Lett.* **B122**
2398 (1983) 103–116.
- 2399 [14] UA2 Collaboration, “Observation of single isolated electrons of high transverse mo-
2400 mentum in events with missing transverse energy at the CERN $\bar{p}p$ collider”, *Phys.*
2401 *Lett.* **B122** (1983) 476–485. doi:10.1016/0370-2693(83)91605-2.

- 2402 [15] UA1 Collaboration, “Experimental observation of lepton pairs of invariant mass
 2403 around $95 \text{ GeV}/c^2$ at the CERN SPS collider”, *Phys. Lett.* **B126** (1983) 398–410.
 2404 doi:10.1016/0370-2693(83)90188-0.
- 2405 [16] UA2 Collaboration, “Evidence for $Z^0 \rightarrow e^+e^-$ at the CERN $\bar{p}p$ collider”, *Phys. Lett.*
 2406 **B129** (1983) 130–140. doi:10.1016/0370-2693(83)90744-X.
- 2407 [17] S. P. Martin, “A Supersymmetry Primer”, *arXiv hep-ph* (sep, 1997). 128 pages.
 2408 Version 5 (December 2008) contains a change in convention that flips the signs of
 2409 sigma and sigmabar matrices. It also contains a total of about 2 pages of updates,
 2410 mostly on supersymmetry breaking issues. Errata and a version with larger type (12
 2411 pt, 142 pages) can be found at <http://zippy.physics.niu.edu/primer.html>.
- 2412 [18] CERN Computing Newsletter.
- 2413 [19] D. L. Rainwater, D. Zeppenfeld, and K. Hagiwara, “Searching for $H \rightarrow \tau^+\tau^-$
 2414 in weak boson fusion at the LHC”, *Phys. Rev.* **D59** (1999) 014037, arXiv:hep-
 2415 ph/9808468. doi:10.1103/PhysRevD.59.014037.
- 2416 [20] Particle Data Group Collaboration, “Review of particle physics”, *J. Phys.* **G37**
 2417 (2010) 075021. doi:10.1088/0954-3899/37/7A/075021.
- 2418 [21]
- 2419 [22] LHC Higgs Cross Section Working Group Collaboration, “Handbook of LHC Higgs
 2420 Cross Sections: 1. Inclusive Observables”, arXiv:1101.0593.
- 2421 [23] M. Carena, S. Heinemeyer, C. Wagner et al., “MSSM Higgs boson searches at the
 2422 Tevatron and the LHC: Impact of different benchmark scenarios”, *The European
 2423 Physical Journal C - Particles and Fields* **45** (2006) 797–814. 10.1140/epjc/s2005-
 2424 02470-y.
- 2425 [24] CMS Collaboration, “The CMS experiment at the CERN LHC”, *JINST* **3** (2008)
 2426 S08004.
- 2427 [25] CMS Collaboration, “Measurement of Momentum Scale and Resolution using Low-
 2428 mass Resonances and Cosmic-Ray Muons”, *CMS PAS CMS-PAS-TRK-10-004*
 2429 (2010).
- 2430 [26] CMS Collaboration, “Tracking and Primary Vertex Results in First 7 TeV Collisions”,
 2431 *CMS PAS CMS-PAS-TRK-10-005* (2010).
- 2432 [27] G. L. Bayatian et al., “CMS Physics Technical Design Report Volume I: Detector
 2433 Performance and Software”. Technical Design Report CMS. CERN, Geneva, 2006.
- 2434 [28] CMS Collaboration, “CMS Strategies for tau reconstruction and identification using
 2435 particle-flow techniques”, *CMS PAS CMS-PAS-PFT-08-001* (2008).
- 2436 [29] CMS Collaboration, “Particle-Flow Event Reconstruction in CMS and Performance
 2437 for Jets, Taus, and MET”, *CMS PAS CMS-PAS-PFT-09-001* (2009).
- 2438 [30] A. Hoecker et al., “TMVA - Toolkit for Multivariate Data Analysis”, *ArXiv Physics
 2439 e-prints* (March, 2007) arXiv:arXiv:physics/0703039.

- 2440 [31] A. Kolmogorov, “On the representation of continuous functions of several variables
 2441 by superposition of continuous functions of one variable and addition”, *Doklady
 2442 Akademii Nauk SSSR* **114** (1957).
- 2443 [32] J. C. *et al.*, “Size of signal cones and isolation rings in the CMS tau identification
 2444 algorithm”, *CMS Note* **2008/026** (2008).
- 2445 [33] M. Bachtis, S. Dasu, and A. Savin, “Prospects for measurement of $\sigma(pp \rightarrow Z) \cdot B(Z \rightarrow \tau^+\tau^-)$ with CMS in pp Collisions at $\sqrt{s} = 7$ TeV”, *CMS Note*
 2446 **2010/082** (2010).
- 2447 [34] CMS Collaboration, “Study of tau reconstruction algorithms using pp collisions data
 2448 collected at $\sqrt{s} = 7$ TeV”, *CMS PAS CMS-PAS-PFT-10-004* (2010).
- 2449 [35] G. P. S. M. Cacciari and G. Soyez, “The anti-kt jet clustering algorithm”, *JHEP*
 2450 **04** (2008) 063, arXiv:0802.1189.
- 2451 [36] CMS Collaboration, “Commissioning of the Particle–Flow reconstruction in
 2452 Minimum–Bias and Jet Events from pp Collisions at 7 TeV”, *CMS PAS PFT-10-*
 2453 **002** (2010).
- 2454 [37] S. M. T. Sjöstrand and P. Skands, “PYTHIA 6.4 Physics and Manual”, 2000.
- 2455 [38] S. Jadach, Z. Was, R. Decker *et al.*, “The Tau Decay Library Tauola: Version 2.4”,
 2456 *Comput. Phys. Commun.* **76** (1993) 361.
- 2457 [39] S. Agostinelli, J. Allison, K. Amako *et al.*, “G4—a simulation toolkit”, *Nuclear
 2458 Instruments and Methods in Physics Research Section A: Accelerators, Spec-
 2459 trometers, Detectors and Associated Equipment* **506** (2003), no. 3, 250 – 303.
 2460 doi:10.1016/S0168-9002(03)01368-8.
- 2461 [40] CDF Collaboration, “Search for MSSM Higgs decaying to τ pairs in $p\bar{p}$ collision at
 2462 $\sqrt{s} = 1.96$ TeV at CDF”, *Phys. Rev. Lett.* **96** (2006).
- 2463 [41] CMS Collaboration, “CMS technical design report, volume II: Physics performance”,
 2464 *J. Phys.* **G34** (2007) 995–1579. doi:10.1088/0954-3899/34/6/S01.
- 2465 [42] L. Bianchini, “Improved Collinear Approximation for VBF $H \rightarrow \tau\tau \rightarrow 3\nu + \ell + \tau_{had}$ ”,
 2466 *CMS Note* **2010/226** (2010).
- 2467 [43] B. K. Bullock, K. Hagiwara, and A. D. Martin, “Tau Polarization And Its Corre-
 2468 lations As A Probe Of New Physics”, *Nucl. Phys.* **B 395** (1993) 499.
- 2469 [44] CMS Collaboration, “Measurements of Inclusive W and Z Cross Sections in pp Col-
 2470 lisions at $\sqrt{s} = 7$ TeV”, *CMS PAS EWK-10-002* (2010).
- 2471 [45] CMS Collaboration, “MET Performance in Events Containing Electroweak Bosons
 2472 from pp Collisions at $\sqrt{s} = 7$ TeV”, *CMS PAS JME-10-005* (2010).
- 2473 [46] C. C. Almenar, “Search for the neutral MSSM Higgs bosons in the $\tau\tau$ decay channels
 2474 at CDF Run II”. PhD thesis, Departament de Física Atomica, Molecular i Nuclear
 2475 (Universitat de València and IFIC (CSIC - Universitat de València), 2008.
- 2476

- 2477 [47] L. Lusito and C. Veelken, “Estimation of Background contributions to Tau analyses
2478 via Template Fitting”, *CMS Note* **2010/088** (2010).
- 2479 [48] CMS Collaboration, “Performance of tau reconstruction algorithms in 2010 data col-
2480 lected with CMS”, *CMS PAS TAU-11-001* (2011).
- 2481 [49] D. Jang, “Search for MSSM Higgs decaying to τ pairs in $p\bar{p}$ collision at $\sqrt{s} =$
2482 1.96 TeV at CDF”, *Ph.D. Thesis, Rutgers University* (2006).
- 2483 [50] J. Conway, E. Friis, and C. Veelken, “Measurement of the $Z/\gamma^* \rightarrow \tau^+\tau^-$ Production
2484 Cross-section in the $\mu + \tau_{had}$ final state using the HPS+TaNC Tau id. algorithm”,
2485 *CMS Note* **2011/021** (2011).
- 2486 [51] J. Conway, E. Friis, M. Squires et al., “The Tau Neural Classifier algorithm: tau
2487 identification and decay mode reconstruction using neural networks”, *CMS Note*
2488 **2010/099** (2010).
- 2489 [52] T. Früboes and M. Zeise, “The TauAnalysis/MCEmbeddingTools Package”.
2490 <https://twiki.cern.ch/twiki/bin/view/CMS/SWGuideTauAnalysisMCEmbeddingTools>.
- 2491 [53] CMS Collaboration, “Measurement of the Inclusive $Z \rightarrow \tau\tau$ Cross Section in pp Col-
2492 lisions at $\sqrt{s} = 7$ TeV”, *to be published* (2011).
- 2493 [54] S. Bolognesi, M. A. Borgia, R. Castello et al., “Calibration of track momentum using
2494 dimuon resonances in CMS”, *CMS Note* **2010/059** (2010).
- 2495 [55] CMS Collaboration, “Jet Energy Corrections determination at $\sqrt{s} = 7$ TeV”, *CMS
2496 PAS JME-10-010* (2010).
- 2497 [56] G. Bauer et al., “Modeling of $W \rightarrow \ell\nu$ MET with Boson Recoil”, *CMS Note*
2498 **2010/332** (2010).
- 2499 [57] G. Cerati et al., “Search for MSSM neutral Higgs $\rightarrow \tau^+\tau^-$ Production using the
2500 TaNC Tau id. algorithm”, *CMS Note* **2010/460** (2010).
- 2501 [58] CMS Collaboration, “Absolute luminosity normalization”, *CMS Detector Perfor-
2502 mance Summary* **CMS-DPS-2011-002** (2008).
- 2503 [59] J. Alcaraz. <https://twiki.cern.ch/twiki/bin/view/CMS/SWGuideEWKUtilities>.
- 2504 [60] P. M. Nadolsky et al., “Implications of CTEQ global analysis for collider observ-
2505 ables”, *Phys. Rev.* **D 78** (2008) 013004, arXiv:0802.0007.
- 2506 [61] PDF4LHC Working Group. <http://www.hep.ucl.ac.uk/pdf4lhc/PDF4LHCrecos.pdf>.
- 2507 [62] R. C. G. D. Bourilkov and M. R. Whalley, “LHAPDF: PDF use from the Tevatron
2508 to the LHC”, arXiv:0605.0240.
- 2509 [63] LHC Higgs Cross Section Working Group Collaboration *arXiv:hep-ex/1101.0593*
2510 (2011).